



UNIVERSIDADE FEDERAL DA BAHIA
INSTITUTO DE GEOCIÊNCIAS
PROGRAMA DE PESQUISA E PÓS-GRADUAÇÃO EM GEOLOGIA
ÁREA DE CONCENTRAÇÃO:
PETROLOGIA, METALOGÊNESE E EXPLORAÇÃO MINERAL

TESE DE DOUTORADO

**MINERALIZAÇÕES DE FOSFATO PALEOPROTEROZOICO NO
NORDESTE DO CRÁTON DO SÃO FRANCISCO: CONDIÇÕES
PALEOAMBIENTAIS E O EVENTO LOMAGUNDI-JATULI**

TATIANA SILVA RIBEIRO

SALVADOR

2023

MINERALIZAÇÕES DE FOSFATO PALEOPROTEROZOICO NO NORDESTE DO CRÁTON DO SÃO FRANCISCO: CONDIÇÕES PALEOAMBIENTAIS E O EVENTO LOMAGUNDI-JATULI

Tatiana Silva Ribeiro

Orientador: Prof. Dr. Aroldo Misi

Tese apresentada ao Curso de Pós-graduação em Geologia, Instituto de Geociências da Universidade Federal da Bahia, como requisito parcial à obtenção do Título de Doutora em Geologia, Área de Concentração: Petrologia, Metalogênese e Exploração Mineral.

SALVADOR

2023

Ficha catalográfica elaborada pela Biblioteca Universitária de Ciências e Tecnologias Prof. Omar Catunda, SIBI – UFBA.

R484 Ribeiro, Tatiana Silva

Mineralizações de fosfato Paleoproterozoico no nordeste do Cráton do São Francisco: condições paleoambientais e o Evento Lomagundi-Jatuli / Tatiana Silva Ribeiro. – Salvador, 2023.

130 f.

Orientador: Prof. Dr. Aroldo Misi

Tese (Doutorado) – Universidade Federal da Bahia. Instituto de Geociências, 2023.

1. Fosfato. 2. Petrologia. 3. Mármore. I. Misi, Aroldo. II. Universidade Federal da Bahia. III. Título.

CDU 552.3

TATIANA SILVA RIBEIRO

MINERALIZAÇÕES DE FOSFATO PALEOPROTEROZOICO NO NORDESTE DO CRÁTON DO SÃO FRANCISCO: CONDIÇÕES PALEOAMBIENTAIS E O EVENTO LOMAGUNDI-JATULI

Tese apresentada ao Programa de Pós-Graduação em Geologia da Universidade Federal da Bahia, como requisito para a obtenção do Grau de Doutora em Geologia na área de concentração em Petrologia, Metalogênese e Exploração Mineral em 21/12/2023.

TESE APROVADA PELA BANCA EXAMINADORA:



Dr. Aroldo Misi
Orientador – PPPGG/UFBA



Documento assinado digitalmente

JULIANA CHARAO MARQUES

Data: 15/02/2024 19:09:07-0300

Verifique em <https://validar.iti.gov.br>

Dra. Juliana Charão Marques Examinador
Externo – PPPGG/ UFRGS



Documento assinado digitalmente

PAULO CESAR BOGGIANI

Data: 15/02/2024 18:18:27-0300

Verifique em <https://validar.iti.gov.br>

Dr. Paulo Cesar Boggiani Examinador
Externo – PPPGG/USP



Documento assinado digitalmente

CARLSON DE MATOS MAIA LEITE

Data: 15/02/2024 11:36:38-0300

Verifique em <https://validar.iti.gov.br>

Dr. Carlson de Matos Maia Leite
Examinador Interno – PPPGG/ UFRGS



Dra. Simone Cerqueira Pereira Cruz
Examinador Interno – PPPGG/UFBA

Salvador – BA
2023

*"Resiliência não é apenas superar, é florescer,
mesmo nas condições mais adversas."*

AGRADECIMENTOS

Gostaria de expressar os meus sinceros agradecimentos a todas as pessoas e instituições que contribuíram para a realização desta tese. Em primeiro lugar, à Deus por ter me dado a oportunidade de realizar e concluir esse trabalho com resiliência, pois, mesmo nas situações mais adversas, a fé e gratidão sempre foram as minhas melhores escolhas. À minha família por apoio incondicional e compreensão nos momentos de ausência, especialmente a Antônio, Ana Lúcia e Artur, e ao meu esposo Iderson.

Minha profunda gratidão aos amigos(as) e colegas que estiveram ao meu lado durante esta jornada acadêmica desafiadora. Sem o apoio de vocês, essa conquista não teria sido possível.

Em especial, ao meu amigo Luís Rodrigues que participou, efetivamente, de todo o meu doutorado. Ele sempre esteve disposto a ouvir, discutir e compartilhar novas ideias, independente do fuso horário. Agradeço pelas suas importantes contribuições na construção e discussão. Juntos aprendemos e crescemos, superando desafios e celebrando vitórias ao longo desses anos.

Agradeço também a Pedro Maciel por toda a sua sabedoria, disposição em ajudar e importantes contribuições nas figuras e na discussão deste trabalho.

Aos meus orientadores (mestres e amigos) Aroldo Misi e Haroldo Sá, por ter me guiado ao longo deste caminho acadêmico. Suas orientações e conselhos foram muito importantes na minha formação acadêmica e profissional. Registro aqui toda a minha admiração a meu orientador, pelo seu otimismo e coragem, um exemplo de vida acadêmica e pessoal.

Aos professores Débora Rios, Ângela Leal, Ernane Melo e Simone Cruz que fazem parte da minha história desde a graduação e são assim referências para mim.

Aos amigos do Grupo de Metalogênese e Modelos Metalogenéticos.

Aos novos amigos da Universidade Estadual de Feira de Santana que também caminharam comigo até aqui.

Ao Instituto de Geociências da Universidade Federal da Bahia, Companhia Baiana de Pesquisa Mineral (CBPM) pelo financiamento do projeto de pesquisa e apoio de campo. O presente trabalho foi realizado com o apoio da CAPES - Código de financiamento 001.

Esta tese é o resultado de esforços coletivos e amizades que se fortaleceram ao longo dos anos. Sou profundamente grata por ter cada um de vocês em minha vida.

RESUMO

No Nordeste da Bahia são encontradas importantes sucessões metassedimentares associadas ao Cráton do São Francisco. São corpos alongados N-S e NW-SE, intrudidos por granitoides e metamorfizados nas fácies xisto-verde a granulito. Destacam-se as sucessões siliciclásticas, pelíticas e químicas como mármore, calcissilicáticas, quartzitos, grafita-xistos, formações ferríferas e rochas aluminosas do Complexo Tanque Novo – Ipirá (TNIC), da região do Vale do Jacurici (JV) e do Complexo Rio Salitre (RSC). No TNIC os mármore e calcissilicáticas são hospedeiras de mineralizações primárias de fosfato (apatita) disseminada com teores de P_2O_5 de até 3,2%. Apesar do metamorfismo é possível identificar registros das assinaturas primárias a partir do comportamento dos elementos terras-raras e ítrio. Quando normalizadas para o Folhelho Pós-Arqueano (*Post-Archean Australian Shale*), são marcadas por padrões depletados de elementos terras-raras leves, anomalias negativas verdadeiras de Ce, anomalias positivas de Y e Gd. As anomalias de Eu são variáveis e herdadas da composição da fonte ou alteradas por fluidos metassomáticos. A formação das sequências carbonáticas do TNIC e JV ocorreram em margem continental de um paleooceno e em um mar aberto, ambos com *inputs* continentais, provenientes das margens ou de arcos magmáticos. Enquanto no RSC estão relacionadas com um mar aberto desenvolvido em rifte continental. As excursões positivas $\delta^{13}C$ em mármore do TNIC possuem valores entre +6,13 a + 7,36%. Duas amostras apresentam $\delta^{13}C$ de +9,38 a +9,69 e uma amostra com $\delta^{13}C$ negativo (- 5,72%) foi modificada por efeitos metassomáticos em zona escarnítica. No RSC os mármore também apresentam excursões $\delta^{13}C$ de +5.38 e +6.78%. Os dados isotópicos de $\delta^{13}C$ são similares aos de carbonatos marinhos da Formação Paso Severino (Uruguai), com $\delta^{13}C$ de +9,0%. O evento global Lomagundi-Jatuli (~2,3 a 2,1 Ga) possui excursões positivas de $\delta^{13}C$ entre +5 e +10% em carbonatos marinhos de diversos crátons mundiais de idade paleoproterozoica que abrigam mineralizações de fosfato, como o Cráton Rio de La Plata (Argentina), o Complexo Slyudyanka (Rússia) e os mármore do Vale do Jacurici no Cráton do São Francisco. A idade máxima de deposição do TNIC é de 2128 Ma (U/Pb – LA-ICPMS) obtida em quartzito da sequência metassedimentar superior. Desta forma, as deposições de fosfato e ferro de origem continental, estão associadas como registros de maior taxa de oxigenação da atmosfera e oceanos e atividade biogênica, sendo compatíveis com as mudanças paleoclimáticas ocorridas no Paleoproterozoico. As sequências carbonáticas foram precipitadas no final do Grande Evento de Oxigenação da Terra e no final do evento Lomagundi-Jatuli, depois da quarta e última (2,2 Ga) de uma série de glaciações iniciadas em 2,42 Ga. Os mármore são correlacionáveis com as rochas metassedimentares no terreno do Vale do Jacurici e Complexo Rio Salitre quanto às condições paleoambientais, à origem marinha e às mineralizações de fosfato. Esses dados são compatíveis com o evento fosfogenético mais antigo em bacias paleoproterozoicas e registram a oxigenação atmosférica e oceânica.

Palavras-chave: Fosfogênese, Lomagundi-Jatuli, Mármore, Calcissilicáticas.

ABSTRACT

In the Northeast region of Bahia, important metasedimentary successions associated with the São Francisco Cráton. They are elongated N-S and NW-SE bodies, intruded by granitoids and metamorphosed in the high amphibolite to granulite facies. The siliciclastic, pelitic and chemical successions stand out, such as marble, calcisilicate rock, quartzite, graphite-schist, iron formations and aluminous rocks from the Tanque Novo – Ipirá Complex (TNIC), the Vale do Jacurici region (JV) and the Rio Salitre Complex (RSC). TNIC marble and calcisilicates are hosts of primary phosphate mineralization (apatite) with a disseminated form and P_2O_5 contents of up to 3.2%. Despite metamorphism, it is possible to identify records of primary signatures based on the behavior of rare earth elements and yttrium. When normalized to the Post-Archaean Shale (PAAS), they are marked by light rare-earth element depleted patterns, true negative Ce anomalies, positive Y and Gd anomalies. Eu anomalies are variable and inherited from the source composition or altered by metasomatic fluids. The formation of the carbonate sequence from TNIC and JV occurred on the continental margin of a paleo ocean and in an open sea, both with continental inputs, coming from the margins or magmatic arcs. In the RSC, they are related to an open sea developed into a continental rift. The positive $\delta^{13}C$ excursions in TNIC marbles have values between +6.13 to + 7.36%. Two samples have $\delta^{13}C$ from +9.38 to +9.69 and one sample with negative $\delta^{13}C$ (- 5.72%) was reduced by metasomatic effects in the skarn zone. The $\delta^{13}C$ isotopic data are similar to marine carbonates from the Paso Severino Formation (Uruguay), with $\delta^{13}C$ of +9.0%. On RSC the marbles also present $\delta^{13}C$ excursions of +5.38 and +6.78%. The global Lomagundi-Jatuli event (~2.3 to 2.1 Ga) has positive $\delta^{13}C$ excursions between +5 and +10% in marine carbonates from several global cratons of Paleoproterozoic age that harbor phosphate mineralization, such as the Rio de La Plata (Argentina), Slyudyanka Complex (Russia) and marbles from the Jacurici Valley in the São Francisco Craton. The maximum age of deposition of the TNIC is 2128 Ma (U/Pb – LA-ICPMS) obtained in quartzite from the upper metasedimentary sequence. Thus, the deposition of phosphate and iron of continental origin are associated with a record of higher oxygenation rates of the atmosphere and oceans and biogenic activity, being compatible with the paleoclimatic changes that occurred in the Paleoproterozoic. The carbonate sequence were precipitates at the end of the Great Earth Oxygenation Event and at the end of the Lomagundi-Jatuli event, after the fourth and final (2.2 Ga) of a series of glaciations beginning in 2.42 Ga. The marbles are correlated with the metasediments in the Jacurici Valley terrain in terms of paleoenvironmental conditions, marine origin and phosphate mineralization. These data are compatible with the earliest phosphogenetic event in Paleoproterozoic basins and record atmospheric and oceanic oxygenation.

Keywords: Phosphogenesis, Lomagundi-Jatuli, Marbles, Calcisilicates.

SUMÁRIO

| | |
|--|-----|
| CAPÍTULO 1 – INTRODUÇÃO GERAL | 8 |
| CAPÍTULO 2 – ARTIGO 1 - EVIDENCE OF PALEOPROTEROZOIC PHOSPHOGENESIS IN THE SALVADOR-CURAÇÁ OROGEN (TANQUE NOVO-IPIRÁ COMPLEX), NORTHEASTERN SÃO FRANCISCO CRATON, BRAZIL | 15 |
| CAPÍTULO 3 – ARTIGO 2 - POSITIVE $\delta^{13}\text{C}_{\text{carb}}$ EXCURSIONS IN PALEOPROTEROZOIC MARBLES FROM THE NORTHEAST SÃO FRANCISCO CRATON, BRAZIL: PHOSPHOGENETIC AND GEOTECTONIC IMPLICATIONS | 46 |
| CAPÍTULO 4 – CONCLUSÕES | 96 |
| APÊNDICE A – JUSTIFICATIVA DA PARTICIPAÇÃO DOS CO-AUTORES | 100 |
| APÊNDICE B – MICROSCOPIA ELETRÔNICA DE VARREDURA | 103 |
| APÊNDICE C – DIFRATOMETRIA DE RAIOS-X | 115 |
| ANEXO A – REGRAS DE FORMATAÇÃO DA BRAZILIAN JOURNAL OF GEOLOGY | 119 |
| ANEXO B – REGRAS DE FORMATAÇÃO DA INTERNATIONAL GEOLOGY REVIEW | 126 |
| ANEXO C – COMPROVANTE DE SUBMISSÃO DO ARTIGO 1 | 128 |
| ANEXO D – COMPROVANTE DE PUBLICAÇÃO DO ARTIGO 1 | 129 |
| ANEXO E – COMPROVANTE DE SUBMISSÃO DO ARTIGO 2 | 130 |

A transição Neoarqueano – Paleoproterozoico é marcada por mudanças paleoambientais, paleoclimáticas e paleogeográficas dramáticas induzidas por mudanças geotectônicas. A separação inicial do supercontinente *Kenorland* (2.5 – 2.4 Ga), após a primeira deglaciação Huroniana formou as primeiras bacias sedimentares desta era (Bekker e Eriksson, 2003). Nesta transição a alta produção fotossintética de cianobactérias promoveu um aumento do conteúdo de oxigênio nos oceanos e na atmosfera, denominado *Great Oxigenation Earth* (GOE) e teve consequências positivas na formação das mineralizações de fosfatos em escala global (Nelson et al. 2010, Pufahl and Hiatt 2012, Papineau et al. 2013).

Dessa forma os depósitos de fosfatos paleoproterozoicos (Sideriano a Estateriano) estão associados a essas mudanças na hidrosfera e atmosfera, onde uma sequência de glaciações e deglaciações combinadas com a presença de oxigênio geraram um intenso intemperismo químico, aumentando assim o aporte de sedimentos continentais com P e Fe para os oceanos (Figura 1). A ação de bactérias anaeróbicas e a presença de matéria orgânica auxiliaram a disponibilizar e fixar o fósforo em sedimentos marinhos sob diversas condições de oxigenação (Papineu, 2010 e Nelson et al, 2010).

Esse mesmo período registra importantes excursões positivas de $\delta^{13}\text{C}$ entre +5 e 10‰ (e superiores) em unidades carbonáticas marinhas com dezenas a várias centenas de metros de espessura desenvolvido entre 2.3 e 2.1 Ga (Melezhik et al. 2007; Martin et al. 2013; Gumsley et al. 2017), caracterizando o Evento Lomagudi – Jatuli (ELJ). O ELJ é ainda muito discutido quanto à sua origem, se configura um evento global ou local, como é demonstrado por Hodgskiss et al., (2023). Entretanto, este evento possui uma magnitude e duração únicas na história da Terra e desenvolveu-se em todos os continentes após a glaciação huroniana (Melezhik et al., 2005b), sendo é posterior ao acúmulo inicial de O_2 atmosférico (Bekker et al., 2004; Hannah et al., 2004).

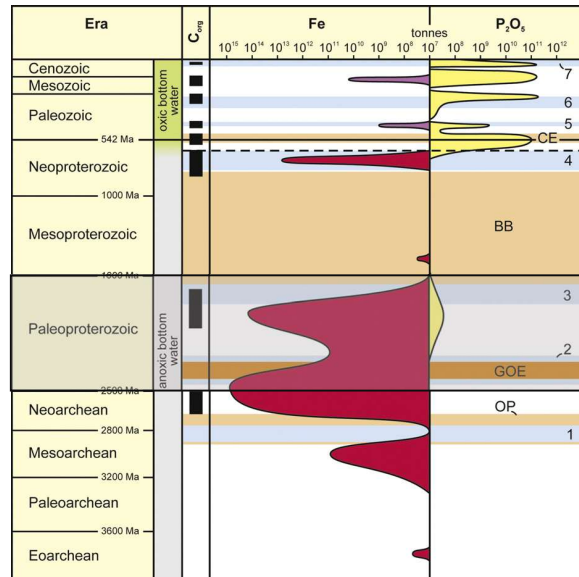


Figura 1 - Distribuição temporal de formações de ferríferas (vermelha), *ironstone* (roxo), fosforito (amarelo) e folhelho negro (preto), com destaque para o pico fosfogenético pós Great Oxygen Event (Grande Evento de Oxigenação) – GOE. Com base na idade do depósito, estimativa de recursos e cronologia de eventos da Terra, adaptado de Pufahl e Hiatt (2012). Eventos: OP = aparecimento da fotossíntese aeróbica; GOE = Great Oxygen Event; BB = Boring Billion; CE = Explosão Cambriana. Glaciações: 1 = Mesoarqueano; 2 = Huroniano; 3 = Paleoproterozoico; 4 = "Snowball Earth" Neoproterozoico; 5 = Ordoviciano; 6 = Permiano; 7 = Neogeno.

A área de estudo está localizada na região nordeste do embasamento do Cráton do São Francisco, e compreende as rochas metassedimentares metamorfizadas nas fácies anfíbolito alto a granulito do Complexo Tanque Novo-Ipirá (Ribeiro, 2016; Ribeiro, 2017 e Ribeiro et al, 2021) e Vale do Jacurici (Gama, 2014, Gama et al, 2021), no Orógeno Salvador-Curaçá. Além do Complexo Rio Salitre (Sá, 1982; Sá, 1984; Leite, 1983; Leite, 1984, Oliveira, 2016), localizado na bloco Gavião e metamorfizados na fácies xisto-verde (Figura 2 A – B). Nessas três áreas as mineralizações primárias de fosfato associam-se com rochas calcissilicáticas, mármore, formações ferríferas, quartzitos e grafita-xistos.

Os Complexos Tanque Novo – Ipirá e Salitre abrigam mineralizações primárias de fosfato disseminada e teores de P_2O_5 de até 11% em mármore e rochas calcissilicáticas (Ribeiro et al. 2021, Oliveira, 2016). Nas rochas metassedimentares do Vale do Jacurici, as mineralizações chegam até 4,56 % em mármore e rochas calcissilicáticas (Gama et al., 2021). Notadamente, no Orógeno Salvador-Curaçá as litofácies carbonáticas e calcissilicáticas apresentam implicações metalogenéticas, relacionadas principalmente com mármore dolomítico, rochas calcissilicáticas e escarnitos. Os escarnitos estão associados com a reconcentração do fosfato, formando apatitas hidrotermais em zonas de contato de pegmatitos com os metassedimentos mineralizados no Complexo Tanque Novo - Ipirá. Enquanto na bloco Gavião, além destas litofácies, as sequências pelíticas também registram ocorrências de fósforo.

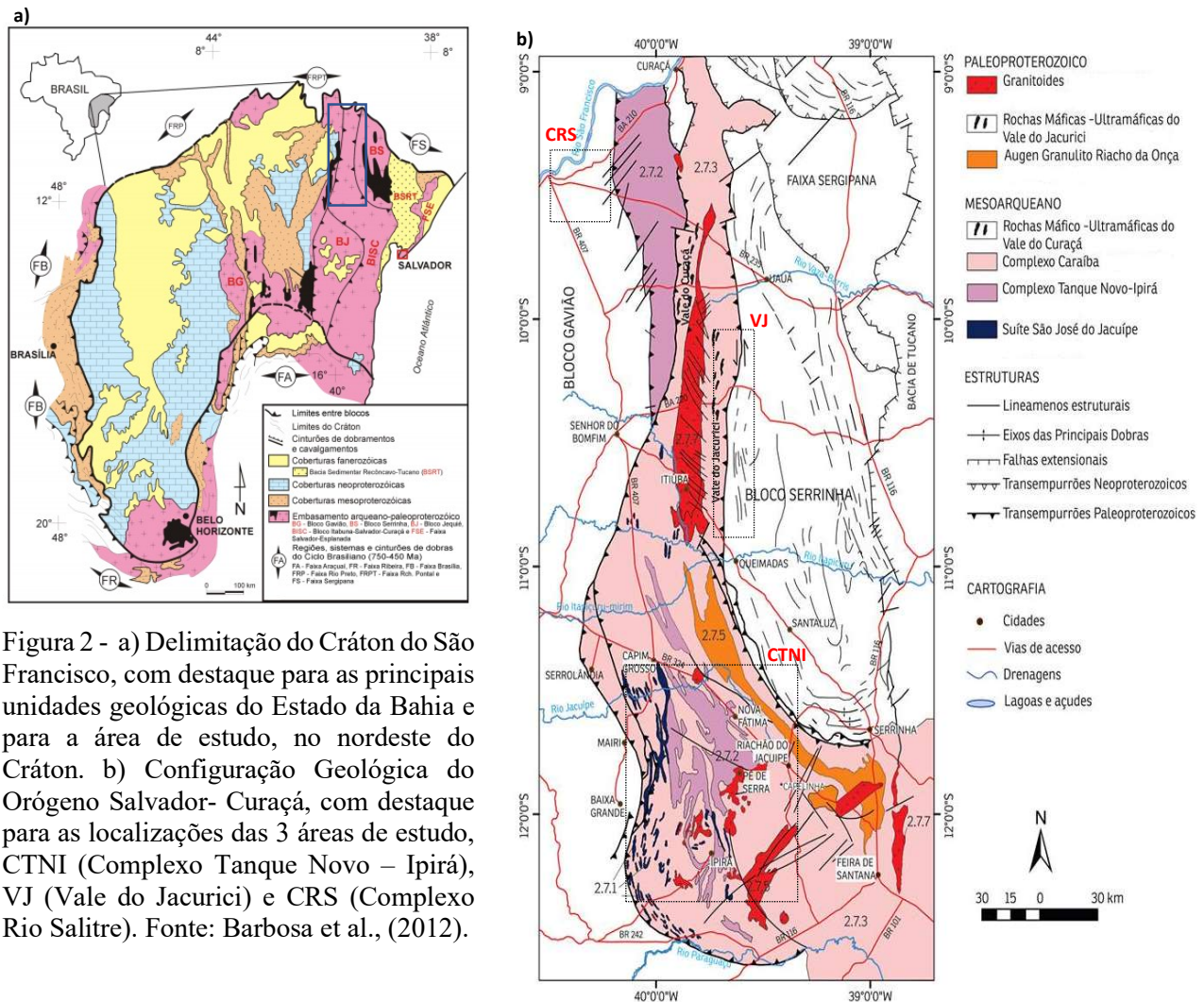


Figura 2 - a) Delimitação do Cráton do São Francisco, com destaque para as principais unidades geológicas do Estado da Bahia e para a área de estudo, no nordeste do Cráton. b) Configuração Geológica do Orógeno Salvador- Curaçá, com destaque para as localizações das 3 áreas de estudo, CTNI (Complexo Tanque Novo – Ipirá), VJ (Vale do Jacurici) e CRS (Complexo Rio Salitre). Fonte: Barbosa et al., (2012).

Em conjunto, o estudo geoquímico dessas rochas proporciona importantes informações de reconstrução de condições paleoambientais, sobretudo em cinturões orogenéticos precambrianos, em que estruturas sedimentares primárias são raramente preservadas. A complexa associação mineralógica e assinaturas geoquímicas primordiais preservadas em elementos terras raras e isótopos estáveis de C e O, representam as ferramentas básicas nesta linha de pesquisa, tendo em vista que o comportamento desses elementos e da fosfogênese no ambiente sedimentar marinho é controlado principalmente pelas condições da hidrosfera, atmosféricas, biosféricas e litosféricas as quais são peculiares e oscilam ao longo do tempo geológico (Veizer et al., 1992; Bau, 1999; Gaertner et al., 2011; Swart, 2015).

O comportamento dos elementos terras-raras e do ítrio (ETRY) normalizados para o folhelho PAAS (*Post-Archean Australian Shale*) permite interpretar as condições paleoambientais e pós deposicionais dessas rochas. Aliado aos estudos isotópicos de C e O é possível também investigar os efeitos diagenéticos e metamórficos das sucessões carbonáticas (Bau, 1999; Mohanty et al., 2015).

O padrão observado em rochas metassedimentares que são correlacionados à água do mar, quando essas rochas são normalizadas ao PAAS, é representado por depleção de elementos terras-raras leves (ETRL) relativo aos elementos terras-raras pesados (ETRP), anomalia negativa de Ce e positivas de La e Gd (De Baar et al., 1991, Bau e Dulski 1996, Northdurft et al. 2004, Bolhar et al.,s 2004, Piper e Bau 2013).

Esse padrão é registrado em diversos tipos de precipitados químicos, como carbonatos, cherts, BIFs e fosforitos (por exemplo, Joosu et al., 2016). Planavsky et al. (2010) corrobora que os padrões de ETRY tem uma tendência temporal, que reflete a evolução redox dos oceanos. Assim, carbonatos e BIFS arqueanos e paleoproterozoicos (2.4 a 1.9 Ma) são caracterizados por padrões empobrecidos de ETRL relativos aos pesados, anomalias negativas de Ce, anomalias positivas de Y e anomalias ligeiramente positivas de Gd (Planavsky et al.,2010).

Portanto, este trabalho busca investigar e caracterizar o potencial da mineralização de fosfato primário e as condições paleoambientais de deposição e precipitação dos mármores e rochas calcissilicáticas do Complexo Tanque Novo-Ipirá; sua relação com as rochas metassedimentares do Vale do Jacurici, Complexo Rio Salitre e outras sequências mundiais de mesma idade. Para atingir esse propósito, foram realizados os seguintes objetivos específicos:

1. Investigar a associação mineralógica e reações metamórficas nos mármores e nas rochas calcissilicáticas do Complexo Tanque Novo – Ipirá, com a determinação do tipo, forma, disposição e teores de P₂O₅ das ocorrências de fosfatos.
2. Determinar a idade inédita da deposição da sequência superior do Complexo Tanque Novo – Ipirá e sua relação com as possíveis fontes que contribuíram com a paleobacia.
3. Avaliar as condições paleoambientais das sucessões associados com os *inputs* continentais/contaminação detrítica da bacia, interação com os fluidos hidrotermais bacinais e fluidos metamórficos relacionados com a colisão Riacciana - Orosiniana. A partir disso, buscar a assinatura geoquímica original, preservada, para discussão das condições de oxigenação da paleobacia e correlação com os modelos de mineralização de fosfato sedimentar de idade paleoproterozoica.
4. Avaliar os novos dados de isótopos de C e O dos carbonatos do Complexo Tanque Novo – Ipirá e Complexo Rio Salite e sua comparação com os do Vale do Jacurici e bacias mundiais, das condições tectônicas durante a precipitação dessas sequências carbonáticas e relação genética com a alteração do ciclo do carbono durante o Evento Lomagundi - Jatuli.

A presente pesquisa é composta por dois artigos científicos de relevância no campo da Geologia. O primeiro artigo (Capítulo 2) investiga as evidências da fosfogênese paleoproterozóica no Orógeno Salvador-Curaçá, com foco nas mineralizações primárias, de origem sedimentar-marinha, associadas aos metassedimentos do Complexo Tanque Novo - Ipirá. Esse estudo já foi publicado na *Brazilian*

Journal of Geology, com Qualis A2, atestando sua contribuição significativa para o avanço do conhecimento nessa área. O segundo artigo (Capítulo 3) é dedicado a uma abrangente interpretação das excursões positivas de $\delta^{13}\text{C}$ nos mármores dos Complexos Tanque Novo-Ipirá, Rio Salitre e dos metassedimentos do Vale do Jacurici; sobre as implicações para a fosfogênese paleoproterozoica no Cráton do São Francisco e bacias mundiais de mesma idade, e sua relação com o Evento Lomagundi-Jatuli. Esse trabalho foi submetido à *International Geology Review*, classificada como Qualis A1.

Ambos os artigos são fundamentais para compreendermos a interconexão entre as sucessões metassedimentares paleoproterozoicas e mineralizações associadas, que são consequências de uma era da Terra afetada pelo Grande Evento de Oxigenação, que contribuiu com a evolução geoquímica da interface hidrosfera-atmosfera-litosfera, e para a formação dos primeiros depósitos econômicos globais de fosfatos. Pretende-se responder às várias questões pertinentes, tais como: i) quais as rochas hospedeiras da mineralização? ii) apesar do metamorfismo, as condições paleoambientais podem ser reconhecidas? iii) quais as condições de precipitação da mineralização? iv) como as mudanças na Terra durante o Arqueano-Paleoproterozoico podem ter afetado a formação dessas rochas? v) a mineralização está associada com um evento global e/ou local? vi) Existe correlação temporal e isotópica entre as sucessões metassedimentares do Cráton do São Francisco com a quebra do Supercontinente Kenorland?

Espera-se que essas pesquisas contribuam para o avanço do conhecimento científico e para a exploração mineral dessas rochas, visto que o fósforo, assim como o Ca, Mg e K presente nessas rochas são macronutrientes essenciais para as plantas. Desta forma podem contribuir para o setor agrícola como agrominerais fosfáticos, carbonáticos e/ou silicáticos, assim como para a indústria de fertilizantes tradicionais.

REFERÊNCIAS

- BAU, M.; DULSKI, P. Distribution of yttrium and rare-earth elements in the Penge and Kuruman iron-formations, Transvaal Supergroup, South Africa. *Precambrian Research*, Amsterdam, v. 79, n. 1-2, p. 37-55, July 1996.
- Bau, M. (1999). Scavenging of dissolved yttrium and rare earths by precipitating iron oxyhydroxide: experimental evidence for Ce oxidation, Y-Ho fractionation, and lanthanide tetrad effect. *Geochimica et Cosmochimica Acta*, 63(1), 67-77. [https://doi.org/10.1016/S0016-7037\(99\)00014-9](https://doi.org/10.1016/S0016-7037(99)00014-9).
- Bekker, A., Eriksson, K.A., 2003. A Paleoproterozoic drowned carbonate platform on the southeastern margin of the Wyoming Craton: a record of the Kenorland breakup. *Precambrian Res.* 120, 327–364.
- Bekker, A., Holland, H.D., Wang, P.L., Rumble, D., III, Hannah, J.L., Coetzee, L.L., and Beukes, N.J., 2004. Dating the rise of atmospheric oxygen: *Nature*, v. 427, p. 117–120, doi: 10.1038/nature02260.

- Bolhar R., Kamber B.S., Moorbath S., Fedo C.M., Whitehouse M.J. 2004. Characterisation of early Archaean chemical sediments by trace element signatures. *Earth and Planetary Science Letters*, 222(1):43-60. <https://doi.org/10.1016/j.epsl.2004.02.016>.
- De Baar H.J.W., Schijf J., Byrne R.H. 1991. Solution chemistry of the rare earth elements in seawater. *European Journal of Solid State and Inorganic Chemistry*, 28(Suppl.):357-373.
- Gama, M. (2014). Caracterização petrográfica e litogeoquímica das rochas metacarbonáticas e calcissilicáticas do Vale do Rio Jacurici, Bahia. Trabalho de Conclusão de Curso. Bahia: Instituto de Geociências – UFBA.
- Gama M. A., Misi A., Sá J.H.S., Oliveira L.R.S.S., Ribeiro T.S (2021). Caracterização petrográfica e litogeoquímica dos mármore e rochas calcissilicáticas do Vale do Jacurici, Bahia: condições paleoambientais e processos fosfogenéticos. *Geologia USP, Série Científica*, São Paulo, v. 21, n. 2, p. 12-143. <https://doi.org/10.11606/issn.2316-9095.v21-161794>.
- Gaertner, C., Broecker, M., Strauss, H., Farber, K. (2011). Strontium-, carbon- and oxygen-isotope compositions of marbles from the Cycladic blueschist belt. *Greece Geology*, 148, 511-528. <https://doi.org/10.1017/S001675681100001X>.
- Gumsley, A.P., Chamberlain, K.R., Bleeker, W., Bekker, A., 2017 Timing and tempo of the Great Oxidation Event. *Earth, Atmospheric, and Planetary Sciences* 114 (8), 1811-18816. DOI: <https://doi.org/10.1073/pnas.1608824114>.
- Hannah, J.L., Bekker, A., Stein, H.J., Markey, R.J., and Holland, H.D., 2004, Primitive Os and 2316 Ma age for marine shale: Implications for Paleoproterozoic glacial events and the rise of atmospheric oxygen: *Earth and Planetary Science Letters*, v. 225, p. 43–52, doi: 10.1016/j.epsl.2004.06.013.
- Joosu L., Lepland A., Kreitsmann T., Upraus K., Roberts N.M.W., Paiste P., Martin A.P., Kirsimäe K. 2016. Petrography and the REE-composition of apatite in the Paleoproterozoic Pilgularvi Sedimentary Formation, Pechenga Greenstone Belt, Russia. *Geochimica et Cosmochimica Acta*, 186:135-153. <https://doi.org/10.1016/j.gca.2016.04.043>.
- Leite, C.M.M-1983- “Projeto Serrote da Batateira”, Estado da Bahia, Convênio SME/CBPM, Salvador.
- Leite, C.M.M-1984- “Projeto Juazeiro”, Estado da Bahia, Convênio SME/CBPM, Salvador.
- Martin, A.P., Condon, S.J., Prave, A.R., Lepland, A., 2013. A review of temporal constraints for the Palaeoproterozoic large, positive carbonate isotope excursion (the Lomagundi-Jatuli Event). *Earth Sci. Rev.* 127, 242–261.
- Melezhik, V.A., Fallick, A.E., Rychanchik, D.V., and Kuznetsov, A.B., 2005b, Paleoproterozoic evaporites in Fennoscandia: Implications for seawater sulphate, $\delta^{13}\text{C}$ excursions and the rise of atmospheric oxygen: *Terra Nova*, v. 17, p. 141– 148, doi: 10.1111/j.1365-3121.2005.00600.x.
- Melezhik, V.A., Huhma, H., Condon, D.J., Fallick, A.E., Whitehouse, M.J., 2007. Temporal constraints on the Paleoproterozoic Lomagundi-Jatuli carbon isotopic event. *Geology* 35, 655–658.
- Mohanty S.P., Barik A., Sarangi S., Sarkar A. 2015. Carbon and oxygen isotope systematics of a Paleoproterozoic cap-carbonate sequence from the Sausar Group, Central India. *Palaeogeography, Palaeoclimatology and Palaeoecology*, 417:195-209. <http://dx.doi.org/10.1016/j.palaeo.2014.10.036si>.
- Nelson, G.J., Pufahl, P.K., Hiatt, E.E., 2010. Paleooceanographic constraints on Precambrian phosphorite accumulation, Baraga Group, Michigan, USA. *Sedimentary Geology* 226, 9–21.

- Northdurft L.D, Webb G.E, Kamber B.S. 2004. Rare earth element geochemistry of Late Devonian reefal carbonates, Canning Basin Western Australia: confirmation of a seawater REE proxy in ancient limestones. *Geochimica et Cosmochimica Acta*, 68(2):263-283. [https://doi.org/10.1016/S0016-7037\(03\)00422-8](https://doi.org/10.1016/S0016-7037(03)00422-8).
- Oliveira, L. O. 2016. Fosforitos da Região de Juazeiro, Bahia: Paleoambientes, Geocronologia, Controles da Mineralização e Correlações Estratigráficas. Dissertação de Mestrado, Universidade Federal da Bahia, Salvador, 195 p.
- Papineau et al. (2013) – High phosphate availability as a possible cause for massive cyanobacterial production of oxygen in the Paleoproterozoic atmosphere.
- Papineau, D., 2010. Global biogeochemical changes at both ends of the Proterozoic: insights from phosphorites. *Astrobiology* 10, 165–181.
- Piper D.Z., Bau M. 2013. Normalized Rare Earth Elements in Water, Sediments, and Wine: Identifying Sources and Environmental Redox Conditions. *American Journal of Analytical Chemistry*, 4(10A):69-83. <http://dx.doi.org/10.4236/ajac.2013.410A1009>.
- Planavsky N., Bekker A., Rouxel O.J., Kamber B., Hofmann A., Knudsen A., Lyons T.W. 2010. Rare earth element and yttrium compositions of Archean and Paleoproterozoic Fe formations revisited: new perspectives on the significance and mechanisms of deposition. *Geochimica et Cosmochimica*, 74(22):6387-6405. <https://doi.org/10.1016/j.gca.2010.07.021>.
- Pufahl, P.K., Hiatt, E.E., 2012. Oxygenation of the Earth's atmosphere–ocean system: a review of physical and chemical sedimentologic responses. *Marine and Petroleum Geology* 32, 1–20.
- Ribeiro T.S. 2016. Caracterização Geológica das Rochas Calcissilicáticas e Metacarbonáticas do Complexo Tanque Novo- Ipirá na Folha Pintadas-Ba: Potencial Metalogenético para Fosfato, Salvador. MS Dissertation, Instituto de Geociências, Universidade Federal de Bahia, Salvador, 181 p.
- Ribeiro T. S. (2017). Complexo Tanque Novo-Ipirá: Geologia e potencialidade para fosfato na folha Pintadas, Bahia. CBPM. Série Arquivos Abertos, 42.
- Ribeiro T.S., Misi A., Oliveira., L.R.S.S., Sá J.H.S., Debruyne. D., Câmara I. Evidence of Paleoproterozoic phosphogenesis in the Salvador-Curaçá Orogen (Tanque Novo-Ipirá Complex), northeastern São Francisco Craton, Brazil. (2021). *Brazilian Journal of Geology*, 51(3): <https://doi.org/10.1590/2317-4889202120190137>.
- Sá, J. H. S. e OLIVEIRA, N. P. – 1982- “Relatório sobre os levantamentos Realizados na Ilha do Fogo e Serrote da Batateira, Juazeiro-Bahia”. CPM/SME, Relatório Interno, 5 p. ilustr., Salvador.
- Sá, J. H. S.; LEITE, C. M. M.; CONCEIÇÃO V. M.; OLIVEIRA, N. P., 1984. Depósitos de rochas fosfáticas no município de Juazeiro, Bahia. In: XXXIII Congresso Brasileiro de Geologia, 1984. Anais... Rio de Janeiro, SBG.
- Swart P.K. 2015. The geochemistry of carbonates diagenesis: The past, present and future. *Sedimentology*, 62(5):1233-1304. <https://doi.org/10.1111/sed.12205>.
- Veizer, J., Plumb, K. A., Clayton, R. N., Hinton, R. W., Grotzinger, J. P. (1992). Geochemistry of Precambrian carbonates: V. Late Paleoproterozoic seawater. *Geochimica et Cosmochimica Acta*, 56(6), 2487-2501. [https://doi.org/10.1016/0016-7037\(92\)90204-V](https://doi.org/10.1016/0016-7037(92)90204-V).

**ARTIGO 1 - EVIDENCE OF PALEOPROTEROZOIC PHOSPHOGENESIS IN THE
SALVADOR-CURAÇÁ OROGEN (TANQUE NOVO-IPIRÁ COMPLEX),
NORTHEASTERN SÃO FRANCISCO CRATON, BRAZIL**

Evidência de fosfogênese Paleoproterozoica no Orógeno Salvador Curaçá (Complexo Tanque Novo – Ipirá), Nordeste do Cráton do São Francisco, Brasil.

Evidence of Paleoproterozoic phosphogenesis in the Salvador-Curaçá Orogen (Tanque Novo – Ipirá Complex), northeastern São Francisco Craton Brazil.

DOI: <https://doi.org/10.1590/2317-4889202120190137>

Revista: Brazilian Journal of Geology

Autores:

Tatiana Silva Ribeiro

Aroldo Misi




Luís Rodrigues dos Santos de Oliveira

José Haroldo da Silva Sá

David Debruyne

Ib Silva Câmara

Evidence of Paleoproterozoic phosphogenesis in the Salvador-Curaçá Orogen (Tanque Novo-Ipirá Complex), northeastern São Francisco Craton, Brazil

Tatiana Silva Ribeiro^{1*} , Aroldo Misi² , Luís Rodrigues dos Santos de Oliveira² , José Haroldo da Silva Sá² , David Debruyne³ , Ib Silva Câmara¹ 

Abstract

This paper analyzes mineralogical, geochemical, and geochronological aspects, along with the effect of hydrothermal/metamorphic overprints, to identify the presence of primary phosphate as well as depositional and paleoenvironmental conditions in marble and calcisilicate sequences recrystallized under transitional amphibolite-granulite metamorphic conditions in the Tanque Novo-Ipirá Complex within the Salvador-Curaçá Orogen, northeastern São Francisco Craton, state of Bahia, Brazil. Petrographic studies have identified up to 10 vol.% disseminated apatite and whole-rock P_2O_5 contents up to 3.2 wt.%. Post-depositional events affected the lithofacies to varying degrees. Late hydrothermalism did not modify the rare earth element and yttrium (REEY) patterns considerably. When normalized to Post-Archean Australian Shale (PAAS), these lithofacies are marked by flat pattern REEY, true negative Ce anomalies, and positive Y and Gd. The highly variable Eu anomalies were inherited from the source composition but may have been affected by interaction with fluids. U-Pb LA-ICP-MS (laser ablation multicollector inductively coupled plasma mass spectrometry) ages indicate a maximum depositional age of 2128 Ga, as well as Paleoproterozoic and Neoproterozoic sources. Samples with anomalous phosphorus show Y/Ho ratios >30 and Ce/Ce* anomalies between 0.53 and 1.0 with an average of 0.70, suggesting a sub-oxic environment for phosphate precipitation.

KEYWORDS: phosphogenesis; Paleoproterozoic; Tanque Novo-Ipirá Complex; São Francisco Craton; paleobasin.

INTRODUCTION

Calcisilicate rocks and marbles are common in metamorphic terrains associated with orogenic belts and are often intercalated with other pelitic and siliciclastic metasediments. The decarbonation reactions that occur during the medium- to high-grade metamorphism of these rocks generate a variety of Ca–Mg-rich silicates, such as zoisite, tremolite, grossular, amphibole, diopside, and olivine (Bucher and Grapes 2010).

These rocks are of great importance due to their metallogenic potential, especially for phosphate and skarn-type

deposits, besides calcite mining. This complex mineralogical association can preserve several original geochemical signatures that, combined with field data, can be used for reconstructions, determination of paleoenvironmental conditions, and stratigraphic correlations. The most widespread geochemical tools used for these purposes include rare earth elements and yttrium (REEY) patterns, stable isotopes (carbon, oxygen, and sulfur), $^{87}Sr/^{86}Sr$ isotopes, and studies involving francolite or carbonate-fluorapatite, the main ore minerals in marine phosphorites (Veizer *et al.* 1999, Bau 1993, Papineau 2010, Nelson *et al.* 2010, Pufahl and Hiatt 2012, Swart 2015).

Biogenic phosphorites are formed in marine environments associated with a complex phosphogenic system, controlled by the availability of oxygen in the paleobasin and by the flow of continental iron- and phosphorus-rich sediments (Glenn *et al.* 1994, Papineau *et al.* 2013). However, the first Paleoproterozoic phosphogenic pulse produced phosphorites that may contain less than 18 wt.% P_2O_5 (Pufahl 2010, Papineau 2010, Papineau *et al.* 2013, Hiatt 2015).

The oldest sedimentary phosphate mineralizations occurred in the Paleoproterozoic age and are related to the global Great Oxidation Event (GOE) that started around 2.5 Ga (Pufahl 2010, Papineau 2010). The main Paleoproterozoic deposits are located in Russia, China, North America (Baraga Group between Canada and the United States), Finland, North Korea, Africa, and India (Papineau 2010).

¹Graduate degree in Geology, Institute of Geosciences, Universidade Federal da Bahia – Salvador (BA), Brazil. E-mails: tatiana_geologia@yahoo.com.br, ibsilvacamara@hotmail.com

²Group of Metallogenesis, Metallogenic Models, and Mineral Exploration, Geophysics and Geology Research Center, Universidade Federal da Bahia – Salvador (BA), Brazil. E-mails: aroldo.misi@gmail.com, rodrigues.oliveira@hotmail.com, haroldo.sa@gmail.com

³Geological Engineering Center, Universidade Federal de Pelotas – Pelotas (RS), Brazil. E-mail: david3bruyne3@gmail.com.

*Corresponding author.

Supplementary data

Supplementary data associated with this article can be found in the online version: [Supplementary Figure 1](#) and [Supplementary Figures 2 and 3](#).



This paper examines the primary phosphorus mineralization potential of calcsilicate rocks and marbles in the Paleoproterozoic Tanque Novo-Ipirá Complex. This complex is composed of calcsilicate rocks, marbles, metapsammites, banded iron formations (BIFs), and paragneisses, metabasites, and meta-ultrabasites metamorphosed at amphibolite to granulite facies conditions. We investigated the calcsilicate rocks and marbles of the complex using petrographic, mineralogical, geochemical, and geochronological (U-Pb laser ablation multicollector inductively coupled plasma mass spectrometry — LA-ICP-MS) methods in order to identify the geological conditions in which these rocks were generated and identify the maximum deposition age of this Paleoproterozoic sequence.

The relevance of the present work is highlighted by the growing agricultural need for phosphorus and its derived fertilizer products, given the growing world population, which drives the search for new phosphate deposits, including those in intensely metamorphosed Paleoproterozoic basins.

REGIONAL AND LOCAL GEOLOGICAL CONTEXT

The Archean São Francisco Craton (SFC), consolidated during the Transamazonian (Orosirian) cycle at the end of the Paleoproterozoic, was partially reworked in the Neoproterozoic and Cambrian, during the Brazilian cycle (Alkmim *et al.* 1993, Barbosa and Sabaté 2003, Barbosa and Dominguez 2006). The study area is located in the north-east portion of the SFC, in the Tanque Novo-Ipirá Complex within the northern segment Itabuna-Salvador-Curaçá Orogen (Fig. 1). The Itabuna-Salvador-Curaçá Orogen was formed over a time span of about 200–300 million years, during the Paleoproterozoic, when a block of the same name collided with other Archean-age blocks (Gavião, Jequié, and Serrinha blocks), leading to the formation of an important mountain chain (Barbosa and Sabaté 2003).

The Salvador-Curaçá Orogen is located in the eastern region of Bahia, extending for approximately 700 km from north to south. It corresponds to a ductile shear belt that was generated in a transpressive regime during the Paleoproterozoic collision of the Gavião, Jequié, Salvador-Curaçá, and Serrinha blocks, and evolved progressively during successive compressive episodes (Kosin *et al.* 2003). Transient, ductile, sinistral shear zones with westward vergence in the Gavião Block, as well as corresponding shear zones with eastward vergence in the Serrinha Block (Leite 2002), delimit this orogen. Barbosa and Sabaté (2003) interpret these features as asymmetrical positive flower structures generated during the final Paleoproterozoic orogeny.

The Salvador-Curaçá Orogen can be subdivided into three main domains in its northern segment (Melo *et al.*, 1991): the Caraíba Complex, the São José do Jacuípe Suite, and the Tanque Novo-Ipirá Complex. Several granulite suites are present and classified according to deformation phases besides Cenozoic cover rocks. Sensitive High-Resolution Ion Microprobe (SHRIMP) U-Pb ages

obtained in tonalitic and enderbitic granulites from the Caraíba Complex revealed two age populations: 2.7–2.6 Ga and 2.08–2.07 Ga (Silva *et al.* 1997), preserved in zircon cores and rims, respectively. The 2.7–2.6 Ga ages are interpreted as a period of island arc magmatism, whereas the 2.08–2.07 Ga ages are related to high-grade metamorphism (Silva 1996).

Melo *et al.* (1991) classified the Ipirá Complex into five different units:

- Pintadas;
- Serra do Camisã;
- Juazeirinho;
- Angico;
- Umbuzeiro.

Out of these five units, only the Pintadas and Serra do Camisã occur in the study area. The lower sequence is regarded as an oceanic floor sequence associated with paragneisses, kinzigites, and metabasites of the Pintadas Unit. The upper Serra do Camisã Unit includes marbles and calcsilicate rocks, both lithofacies hosting apatite deposits, in addition to iron formations, graphite schists, and quartzites and the absence of alumina-rich gneisses (Melo *et al.* 1991).

Kosin *et al.* (2003) combined the Tanque Novo Group and the Ipirá Complex into the Tanque Novo-Ipirá Complex, understood as a metavolcano-sedimentary sequence developed between the Archean and Paleoproterozoic that experienced high-grade amphibolite to granulite facies metamorphism. It was subdivided into six informal units, based on their lithological assemblages:

- kinzigitic or garnet-rich biotite gneisses and migmatites, associated with calcsilicate, quartzite, BIF, graphitic rocks, and metamorphic and meta-ultramafic rocks;
- calcsilicate rocks, quartzite, marbles, amphibolite, and BIF;
- garnetiferous hornblende-biotite gneiss, with quartz-feldspathic bands and orthopyroxene, interspersed with amphibolitic levels;
- graphite gneiss associated with calcsilicate rocks with intercalations of ferrous quartzite, migmatized gneiss, kinzigitic gneiss, and quartz-feldspathic gneiss, with or without garnet;
- banded gneiss, with alternation of granitic-granodioritic and gabbroic-dioritic bands, and intercalations of tonalitic gneiss, amphibolite, and subordinate calcsilicate rocks;
- orthopyroxene quartz-feldspathic gneiss, with or without garnet and rare biotite.

These rocks experienced different degrees of migmatization and show diffuse contact with granitoid bodies.

Depleted mantle Nd model ages of alumina-rich gneisses in the Tanque Novo Group (Curaçá River Valley) indicate model ages of 2.6 Ga (Oliveira *et al.* 2002).

The study area is characterized by carbonate, calcsilicate, and siliciclastic lithofacies occurring in discontinuous narrow strips of up to 10 kilometers wide and showing strong deformation (mainly folding), geometrically consistent with regional structures (Fig. 2). The current structural situation reflects a

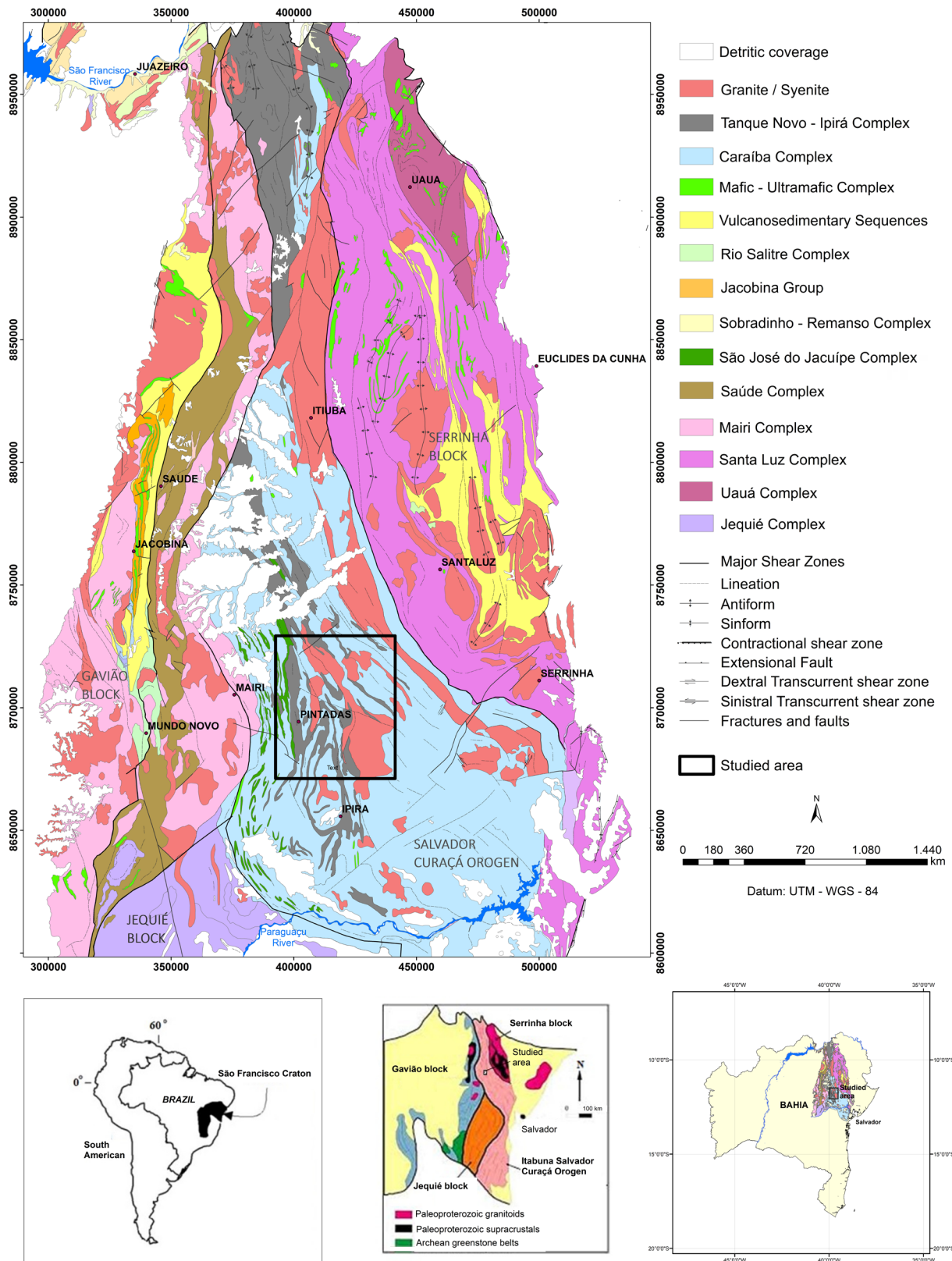
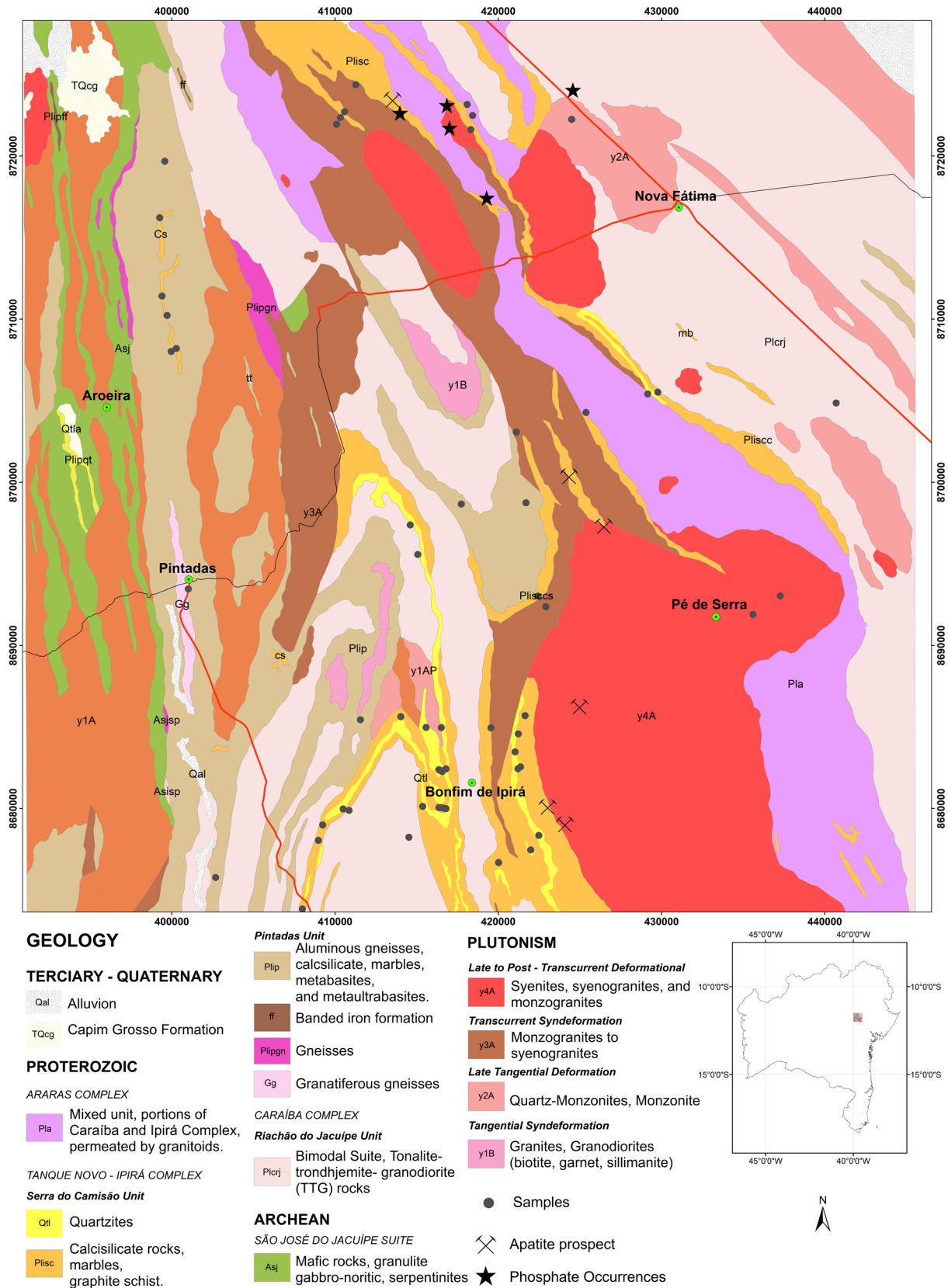


Figure 1. Simplified geological map of the northern segment of the Salvador-Curaçá Orogen (after Oliveira *et al.* 2010), showing the location of the study area.

complex polyphase deformation involving crustal shortening. These lithofacies emerge discontinuously in N-S to NNW-SSE-oriented lenticular or spindle-shaped bodies, generally with subvertical dipping layers.

The marbles in the metasedimentary sequence gradually grade into calcsilicate rocks and metapsammites, depending on the relative amount of detrital material. The units in the study area can be subdivided into:

- Marbles;
- Calcisilicate (gneiss and granofels);
- Metapsammite;
- Skarn;
- Graphite schist;
- Granitoids.



Source: Modified from Melo *et al.* (1991).

Figure 2. Geological map of the study area with the indication of points of samples collected during fieldwork.

The orthogneisses of the Caraíba Complex constitute the basement rocks. They are associated with intense plutonism related to different deformation phases. The N–S-oriented ductile and brittle deformation structures with dips of 45–85° are most easily identified in calcsilicate rocks. Figure 3 shows two geological sections in the Bonfim de Ipirá and southern Ipirá regions, respectively.

ANALYTICAL METHODS

Samples — free of visible effects of weathering, alteration, and late veins — were collected from a representative section between the towns of Ipirá and Pintadas. In total, they consisted of 8 marbles, 28 calcsilicate rock samples, 2 graphite schists, and 4 metapsammites.

Tests for the presence of phosphate in rock samples were performed with ammonium molybdate and HCl (hydrochloric acid) or HNO₃ (nitric acid) during fieldwork. This qualitative colorimetric test allows detecting the presence of P₂O₅ anomalies through the formation of an ammonium phosphomolybdate precipitate with an intense yellow to greenish-yellow color.

Petrographic studies were carried out with an Olympus BX60 petrographic microscope at the Microscopy Laboratory of the Geosciences Institute of the Universidade Federal da Bahia. X-ray diffraction (XRD) analyses were performed with a second-generation Bruker Diffractometer D2 Phaser at the Mineral Technology Laboratory – X-ray of the Universidade Federal da Bahia (LAPAG) to identify the type of carbonate

(calcite and/or dolomite), apatite, and serpentine present. The Diffrac Suite EVA software was used for XRD data processing. Thin sections were also investigated with a JEOL JSM-6610LV Scanning Electron Microscope (SEM) at the Electron Microscopy Multiuser Laboratory of the Universidade Federal da Bahia (LAMUME); graphs were generated with the AZtec software.

Geochemical studies were prepared and analyzed in the SGS Geosol Laboratory in Belo Horizonte, Minas Gerais. Marbles and calcsilicate rock samples, typically weighing 250 g, were crushed to 3 mm particles, homogenized, quartered in Jones, and sprayed on a 150-mesh steel mill.

Major-element abundances (SiO₂, Ti₂O, Al₂O₃, MgO, Fe₂O₃, MnO, CaO, Na₂O, K₂O, and P₂O₅) were measured using X-ray fluorescence. In this analysis, 0.5 g of the samples was fully digested by fusion with lithium tetraborate in a Vulcan automatic machine at 1,000°C. The analysis was performed on a fused tablet by X-ray fluorescence spectrometry, WDXRF type, simultaneous PANalytical Axios Fast model, obtaining results with a natural basis.

Trace elements (Ba, Rb, Ga, Zr, Sr, Cr, Ni, Co, and Y) and rare earth elements (REE) were determined by complete digestion by fusion in a muffle at 950°C, with lithium metaborate (LiBO₂), dissolving with an acid solution of nitric acid and tartaric acid (HNO₃ and C₄H₆O₆). Trace elements were read by ICP-Optical Emission Spectrometry (ICP-OES), Optima 7300DV model. This solution also quantified REEs read by ICP-MS, NexION 300X ICP-MS model. REEY

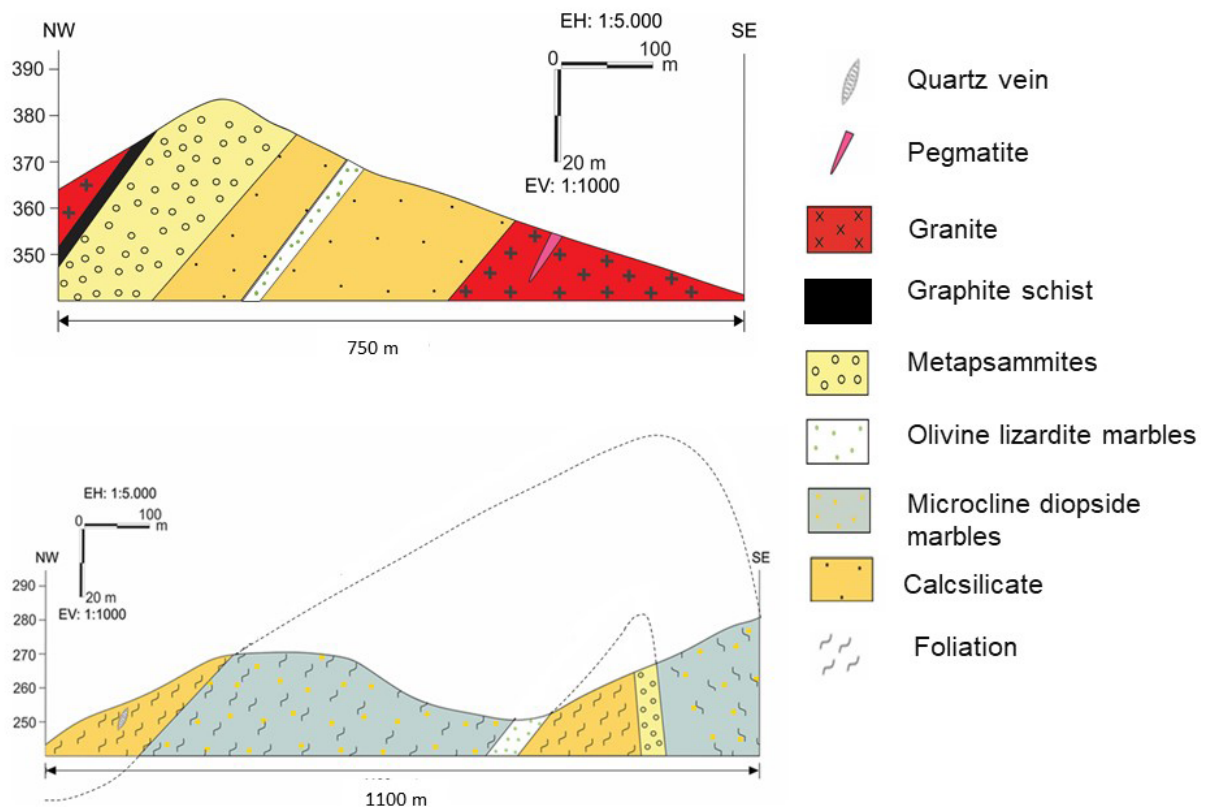


Figure 3. Geological sections of the Serra do Camisão Unit. (A) Bonfim de Ipirá region. (B) Southern Ipirá region, calcsilicate rocks and marbles with microcline and diopside are herein represented with foliation. This section shows a compositional gradation between marbles and calcsilicate rocks up to quartzite.

concentrations were normalized according to the average Post-Archean Australian Shale (PAAS) composition reported by McLennan (1989).

Handpicked zircons were mounted in 2-cm diameter epoxy resin and polished to suitably generate reflected and cathodoluminescence images in order to characterize their internal complexities and choose the best location for the subsequent spot analyses.

The zircon U-Pb LA-ICP-MS was performed at the Institute of Geosciences of the Universidade de São Paulo at the High-Resolution Geochronology Laboratory (GEOLAB), using the Thermo-Fisher Neptune LA-ICP-MS, equipped with a 193 nm ArF laser photon system. The 29- μm diameter spot works with a frequency of 6 Hz and intensity of 6 μJ . The ablated material was carried by Ar (~ 0.7 L/min) and He (~ 0.6 L/min) in analyses of 60 cycles of 1 s (more details can be found in Sato *et al.* 1995).

The analytical procedure of the U-Pb method included the analysis of NIST (National Institute of Standards) synthetic glass standards, external reference materials, and blanks. Both NIST glass and external reference materials were used to normalize the $^{207}\text{Pb}/^{206}\text{Pb}$ ratio, whereas the external reference material was used to normalize the $^{206}\text{Pb}/^{238}\text{U}$ ratio. Residual common Pb and instrumental discrimination were corrected using the known terrestrial composition (Stacey and Kramers 1975) and the reference zircon standard (GJ-1) (Jackson *et al.* 2004), respectively. Data are portrayed in a concordia diagram generated in the ISOPLOT 4 software (Ludwig 2003).

FIELD ASPECTS AND PETROGRAPHY

Marbles

The greenish-white to grayish and sometimes orange-colored marbles crop out as isolated bodies associated with calc-silicate rocks in the Serra do Camisão Unit. Most marbles are medium- to coarse-grained, except for the subordinate fine- to medium-grained white serpentine-bearing marble. These rocks have a massive appearance, except for the orange-colored marble, which displays orange calcite bands intercalated with diopside bands (Figs. 4A and 4B). Petrographically, the marbles were separated into two groups according to the textural and compositional characteristics described below.

Group 1

Group 1 marbles consist of calcite/dolomite (30–50 vol.%) associated with olivine (5–20 vol.%), serpentine (10–50 vol.%), garnet (2–10 vol.%), diopside (5–20 vol.%), talc (10 vol.%), opaque minerals (2 vol.%), tremolite (10–20 vol.%), and apatite. Calcite presents a poikiloblastic sieve texture included in a medium-grained matrix and curved contacts with phases belonging to the serpentine and garnet group. Apatite, olivine, and garnet occur as inclusions. Preserved olivine crystals are subidiomorphic, intensely fractured, and contain inclusions of opaque and serpentine minerals. Phases of the serpentine group constitute about 30 vol.% of the average total rock volume in Group 1. The mesh-type texture formed by serpentine

surrounding central zones with relict olivine can be visualized in Figure 4C. Rims or microveins filled with opaque minerals are common. Where the serpentinization process is intense, the mesh texture evolves to a curtain-like texture (bipartite subparallel veins); relict olivine cores are absent, and serpentine recrystallizes and is replaced by talc (Fig. 4D).

Group 2

Group 2 marbles contain calcite (35–40 vol.%), microcline (25–30 vol.%), diopside (25–35 vol.%), tremolite (10–15 vol.%), hornblende (5–10 vol.%), chlorite (5 vol.%), zircon (<5 vol.%), titanite (<5 vol.%), and opaque minerals (<5 vol.%). Calcite makes up about 40% of the average total rock volume in Group 2, and subidiomorphic calcite crystals exhibit straight contacts with each other. Subidiomorphic to xenomorphic microcline crystals occur only in Group 2 and occasionally preserve tartan twinning. Microcline is moderately to intensely sericitized and contains zircon inclusions. It is associated with calcite, in curved contacts filling the interstitial areas between the calcite crystals (Fig. 4E). Diopside is present as xenomorphic crystals partially transformed to tremolite in re-entrant contacts between diopside and hornblende (Fig. 4F). Hornblende is present as non-oriented subidiomorphic, prismatic, and chloritized crystals with opaque and titanite inclusions in re-entrant contacts with diopside. Figure 4F illustrates a reaction corona with a nucleus consisting of tremolitized diopside, recognizable by its lower relief and fibrous aspect, formed during hydrothermal alteration. Hornblende is altered to chlorite at the edges of the reaction zone.

The XRD analysis confirmed the presence of dolomite in Group 1 and classified the serpentine as lizardite (Suppl. 1). SEM analysis allowed investigating the calcite-lizardite [$\text{Mg}_3\text{Si}_2\text{O}_3(\text{OH})_4$] contacts in more detail, as illustrated in Figure 5A, which also shows a serpentinized olivine pseudomorph inclusion in calcite. Dolomite crystals show calcite intergrowths (Fig. 5B). The presence of phlogopite was detected by SEM analysis; this mineral displays slightly curved contacts with calcite and is partially chloritized at the rims, as evidenced by the difference in texture and chemical composition at its edges (Fig. 5C).

Based on their compositional and modal characteristics, marbles of Group 1 were classified as lizardite marbles and olivine-lizardite marbles. If present (<5 vol.%), garnet was included in the name (garnet lizardite marble). Group 2 marbles were classified as diopside marbles and microcline marbles.

Calcsilicates

Calcsilicates occur as lenticular and discontinuous bodies affected by multiple deformation phases, associated with quartzites and marble lenses. They are fine- to medium-grained, greenish-white to grayish, and show clear foliation planes (Fig. 6A).

These calcsilicates contain diopside (15–55 vol.%), tremolite (15–35 vol.%), plagioclase (10–20 vol.%), K-feldspar (10–20 vol.%), quartz (5–22 vol.%), biotite (2 vol.%), titanite (<5 vol.%), hornblende (2–10 vol.%), opaque (<5 vol.%), zircon (<5 vol.%), calcite (5–20 vol.%), and apatite. Occasionally, a compositional banding can be observed, characterized by

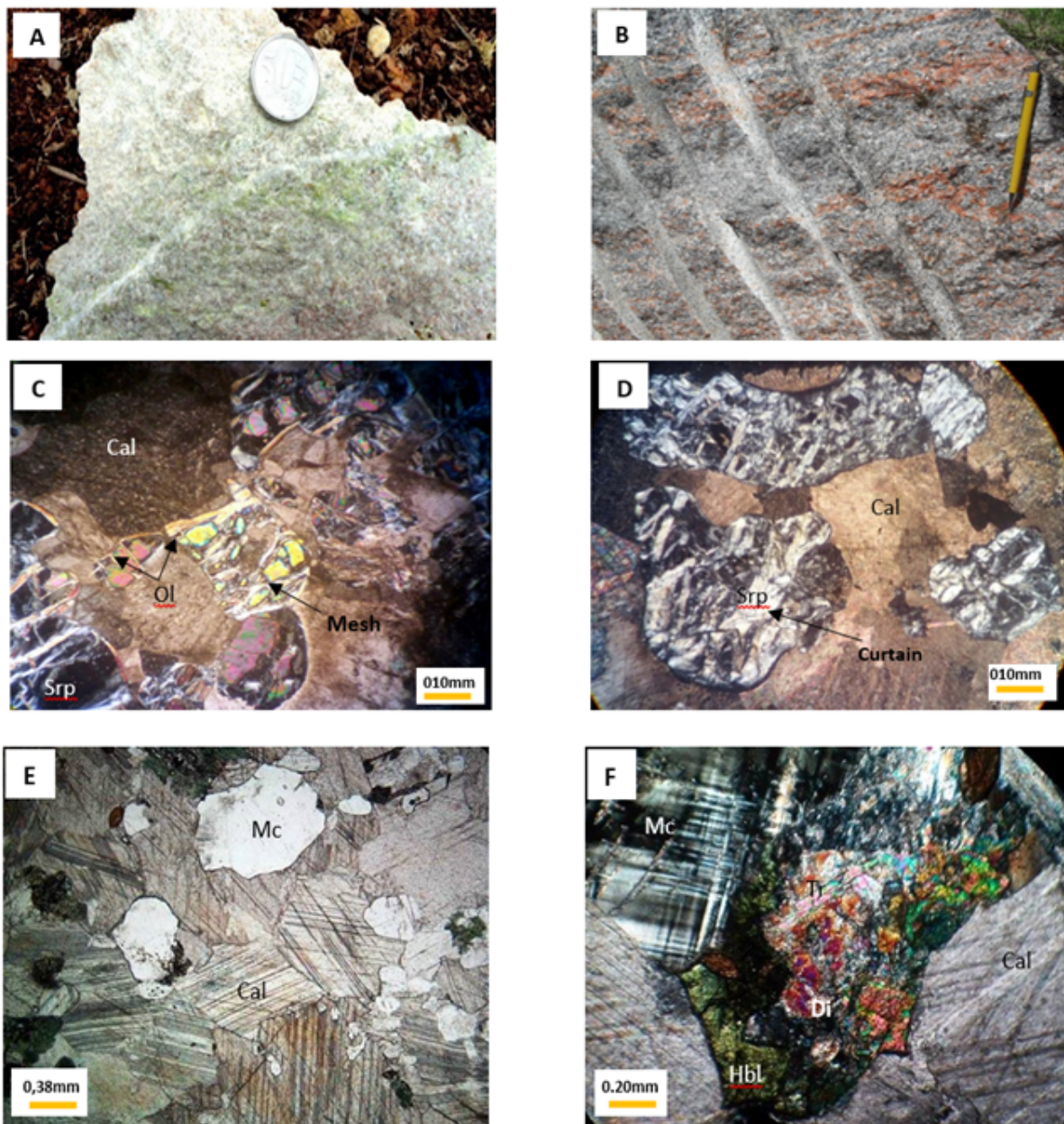


Figure 4. (A) Calcite and greenish-white serpentine marbles. (B) Outcrop showing a banded marble with alternating orange calcite layers and dark diopside-bearing layers (MM-TR-293 sample). (C) Mesh texture evidenced by serpentinized (Srp) olivine (Ol) associated with calcite (Cal) (XPL). (D) Curtain-type texture within serpentinized olivine pseudomorphs (XPL). (E) Marble with polygonal granoblastic texture (Mc) (PPL). (F) Reaction corona between diopside (Di), tremolite (Tr), and hornblende (Hbl) (PPL). XPL: cross-polarized light; PPL: plane-polarized light.

alternating bands of diopside and/or tremolite and bands of variable compositions ranging from quartz to feldspar + quartz (calcsilicate gneisses). Massive occurrences are also present, discretely foliated or exclusively composed of diopside, hornblende, tremolite, and plagioclase denominated tremolite-diopside-granofels. Figure 6B shows a positive phosphate test.

Calcsilicate gneisses and tremolite-diopside-granofels form skarns in hydrothermally altered contact zones and potassic alteration zones. Dark green and greenish-gray skarns are medium- to coarse-grained and composed of tremolite, diopside, scapolite, and potassium feldspar, criss-crossed by calcite and quartz-feldspathic veins (Fig. 6C). This interaction is sometimes evidenced by the formation of centimeter-sized blue apatite crystals disseminated in the diopsidite associated with pegmatites.

Petrographically, calcsilicate rocks show polygonal to decussate granoblastic textures, mainly in tremolite-diopside-granofels, along with occasional porphyroblastic and mylonitic textures in calcsilicate gneisses. Figure 6D presents the gneissic banding formed by pyroxene- and amphibole-rich layers alternated with feldspar- and quartz-rich layers. These rocks are classified as calcsilicate gneisses, diopsidites, and diopsidites with microcline.

Diopside in calcsilicate gneisses comprises about 40% of the rock volume and forms predominantly hypidiomorphic crystals along with some idiomorphic ones. They display limited to moderate degrees of hydrothermal alteration. Diopside is altered to hornblende at the rims (Fig. 6E).

Feldspar crystals are subidiomorphic and present moderate to high degrees of hydrothermal alteration, mostly to

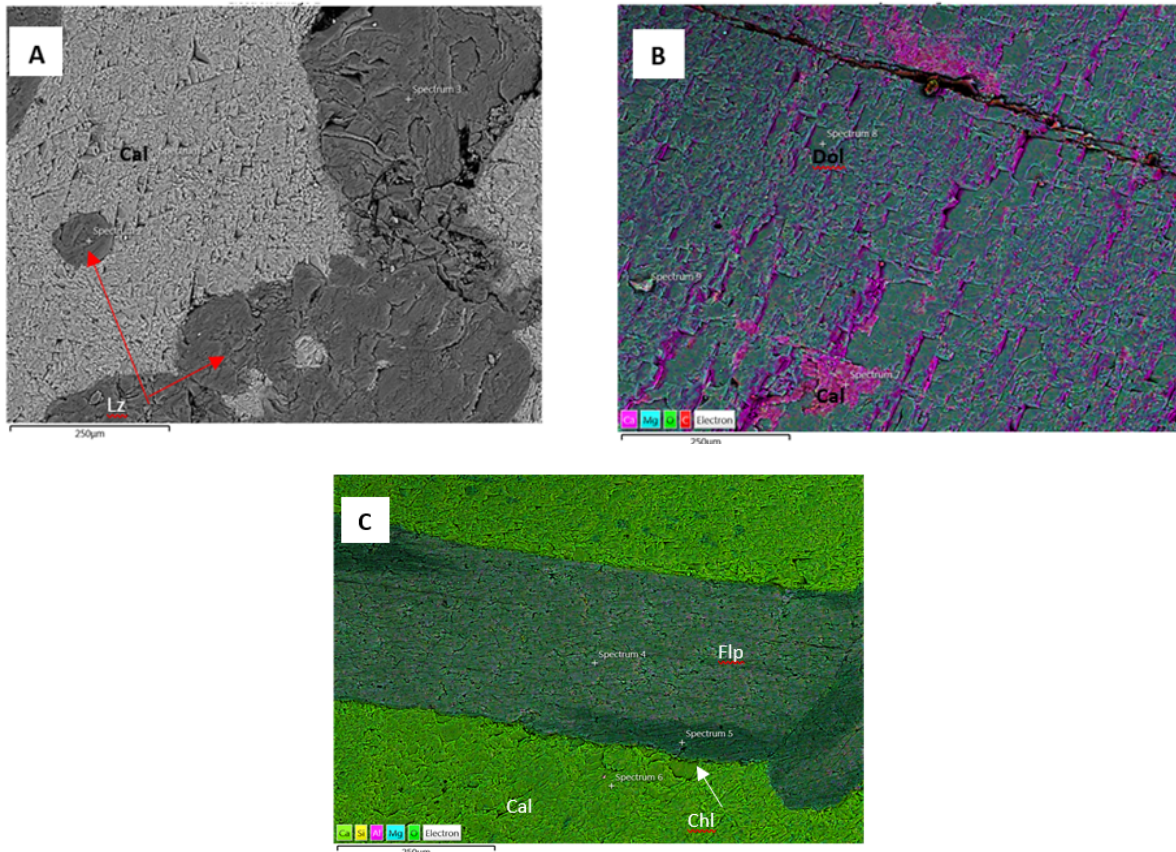


Figure 5. Scanning electron microscopy (SEM) image of Group 1 marbles (MM-TR-302 and 386A samples). (A) Backscattered electron image of calcite and lizardite. (B) Energy-dispersive spectrometry (EDS) image of dolomite interspersed with calcite. (C) EDS image of phlogopite, chlorite, and calcite.

epidote (saussuritization) and sericitization. Plagioclases and K-feldspar (microcline) could be distinguished by the characteristic twinning in some samples. When this aspect is absent, they are defined as feldspar. The Michel Levi method indicates a labradorite composition for plagioclase, confirming the works of Oliveira (1976) and Polleto (2014). The presence of detrital zircon is evidenced in Figure 6F.

Apatite in marbles and calcsilicates

Apatite makes up about 5 to 10 vol.% of the total rock volume in calcsilicate and marble sequences of the Tanque Novo-Ipirá Complex. It is present in both marble groups and most commonly occurs as colorless, white to greyish subdiomorphic to xenomorphic prismatic inclusions in calcite (Fig. 7A). More rarely, they occur as idiomorphic crystals in straight contact with calcite and interstitial quartz (Fig. 7B). In calcsilicate rocks, apatite forms subdiomorphic to idiomorphic crystals with a prismatic habit oriented according to the foliation. They are associated with feldspar, hornblende, and diopside separated by straight to curved contacts (Figs. 7C and 7D). The XRD analysis shows that fluorapatite is associated with calcite and diopside in the Group 1 marble and in diopsidites, respectively (Suppls. 2 and 3).

Metapsammites

Metapsammites occur in the south and south-central regions of the study area, between the Bonfim de Ipirá and

Ipirá districts. The best preserved metapsammite outcrops are found on mountain tops, such as Serra do Camisão, where they are associated with the main phosphate mineralizations in this region. Their quartz contents vary from 40 to 60 vol.%. Other associated minerals include feldspar, garnet, diopside, biotite, sericite, and zircon. These rocks have porphyroblastic garnet crystal and granular granoblastic textures (Figs. 8A–8C).

Graphite schists

Graphite schists occur in contact with metapsammite and marble in bodies of reduced widths but with extensive continuity (2.3 km, N-S direction) that were not mapped on the 1:100,000 scale. Brown clay-rich sands and residual soil characterize the weathering profile. Two samples were petrographically described: graphite-feldspar schist sample, located north of Bonfim-Ipirá, and schist with graphite, dolomite, sericite, and quartz, associated with possible organic structures located south of Bonfim do Ipirá (Figs. 9A and 9B).

RESULTS

Analytical results are listed in Tables 1 and 2. Ce, Pr, Eu, and Gd anomalies were calculated according to the method of Bau and Dulski (1996): $Ce/Ce_{SN}^* [Ce_{SN}/(0.5 Pr_{SN} + 0.5 La_{SN})]$, $Pr/Pr_{SN}^* [Pr_{SN}/(0.5 Ce_{SN} + 0.5 Nd_{SN})]$, $Eu/Eu_{SN}^* [Eu_{SN}/(0.67 Sm_{SN} + 0.33 Tb_{SN})]$ and $Gd/Gd_{SN}^* [Gd_{SN}/(0.33 Sm_{SN} + 0.67 Tb_{SN})]$.

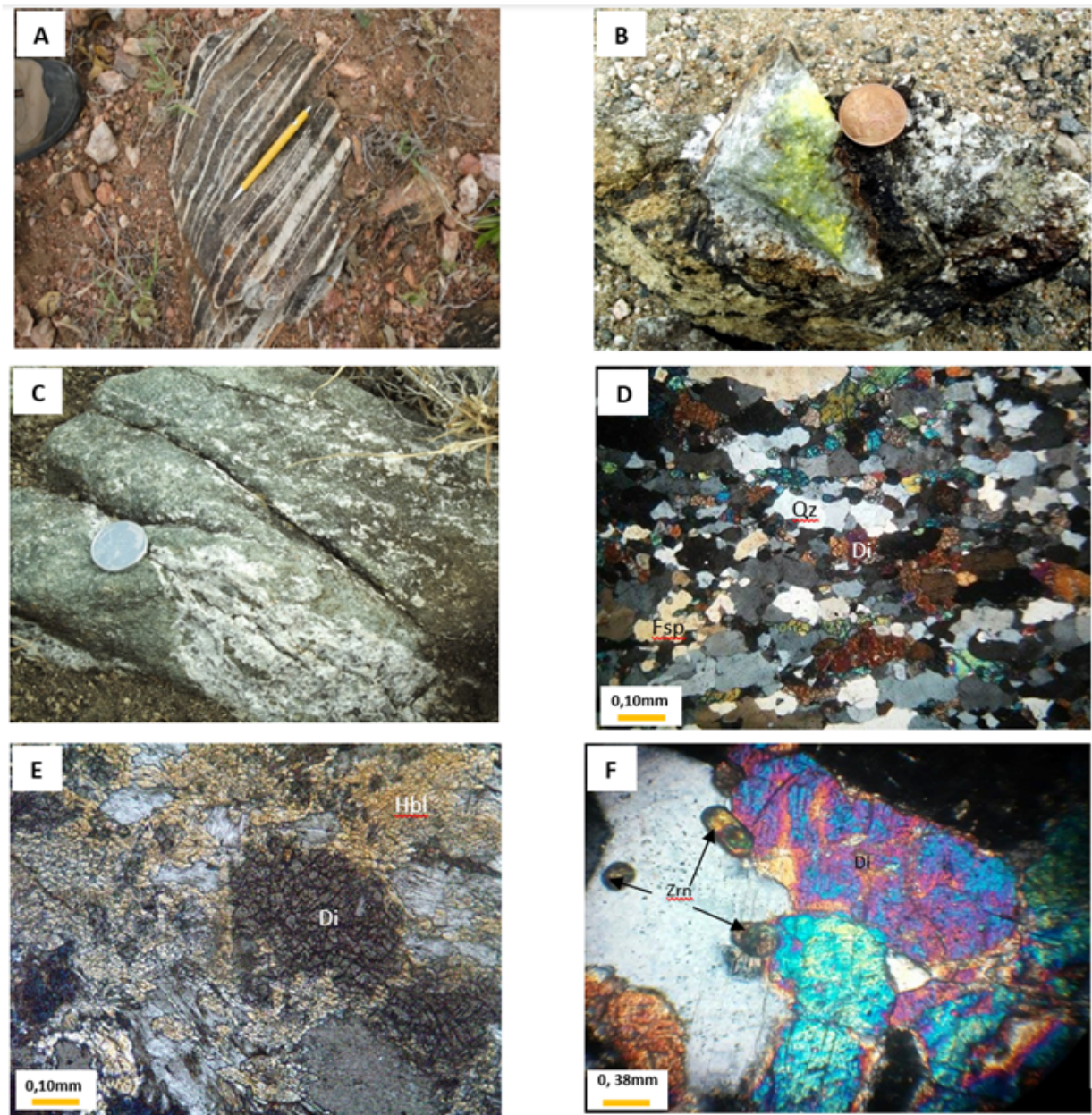


Figure 6. (A) Detail of compositional bandings showing quartz bands parallel to foliation. (B) Positive colorimetric test for phosphorus in a calcisilicate rock. (C) Outcrop of a calcisilicate rock in a contact zone (skarn) near the Gavião district showing injections/remobilization of carbonate veins. (D) Stretched quartz (Qz) and feldspar (Fsp) crystals in bands and diopside (Di). (E) Reaction corona of hornblende (Hbl) around diopside (Di). (F) Idiomorphic and subidiomorphic zircon (Zrn) crystals in diopside.

Major and trace element geochemistry

The SiO_2 concentration in marbles ranges from 9.5 to 15.92 wt.% in Group 1 and 14 to 21 wt.% in Group 2. The average MgO content is 15.7 wt.% in Group 1 and 1.3 wt.% in Group 2, whereas the average abundance of CaO in the groups is 33.5 and 40.16 wt.%, respectively. The Al_2O_3 concentrations in Group 1 marbles range from 0.52 to 1.44 wt.%, whereas rocks of Group 2 present 4.38 to 7.14 wt.% Al_2O_3 .

In calcisilicate rocks, the SiO_2 concentration ranges from 47 to 68 wt.%, with an average of 57.8 wt.%. CaO and MgO contents are highly variable: the CaO content averages 16.23 wt.%, ranging from 2.2 to 24.62 wt.%, whereas MgO concentrations range between 1.2 and 20.83 wt.%, with an average of 11.2 wt.%. The average Al_2O_3 and K_2O contents are 6.74 and 2.10 wt.%, respectively, and the K_2O content ranges between 0.05 and 7.48 wt.%.

Samples from the Group 1 plot in the field of calcitic-dolomitic to dolomitic marbles and from Group 2 are classified as calcisilicate marbles (Fig. 10A).

The P_2O_5 concentration in calcisilicate rocks averages 0.13 wt.%, but anomalously high contents of 2.03 and 3.20 wt.% were measured in MM-TR-389B and MM-TR-55B samples, respectively.

In Group 1 marbles, the P_2O_5 content averages 0.86 wt.% (0.04 to 2.33 wt.%), and the highest concentrations are found in MM-TR-297, MM-TR-302, and KP-49 samples (0.99, 1.58, and 2.33 wt.%, respectively). Marbles of Group 2 present lower P_2O_5 concentrations — 0.14 to 0.19 wt.% (Fig. 10B).

Rare Earth Elements and Yttrium (REEY) Behavior

Marbles of Group 1 have ΣREE ranging from 7.87 to 45.88 ppm (average 23.3). Marbles of Group 2 have higher

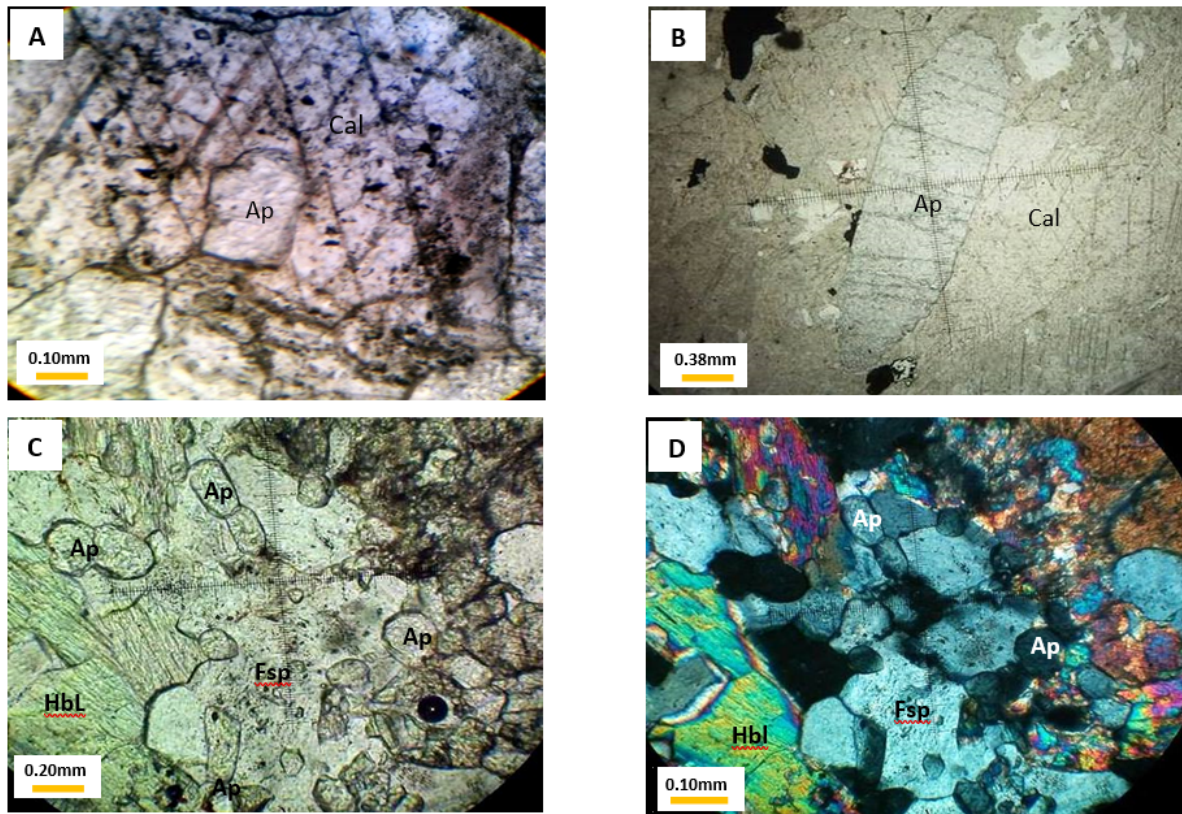


Figure 7. (A) Apatite (Ap) inclusions in calcite (Cal); (B) Idiomorphic apatite in marble; (C & D) Apatite crystals oriented in a calcisilicate rock (C: PPL; D: XPL). PPL: plane-polarized light; XPL: cross-polarized light.

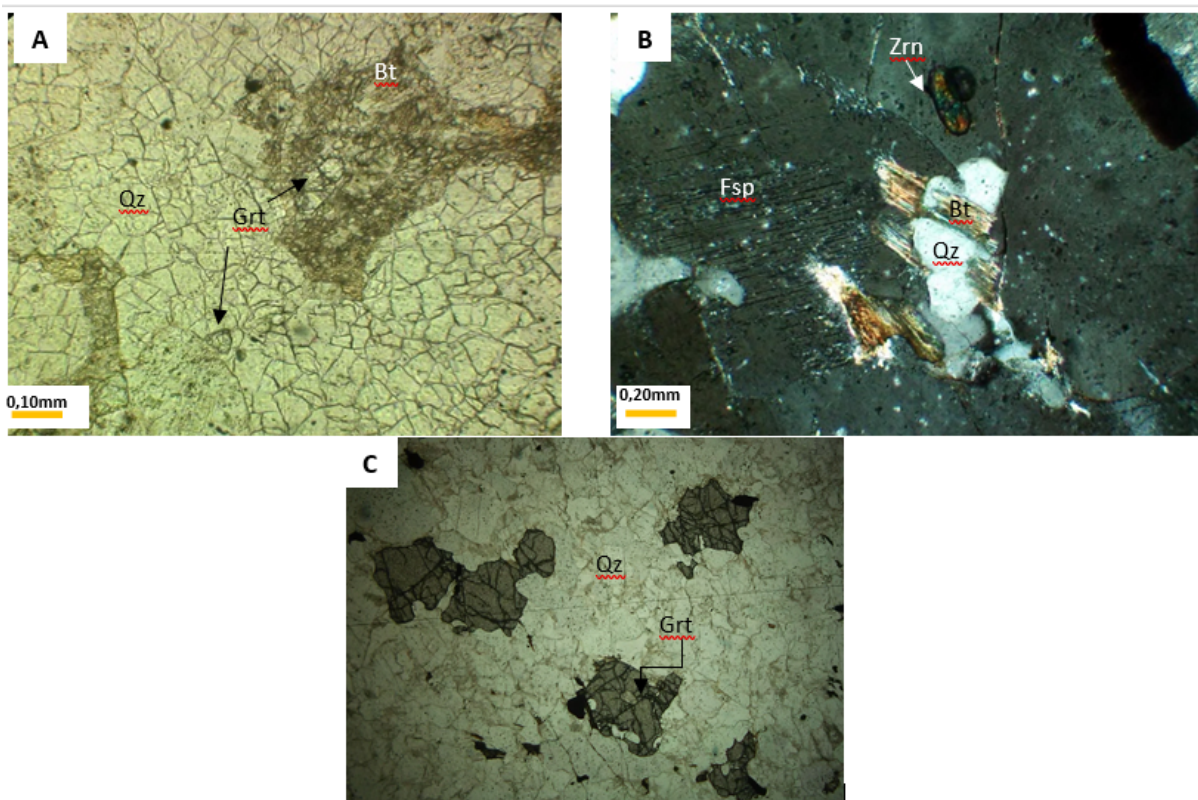


Figure 8. (A) Metapsammite with granular granoblastic texture containing garnet, feldspar, and sericite. (B) Inclusion of biotite in sericitized feldspar alongside idiomorphic zircon inclusions. (C) Metapsammite with porphyroblastic texture containing garnet and quartz.

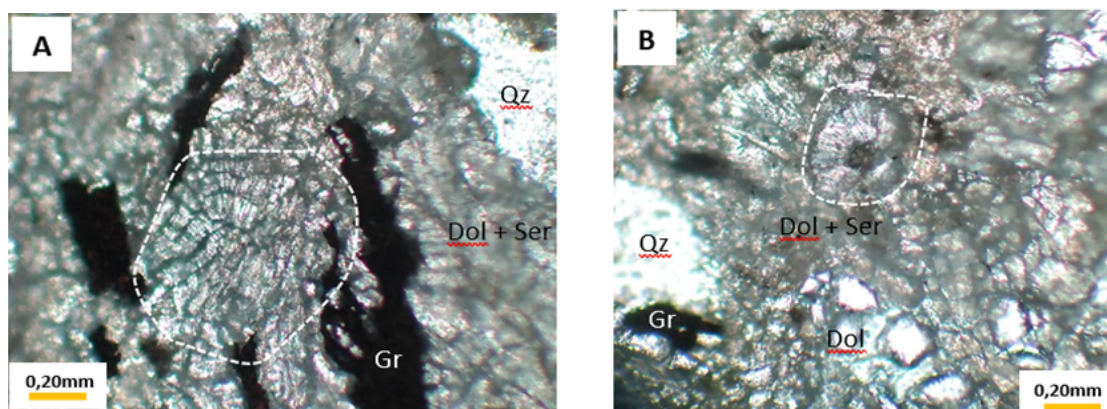


Figure 9. (A) Graphite associated with inferred organic structures (dashed line), dolomite, and quartz. (B) Dolomite associated with organic structures and quartz in a sericitic matrix.

Σ REE contents (79.92 and 59.36 ppm). Calcisilicate rocks show Σ REE contents of 22.10–323.42 ppm (average 85.87). Y contents range between 28 and 40 ppm in marbles of Group 1 and between 26 and 27 ppm in marbles of Group 2.

Most rocks have flat, REE-depleted patterns with respect to PAAS, negative Ce anomalies, variable but generally positive Eu anomalies, and positive Y anomalies. REE-normalized patterns of Group 2 marbles are flatter and closer to the PAAS composition. Marbles exhibit a small enrichment in light REE (LREE) compared to heavy REE (HREE), as evidenced by Pr/Yb_{SN} ratios, ranging from 0.60 to 2.73 in Group 1 marbles and around 1.3 in Group 2 marbles. LREE enrichment is most prominent in calcisilicate rocks (Pr/Yb_{SN} 0.80–3.81).

Most samples show negative Ce anomalies. Marbles of Group 1 have Ce/Ce* values of 0.12–0.57, except for the TR-386 sample (1.91), whereas marbles of Group 2 show Ce/Ce* values of 0.88 and 0.86. Most calcisilicate samples (n=24/29) present negative Ce anomalies (Ce/Ce* 0.46–0.99), excluding 5 samples in which Ce/Ce* varies from 1.01 to 1.27. The measured Eu anomalies are highly variable: Group 1 marbles show Eu/Eu* values of 0.92 to 1.82, while these values range between 0.98 and 1.08 in Group 2 marbles and between 0.45 and 1.56 in calcisilicate rocks. Calcisilicate rocks have Y/Ho ratios between 23.4 and 37.4. Group 1 marbles display Gd/Gd* values of 1.08–1.36, whereas these ratios vary from 1.10 to 1.15 in Group 2 and from 0.94 to 1.94 in calcisilicate rocks.

Geochronology

Zircon crystals extracted from the calcisilicate rock sample (MM-TR-26) are pale brown, light pink, and colorless, with a subidiomorphic to idiomorphic prismatic habit. Twenty spots in 19 zircons (Tab. 3) yielded 2 concordant ages of 2595 ± 18 Ma, placed in the crystal core, whereas the rims gave an age of 2082 ± 14 Ma, which was interpreted as a late Paleoproterozoic metamorphic event (Fig. 11).

The $^{207}\text{Pb}/^{206}\text{Pb}$ age of the oldest zircon is 2736 Ma, registered in only one crystal. The sample has a higher frequency of Paleoproterozoic crystals from 2453 to 2128 Ma and older Neoproterozoic populations aged between 2736 and 2573 Ma. The youngest zircon found is 2128 Ma, not the age of the most

frequent Paleoproterozoic population, but it marks the maximum deposition limit of the metasedimentary package. Zircons have U (53–374 ppm) and Th (20–374 ppm) content and Th/U ratios varying between 0.21–1.88 ppm.

DISCUSSION

The intense deformation and metamorphism hinder the reconstruction of the metasedimentary succession of the Tanque Novo-Ipirá Complex. Primary sedimentary structures were obliterated, making it difficult to interpret the depositional environment, but correlations between elements and geochemical patterns, especially REEY signatures, provide information about their origin and possible paleoenvironmental conditions during and after sedimentation.

The mineral association of metasediments reflects two mineral parageneses: prograde and retrograde assemblage. The prograde mineral assemblage consists of olivine + diopside + garnet + calcite, while the retrograde assemblage comprises serpentine + tremolite + microcline + biotite + hornblende + talc + sericite. According to Ribeiro (2016) and considering that the metamorphism was essentially anhydrous and developed under conditions of high CO₂ fugacity, the association of forsterite + calcite, responsible for the progressive paragenesis, was derived from the $\text{Di} + 3\text{Dol} = 4\text{Cal} + \text{Fo} + 2\text{CO}_2$ reaction (Winkler 1979). The variation of equilibrium conditions for this reaction according to different values of temperature and CO₂ fugacity suggests a pressure range of 4 to 7 kbar and temperature conditions between 710 and 810°C (Berman 1991), respectively, indicating that progressive metamorphism has reached transitional amphibolite-granulite metamorphic conditions.

Olivine serpentinization should have occurred at 500°C under low XCO₂ conditions (about 5%), which represents the stability field of this mineral (Evans 2010). Serpentine talcification requires greater CO₂ fugacity and would have occurred at temperatures of 350–450°C (Winkler 1979).

Although REEY are often relatively immobile, they can be mobilized during metamorphic processes, especially during metasomatic events (Bau 1991, 1993, 1999, Borisov *et al.* 2018). However, REEY patterns experience limited change

Table 1. Major, trace, and rare earth element concentrations in the analyzed marble (MRM) samples.

| Sample | Group 1 | | | | | Group 2 | | |
|------------------------------------|-----------|-----------|-----------|-----------|----------|-----------|-----------|-----------|
| | MM-TR-69A | MM-TR-275 | MM-TR-297 | MM-TR-302 | MM-KP-49 | MM-TR-56A | MM-TR-293 | MM-TR-299 |
| | MRM | MRM | MRM | MRM | MRM | MRM | MRM | MRM |
| SiO ₂ (wt.%) | 10.95 | 11.13 | 12.12 | 11.01 | 12.99 | 9.50 | 21.21 | 14.05 |
| TiO ₂ | <0.01 | 0.06 | 0.05 | 0.08 | 0.12 | 0.03 | 0.31 | 0.09 |
| Al ₂ O ₃ | 0.65 | 1.44 | 0.67 | 1.20 | 1.00 | 1.12 | 7.14 | 4.38 |
| Fe ₂ O ₃ (t) | 0.48 | 1.24 | 1.24 | 1.36 | 0.96 | 0.85 | 3.85 | 1.54 |
| MnO | 0.09 | 0.07 | <0.01 | 0.14 | 0.04 | 0.07 | 0.08 | 0.07 |
| MgO | 16.88 | 18.04 | 13.95 | 15.00 | 17.65 | 12.38 | 1.84 | 0.79 |
| CaO | 34.93 | 28.33 | 32.10 | 36.52 | 29.58 | 38.21 | 39.93 | 40.39 |
| K ₂ O | 0.04 | 0.07 | 0.08 | 0.11 | 0.11 | 0.05 | 2.40 | 1.38 |
| Na ₂ O | <0.01 | <0.01 | <0.01 | 0.11 | 0.12 | 0.02 | 0.20 | 0.07 |
| P ₂ O ₅ | 0.10 | 0.28 | 0.99 | 1.58 | 2.33 | 0.72 | 0.14 | 0.19 |
| LOI | 35.80 | 34.65 | 34.44 | 34.43 | 33.30 | 36.42 | 27.33 | 32.89 |
| Sum | 99.92 | 95.31 | 95.64 | 101.54 | 98.20 | 99.37 | 104.43 | 95.84 |
| Ba (ppm) | 130.00 | 9.00 | 9.00 | 333.00 | 33.00 | 1,814.00 | 150.00 | 133.00 |
| Hf | <0.05 | 0.52 | 0.94 | 0.21 | 1.32 | <0.05 | 2.37 | 1.18 |
| Rb | 1.60 | 0.40 | 0.40 | 0.40 | N.A. | 1.30 | 63.30 | 48.80 |
| Ga | 0.70 | 3.10 | 2.30 | 2.90 | 1.70 | 1.70 | 10.20 | 6.70 |
| Zr | 9.00 | 22.00 | 28.00 | 9.00 | 72.00 | 20.00 | 87.00 | 76.00 |
| Sr | 70.00 | 32.00 | 88.00 | 66.00 | 46.00 | 30.00 | 510.00 | 852.00 |
| Cr | 4.00 | 2.00 | 3.00 | 13.00 | 6.00 | 5.00 | 41.00 | 8.00 |
| Ni | 7.00 | 14.00 | 10.00 | 15.00 | 18.00 | 12.00 | 13.00 | 3.00 |
| Co | 4.00 | <3 | <3 | 4.00 | 2.50 | 4.00 | 3.00 | <3 |
| V | 7.00 | 3.00 | 5.00 | 13.00 | <5 | 8.00 | 25.00 | 10.00 |
| U | 1.39 | 0.11 | 2.44 | 0.32 | 0.24 | 0.46 | 2.16 | 3.87 |
| Y | 12.68 | 3.09 | 11.95 | 17.98 | 3.58 | 5.10 | 11.66 | 9.01 |
| La | 39.00 | 16.30 | 19.60 | 12.00 | 9.70 | 51.90 | 29.50 | 22.50 |
| Ce | 10.50 | 9.80 | 15.20 | 11.90 | 8.00 | 7.10 | 46.00 | 33.90 |
| Pr | 5.13 | 1.00 | 1.80 | 1.51 | 0.86 | 1.23 | 4.74 | 3.53 |
| Nd | 19.70 | 4.00 | 7.80 | 6.50 | 3.20 | 3.10 | 17.30 | 12.90 |
| Sm | 3.00 | 0.60 | 1.80 | 1.40 | 0.60 | 0.50 | 2.80 | 2.20 |
| Eu | 0.63 | 0.14 | 0.35 | 0.31 | 0.14 | 0.22 | 0.58 | 0.42 |
| Gd | 2.61 | 0.74 | 2.06 | 1.90 | 0.55 | 0.71 | 2.67 | 2.02 |
| Tb | 0.41 | 0.11 | 0.31 | 0.29 | 0.08 | 0.12 | 0.37 | 0.30 |
| Dy | 1.81 | 0.56 | 1.85 | 1.98 | 0.48 | 0.58 | 2.12 | 1.63 |
| Ho | 0.38 | 0.11 | 0.41 | 0.45 | 0.10 | 0.15 | 0.45 | 0.33 |
| Er | 0.91 | 0.32 | 1.25 | 1.26 | 0.27 | 0.35 | 1.33 | 0.98 |
| Tm | 0.12 | 0.05 | 0.16 | 0.17 | 0.05 | 0.06 | 0.18 | 0.13 |
| Yb | 0.60 | 0.20 | 0.90 | 0.80 | 0.20 | 0.30 | 1.20 | 0.90 |
| Lu | 0.08 | 0.05 | 0.14 | 0.11 | 0.05 | 0.06 | 0.18 | 0.12 |
| ΣREE | 45.88 | 17.68 | 34.03 | 28.58 | 14.58 | 14.48 | 79.92 | 59.36 |
| ΣLREE | 77.96 | 31.84 | 46.55 | 33.62 | 22.50 | 64.05 | 100.92 | 75.45 |
| ΣHREE | 6.92 | 2.14 | 7.08 | 6.96 | 1.78 | 2.33 | 8.50 | 6.41 |
| Ce/Ce* | 0.16 | 0.46 | 0.53 | 0.62 | 0.57 | 0.12 | 0.88 | 0.86 |
| Pr/Pr* | 1.63 | 0.94 | 0.97 | 1.00 | 1.00 | 1.54 | 0.99 | 0.99 |
| Y/Y* | 1.22 | 0.99 | 1.09 | 1.52 | 1.30 | 1.37 | 0.95 | 0.98 |
| Y/Ho | 33.37 | 28.09 | 29.15 | 39.96 | 35.80 | 34.00 | 25.91 | 27.30 |
| Eu/Sm | 0.21 | 0.23 | 0.19 | 0.22 | 0.23 | 0.44 | 0.21 | 0.19 |
| Ba/Nd | 6.60 | 2.25 | 1.15 | 51.23 | 10.31 | 585.16 | 8.67 | 10.31 |
| Eu/Eu* | 1.09 | 1.09 | 0.93 | 0.98 | 1.22 | 1.83 | 1.08 | 0.99 |
| Gd/Gd* | 1.04 | 1.33 | 1.26 | 1.39 | 1.11 | 1.37 | 1.16 | 1.10 |
| MgO+CaO | 51.81 | 46.37 | 46.05 | 51.52 | 47.23 | 50.59 | 41.77 | 41.18 |
| Dy/Sm _N | 0.72 | 1.11 | 1.22 | 1.68 | 0.95 | 1.38 | 0.90 | 0.88 |
| Pr/Sm _N | 1.07 | 1.05 | 0.63 | 0.68 | 0.90 | 1.55 | 1.06 | 1.01 |
| ΣREEY-La | 5.76 | 1.66 | 4.84 | 4.78 | 1.49 | 1.90 | 6.81 | 5.09 |
| Pr/Yb _N | 2.73 | 1.60 | 0.64 | 0.60 | 1.37 | 1.31 | 1.26 | 1.25 |
| Sm/Yb _N | 2.54 | 1.52 | 1.02 | 0.89 | 1.52 | 1.22 | 1.19 | 1.24 |
| Sm/Pr _N | 0.93 | 0.95 | 1.59 | 1.48 | 1.11 | 0.94 | 0.94 | 0.99 |

REE: rare earth elements; LREE: light REE; HREE: heavy REE; REEY: REE and yttrium; N.A.: not analyzed.

Table 2. Major, trace, and rare earth element concentrations in the analyzed calcsilicate (CLC) samples.

| Sample | MM-TR-55 | MM-TR-61 | MM-TR-374 | MM-TR-15B | MM-TR-5A | MM-TR-15A | MM-TR-1D | MM-TR-56B | MM-TR-216 | MM-TR-22 | MM-TR-389B | MM-TR-260A | MM-TR-14 |
|------------------------------------|----------|----------|-----------|-----------|----------|-----------|----------|-----------|-----------|----------|------------|------------|----------|
| | CLC | CLC | CLC | CLC | CLC | CLC | CLC | CLC | CLC | CLC | CLC | CLC | CLC |
| SiO ₂ (wt.%) | 47.03 | 49.03 | 49.70 | 50.95 | 51.00 | 51.46 | 53.96 | 54.20 | 54.28 | 54.93 | 57.34 | 57.74 | 58.48 |
| TiO ₂ | 0.74 | 0.87 | 1.15 | 0.16 | 0.10 | 0.10 | 0.10 | 0.12 | 0.11 | 0.06 | 0.25 | 0.06 | 0.21 |
| Al ₂ O ₃ | 7.48 | 13.89 | 12.64 | 8.46 | 3.28 | 4.31 | 3.34 | 3.72 | 4.83 | 3.59 | 7.04 | 5.84 | 8.80 |
| Fe ₂ O ₃ (t) | 7.79 | 11.78 | 13.92 | 3.20 | 2.38 | 3.12 | 2.86 | 1.85 | 2.98 | 1.70 | 3.36 | 1.18 | 4.21 |
| MnO | 0.24 | 0.51 | 0.27 | 0.14 | 0.26 | 0.13 | 0.12 | 0.22 | 0.38 | 0.09 | 0.21 | 0.09 | 0.20 |
| MgO | 11.96 | 2.66 | 8.52 | 11.42 | 16.32 | 14.91 | 15.60 | 15.92 | 12.20 | 15.86 | 9.84 | 10.34 | 12.20 |
| CaO | 21.33 | 15.75 | 13.16 | 16.63 | 24.62 | 22.66 | 23.78 | 22.62 | 20.15 | 22.22 | 11.37 | 14.78 | 12.12 |
| K ₂ O | 0.05 | 0.30 | 1.26 | 1.81 | 0.11 | 0.53 | 0.24 | 0.65 | 1.28 | 0.85 | 4.75 | 4.97 | 0.75 |
| Na ₂ O | 0.14 | 1.77 | 1.12 | 1.44 | 0.16 | 0.44 | 0.39 | 0.31 | 0.43 | 0.44 | 0.51 | 0.26 | 1.32 |
| P ₂ O ₅ | 0.06 | 0.19 | 0.12 | 0.15 | 0.36 | 0.17 | 0.09 | 0.16 | <0.01 | 0.12 | 2.03 | 0.10 | 0.04 |
| LOI | 0.96 | 0.85 | 1.32 | 1.07 | 0.63 | 1.04 | 0.63 | 0.74 | 0.99 | 0.54 | 1.08 | 0.19 | 1.71 |
| Sum | 97.78 | 97.60 | 103.18 | 95.43 | 99.22 | 98.87 | 101.11 | 100.51 | 97.63 | 100.40 | 97.78 | 95.55 | 100.04 |
| Ba (ppm) | 316.00 | 344.00 | 832.00 | 1,575.00 | 166.00 | 452.00 | 158.00 | 5,417.00 | 581.00 | 1,038.00 | 14,098.00 | 1,239.00 | 163.00 |
| Hf | 3.18 | 3.83 | 1.70 | 2.42 | 0.48 | 0.42 | 1.78 | 0.37 | 2.68 | 0.35 | 3.36 | 1.76 | 2.32 |
| Rb | 1.10 | 7.00 | 57.90 | 56.20 | 3.20 | 26.50 | 11.60 | 22.50 | 54.50 | 32.00 | 101.50 | 92.10 | 24.60 |
| Ga | 16.70 | 16.70 | 17.60 | 10.30 | 4.60 | 7.20 | 7.10 | 5.70 | 9.70 | 5.20 | 10.20 | 6.50 | 12.60 |
| Zr | 153.00 | 184.00 | 76.00 | 98.00 | 46.00 | 32.00 | 48.00 | 35.00 | 89.00 | 31.00 | 145.00 | 63.00 | 67.00 |
| Sr | 155.00 | 164.00 | 146.00 | 172.00 | 15.00 | 70.00 | 31.00 | 54.00 | 106.00 | 46.00 | 115.00 | 74.00 | 75.00 |
| Cr | 16.00 | 8.00 | N.A. | 5.00 | 4.00 | 3.00 | 3.00 | 5.00 | 2.00 | 4.00 | N.A. | 3.00 | 6.00 |
| Ni | 100.00 | 54.00 | 172.00 | 37.00 | 24.00 | 29.00 | 19.00 | 33.00 | 34.00 | 20.00 | 42.00 | 15.00 | 39.00 |
| Co | 23.50 | 27.90 | 58.50 | 7.90 | 3.30 | 6.10 | 5.60 | 7.70 | 6.50 | 3.10 | 7.60 | 2.40 | 10.10 |
| V | 88.00 | 125.00 | 207.00 | 30.00 | <5 | <5 | 20.00 | <5 | 24.00 | <5 | <5 | <5 | 44.00 |
| U | 2.16 | 2.06 | 0.53 | 3.14 | 0.66 | 3.94 | 0.70 | 1.18 | 2.45 | 1.18 | 2.28 | 0.53 | 1.80 |
| Y | 23.37 | 39.23 | 23.55 | 20.22 | 11.99 | 12.30 | 25.27 | 8.58 | 15.95 | 11.34 | 29.17 | 4.04 | 15.51 |
| La | 33.70 | 46.20 | 18.30 | 50.30 | 14.40 | 15.60 | 31.10 | 9.60 | 22.20 | 16.30 | 32.20 | 11.20 | 31.40 |
| Ce | 57.50 | 72.60 | 42.50 | 62.50 | 16.00 | 28.60 | 44.50 | 13.60 | 46.80 | 18.60 | 67.50 | 11.50 | 41.20 |
| Pr | 6.86 | 9.15 | 5.09 | 7.95 | 3.20 | 3.18 | 6.44 | 3.86 | 6.13 | 2.85 | 7.30 | 1.41 | 5.34 |
| Nd | 26.90 | 37.00 | 19.10 | 28.40 | 12.50 | 10.90 | 26.20 | 12.70 | 23.70 | 9.60 | 25.90 | 6.00 | 18.80 |

Continue...

Table 2. Continuation.

| Sample | MM-TR-55 | | MM-TR-61 | | MM-TR-374 | | MM-TR-15B | | MM-TR-5A | | MM-TR-15A | | MM-TR-ID | | MM-TR-56B | | MM-TR-216 | | MM-TR-22 | | MM-TR-389B | | MM-TR-260A | | MM-TR-14 | | |
|--------------------|----------|--------|----------|--------|-----------|-------|-----------|--------|----------|--------|-----------|--------|----------|--------|-----------|--------|-----------|--------|----------|--------|------------|--------|------------|--------|----------|-------|--------|
| | CLC | CLC | CLC | CLC | CLC | CLC | CLC | CLC | CLC | CLC | CLC | CLC | CLC | CLC | CLC | CLC | CLC | CLC | CLC | CLC | CLC | CLC | CLC | CLC | CLC | CLC | CLC |
| Sm | 4.10 | 5.70 | 4.30 | 4.40 | 2.60 | 1.80 | 5.10 | 1.10 | 4.50 | 1.70 | 5.40 | 1.10 | 4.50 | 1.70 | 5.40 | 1.10 | 4.50 | 1.70 | 5.40 | 1.10 | 4.50 | 1.10 | 4.50 | 1.10 | 4.50 | 1.10 | 3.00 |
| Eu | 1.09 | 1.46 | 1.31 | 0.99 | 0.48 | 0.37 | 0.62 | 0.42 | 0.54 | 0.40 | 0.83 | 0.20 | 0.54 | 0.40 | 0.83 | 0.20 | 0.54 | 0.40 | 0.83 | 0.20 | 0.54 | 0.20 | 0.54 | 0.20 | 0.54 | 0.20 | 0.73 |
| Gd | 4.24 | 5.91 | 4.65 | 3.59 | 2.31 | 1.72 | 5.01 | 2.25 | 4.06 | 1.85 | 5.07 | 1.01 | 4.06 | 1.85 | 5.07 | 1.01 | 4.06 | 1.85 | 5.07 | 1.01 | 4.06 | 1.01 | 4.06 | 1.01 | 4.06 | 1.01 | 2.85 |
| Tb | 0.67 | 0.99 | 0.69 | 0.67 | 0.37 | 0.32 | 0.82 | 0.27 | 0.60 | 0.35 | 0.75 | 0.14 | 0.60 | 0.35 | 0.75 | 0.14 | 0.60 | 0.35 | 0.75 | 0.14 | 0.60 | 0.14 | 0.60 | 0.14 | 0.60 | 0.14 | 0.42 |
| Dy | 3.65 | 5.53 | 4.13 | 3.10 | 1.98 | 1.69 | 4.40 | 1.28 | 3.25 | 1.61 | 4.43 | 0.73 | 3.25 | 1.61 | 4.43 | 0.73 | 3.25 | 1.61 | 4.43 | 0.73 | 3.25 | 0.73 | 3.25 | 0.73 | 3.25 | 0.73 | 2.35 |
| Ho | 0.79 | 1.26 | 0.80 | 0.66 | 0.45 | 0.35 | 0.88 | 0.31 | 0.60 | 0.38 | 0.88 | 0.17 | 0.60 | 0.38 | 0.88 | 0.17 | 0.60 | 0.38 | 0.88 | 0.17 | 0.60 | 0.17 | 0.60 | 0.17 | 0.60 | 0.17 | 0.51 |
| Er | 2.24 | 3.40 | 2.30 | 1.72 | 1.14 | 1.07 | 2.28 | 0.77 | 1.77 | 1.00 | 2.42 | 0.46 | 1.77 | 1.00 | 2.42 | 0.46 | 1.77 | 1.00 | 2.42 | 0.46 | 1.77 | 0.46 | 1.77 | 0.46 | 1.77 | 0.46 | 1.48 |
| Tm | 0.32 | 0.48 | 0.30 | 0.28 | 0.18 | 0.17 | 0.32 | 0.11 | 0.23 | 0.15 | 0.33 | 0.08 | 0.23 | 0.15 | 0.33 | 0.08 | 0.23 | 0.15 | 0.33 | 0.08 | 0.23 | 0.08 | 0.23 | 0.08 | 0.23 | 0.08 | 0.21 |
| Yb | 2.00 | 3.30 | 1.90 | 1.70 | 1.00 | 1.00 | 2.00 | 0.80 | 1.50 | 0.90 | 2.00 | 0.40 | 1.50 | 0.90 | 2.00 | 0.40 | 1.50 | 0.90 | 2.00 | 0.40 | 1.50 | 0.40 | 1.50 | 0.40 | 1.50 | 0.40 | 1.30 |
| Lu | 0.29 | 0.49 | 0.25 | 0.26 | 0.16 | 0.17 | 0.30 | 0.12 | 0.22 | 0.15 | 0.27 | 0.08 | 0.22 | 0.15 | 0.27 | 0.08 | 0.22 | 0.15 | 0.27 | 0.08 | 0.22 | 0.08 | 0.22 | 0.08 | 0.22 | 0.08 | 0.20 |
| ΣREE | 110.65 | 147.27 | 87.32 | 116.22 | 42.37 | 51.34 | 98.87 | 37.59 | 93.90 | 39.54 | 123.08 | 23.28 | 93.90 | 39.54 | 123.08 | 23.28 | 93.90 | 39.54 | 123.08 | 23.28 | 93.90 | 23.28 | 93.90 | 23.28 | 93.90 | 23.28 | 78.39 |
| ΣLREE | 130.15 | 172.11 | 90.60 | 154.54 | 49.18 | 60.45 | 113.96 | 41.28 | 103.87 | 49.45 | 139.13 | 31.41 | 103.87 | 49.45 | 139.13 | 31.41 | 103.87 | 49.45 | 139.13 | 31.41 | 103.87 | 31.41 | 103.87 | 31.41 | 103.87 | 31.41 | 100.47 |
| ΣHREE | 14.20 | 21.36 | 15.02 | 11.98 | 7.59 | 6.49 | 16.01 | 5.91 | 12.23 | 6.39 | 16.15 | 3.07 | 12.23 | 6.39 | 16.15 | 3.07 | 12.23 | 6.39 | 16.15 | 3.07 | 12.23 | 3.07 | 12.23 | 3.07 | 12.23 | 3.07 | 9.32 |
| Ce/Ce* | 0.87 | 0.78 | 0.93 | 0.71 | 0.54 | 0.94 | 0.72 | 0.50 | 0.99 | 0.62 | 1.01 | 0.65 | 0.99 | 0.62 | 1.01 | 0.65 | 0.99 | 0.62 | 1.01 | 0.65 | 0.99 | 0.65 | 0.99 | 0.65 | 0.99 | 0.65 | 0.73 |
| Pr/Pr* | 1.03 | 1.03 | 1.05 | 1.11 | 1.27 | 1.06 | 1.10 | 1.60 | 1.08 | 1.25 | 1.03 | 0.99 | 1.08 | 1.25 | 1.03 | 0.99 | 1.08 | 1.25 | 1.03 | 0.99 | 1.08 | 0.99 | 1.08 | 0.99 | 1.08 | 0.99 | 1.13 |
| Y/Y* | 1.10 | 1.18 | 1.03 | 1.13 | 1.01 | 1.28 | 1.02 | 1.08 | 0.91 | 1.15 | 1.18 | 0.91 | 0.91 | 1.15 | 1.18 | 0.91 | 0.91 | 1.15 | 1.18 | 0.91 | 0.91 | 0.91 | 0.91 | 0.91 | 0.91 | 1.13 | 1.13 |
| Y/Ho | 29.58 | 31.13 | 29.44 | 30.64 | 26.64 | 35.14 | 28.72 | 27.68 | 26.58 | 29.84 | 33.15 | 23.76 | 26.58 | 29.84 | 33.15 | 23.76 | 26.58 | 29.84 | 33.15 | 23.76 | 26.58 | 23.76 | 26.58 | 23.76 | 26.58 | 30.41 | 30.41 |
| Eu/Sm | 0.27 | 0.26 | 0.30 | 0.23 | 0.18 | 0.21 | 0.12 | 0.38 | 0.12 | 0.24 | 0.15 | 0.18 | 0.12 | 0.24 | 0.15 | 0.18 | 0.12 | 0.24 | 0.15 | 0.18 | 0.15 | 0.18 | 0.15 | 0.18 | 0.15 | 0.24 | 0.24 |
| Ba/Nd | 11.75 | 9.30 | 43.56 | 55.46 | 13.28 | 41.47 | 6.03 | 426.54 | 24.51 | 108.13 | 544.32 | 206.50 | 24.51 | 108.13 | 544.32 | 206.50 | 24.51 | 108.13 | 544.32 | 206.50 | 544.32 | 206.50 | 544.32 | 206.50 | 544.32 | 8.67 | 8.67 |
| Eu/Eu* | 1.29 | 1.22 | 1.49 | 1.12 | 0.94 | 0.97 | 0.59 | 1.57 | 0.63 | 1.04 | 0.79 | 0.96 | 0.63 | 1.04 | 0.79 | 0.96 | 0.63 | 1.04 | 0.79 | 0.96 | 0.79 | 0.96 | 0.96 | 0.96 | 0.96 | 1.25 | 1.25 |
| Gd/Gd* | 1.17 | 1.14 | 1.23 | 0.94 | 1.05 | 1.04 | 1.11 | 1.95 | 1.09 | 1.12 | 1.12 | 1.13 | 1.09 | 1.12 | 1.12 | 1.13 | 1.09 | 1.12 | 1.12 | 1.13 | 1.12 | 1.13 | 1.13 | 1.13 | 1.13 | 1.13 | 1.13 |
| MgO+CaO | 33.29 | 18.41 | 21.68 | 28.05 | 40.94 | 37.57 | 39.38 | 38.54 | 32.35 | 38.08 | 21.21 | 25.12 | 32.35 | 38.08 | 21.21 | 25.12 | 32.35 | 38.08 | 21.21 | 25.12 | 21.21 | 25.12 | 25.12 | 25.12 | 25.12 | 24.32 | 24.32 |
| Dy/Sm _N | 1.06 | 1.15 | 1.14 | 0.84 | 0.90 | 1.11 | 1.02 | 1.38 | 0.86 | 1.12 | 0.97 | 0.93 | 0.86 | 1.12 | 0.97 | 0.93 | 0.86 | 1.12 | 0.97 | 0.93 | 0.97 | 0.93 | 0.93 | 0.93 | 0.93 | 0.93 | 0.93 |
| Pr/Sm _N | 1.05 | 1.01 | 0.74 | 1.14 | 0.77 | 1.11 | 0.79 | 2.21 | 0.86 | 1.05 | 0.85 | 0.81 | 0.86 | 1.05 | 0.85 | 0.81 | 0.86 | 1.05 | 0.85 | 0.81 | 0.85 | 0.81 | 0.81 | 0.81 | 0.81 | 1.12 | 1.12 |
| ΣREEY-La | 11.21 | 16.55 | 10.91 | 10.44 | 5.71 | 5.20 | 11.45 | 4.41 | 9.06 | 4.90 | 12.15 | 2.42 | 9.06 | 4.90 | 12.15 | 2.42 | 9.06 | 4.90 | 12.15 | 2.42 | 9.06 | 2.42 | 9.06 | 2.42 | 9.06 | 2.42 | 7.60 |
| Pr/Yb _N | 1.10 | 0.89 | 0.86 | 1.49 | 1.02 | 1.02 | 1.03 | 1.54 | 1.31 | 1.01 | 1.17 | 1.13 | 1.31 | 1.01 | 1.17 | 1.13 | 1.31 | 1.01 | 1.17 | 1.13 | 1.17 | 1.13 | 1.13 | 1.13 | 1.13 | 1.31 | 1.31 |
| Sm/Yb _N | 1.04 | 0.88 | 1.15 | 1.32 | 1.32 | 0.91 | 1.30 | 0.70 | 1.52 | 0.96 | 1.37 | 1.40 | 1.52 | 0.96 | 1.37 | 1.40 | 1.52 | 0.96 | 1.37 | 1.40 | 1.37 | 1.40 | 1.40 | 1.40 | 1.40 | 1.17 | 1.17 |
| Sm/Pr _N | 0.95 | 0.99 | 1.34 | 0.88 | 1.29 | 0.90 | 1.26 | 0.45 | 1.17 | 0.95 | 1.18 | 1.24 | 1.17 | 0.95 | 1.18 | 1.24 | 1.17 | 0.95 | 1.18 | 1.24 | 1.18 | 1.24 | 1.24 | 1.24 | 1.24 | 0.89 | 0.89 |

Continue...

Table 2. Continuation.

| Sample | MM-TR-305 | MM-TR-181B | MM-TR-104B | MM-TR-319 | MM-TR-134A | MM-TR-286 | MM-TR-176 | MM-TR-132 | MM-TR-306 | MM-TR-384 | MM-TR-161 | MM-TR-129A |
|------------------------------------|-----------|------------|------------|-----------|------------|-----------|-----------|-----------|-----------|-----------|-----------|------------|
| | CLC | CLC | CLC | CLC | CLC | CLC | CLC | CLC | CLC | CLC | CLC | CLC |
| SiO ₂ (wt.%) | 60.26 | 60.73 | 63.76 | 64.64 | 64.87 | 67.17 | 67.20 | 60.53 | 61.34 | 66.92 | 68.55 | 58.56 |
| TiO ₂ | 0.08 | 0.09 | 0.10 | 0.08 | 0.10 | 0.08 | 0.10 | 0.15 | 0.61 | 0.13 | 0.73 | 0.11 |
| Al ₂ O ₃ | 3.58 | 5.67 | 6.93 | 3.38 | 6.42 | 4.36 | 10.18 | 7.50 | 13.78 | 5.85 | 14.28 | 6.71 |
| Fe ₂ O ₃ (t) | 1.78 | 1.53 | 1.24 | 1.27 | 1.27 | 1.61 | 0.90 | 1.38 | 3.62 | 1.24 | 4.67 | 2.21 |
| MnO | 0.18 | 0.09 | 0.09 | 0.11 | 0.04 | 0.09 | 0.04 | 0.10 | 0.15 | 0.18 | 0.07 | 0.13 |
| MgO | 14.36 | 12.19 | 10.14 | 10.27 | 7.81 | 8.71 | 6.52 | 11.44 | 3.74 | 8.31 | 1.24 | 13.05 |
| CaO | 20.38 | 17.71 | 13.54 | 13.42 | 10.36 | 12.32 | 8.82 | 15.23 | 7.55 | 11.02 | 2.20 | 20.03 |
| K ₂ O | 0.78 | 3.73 | 4.60 | 2.67 | 3.80 | 2.68 | 7.48 | 3.41 | 3.58 | 4.33 | 3.31 | 1.75 |
| Na ₂ O | 0.57 | 0.32 | 0.82 | 0.29 | 0.68 | 0.64 | 0.61 | 1.06 | 6.25 | 0.50 | 3.87 | 0.49 |
| P ₂ O ₅ | 0.24 | 0.16 | 0.08 | 0.14 | 0.08 | 0.05 | 0.10 | 0.20 | 0.07 | 0.05 | 0.38 | 0.25 |
| LOI | 0.71 | 0.35 | 0.22 | 0.33 | 0.32 | 0.18 | 0.53 | 0.71 | 0.19 | 0.25 | 1.27 | 0.90 |
| Sum | 102.92 | 102.57 | 101.52 | 96.60 | 95.75 | 97.89 | 102.48 | 101.71 | 100.88 | 98.78 | 100.57 | 104.19 |
| Ba (ppm) | 971.00 | 717.00 | 695.00 | 521.00 | 702.00 | 645.00 | 723.00 | 620.00 | 526.00 | 2,977.00 | 1,549.00 | 400.00 |
| Hf | 3.24 | 3.03 | 0.76 | 2.93 | 2.81 | 1.99 | 2.12 | 4.42 | 4.44 | 2.16 | 8.27 | 3.34 |
| Rb | 16.70 | 70.40 | 72.20 | 54.30 | 83.10 | 50.40 | 122.90 | 79.40 | 33.70 | 74.80 | 62.10 | 62.70 |
| Ga | 5.80 | 7.00 | 7.40 | 4.00 | 6.30 | 5.70 | 8.10 | 8.10 | 10.10 | 5.70 | 18.20 | 9.30 |
| Zr | 135.00 | 99.00 | 59.00 | 131.00 | 57.00 | 63.00 | 45.00 | 131.00 | 212.00 | 104.00 | 342.00 | 85.00 |
| Sr | 87.00 | 47.00 | 62.00 | 44.00 | 65.00 | 65.00 | 36.00 | 77.00 | 145.00 | 76.00 | 506.00 | 88.00 |
| Cr | 2.00 | 3.00 | 4.00 | 4.00 | 3.00 | 4.00 | 4.00 | 2.00 | 11.00 | N.A | 12.00 | 3.00 |
| Ni | 24.00 | 13.00 | 30.00 | 18.00 | 17.00 | 24.00 | 12.00 | 14.00 | 33.00 | 24.00 | 12.00 | 24.00 |
| Co | 4.40 | 2.70 | 3.50 | 3.80 | 2.40 | 5.50 | 1.30 | 5.10 | 8.90 | 6.10 | 7.60 | 4.30 |
| V | 14.00 | 8.00 | <5 | <5 | 16.00 | <5 | <5 | <5 | 33.00 | <5 | 72.00 | 29.00 |
| U | 1.56 | 1.32 | 0.23 | 1.29 | 0.69 | 0.48 | 0.60 | 1.05 | 1.87 | 0.32 | 1.66 | 2.48 |
| Y | 10.30 | 13.68 | 10.38 | 6.84 | 9.57 | 7.69 | 3.74 | 11.82 | 31.23 | 6.93 | 22.44 | 21.03 |
| La | 22.70 | 30.30 | 19.40 | 24.30 | 34.20 | 15.80 | 14.20 | 24.70 | 52.60 | 3.20 | 133.80 | 74.40 |
| Ce | 27.60 | 49.70 | 20.20 | 18.90 | 27.70 | 19.80 | 23.80 | 59.00 | 84.60 | 19.40 | 187.40 | 120.60 |
| Pr | 3.49 | 5.63 | 4.15 | 1.92 | 5.57 | 2.39 | 2.66 | 5.17 | 9.26 | 2.23 | 22.64 | 14.10 |

Continue...

Table 2. Continuation.

| Sample | MM-TR-305 | | MM-TR-181B | | MM-TR-104B | | MM-TR-319 | | MM-TR-134A | | MM-TR-69C | | MM-TR-286 | | MM-TR-176 | | MM-TR-132 | | MM-TR-306 | | MM-TR-384 | | MM-TR-161 | | MM-TR-129A |
|--------------------|-----------|--------|------------|-------|------------|--------|-----------|-------|------------|--------|-----------|--------|-----------|-----|-----------|-----|-----------|-----|-----------|-----|-----------|-----|-----------|-----|------------|
| | CLC | CLC | CLC | CLC | CLC | CLC | CLC | CLC | CLC | CLC | CLC | CLC | CLC | CLC | CLC | CLC | CLC | CLC | CLC | CLC | CLC | CLC | CLC | CLC | |
| Nd | 12.70 | 21.00 | 15.10 | 6.80 | 21.20 | 3.80 | 9.50 | 9.60 | 19.10 | 38.10 | 7.40 | 78.90 | 49.90 | | | | | | | | | | | | |
| Sm | 2.20 | 3.80 | 2.30 | 1.00 | 3.40 | 0.80 | 1.70 | 1.50 | 3.40 | 8.90 | 1.40 | 11.40 | 8.00 | | | | | | | | | | | | |
| Eu | 0.48 | 0.63 | 0.55 | 0.20 | 0.61 | 0.25 | 0.36 | 0.29 | 0.54 | 2.10 | 0.31 | 2.03 | 0.65 | | | | | | | | | | | | |
| Gd | 2.20 | 3.53 | 1.99 | 1.30 | 3.12 | 0.79 | 1.62 | 1.25 | 3.03 | 8.10 | 1.25 | 8.98 | 6.44 | | | | | | | | | | | | |
| Tb | 0.31 | 0.52 | 0.29 | 0.21 | 0.41 | 0.15 | 0.25 | 0.17 | 0.44 | 1.23 | 0.17 | 1.14 | 0.86 | | | | | | | | | | | | |
| Dy | 1.76 | 2.69 | 1.64 | 1.05 | 1.98 | 0.74 | 1.39 | 0.76 | 2.41 | 6.89 | 0.95 | 5.13 | 4.37 | | | | | | | | | | | | |
| Ho | 0.36 | 0.55 | 0.32 | 0.23 | 0.34 | 0.14 | 0.29 | 0.14 | 0.48 | 1.32 | 0.20 | 0.91 | 0.81 | | | | | | | | | | | | |
| Er | 1.15 | 1.47 | 0.79 | 0.67 | 0.88 | 0.48 | 0.90 | 0.41 | 1.39 | 3.98 | 0.58 | 2.39 | 2.23 | | | | | | | | | | | | |
| Tm | 0.14 | 0.21 | 0.10 | 0.08 | 0.11 | 0.06 | 0.14 | 0.06 | 0.19 | 0.50 | 0.09 | 0.31 | 0.30 | | | | | | | | | | | | |
| Yb | 1.10 | 1.30 | 0.70 | 0.50 | 0.70 | 0.40 | 0.80 | 0.40 | 1.20 | 2.90 | 0.60 | 1.90 | 1.90 | | | | | | | | | | | | |
| Lu | 0.16 | 0.20 | 0.11 | 0.10 | 0.10 | 0.07 | 0.15 | 0.07 | 0.18 | 0.34 | 0.07 | 0.29 | 0.27 | | | | | | | | | | | | |
| ΣREE | 53.65 | 91.23 | 48.24 | 32.96 | 66.12 | 22.10 | 39.29 | 41.11 | 96.53 | 168.22 | 34.65 | 323.42 | 210.43 | | | | | | | | | | | | |
| ΣLREE | 69.17 | 111.06 | 61.70 | 53.12 | 92.68 | 33.17 | 49.55 | 52.05 | 111.91 | 195.56 | 33.94 | 436.17 | 267.65 | | | | | | | | | | | | |
| ΣHREE | 7.18 | 10.47 | 5.94 | 4.14 | 7.64 | 2.83 | 5.54 | 3.26 | 9.32 | 25.26 | 3.91 | 21.05 | 17.18 | | | | | | | | | | | | |
| Ce/Ce* | 0.59 | 1.16 | 1.20 | 1.02 | 0.88 | 0.52 | 0.69 | 0.87 | 0.78 | 0.56 | 0.81 | 0.89 | 0.46 | | | | | | | | | | | | |
| Pr/Pr* | 1.10 | 1.03 | 1.34 | 0.99 | 1.30 | 1.26 | 1.02 | 1.03 | 0.90 | 0.96 | 1.09 | 1.10 | 1.07 | | | | | | | | | | | | |
| Y/Y* | 1.03 | 0.90 | 1.14 | 1.11 | 0.93 | 1.05 | 0.97 | 0.91 | 0.88 | 0.82 | 1.27 | 0.83 | 0.89 | | | | | | | | | | | | |
| Y/Ho | 28.61 | 24.87 | 32.44 | 29.74 | 28.15 | 30.43 | 26.52 | 26.71 | 24.63 | 23.66 | 34.65 | 24.66 | 25.96 | | | | | | | | | | | | |
| Eu/Sm | 0.22 | 0.17 | 0.24 | 0.20 | 0.18 | 0.31 | 0.21 | 0.19 | 0.16 | 0.24 | 0.22 | 0.18 | 0.08 | | | | | | | | | | | | |
| Ba/Nd | 76.46 | 34.14 | 46.03 | 76.62 | 33.11 | 145.26 | 67.89 | 75.31 | 32.46 | 13.81 | 402.30 | 19.63 | 8.02 | | | | | | | | | | | | |
| Eu/Eu* | 1.12 | 0.86 | 1.27 | 0.88 | 0.97 | 1.44 | 1.07 | 1.06 | 0.84 | 1.22 | 1.19 | 1.01 | 0.45 | | | | | | | | | | | | |
| Gd/Gd* | 1.19 | 1.11 | 1.06 | 1.33 | 1.14 | 1.06 | 1.11 | 1.06 | 1.09 | 1.09 | 1.11 | 1.03 | 1.04 | | | | | | | | | | | | |
| MgO+CaO | 34.74 | 29.90 | 23.68 | 23.69 | 18.17 | 27.78 | 21.03 | 15.34 | 26.67 | 11.29 | 19.33 | 3.44 | 33.08 | | | | | | | | | | | | |
| Dy/Sm _N | 0.95 | 0.84 | 0.85 | 1.25 | 0.69 | 1.10 | 0.97 | 0.60 | 0.84 | 0.92 | 0.80 | 0.53 | 0.65 | | | | | | | | | | | | |
| Pr/Sm _N | 1.00 | 0.93 | 1.13 | 1.21 | 1.03 | 1.19 | 0.88 | 1.11 | 0.96 | 0.65 | 1.00 | 1.25 | 1.11 | | | | | | | | | | | | |
| ΣREEY-La | 5.46 | 8.17 | 4.98 | 3.12 | 6.16 | 2.26 | 4.28 | 2.95 | 7.46 | 18.52 | 3.20 | 20.37 | 14.47 | | | | | | | | | | | | |
| Pr/Yb _N | 1.01 | 1.38 | 1.89 | 1.23 | 2.54 | 1.21 | 0.95 | 2.12 | 1.38 | 1.02 | 1.19 | 3.81 | 2.37 | | | | | | | | | | | | |
| Sm/Yb _N | 1.02 | 1.49 | 1.67 | 1.02 | 2.47 | 1.02 | 1.08 | 1.91 | 1.19 | 3.05 | 0.85 | 1.52 | 2.14 | | | | | | | | | | | | |
| Sm/Pr _N | 1.00 | 1.07 | 0.88 | 0.83 | 0.97 | 0.84 | 1.13 | 0.90 | 1.00 | 0.80 | 0.65 | 0.82 | 0.90 | | | | | | | | | | | | |

REE: rare earth elements; LREE: light REE; HREE: heavy REE; REEY: REE and yttrium; N.A.: not analyzed.

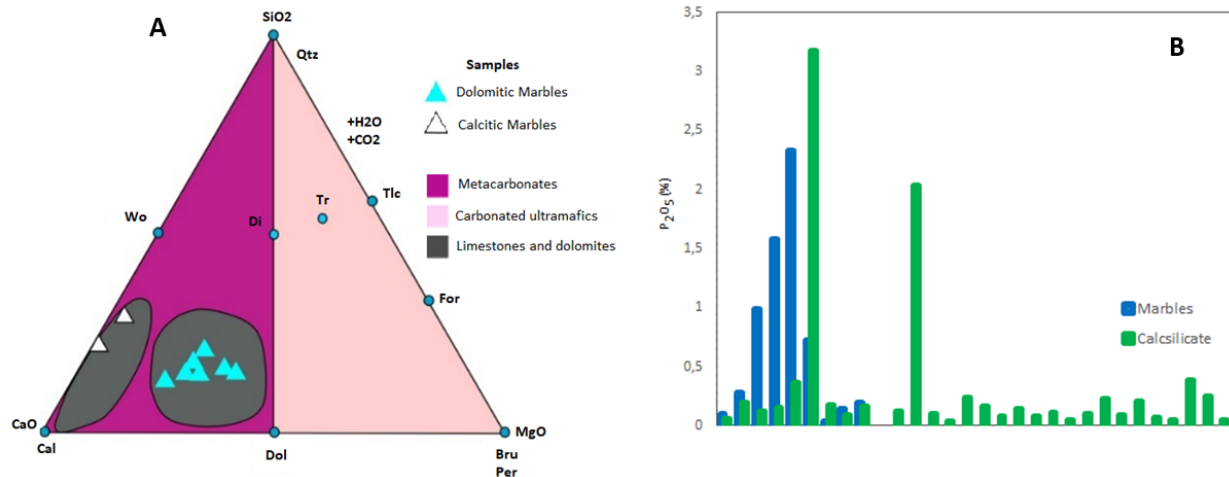


Figure 10. (A) CMS-HC system (CaO-MgO-SiO₂-H₂O-CO₂) (Winter 2001) showing the dolomitic and calcitic marbles studied. (B) P₂O₅ (%) content in the lithofacies.

Table 3. U-Pb isotope data in the MM-TR-26 calcsilicate sample.

| Sample | Spot | Age | | | | | | | | | | Location | Conc. 206/238 207/235 |
|----------|------|--------------------------------------|-----|-----|------|----------------------|---------|----------------------|---------|----------------------|---------|--------------|-----------------------------|
| | | ²⁰⁶ Pb/ ²⁰⁴ Pb | Th | U | Th/U | T _{206/238} | 1 sigma | T _{207/235} | 1 sigma | T _{207/206} | 1 sigma | | |
| | | ppm | ppm | | | | | | | | | | |
| MM-TR-26 | 20 | 767.2 | 200 | 258 | 0.77 | 2,070 | 25 | 2,073 | 17 | 2,077 | 23 | Edge | 100 |
| MM-TR-26 | 52 | 772.1 | 188 | 261 | 0.72 | 2,076 | 24 | 2,074 | 15 | 2,072 | 18 | Edge | 100 |
| MM-TR-26 | 96 | 594.8 | 156 | 177 | 0.88 | 2,090 | 23 | 2,082 | 17 | 2,073 | 23 | Edge | 100 |
| MM-TR-26 | 49 | 165.3 | 174 | 217 | 0.80 | 2,092 | 24 | 2,085 | 15 | 2,077 | 18 | Edge | 100 |
| MM-TR-26 | 11 | 604.7 | 185 | 251 | 0.74 | 2,095 | 25 | 2,095 | 15 | 2,096 | 18 | Edge | 100 |
| MM-TR-26 | 50 | 449.9 | 113 | 168 | 0.67 | 2,602 | 29 | 2,597 | 16 | 2,593 | 17 | Core | 100 |
| MM-TR-26 | 57 | 70,947.9 | 20 | 93 | 0.21 | 2,602 | 29 | 2,603 | 16 | 2,603 | 17 | Core | 100 |
| MM-TR-26 | 80 | 1,220.3 | 374 | 220 | 1.70 | 2,608 | 28 | 2,589 | 16 | 2,573 | 19 | Core | 101 |
| MM-TR-26 | 79 | 293.1 | 258 | 137 | 1.88 | 2,135 | 24 | 2,131 | 15 | 2,128 | 19 | Intermediary | 100 |
| MM-TR-26 | 68 | 76.8 | 138 | 163 | 0.85 | 2,156 | 24 | 2,141 | 15 | 2,127 | 19 | Edge | 101 |
| MM-TR-26 | 18 | 149,124.1 | 155 | 290 | 0.53 | 2,228 | 27 | 2,241 | 16 | 2,253 | 18 | Intermediary | 99 |
| MM-TR-26 | 9 | 194.3 | 246 | 374 | 0.66 | 2,259 | 27 | 2,249 | 16 | 2,239 | 18 | Edge | 100 |
| MM-TR-26 | 75 | 514.2 | 210 | 185 | 1.14 | 2,351 | 26 | 2,368 | 15 | 2,382 | 18 | Intermediary | 99 |
| MM-TR-26 | 54 | 1,510.1 | 279 | 199 | 1.41 | 2,408 | 27 | 2,418 | 16 | 2,426 | 17 | Intermediary | 100 |
| MM-TR-26 | 53 | 438.8 | 54 | 53 | 1.03 | 2,417 | 27 | 2,414 | 17 | 2,412 | 21 | Intermediary | 100 |
| MM-TR-26 | 67 | 142,191.1 | 192 | 220 | 0.87 | 2,443 | 27 | 2,451 | 16 | 2,458 | 18 | Intermediary | 100 |
| MM-TR-26 | 76 | 113,967.7 | 127 | 176 | 0.72 | 2,449 | 27 | 2,451 | 16 | 2,453 | 18 | Intermediary | 100 |
| MM-TR-26 | 33 | 114.7 | 60 | 170 | 0.35 | 2,642 | 29 | 2,645 | 16 | 2,647 | 17 | Core | 100 |
| MM-TR-26 | 10 | 337.8 | 222 | 128 | 1.74 | 2,675 | 30 | 2,665 | 17 | 2,657 | 17 | Core | 100 |
| MM-TR-26 | 39 | 179.2 | 142 | 129 | 1.10 | 2,699 | 30 | 2,720 | 16 | 2,736 | 17 | Core | 99 |

Conc.: concordia.

during high-grade metamorphism under anhydrous conditions (Cullers *et al.* 1974, Bau 1991, 1993, Alexander *et al.* 2008), thus providing information about protoliths under these conditions.

Nevertheless, diagenetic and weathering processes can modify REEY patterns, and mixing with detrital sediments in the basin during deposition can also change the primary REEY signature in carbonate rocks (Shields and Stille 2001, Northdurft *et al.* 2004, Ling *et al.* 2013, Piper and Bau 2013, Zhu and Jiang 2017).

Detrital contamination

The mechanisms that may alter the REEY signature in marine chemical sediments, such as carbonates, are diagenesis, weathering, hydrothermalism, and detrital contamination. Terrigenous inputs contribute to the mixture of silicates and oxides within chemical sedimentary rocks (Northdurft *et al.* 2004, Ling *et al.* 2013, Piper and Bau 2013, Zhu and Jiang 2017). Terrigenous sediments typically have a higher content of REE and trace elements, such as Zr, Th, and Hf, than carbonates (Taylor and McLennan 1985). According to Ling

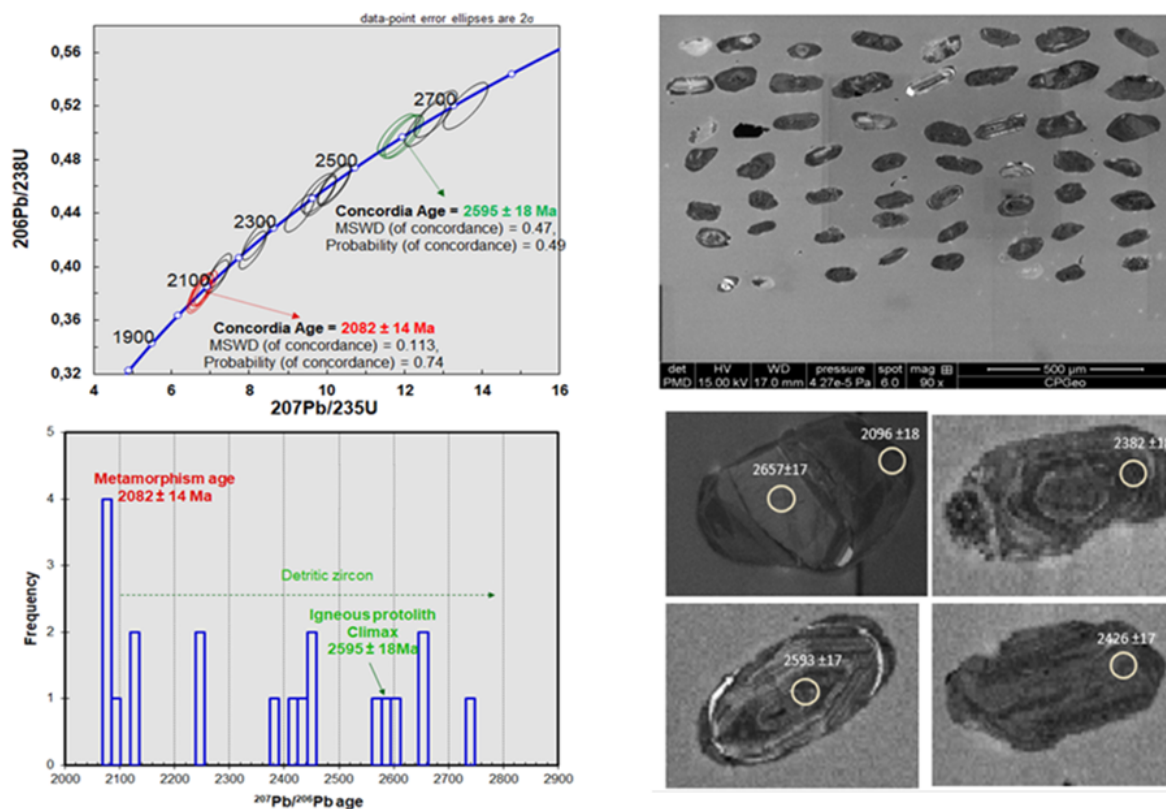


Figure 11. The left column shows the concordia diagram and the frequency distribution of the analyzed ages. The right column represents cathodoluminescence images of detrital zircons, with the location of the analyzed points and $^{207}\text{Pb}/^{206}\text{Pb}$ age. MSWD: mean squared weighted deviation.

et al. (2013) and Zhu and Jiang (2017), these REE can be partially transferred to carbonates during diagenesis. Depending on the degree of detrital contamination, the seawater signature may be partially or totally suppressed. The participation of silicates, oxides, and sulfides can be identified by the Y/Ho ratio in relation to lithophile (Zr, Th, Hf), chalcophile (Pb, Cu), and siderophile (Ni, Co, Cr) elements (Bolhar and Van Kranendonk 2007, Wang *et al.* 2018).

Y-Ho pairs are commonly assumed to be exclusively related to detrital components and are therefore used as a proxy for contamination of chemical sediments by detrital sediments in the basin (Bau and Dulski 1996, Bolhar *et al.* 2004).

Ho is removed through absorption by particulate matter in the marine system twice as fast as Y (Nozaki *et al.* 1997), generating positive Y anomalies, especially in open marine environments (Y/Ho 40–80), and smaller anomalies (Y/Ho 33–40) that characterize coastal or lagoonal environments (Bau *et al.* 1997, De Baar *et al.* 1985, Nozaki *et al.* 1997, Tostevin *et al.* 2016). Continental water bodies have Y/Ho ratios close to crustal and PAAS values — around 28 (McLennan, 1989). Y solubility increases in oxidizing environments (Bolhar *et al.* 2004), and Ho is preferably absorbed by suspended particles. Therefore, chemical sedimentation in equilibrium with seawater generates rocks with high Y/Ho ratios (Bau and Dulski 1996, Bolhar *et al.* 2004, Bau and Alexander 2006).

Y/Ho ratios vary from 24 to 37 in calcisilicate rocks and from 28 to 40 in marbles of Group 1, being confined to 26–27 in marbles of Group 2. Y/Ho ratios in Group 2 marbles and

calcisilicate rocks are comparable to those of non-marine carbonates (25–35) (Bolhar and Van Kranendonk 2007), with lower values for modern seawater and marine chemical sediments (Y/Ho > 45) (Nozaki *et al.* 1997, Kamber and Webb 2001, Lawrence *et al.* 2006), suggesting the influx of continental freshwater and debris into the paleobasin. Samples with Y/Ho ratios below the PAAS value of 28 were likely formed under the influence of continental waters.

The Y/Ho versus Ce/Ce* plot presented in Figure 12A suggests that different sediment sources contributed to the genesis of lithofacies, with greater detrital contributions, such as Group 2 marbles and some calcisilicate rocks. Group 1 marbles contain less detrital material, which is consistent with low ΣREE , Al_2O_3 , and Zr concentrations and higher MgO + CaO and Y/Ho (Figs. 12B–12E). Figure 12C illustrates the compositional difference between the two marble groups. Calcisilicate rocks with a Y/Ho ratio higher than PAAS exhibit different degrees of detrital contamination, similar to those with a ratio < 28, suggesting freshwater input to the paleobasin. Thus, the compositional differences between lithofacies should be related to differences in the rate of detrital contributions.

Diagenesis

Shields and Stille (2001) and Ling *et al.* (2013) demonstrated that diagenetic alteration after deposition of carbonate sediments can modify REE patterns. Nevertheless, Bau and Alexander (2006) identified primary REEY patterns in Precambrian dolomitized carbonates. Negative correlations between Ce/Ce* and Dy/

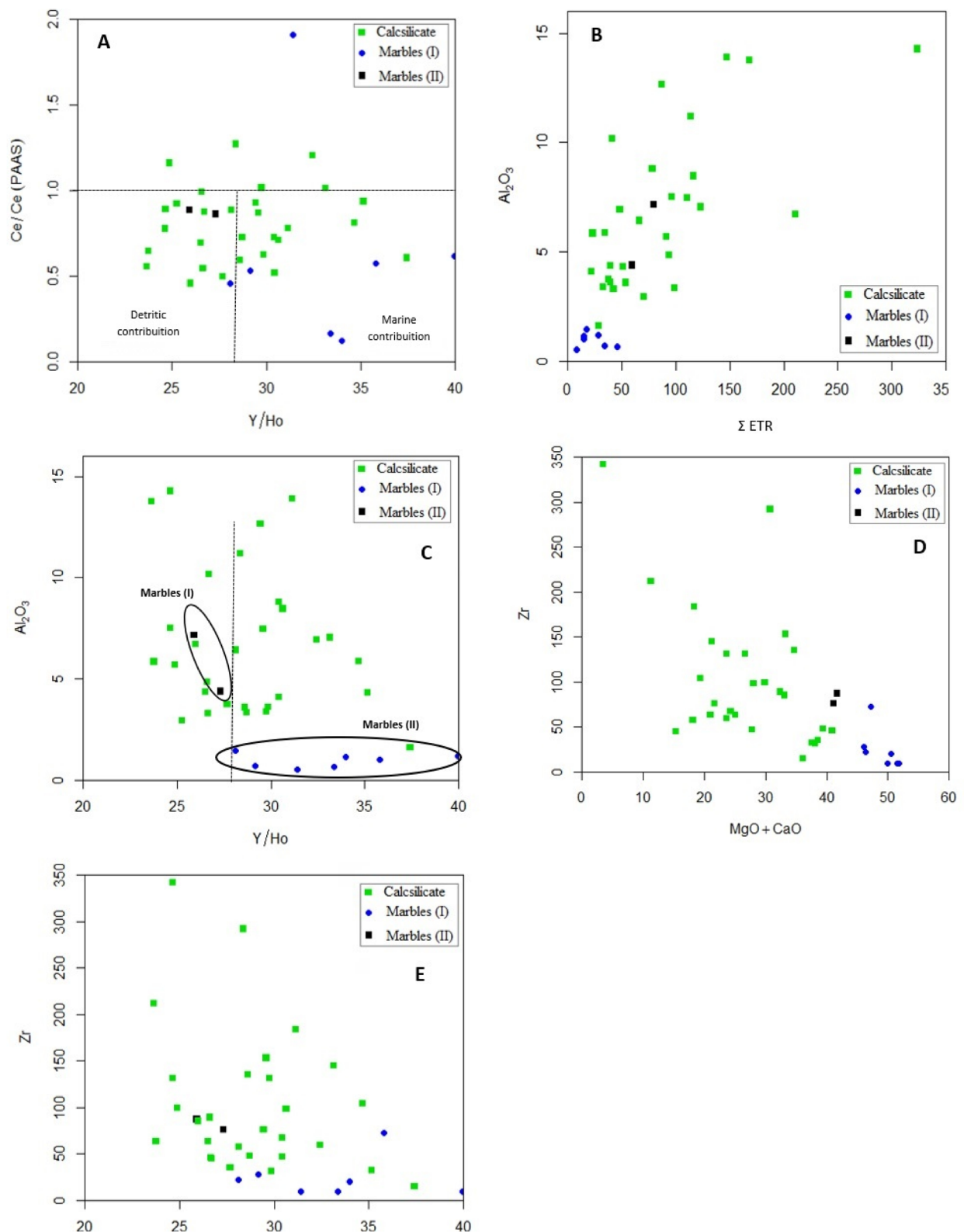


Figure 12. Ce/Ce* vs. Y/Ho diagram indicating a distinct sedimentary source for both marble groups. Largest contribution of continental water (up to 30 ppm) and marine water (>30), according to Kamber and Webb (2001), Ling *et al.* (2013). (B) Al₂O₃ vs. ΣREE (Ling *et al.* 2013). (C) Al₂O₃ vs. Y/Ho demonstrating the compositional difference of the two marble groups (Ling *et al.* 2013). (D) Zr vs. MgO+CaO showing a higher detrital contribution in calcisilicates. (E) Zr vs. Y/Ho (Bolhar *et al.* 2004). REE: rare earth elements.

Sm_N occur when REEY undergoes late diagenetic alteration (*e.g.*, Shields and Stille 2001, Ling *et al.* 2013, Zhu and Jiang 2017).

Some samples of calcisilicate rocks showed a negative correlation, indicating that late diagenetic effects might have affected these samples. Group 1 marbles display a positive correlation (Fig. 13A).

In a reducing environment, Eu⁺³ is reduced to Eu⁺² and can be easily mobilized (Bolhar and Van Kranendonk 2007). Eu is also thermochemically reduced in environments with temperatures above 200–250°C (Sverjensky 1984, Bau and Möller 1992). Eu⁺³ reduction might occur during extreme marine diagenesis, involving an environment rich in organic

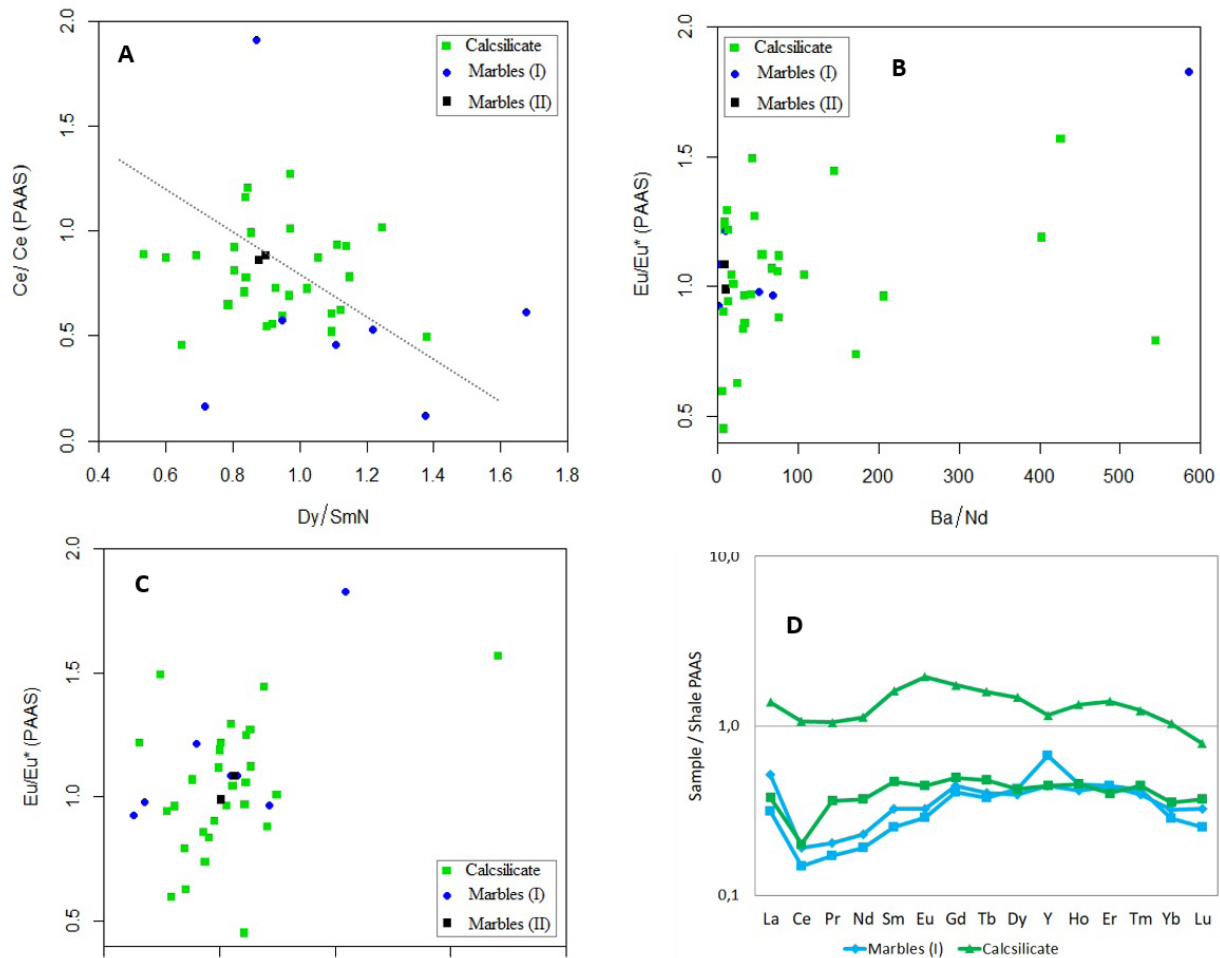


Figure 13. (A) Dy/Sm_N versus Ce/Ce*. (B) Eu/Eu* versus Ba/Nd for all samples. (C) Eu/Eu* versus Pr/Sm_N. (D) MREE-enriched patterns in Group 1 marbles and calcsilicate. REE: rare earth elements; MREE: middle REE.

matter and sulfate (MacRae *et al.* 1992, Shields and Stille 2001). However, in seawater, Eu⁺³ is the most common valence form and is not significantly fractionated during dissolution and precipitation (Shields and Stille 2001). Negative anomalies can also be inherited from source areas or associated with percolation of reducing diagenetic and hydrothermal fluids (Bolhar *et al.* 2004, Zhao *et al.* 2018).

Positive anomalies need to be carefully investigated due to the potential isobaric overlap of BaO⁺ and BaOH⁺ ions on Eu during ICP-MS measurements. Thus, significant interference can sometimes cause false Eu anomalies in rocks with high Ba/Eu ratios, such as carbonates (Dulski 1994, Shields and Stille 2001, Ling *et al.* 2013, Zhu and Jiang 2017). In Figure 13B, Ba/Nd ratios are >145 and show a positive correlation with Eu/Eu*, suggesting that Ba interference causes artificial Eu anomalies; at the same time, samples with Ba/Nd <150 also show high Eu/Eu*. Samples with Ba/Nd >145 were excluded so as to investigate the relationship between Eu/Eu* and Pr/Sm_N in Figure 13C. The positive correlation between Eu/Eu* and Pr/Sm_N indicates that Eu was not decoupled from the redox-insensitive REEY during diagenesis, ruling out the influence of reducing diagenetic fluids (Bolhar and Van Kranendonk 2007, Wang *et al.* 2018, Khelen *et al.* 2019).

Carbonates affected by diagenetic processes have convex-up REE patterns with enrichment of middle REE (MREE) (Bau 1993, Bau *et al.* 1999). Figure 13D shows REEY enrichment in some marbles and calcsilicates; nonetheless, only four samples present the characteristic convex-up REEY pattern. Thus, late diagenetic processes that caused MREE enrichment did not have a significant influence on the composition of lithofacies.

Post-depositional interaction with hydrothermal fluids

Hydrothermal fluids in the paleobasin

REEY patterns in carbonate rocks can also be affected by hydrothermalism as long as the fluid flow is high (Zhong and Mucci 1995, Zhao and Zheng 2013). Therefore, we investigated the influence of high-temperature fluids associated with fumaroles related to the opening of the paleobasin during carbonate deposition.

Positive Eu anomalies generated during deposition of marine sediments have been attributed to high-temperature hydrothermal input processes during carbonate deposition, which are also accompanied by LREE enrichment (Michard *et al.* 1983, Bau 1991, Alexander *et al.* 2008, Frimmel 2009,

Zhu *et al.* 2014, Joosu *et al.* 2015, Zhu and Jiang 2017) or by the presence of Eu in detrital sediments, mainly in calcic plagioclase.

Alexander *et al.* (2008) proposed a mixing model involving high-temperature hydrothermal fluids in seawater during sediment deposition, using MREE/HREE ratios. The studied samples were plotted distant from the mixing line (between 0.1 and 1% hydrothermal fluids). This scenario suggests no influence of high-temperature fluids and that the depositional environment of carbonate rocks was distant from fumaroles. Marbles were plotted in the same region as the post-Archean marine carbonates of Luzhijiang (Wang *et al.* 2018) (Figs. 14A–14C).

In addition to Eu enrichment, Barrett *et al.* (1988) and Khelen *et al.* (2019) state that the influence of hydrothermal fluids as fumarolic sources associated with the generation of mid-ocean ridge basalt (MORB) volcanic rocks can be evidenced by La anomalies. Studies of Archean stromatolites have shown that La enrichment in chemical sediments results from the increased contribution of hydrothermal solutions to seawater (Barrett *et al.* 1988, Khelen *et al.* 2019, Courtois and Treuil 1977). This enrichment was also found in studies investigating the interaction between chemical sediments and

hydrothermal fluids in the Red Sea, where all chemical precipitates are enriched in La (Courtois and Treuil 1977). The positive correlation of REEY with La (Fig. 14C) indicates the preservation of the primary geochemical feature in the studied samples (except the MM-TR-56 A sample), despite the mixing with detrital sediments and possible (minor) disturbances caused by early to late diagenetic effects (Bolhar and Van Kranendonk 2007, Khelen *et al.* 2019).

Late hydrothermalism: effects of the orogenic event

The influence of late hydrothermal fluids is conceivably related to Paleoproterozoic orogeny and syn- and post-tectonic granites. The modern seawater pattern, when normalized to PAAS, is characterized by LREE depletion, a negative Ce anomaly, and positive La and Gd anomalies (*e.g.*, De Baar *et al.* 1991, Bau and Dulski 1996, Northdurft *et al.* 2004, Bolhar *et al.* 2004, Piper and Bau 2013). In addition, seawater Y/Ho ratios are extremely high, with superchondritic values (*e.g.*, Bau and Alexander 2006). Only three samples (two calcisilicates and one marble) show significant LREE enrichment in relation to HREE (Fig. 15A). These samples are hydrothermally

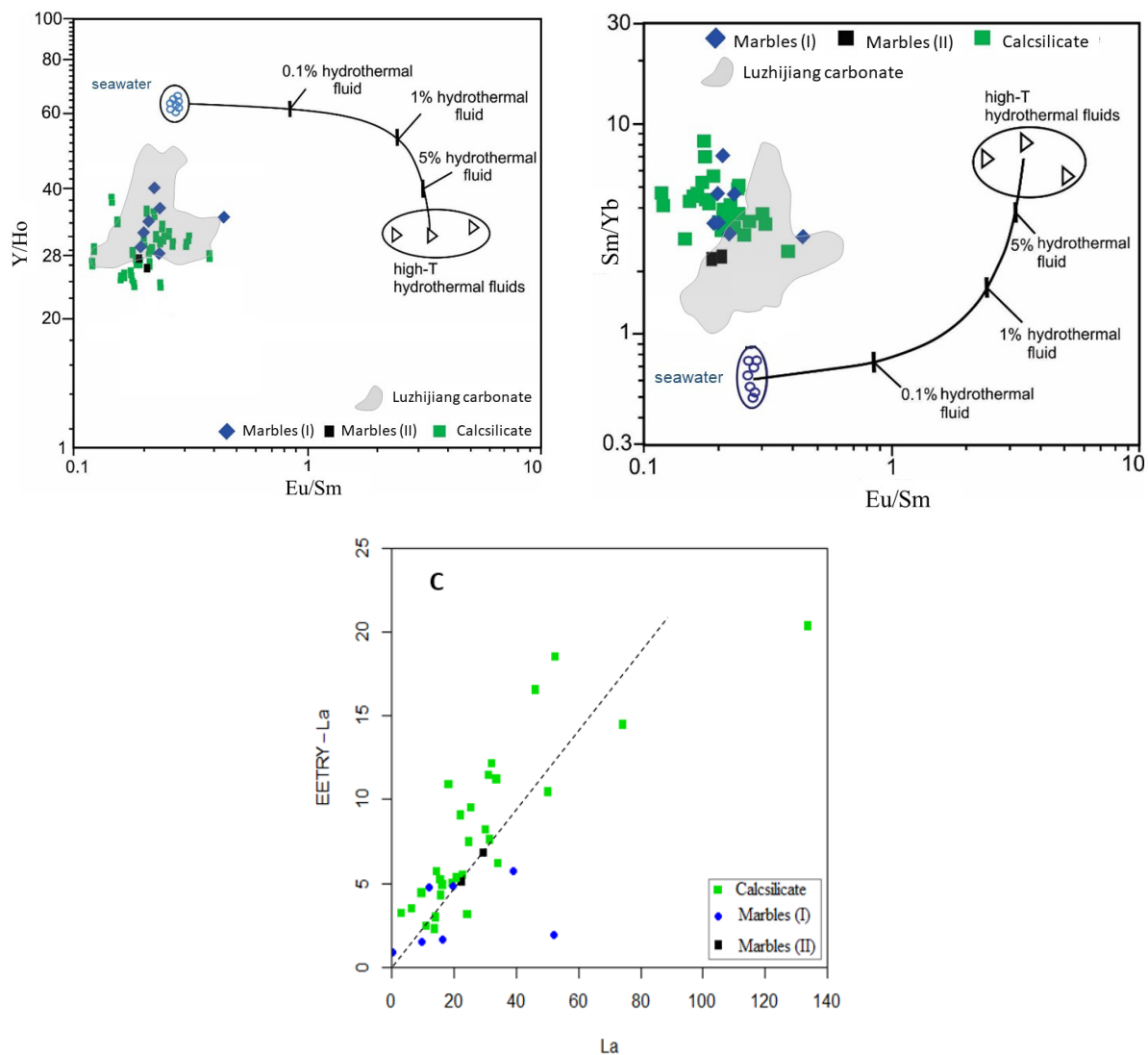


Figure 14. Eu/Sm versus (A) Y/Ho and (B) Sm/Yb indicating that the studied samples are plotted in shallow water and without influence of hydrothermal fluids (Alexander *et al.* 2008), as well marine Luzhijiang carbonate (Wang *et al.* 2018). (C) La vs. Σ REEY-La (Wang *et al.* 2018, Khelen *et al.* 2019). REEY: rare earth elements and yttrium.

altered to varying degrees, as evidenced by the presence of serpentinization, talcification, saussuritization, chloritization, and sericitization. Even considering that many samples show LREE enrichment (Fig. 15B), this enrichment did not significantly affect the REEY patterns, suggesting a hydrothermal alteration progressing under low fluid/rock ratios.

The modification of REE content in rocks by hydrothermal fluids is generally limited, and the analysis of these patterns is not always relevant for petrogenetic studies (Bau 1991). However, in a fluid-dominated system with a fluid/rock ratio >100, it is possible to change the REE patterns, and such changes are often marked by a relative LREE enrichment. In general, rocks that have undergone extremely fluid-dominated changes do not provide reliable data for the interpretation of their primary REE pattern or isotopic studies. In all other situations, REE content is not significantly modified by hydrothermal or metamorphic fluids during rock-fluid interaction (Bau 1991).

Thus, in most marble lithofacies studied, the REEY composition was not affected by diagenetic and fumarolic fluids in the paleobasin. Late hydrothermalism might have affected three samples, and thus these samples were excluded from the analysis of paleoenvironmental conditions. Positive and negative EU anomalies in these lithofacies are probably inherited from their sources. The Eu present in calcic plagioclase is supplied to seawater during continental weathering and transported through river waters, as is the case of the Luoxue carbonates described by Wang *et al.* (2018) (see also Michard *et al.* 1983, Kamber *et al.* 2004, Zhao *et al.* 2009). REEY patterns still preserve important characteristics of paleoenvironmental deposition conditions.

Deposition conditions

Based on considerations associated with detrital contamination, diagenesis, and hydrothermalism, we suggest using the REEY composition of marbles and calcsilicate rocks to characterize deposition conditions. Most samples studied show flat REEY-normalized patterns, with commonly negative Ce

anomalies, positive Y and Gd anomalies, and highly variable Eu anomalies.

Shale-normalized REE patterns of seawater and marine sediment plot below the concentration ratio of 1, while river water plots above the concentration ratio of 1 (Mohanty *et al.* 2015, Singh *et al.* 2015, Tang *et al.* 2016). Figures 16A and 16B have shale-normalized REE distribution patterns; all samples shown are below the concentration level of 1, suggesting a marine depositional environment (hydrothermally altered samples were excluded).

Group 1 marbles and some calcsilicate rocks present LREE depletion, low concentration of lithophile elements, high Y/Ho >30, and (slightly) positive La and Gd anomalies. Their REEY patterns are similar to those of marine Luzhijiang carbonates described by Wang *et al.* (2018) and of Devonian carbonates in the Canning Basin (Northdurft *et al.*, 2004) (Fig. 16C). In contrast, Group 2 marbles lack pronounced anomalies and show flat REEY patterns due to the predominant contribution of siliciclastic sediments to the REEY budget. REEY patterns in sedimentary rocks are mostly controlled by the mineral phases present in the rock. REEY from Group 2 and some calcsilicate samples are enhanced by REEY contributions from detrital material. The REEY distribution is similar to that of Paleoproterozoic calcsilicate rocks from the Fuping Complex (Tang *et al.* 2016) in Figure 16D.

Precipitated chemical sediments in marine and non-marine environments can be differentiated by diagnostic REEY ratios relative to PAAS, such as La, Eu, Ce, and Gd (Bolhar *et al.* 2004, Bolhar and Van Kranendonk 2007, Zhao *et al.* 2009, Johannesson *et al.* 2014). The behavior of these elements has been recorded for various types of chemical precipitates, such as carbonates, cherts, BIF, and phosphorites (*e.g.*, Joosu *et al.* 2016), and seems remarkably consistent over geological time (Bolhar *et al.* 2004).

Cerium occurs as Ce^{+4} or Ce^{+3} , depending on seawater oxygenation conditions (Bolhar *et al.* 2004, Ling *et al.* 2013, Tostevin *et al.* 2016). Increasing La concentrations in the

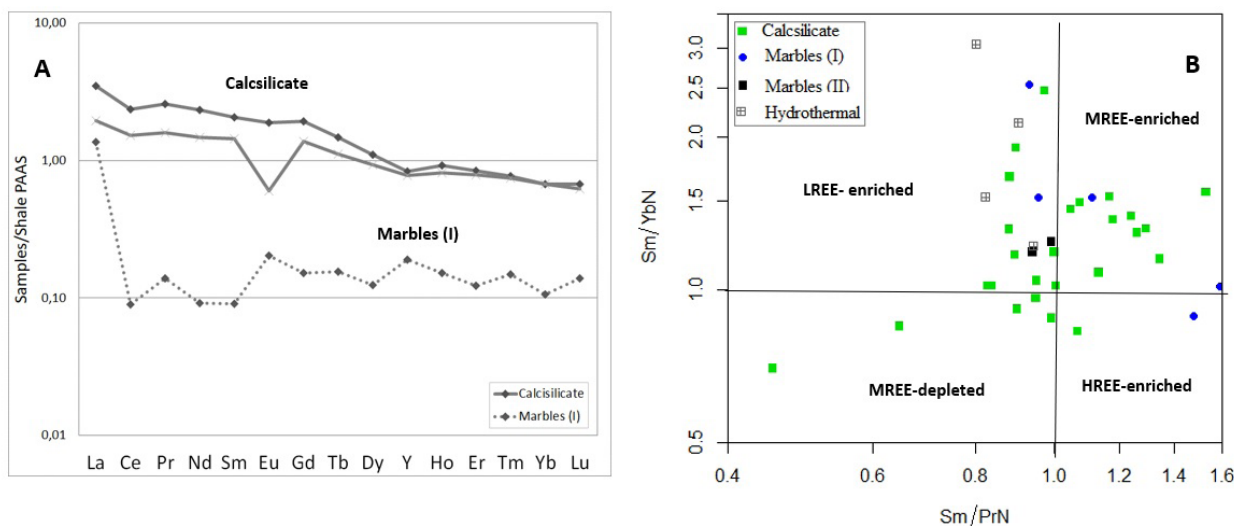


Figure 15. Distribution of REEY patterns in samples with LREE-enriched calcsilicate rocks and enriched La in marbles. (B) Binary plot of Sm/Yb_N and Sm/Pr_N evidencing LREE- and HREE-enriched samples. After Samala *et al.* (2018). REE: rare earth elements; REEY: REE and yttrium; LREE: light REE; HREE: heavy REE.

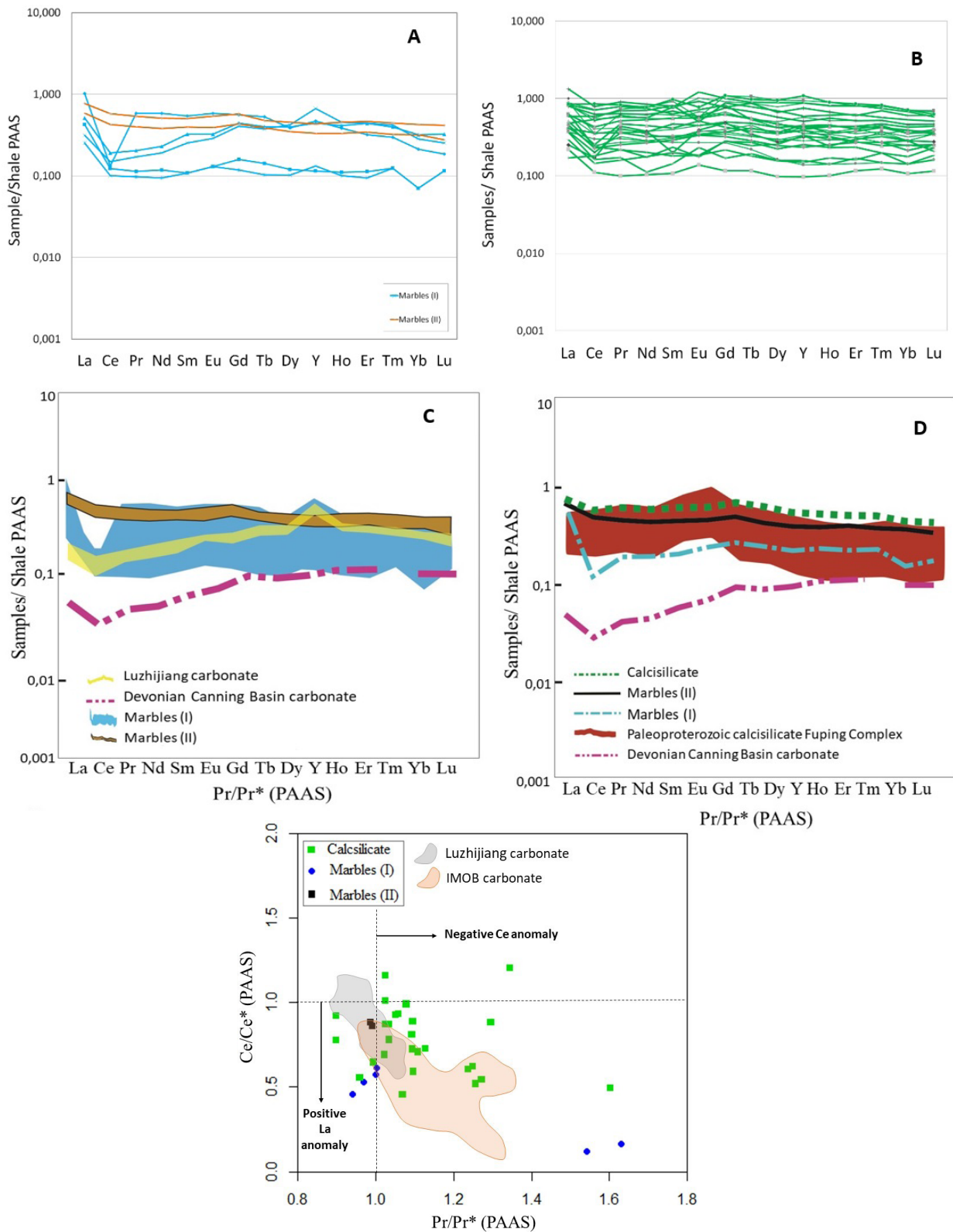


Figure 16. Distribution of REEY patterns from (A) marbles and (B) calcisilicate rocks. (C) Comparison between the REEY distribution in marbles with marine carbonates from Luzhijiang and Devonian Canning Basin (Northdurft *et al.* 2004). Group 1 marbles and Luzhijiang show negative Ce and positive Y. (D) Comparison between the REEY distribution of average calcisilicates and Paleoproterozoic calcisilicate rocks from the Fuping Complex (Tang *et al.* 2016). (E) PAAS-normalized (Ce/Ce^* vs. Pr/Pr^*) diagram indicating fields of true negative and positive Ce anomalies, suggesting that they were deposited in an oxygenated environment (Bau and Dulski 1996 modified by Webb and Kamber 2000); comparison of marine Luzhijiang carbonate (Wang *et al.* 2018) and Indo-Myanmar Orogenic Belt – IMOB (Singh *et al.* 2015). REEY: rare earth elements and yttrium; PAAS: Post-Archean Australian Shale.

marine environment, either by diagenetic or hydrothermal processes, may mask possible Ce anomalies in seawater and its chemical precipitates. True Ce anomalies were investigated using Bau and Dulski's (1996) technique, modified by Webb and Kamber (2000) (Fig. 16E). Most of the studied marble

and calcisilicate samples showed negative Ce and positive La anomalies, similar to marine Luzhijiang carbonates (Wang *et al.* 2018) and the Indo-Myanmar Orogenic Belt (Singh *et al.* 2015). The negative Ce anomalies in these carbonates suggest that they were deposited in a suboxic environment.

Modern oceans are fully oxygenated and exhibit a strong negative Ce anomaly ($Ce/Ce^* < 0.55$) when normalized to PAAS, except for the Black Sea (Planavsky *et al.* 2010, Ling *et al.* 2013). In the Archean, the atmosphere was anoxic, and chemical sedimentary rocks did not present Ce/Ce^* anomalies ($Ce/Ce^* \approx 1$). With increasing oxygen content in the atmosphere at the beginning of the Paleoproterozoic, the sea surface became oxygenated in relation to the Archean, with Ce/Ce^* values between 1 and 0.55 (Kamber and Webb 2001, Van Kranendonk *et al.* 2003). Still, (early) Paleoproterozoic oceans were oxygen-deficient compared to modern oceans, generating stratified water columns with suboxic and anoxic zones (Nelson *et al.* 2010, Planavsky *et al.* 2010, Pufahl 2010, Pufahl and Hiatt 2012). The Paleoproterozoic development of the suboxic ocean surface reflects the photosynthetic oxygen production from the combination of peritidal stromatolites and cyanobacteria (Pufahl and Fralick 2004). Negative Ce anomalies in these metasediments indicate deposition in a suboxic environment.

Gadolinium (III) forms more stable ionic and biogenic complexes than its neighboring REE at typical marine physicochemical conditions (temperature, pH, and pressure), leading to characteristic positive Gd anomalies in marine signatures (Bau 1999). Our results are consistent with these earlier findings, as Group 1 marbles have Gd/Gd^* ranging from 1.04 to 1.36, whereas Group 2 marbles show Gd/Gd^* values between 1.10 and 1.15, and calcsilicate rocks generally present

Gd/Gd^* values slightly above unity, (0.94–1.16), suggesting a marine environment.

Planavsky *et al.* (2010) proposed that REEY patterns have a temporal trend reflecting the evolution of the redox state in the marine environment. Thus, Archean and early Paleoproterozoic (2.4 to 1.9 Ma) carbonates and BIFs are characterized by LREE-depleted patterns, negative Ce anomalies, positive Y anomalies, and slightly positive Gd anomalies. However, these positive anomalies are not directly caused by the redox state of water but by the entry of hydrothermal fluids that are enriched in these elements (Bau 1991, Planavsky *et al.* 2010). These patterns are compatible with the REEY behavior of Group 1 marble and calcsilicate rock samples, with a maximum deposition age of 2128 Ma.

REEY patterns observed in continental waters with carbonate sediments, such as lake or lagoon environments, are characterized by MREE enrichments and absence of La, Eu, and Y anomalies (Lawrence *et al.* 2006, Bolhar and Van Kranendonk 2007). Therefore, given the prominent anomalies identified in our samples, we can exclude a non-marine depositional environment for the studied Paleoproterozoic lithofacies.

Phosphate in metasediments and Precambrian precipitation control

Figure 17 shows the lithostratigraphic variation found in two profiles near Bonfim-Ipirá and Sul-Ipirá. In the Tanque Novo-Ipirá Complex, the basal sequence is interpreted as an

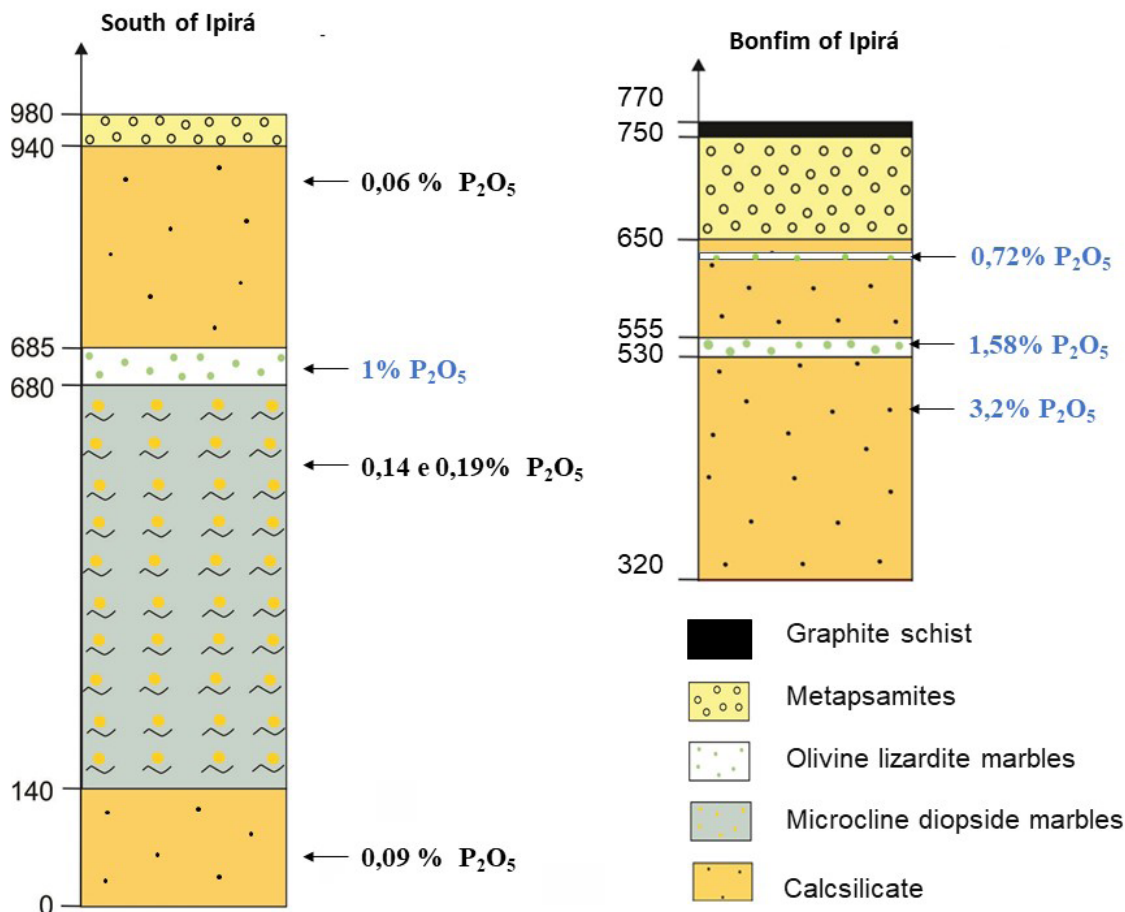


Figure 17. Correlation between lithostratigraphic columns of the region near Bonfim-Ipirá and Sul-Ipirá, evidencing the main lithofacies of the Serra do Camisão Unit.

ocean floor sequence associated with paragneisses, kinzigites, and metabasites of the Pintadas Unit. Paragneisses are absent in the Serra do Camisão Unit — the main study area (Melo *et al.* 1991). The base of this unit contains marbles, diopside-rich granofels, and BIFs, followed by a siliciclastic sequence that comprises impure quartzites, metapsammites, and carbonates with graphite schist at the top.

This lithostratigraphic sequence contains phosphate and is similar to those of phosphorites in the Salitre Complex, in Juazeiro, described by Oliveira (2016). These lithofacies experienced greenschist facies metamorphism and preserve primary structures in the following sequence, from bottom to top: garnet and sericite-schist, serpentine marbles, diopside-tremolite-marbles, calcsilicate, and quartzites in the Batateira mountain range. The Ilha do Fogo profile still preserves the graphitic schist at the top of the sequence in Juazeiro, described by Oliveira (2016).

Marbles and calcsilicate rocks with positive P_2O_5 anomalies (above 0.5%, up to 3.2%) show greater marine influences, with a more carbonate than siliciclastic contribution, notably in marbles of Group 1 and some calcsilicate rocks with Y/Ho ratios >30 (Figs. 18A and 18B). P-mineralized samples present Ce/Ce* values between 0.53 and 1, with an average of 0.70, consistent with a stratified Paleoproterozoic ocean, with phosphorus in the extension of the suboxic zone (Fig. 18C).

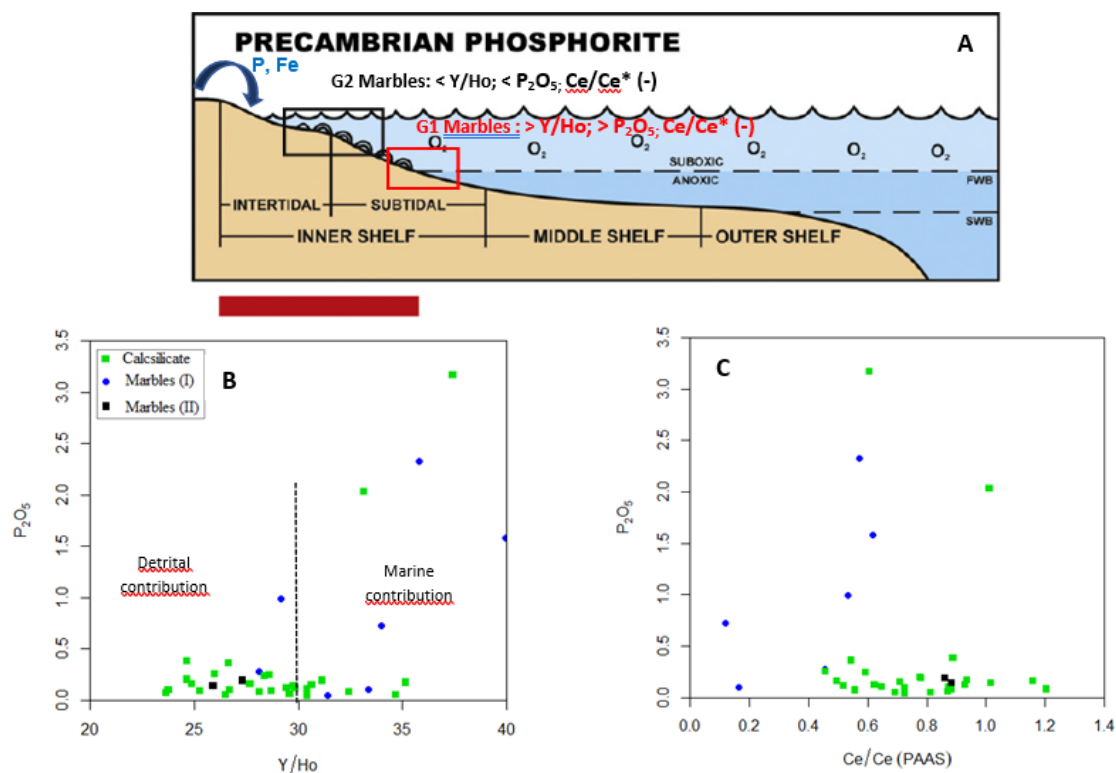
XRD analyses in Group 1 marbles and calcsilicate rocks indicated the presence of fluorapatite with a $Ca_{4.791}F_{0.93}Mn_{0.211}P_3O_{12}$ composition. Previous work has shown that although francolite

has a crypto-microcrystalline texture, it produces X-ray diffraction patterns similar to fluorapatite (McClellan and Lehr 1969, McClellan 1980).

Francolite progressively develops fluorapatite characteristics during weathering and diagenesis (Lucas *et al.* 1980, Jarvis *et al.* 1994, Drummond *et al.* 2015). One of the first modifications is decarbonation with the loss of CO_3^{2-} , accompanied by leaching of other elements (McArthur, 1980, 1985). These processes are even more intense during metamorphism and can transform francolite into fluorapatite by reducing the Na/P_2O_5 and CO_2/P_2O_5 ratios in the francolite structure (McArthur 1985, Girard *et al.* 1993, Drummond *et al.* 2015). Considering these data, the studied apatites could have of synsedimentary origin. However, post-depositional decarbonation may have occurred, mainly at metamorphic conditions.

The main source of phosphorus is the weathering of continental rocks that are subsequently transported to the ocean as dissolved and particulate matter (Benitez-Nelson 2000, Filippelli 2008, 2011). Dissolved P in the marine environment mainly occurs as phosphate species, particularly HPO_4^{2-} , along with $H_2PO_4^-$ and PO_4^{3-} (e.g., Filippelli 2008, 2011). Bioavailable P particles include organic matter-rich detrital sediment, as well as clay minerals and Fe-(oxy)hydroxides with adsorbed P; these components are of fundamental importance for phosphorite formation (Filippelli 2008).

Phosphorus precipitation (HPO_4^{2-}) in a low-oxygen Paleoproterozoic basin could occur at the boundary between anoxic and suboxic zones in the internal carbonate platform.



FWB: fair-weather wave base; SWB: storm wave base.

Figure 18. (A) Precambrian basin configuration and extent of phosphogenesis resulting from Fe-redox pumping. (modified from Nelson *et al.* 2010). The red line represents the position where Precambrian phosphates could be precipitated due to the low oxygen availability in the paleobasin. (B) Y/Ho vs. P_2O_5 plot evidencing the highest phosphorus contents in distal lithofacies near the anoxic–suboxic limit. (C) Ce/Ce* vs. P_2O_5 plot evidencing the highest phosphorus contents for Ce/Ce* values between 0.53 to 1.

This boundary can be found within the water column or the sediment in the case of transition from anoxic and suboxic conditions in both (Lumiste *et al.* 2019).

In an anoxic region, these elements become soluble due to the P-reduction by anaerobic bacteria. HPO_4^{2-} combines with Ca, F, and CO_2 in seawater and subsequently precipitates as carbonate-fluorapatite or francolite in this transition zone, at the point where oxygen enters the basin (Filippelli 2008, 2011, Pufahl 2010, Nelson *et al.* 2010, Papineau 2010, Pufahl and Hiatt 2012, Pufahl and Groat 2017). Nelson *et al.* (2010) pointed out that this model does not emphasize the role of eustatic sea-level cycles, but rather the interaction between autogenic sedimentary processes and seawater oxygenation.

Deposits of Paleoproterozoic phosphate were typically formed on passive continental margins associated with coastal river mouths, creating small stratiform bodies that were accumulated parallel to the shoreline, thus producing peritidal phosphate (e.g., Nelson *et al.* 2010, Pufahl 2010, Drummond *et al.* 2015, Hiatt *et al.* 2015, Caird *et al.* 2017, Pufahl and Groat 2017). Thus, precipitation of primary apatite deposits could be associated with carbonate sediments and silicate-carbonate mixing sites.

The profound changes in the Earth's atmosphere in the late Archean and early Paleoproterozoic promoted a huge increase in the amount of dissolved CO_2 in oceans and, consequently, the deposition of thick carbonate sequences, mainly of dolomitic composition (Windley 1984, Hoffman and Schrag 2002). These carbonates were formed in shallow sea conditions, interdigitated with coastal beaches installed on continental shores (Windley 1984). This model is consistent with the protolith of metasediments studied in this work. The progressive mineral paragenesis observed is the result of metamorphic recrystallization of impure carbonate sediments. When subjected to regional metamorphism, there is a sequence of characteristic mineral reactions defining isogrades, involving forsterite, diopside, tremolite, calcite, dolomite, and quartz (Yardley 1989). Different degrees of alumina added to carbonates via mixing with detrital materials during depositions allow the formation of biotite, hornblende, and garnet (Winkler 1979, Berman 1991).

The P-enrichment in the studied lithofacies chronocorrelates to the first important phosphogenic episode in the geological record. Paleoproterozoic phosphogenesis began after the GOE (Nelson *et al.* 2010, Pufahl 2010, Pufahl and Hiatt 2012, Papineau *et al.* 2013). Pufahl and Hiatt (2012) demonstrated that Paleoproterozoic phosphate deposits are also accompanied by iron and organic carbon deposits.

Paleoproterozoic oxygenation extended through time and was related to deglaciation periods, such as the Huronian deglaciation (Pufahl and Hiatt 2012), which is compatible with the maximum age of deposition of these metasedimentary successions. The continental exposure due to sea-level elevation during deglaciation facilitated the chemical weathering of these rocks and increased the terrestrial input to the marine environment (e.g., Nelson *et al.* 2010, Papineau 2010, Pufahl 2010, Pufahl and Hiatt 2012, Pufahl and Groat 2017).

The geochronological data obtained in this study indicate a maximum age of 2128 Ma (youngest zircon) for the deposition

of metasedimentary rocks. However, the U-Pb zircon core concordant age of 2595 ± 18 Ma obtained for this Complex suggests that this succession has Paleoproterozoic and Neoproterozoic sources. The sediments deposited in the paleobasin might have originated from the erosion of the Archean terrane (or at least a terrane with an Archean inheritance), as the oldest inherited zircon cores are in the 2573–2736 Ma range. Another population has zircon core inherited from Paleoproterozoic, between 2453 and 2128 Ma, and phosphogenesis coincided with the Huronian deglaciation, which began around 2.4 Ga (Papineau 2010, Pufahl and Hiatt 2012, Soares 2019).

The Salvador-Curaçá Orogen contains several rocks that may be compatible with Neoproterozoic zircons: the Caraíba Complex, for which the U-Pb SHRIMP data obtained for tonalitic and enderbite granulites define two populations of different ages (2.7–2.6 Ga and 2.08–2.07 Ga, respectively), preserved in zircon cores and edges (Silva *et al.* 1997); gabronorite from the São José do Jacuípe Suite, yielding an age of 2.69 Ga, as indicated by the U-Pb SHRIMP method on zircons (Silva 1996).

The most prominent source rock is contemporaneous with the Caraíba norite — 2580 Ma (U-Pb SHRIMP; Oliveira *et al.* 2002). Zircon rims record a metamorphic event at 2082 ± 14 Ma, interpreted to reflect the closure of the paleobasin and the formation of the Salvador-Curaçá Orogen. This last event is related to the collision of the Archean Gavião and Serrinha blocks (Barbosa and Sabaté 2003, 2004).

CONCLUSIONS

Calcsilicate rocks and marbles of the Tanque Novo-Ipirá Complex are derived from the regional metamorphism of carbonates and siliciclastic sediments.

Major and trace element patterns are strongly controlled by the presence of siliciclastic phases in the marbles, especially in those from Group 2, which present flat REEY patterns. The inferred metamorphic recrystallization (amphibolite-granulite transitional conditions), as well as retrograde hydrothermal processes, did not significantly affect the immobile geochemical signatures observed in the marbles and calcsilicate rocks. Evidence of a sedimentary protolith deposited in a marine environment is clear through their marine-type REEY patterns, with characteristic negative Ce anomalies and positive Y and Gd anomalies. Negative Ce anomalies indicate at least local oxidizing conditions in the Paleoproterozoic basin, allowing stabilization of Ce^{+4} and, consequently, carbonate and phosphorus precipitation through mixing at the boundary zone between anoxic and suboxic zones.

The high P_2O_5 contents verified in metasedimentary rocks of the Tanque Novo-Ipirá Complex, ranging from 0.01 to 3.2%, particularly in calcsilicate rocks, suggest a potential for phosphate mineralization. The highest contents are found in Group 1 calcsilicate rocks and marbles, which present Ce/Ce* values between 0.53 to 1.0, with a mean of 0.70, interpreted herein as suboxic conditions, reflecting the low oxygen availability during the Paleoproterozoic.

In summary, the data presented in this paper indicate that the study area was a Paleoproterozoic continental-margin

carbonate platform subject to variable detrital input. The negative Ce anomalies in mineralized lithofacies (Group 1 marbles and calcisilicates) are between 0.53 to 1.0, with an average of 0.70, corresponding to a suboxic environment. Phosphate precipitation is compatible with the model presented by Nelson *et al.* (2010), in which precipitation would have occurred at the boundary between anoxic and suboxic zones.

ARTICLE INFORMATION

Manuscript ID: 20190137. Received on: 12/22/2019. Approved on: 03/31/2021.

A.M. supervised the entire manuscript, making corrections and suggestions. L.O. made compilations on the ages of metasedimentary rocks and corrections to petrography, litho geochemistry, and the manuscript process. J.S. provided data on regional geology, assisted in fieldwork and contributed to the manuscript. D.D. assisted in the revision of geochronological and litho geochemical data and reviewed the manuscript. I.C. prepared Figures 3, 14A, 14B, 16C, 16D, and 17 and assisted in the review of petrography.

Competing interests: The authors declare no competing interests.

REFERENCES

- Alexander B.W., Bau M., Andersson P., Dulski P. 2008. Continentally-derived solutes in shallow Archean seawater: rare earth element and Nd isotope evidence in iron formation from the 2.9 Ga Pongola Supergroup, South Africa. *Geochimica et Cosmochimica Acta*, **72**(2):378-394. <https://doi.org/10.1016/j.gca.2007.10.028>
- Alkmim F.F., Neves B.B., Alves J.A.C. 1993. Arcabouço tectônico do Cráton do São Francisco: uma revisão. *O Cráton do São Francisco*, 45-62.
- Barbosa J.S.F., Dominguez J.M.L. 1996. *Geologia da Bahia*: texto explicativo [para o mapa geológico do Estado da Bahia, escala 1:1.000.000. 45 p.
- Barbosa J.S.F., Sabaté P. 2003. Marinho, M. M. O Cráton do São Francisco na Bahia: uma síntese. *Revista Brasileira de Geociências*, **33**:3-6.
- Barbosa J.S.F., Sabaté P. 2004. Archean and Paleoproterozoic crust of the São Francisco cráton, Bahia, Brazil: geodynamic features. *Precambrian Research*, **133**(3):1-27. <https://doi.org/10.1016/j.precamres.2004.03.001>
- Barrett T.J., Fralick P.W., Jarvis I. 1988. Rare-earth-element geochemistry of some Archean iron formations north of Lake Superior, Ontario. *Canadian Journal of Earth Science*, **25**(4):570-580. <https://doi.org/10.1139/e88-055>
- Bau M. 1991. Rare-earth element mobility during hydrothermal and metamorphic fluid - rock interaction and the significance of the oxidation state of europium. *Chemical Geology*, **93**(3-4):219-230. [https://doi.org/10.1016/0009-2541\(91\)90115-8](https://doi.org/10.1016/0009-2541(91)90115-8)
- Bau M. 1993. Effects of syn-depositional and postdepositional processes on the rare-earth element distribution in Precambrian iron-formations. *European Journal of Mineralogy*, **5**(2):257-267.
- Bau M. 1999. Scavenging of dissolved yttrium and rare earths by precipitating iron oxyhydroxide: experimental evidence for Ce oxidation, Y-Ho fractionation, and lanthanide tetrad effect. *Geochimica et Cosmochimica Acta*, **63**(1):67-77. [https://doi.org/10.1016/S0016-7037\(99\)00014-9](https://doi.org/10.1016/S0016-7037(99)00014-9)
- Bau M., Alexander B. 2006. Preservation of primary REE patterns without Ce anomaly during dolomitization of Mid-Paleoproterozoic limestone and the potential re-establishment of marine anoxia immediately after the "Great Oxidation Event". *South African Journal of Geology*, **109**(1-2):81-86. <https://doi.org/10.2113/gssajg.109.1-2.81>
- Bau M., Dulski P. 1996. Distribution of yttrium and rare-earth elements in the Penge and Kuruman iron-formations, Transvaal Supergroup, South Africa. *Precambrian Research*, **79**(1-2):37-55. [https://doi.org/10.1016/0301-9268\(95\)00087-9](https://doi.org/10.1016/0301-9268(95)00087-9)
- Bau M., Möller P. 1992. Rare-earth element fractionation in metamorphic hydrothermal calcite, magnesite and siderite. *Mineralogy and Petrology*, **45**(3-4):231-246. https://ui.adsabs.harvard.edu/link_gateway/1992MinPe..45..231B/doi:10.1007/BF01163114
- Bau M., Möller P., Dulski P. 1997. Yttrium and lanthanides in eastern Mediterranean seawater and their fractionation during redox-cycling. *Marine Chemistry*, **56**(1-2):123-131. [https://doi.org/10.1016/S0304-4203\(96\)00091-6](https://doi.org/10.1016/S0304-4203(96)00091-6)
- Bau M., Romer R., Lüders V., Beukes N.J. 1999. Pb, O, and C isotopes in silicified Mooirdraai dolomite (Transvaal Supergroup, South Africa): implications for the composition of Paleoproterozoic seawater and "dating" the increase of oxygen in the Precambrian atmosphere. *Earth and Planetary Science Letters*, **174**(1-2):43-57. [https://doi.org/10.1016/S0012-821X\(99\)00261-7](https://doi.org/10.1016/S0012-821X(99)00261-7)
- Benitez-Nelson C.R. 2000. The biogeochemical cycling of phosphorus in marine systems. *Earth-Science Reviews*, **51**(1-4):109-135. [https://doi.org/10.1016/S0012-8252\(00\)00018-0](https://doi.org/10.1016/S0012-8252(00)00018-0)
- Berman R.G. 1991. Thermobarometry using multi-equilibrium calculations: a new technique, with petrological applications. *Canadian Mineralogist*, **29**(4):833-855.
- Bolhar R., Kamber B.S., Moorbath S., Fedo C.M., Whitehouse M.J. 2004. Characterisation of early Archean chemical sediments by trace element signatures. *Earth and Planetary Science Letters*, **222**(1):43-60. <https://doi.org/10.1016/j.epsl.2004.02.016>
- Bolhar R., Van Kranendonk M.J. 2007. A non-marine depositional setting for the northern Fortescue Group, Pilbara Craton, inferred from trace element geochemistry of stromatolitic carbonates. *Precambrian Research*, **155**(3-4):229-250. <https://doi.org/10.1016/j.precamres.2007.02.002>
- Borisov M.V., Bychkov D.A., Phelintseva N.F., Ivleva E.A. 2018. Fractionation of Rare-Earth Elements in the Processes of Hydrothermal Ore Formation. *Moscow University Geology Bulletin*, **73**:451-456. <https://doi.org/10.3103/S0145875218050034>
- Bucher K., Grapes R. 2010. *Petrogenesis of metamorphic rocks*. 8. ed. London: Springer, 144 p.
- Caird R.A., Pufahl P.K., Hiatt E.E., Abram M.B., Rocha A.J.D., Kyser T.K. 2017. Ediacaran stromatolites and intertidal phosphorite of the Salitre Formation, Brazil: Phosphogenesis during the Neoproterozoic Oxygenation Event. *Sedimentary Geology*, **350**:55-71. <https://doi.org/10.1016/j.sedgeo.2017.01.005>
- Cullers R.L., Yeh L.T., Chaudhury S.C.V., Guidotti C.V. 1974. Rare earth elements in Silurian pelitic schists from NW marine. *Geochimica et Cosmochimica Acta*, **38**(3):389-400. [https://doi.org/10.1016/0016-7037\(74\)90133-1](https://doi.org/10.1016/0016-7037(74)90133-1)
- Courtois C., Treuil M. 1977. Distribution des terres rares et de quelques éléments en trace dans les sédiments récents des fosses de la Mer Rouge. *Chemical Geology*, **20**:57-72. [https://doi.org/10.1016/0009-2541\(77\)90035-3](https://doi.org/10.1016/0009-2541(77)90035-3)
- De Baar H.J.W., Bacon M.P., Brewer P.G., Bruland K.W. 1985. Rare earth elements in the Atlantic and Pacific Oceans. *Geochimica et Cosmochimica Acta*, **49**(9):1943-1959. [https://doi.org/10.1016/0016-7037\(85\)90089-4](https://doi.org/10.1016/0016-7037(85)90089-4)
- De Baar H.J.W., Schijf J., Byrne R.H. 1991. Solution chemistry of the rare earth elements in seawater. *European Journal of Solid State and Inorganic Chemistry*, **28**(Suppl.):357-373.

ACKNOWLEDGMENTS

The authors thank the Baiana Mineral Research Company for their field support and technical research funding and the UFBA Electron Microscopy (LAMUME) and Mineral Technology laboratories for their support. This study was partially funded by the Coordenação de Aperfeiçoamento de Pessoal de Nível Superior – Brazil (CAPES) – Finance Code 001.

- Drummond J.B., Pufahl P.K., Porto C.G., Carvalho M. 2015. Neoproterozoic peritidal phosphorite from the Sete Lagoas Formation (Brazil) and the Precambrian phosphorus cycle. *Sedimentology*, **62**(7):1978-2008. <https://doi.org/10.1111/sed.12214>
- Dulski P. 1994. Interferences of oxide, hydroxide and chlorite analyte species in the determination of rare-earth elements in geological samples by inductively – coupled plasma-mass spectrum REEY. *Fresenius' Journal of Analytical Chemistry*, **350**:194-203. <https://doi.org/10.1007/BF00322470>
- Evans B.W. 2010. Lizardite versus antigorite serpentinite: Magnetite, hydrogen, and life (?). *Geology*, **38**(10):879-882. <https://doi.org/10.1130/G31158.1>
- Filippelli G.M. 2008. The global phosphorus cycle: Past, present, and future. *Elements*, **4**(2):89-95. <https://doi.org/10.2113/GSELEMENTS.4.2.89>
- Filippelli G.M. 2011. Phosphate rock formation and marine phosphorus geochemistry: The deep time perspective. *Chemosphere*, **84**(6):759-766. <https://doi.org/10.1016/j.chemosphere.2011.02.019>
- Frimmel H.E. 2009. Trace element distribution in Neoproterozoic carbonates as palaeoenvironmental indicator. *Chemical Geology*, **258**(3-4):338-353. <https://doi.org/10.1016/j.chemgeo.2008.10.033>
- Girard J.-P., Flicoteaux R., Walter A.-V., Savin S.M., Nahon D. 1993. Oxygen and carbon stable isotope composition of structural carbonate in weathering apatites from laterites, southern Brazil and western Senegal. *Applied Geochemistry*, **8**(6):617-632. [https://doi.org/10.1016/0883-2927\(93\)90017-B](https://doi.org/10.1016/0883-2927(93)90017-B)
- Glenn C.R., Follmi K.B., Riggs S.R., Baturin G.N., Grimm K.A., Trappe J., Abed A.M., Galli-Olivier C., Garrison R.R., Ilyin A.V., Jehl C., Rohrlisch V., Sadaqah R.M.Y., Schidlowski M., Sheldon R.P., Siegmund H. 1994. Phosphorus and phosphorites: sedimentology and environments of formation. *Eclogae Geologicae Helveticae*, **87**:747-788.
- Hiatt E.E., Pufahl P.K., Edwards C.T. 2015. Sedimentary phosphate and associated fossil bacteria in a Paleoproterozoic tidal flat in the 1.85 Ga Michigamme Formation, Michigan, USA. *Sedimentary Geology*, **319**:24-39. <https://doi.org/10.1016/j.sedgeo.2015.01.006>
- Hoffman F., Schrag D.P. 2002. The snowball Earth hypothesis: testing the limits of global change. *Terra Nova*, **14**(3):129-155. <https://doi.org/10.1046/j.1365-3121.2002.00408.x>
- Jackson S.E., Pearson J.P., Griffin W.L., Belousova E.A. 2004. The Application of Laser Ablation – inductively Coupled Plasma – mass Spectrometry to in situ In situ In situ In situ Zircon Geochronology. *Chemical Geology*, **211**(1-2):47-69. <http://dx.doi.org/10.1016/j.chemgeo.2004.06.017>
- Jarvis I., Burnett W.C., Nathan Y., Almbaydin F.S.M., Attia A.K.M., Castro L.N., Flicoteaux R., Hilmy M.E., Husain V., Qutawnah A.A., Serjani A., Zanin Y.N. 1994. Phosphorite geochemistry—state-of-the-art and environmental concerns. *Eclogae Geologicae Helveticae*, **87**(3):643-700.
- Johannesson K.H., Telfeyan K., Chevis D.A., Rosenheim B.E., Leybourne M.I. 2014. Rare Earth elements in stromatolites – 1. Evidence that modern terrestrial stromatolites fractionate rare Earth elements during incorporation from ambient Waters. *Evolution of Archean Crust and Early Life*, 385-411.
- Joosu L., Lepland A., Kirsimäe K., Romashkin A.E., Roberts N.M.W., Martin A.P., C`rne A.E. 2015. The REE-composition and petrography of apatite in 2 Ga Zaonega Formation, Russia: The environmental setting for phosphogenesis. *Chemical Geology*, **395**:88-107. <https://doi.org/10.1016/j.chemgeo.2014.11.013>
- Joosu L., Lepland A., Kreitsmann T., Upraus K., Roberts N.M.W., Paiste P., Martin A.P., Kirsimäe K. 2016. Petrography and the REE-composition of apatite in the Paleoproterozoic Pilgularvi Sedimentary Formation, Pechenga Greenstone Belt, Russia. *Geochimica et Cosmochimica Acta*, **186**:135-153. <https://doi.org/10.1016/j.gca.2016.04.043>
- Kamber B.S., Bolhar R., Webb G.E. 2004. Geochemistry of late Archean stromatolites from Zimbabwe: evidence for microbial life in restricted epicontinental seas. *Precambrian Research*, **132**(4):379-399. <https://doi.org/10.1016/j.precamres.2004.03.006>
- Kamber B.S., Webb G.E. 2001. The geochemistry of late Archean microbial carbonate: implications for ocean chemistry and continental erosion history. *Geochimica et Cosmochimica Acta*, **65**(15):2509-2525. [https://doi.org/10.1016/S0016-7037\(01\)00613-5](https://doi.org/10.1016/S0016-7037(01)00613-5)
- Khelen C., Manikyamba C., Subramanyam K.S.V., Santosh M., Sohini Ganguly M.S., Kalpana M.S., Subba Rao D.V. 2019. Archean seawater composition and depositional environment–Geochemical and isotopic signatures from the stromatolitic carbonates of Dharwar Craton, India Arubam. *Precambrian Research*, **330**:35-57. <https://doi.org/10.1016/j.precamres.2019.04.020>
- Kosin M.D., Melo R.C., Souza J.D., Oliveira E.P., Carvalho M.J., Leite C.M.M. 2003. Geologia do segmento norte do Orógeno Itabuna-Salvador-Curacá e guia de excursão. *Revista Brasileira de Geociências*, **33**(1):15-26.
- Lawrence M.G., Greig M., Collerson K.D., Kamber B.S. 2006. Rare Earth element and yttrium variability in South East Queensland waterways. *Aquatic Geochemistry*, **12**:39-72. <https://doi.org/10.1007/s10498-005-4471-8>
- Leite C.M.M. 2002. *A evolução geodinâmica da orogênese paleoproterozóica nas regiões de Capim Grosso-Jacobina e Pintadas-Mundo Novo (Bahia - Brasil): metamorfismo, anatexia crustal e tectônica*. PhD Thesis, Universidade Federal da Bahia, Instituto de Geociências, Salvador.
- Ling H., Chen X., Li D., Wang D., Shields-Zhou G., Zhu M. 2013. Cerium anomaly variations in Ediacaran – earliest Cambrian carbonates from the Yangtze Gorges área, South China: Implications for oxygenation of coeval shallow seawater. *Precambrian Research*, **225**:110-127. <https://doi.org/10.1016/j.precamres.2011.10.011>
- Lucas J., Prevot L., Lambay M. 1980. Caractères pétrographiques et microchimiques de phos-pharites précambriens au Bassin des Voltas (Afrique de l'Ouest). *Considerations génétiques: Bulletin de la Société Géologique de France*, **5**:515-524.
- Ludwig K.R. 2003. *Isoplot 3.0: A geochronological toolkit for Microsoft Excel*. Berkeley Geochronology Center, Berkeley, 70.
- Lumiste K., Mand K., Bailey J., Paiste P., Lang L., Lepland A., Kirsimäe K. 2019. REE+Y uptake and diagenesis in Recent sedimentary apatites. *Chemical Geology*, **525**:268-281. <https://doi.org/10.1016/j.chemgeo.2019.07.034>
- MacRae N.D., Nesbitt H.W., Kronberg B.I. 1992. Development of a positive Eu anomaly during diagenesis. *Earth and Planetary Science Letters*, **109**(3-4):585-591. [https://doi.org/10.1016/0012-821X\(92\)90116-D](https://doi.org/10.1016/0012-821X(92)90116-D)
- McArthur J.M. 1980. Post-depositional alteration of the carbonate-fluorapatite phase of Moroccan phosphorites. In: Bentor Y.K., ed. *Marine phosphorites: geochemistry, occurrence and genesis*. SEPM Special Publication, **29**:53-60.
- McArthur J.M. 1985. Francolite geochemistry—compositional controls during formation, diagenesis, metamorphism and weathering. *Geochimica et Cosmochimica Acta*, **49**(1):23-35. [https://doi.org/10.1016/0016-7037\(85\)90188-7](https://doi.org/10.1016/0016-7037(85)90188-7)
- McClellan G.H. 1980. Mineralogy of carbonate fluorapatites. *Journal of the Geological Society*, **137**(6):675-681. <https://doi.org/10.1144/gsjgs.137.6.0675>
- McClellan G.H., Lehr J.R. 1969. Crystal – chemical investigation of natural apatites. *American Mineralogist*, **54**(9-10):1374-1391.
- McLennan S.M. 1989. Rare earth elements in sedimentary rocks; influence of provenance and sedimentary processes. *Reviews in Mineralogy and Geochemistry*, **21**(1):169-200.
- Melo R.C. de (ed.). 1991. *Pintadas, folha SC.24-Y-D-V: Estado da Bahia: texto explicativo*. Salvador: CPRM. Programa Levantamentos Geológicos Básicos do Brasil, 96 p.
- Michard A., Albarède F., Michard G., Minster J.F., Charlou J.L. 1983. Rare-Earth elements and uranium in high – temperature solutions from the East Pacific Rise hydrothermal vent field (13° N). *Nature*, **303**(5920):795-797. <https://doi.org/10.1038/303795a0>
- Mohanty S.P., Barik A., Sarangi S., Sarkar A. 2015. Carbon and oxygen isotope systematics of a Paleoproterozoic cap-carbonate sequence from the Sausar Group, Central India. *Palaeogeography, Palaeoclimatology and Palaeoecology*, **417**:195-209. <http://dx.doi.org/10.1016/j.palaeo.2014.10.036>
- Nelson G.J., Pufahl P.K., Hiatt E.E. 2010. Paleooceanographic constraints on Precambrian phosphorite accumulation, Baraga Group, Michigan, USA. *Sedimentary Geology*, **226**(1-4):9-21. <https://doi.org/10.1016/j.sedgeo.2010.02.001>
- Northdurft L.D., Webb G.E., Kamber B.S. 2004. Rare earth element geochemistry of Late Devonian reefal carbonates, Canning Basin Western Australia: confirmation of a seawater REE proxy in ancient limestones. *Geochimica et Cosmochimica Acta*, **68**(2):263-283. [https://doi.org/10.1016/S0016-7037\(03\)00422-8](https://doi.org/10.1016/S0016-7037(03)00422-8)

- Nozaki Y., Zhang J., Amakawa H. 1997. The fractionation between Y and Ho in the marine environment. *Earth and Planetary Science Letters*, **148**(1-2):329-340. [https://doi.org/10.1016/S0012-821X\(97\)00034-4](https://doi.org/10.1016/S0012-821X(97)00034-4)
- Oliveira A.F.T. 1976. *Petrology and Geochemistry of Marble and calcisilicate, Ipirá-BA*. MS Dissertation, Instituto de Geociências, Universidade Federal da Bahia, Salvador.
- Oliveira E.P., McNaughton N.J., Armstrong R. 2010. Mesoarchaean to paleoproterozoic growth of the northern segment of the Itabuna Salvador-Curaçá orogen, São Francisco Craton, Brazil. In: Kusky T.M., Zhai M.G., Xiao W. (eds.). *The evolving continents: understanding processes of continental growth*. London, Geological Society of London, Special Publications, 338, 263-286.
- Oliveira E.P., Mello E.F., Mcnaughton N., Choudhur, A. 2002. SHRIMP U-Pb age of the basement to the Rio Itapicuru Greenstone Belt, NE São Francisco craton. In: Congresso Brasileiro de Geologia, 41., João Pessoa. *Anais...*
- Oliveira L.R. 2016. *Fosforitos da região de Juazeiro, Bahia: Paleoambientes, Geocronologia, Controles da Mineralização e correlações estratigráficas*. MS Dissertation, Instituto de Geociências, Universidade Federal da Bahia, Salvador, 177 p.
- Papineau D. 2010. Global biogeochemical changes at both ends of Proterozoic: insights from phosphorites. *Astrobiology*, **10**(2):165-181. <https://doi.org/10.1089/ast.2009.0360>
- Papineau D., Purohit R., Fogel M., Shields-Zhou G.A. 2013. High phosphate availability as a possible cause for massive cyanobacterial production of oxygen in the Paleoproterozoic atmosphere. *Earth and Planetary Science Letters*, **362**:225-236. <https://doi.org/10.1016/j.epsl.2012.11.050>
- Piper D.Z., Bau M. 2013. Normalized Rare Earth Elements in Water, Sediments, and Wine: Identifying Sources and Environmental Redox Conditions. *American Journal of Analytical Chemistry*, **4**(10A):69-83. <http://dx.doi.org/10.4236/ajac.2013.410A1009>
- Planavsky N., Bekker A., Rouxel O.J., Kamber B., Hofmann A., Knudsen A., Lyons T.W. 2010. Rare earth element and yttrium compositions of Archean and Paleoproterozoic Fe formations revisited: new perspectives on the significance and mechanisms of deposition. *Geochimica et Cosmochimica Acta*, **74**(22):6387-6405. <https://doi.org/10.1016/j.gca.2010.07.021>
- Polleto K. 2014. *Caracterização petrográfica, litogeoquímica, geofísica e mineralizações de fosfato associadas às rochas supracrustais da unidade serra do camisão, Ipirá - Bahia*. Monography, Instituto de Geociências, Universidade Federal da Bahia, Salvador, 102 p.
- Pufahl P.K. 2010. Bioelemental sediments. In: James N.P., Dalrymple R.W., eds. *Facies models, Geological Association of Canada*. 4. ed. St John's: Geological Association of Canada, p. 477-503.
- Pufahl P.K., Fralick P.W. 2004. Depositional controls on Paleoproterozoic iron formation accumulation, Gogebic Range, Lake Superior Region, USA. *Sedimentology*, **51**(4):791-808. <https://doi.org/10.1111/j.1365-3091.2004.00651.x>
- Pufahl P.K., Groat L.A. 2017. Sedimentary and Igneous Phosphate Deposits: Formation and Exploration an invited paper. *Economic Geology*, **112**(3):483-516. <https://doi.org/10.2113/econgeo.112.3.483>
- Pufahl P.K., Hiatt E.E. 2012. Oxygenation of the Earth's atmosphere-ocean system: a review of physical and chemical sedimentologic responses. *Marine and Petroleum Geology*, **32**(1):1-20. <https://doi.org/10.1016/j.marpetgeo.2011.12.002>
- Ribeiro T.S. 2016. *Caracterização Geológica das Rochas Calcissilicáticas e Metacarbonáticas do Complexo Tanque Novo- Ipirá na Folha Pintadas-Ba: Potencial Metalogenético para Fosfato*, Salvador. MS Dissertation, Instituto de Geociências, Universidade Federal da Bahia, Salvador, 181 p.
- Samala W., Khirekesh Z., Amini A., Bafti B.S. 2018. Diagenetic evolution of the upper Devonian phosphorites, Alborz Mountain Range, northern Iran. *Sedimentary Geology*, **376**:90-112. <https://doi.org/10.1016/j.sedgeo.2018.08.001>
- Sato K., Tassinari C.C.G., Kawashita K., Petronilho L. 1995. O método Geocronológico Sm-Nd no IG/USP e suas aplicações. *Anais da Academia Brasileira de Ciências*, **67**(3):315-336.
- Shields G., Stille P. 2001. Diagenetic constraints on the use of cerium anomalies as palaeoseawater redox proxies: an isotopic and REE study of Cambrian phosphorites. *Chemical Geology*, **175**(1-2):29-48. [https://doi.org/10.1016/S0009-2541\(00\)00362-4](https://doi.org/10.1016/S0009-2541(00)00362-4)
- Silva L.C., Mcnaughton N.J., Melo R.C., Fletcher I.R. 1997. U-Pb SHRIMP ages in the Itabuna-Caraíba TTG high-grade Complex: the first window beyond the Paleoproterozoic overprint of the eastern Jequié Craton, NE Brazil. In: International Symposium on Granites and Association. Mineralis, 1, 282-283. *Abstracts...* Salvador.
- Silva M.G. 1996. Sequências metassedimentares, vulcanossedimentares e greenstone belts do Arqueano e Proterozóico inferior. In: Barbosa J.S.F., Dominguez J.M.L. (eds.). *Geologia da Bahia: texto explicativo para o mapa geológico ao milionésimo*. Salvador: SICM, SGM, p. 85-102.
- Singh A.K., Tewari V.C., Sial A.N., Khanna P.P., Singh N.I. 2015. Rare earth elements and stable isotope geochemistry of carbonates from the mélange zone of Manipur ophiolitic Complex, Indo-Myanmar Orogenic Belt, Northeast India. *Carbonates and Evaporites*, **31**:139-151. <https://doi.org/10.1007/s13146-015-0249-2>
- Soares G.G., Van Kranendonk V.J., Belousova E., Thomson S. 2019. Phosphogenesis in the immediate aftermath of the Great Oxidation Event: Evidence from the Turee Creek Group, Western Australia. *Precambrian Research*, **320**:193-212. <https://doi.org/10.1016/j.precamres.2018.10.017>
- Stacey S., Kramers J.D. 1975. Approximation of terrestrial lead isotope evolution by a two stage model. *Earth and Planetary Science Letters*, **26**(2):207-221. [https://doi.org/10.1016/0012-821X\(75\)90088-6](https://doi.org/10.1016/0012-821X(75)90088-6)
- Sverjensky D.A. 1984. Europium redox equilibria in aqueous solution. *Earth and Planetary Science Letters*, **67**(1):70-78. [https://doi.org/10.1016/0012-821X\(84\)90039-6](https://doi.org/10.1016/0012-821X(84)90039-6)
- Swart P.K. 2015. The geochemistry of carbonates diagenesis: The past, present and future. *Sedimentology*, **62**(5):1233-1304. <https://doi.org/10.1111/sed.12205>
- Tang L., Santosh M., Tsunogae T., Maruoka T. 2016. Paleoproterozoic meta-carbonates from the central segment of the Trans-North China Orogen: Zircon U-Pb geochronology, geochemistry, and carbon and oxygen isotopes. *Precambrian Research*, **284**:14-29. <https://doi.org/10.1016/j.precamres.2016.08.001>
- Taylor S.R., McLennan S.M. 1985. *The Continental Crust: Its composition and evolution; an examination of the geochemical record preserved in sedimentary rocks*. Oxford: Blackwell Scientific Oxford, 312 p.
- Tostevin R., Shields G.A., Tarbuck G.M., He T., Clarkson M.O., Wood R.A. 2016. Effective use of cerium anomalies as a redox proxy in carbonate-dominated marine settings. *Chemical Geology*, **438**:146-162. <https://doi.org/10.1016/j.chemgeo.2016.06.027>
- Van Kranendonk M.J., Webb G.E., Kamber B.S. 2003. Geological and trace element evidence for a marine sedimentary environment of deposition and biogenicity of 3.45 Ga stromatolitic carbonates in the Pilbara Craton, and support for a reducing Archean ocean. *Geobiology*, **1**(2):91-108. <https://doi.org/10.1046/j.1472-4669.2003.00014.x>
- Veizer J., Ala D., Azmy K., Bruckschen P., Buhl D., Bruhn F., Carden G.A.F., Diener A., Ebner S., Godderis Y., Jasper T., Korte C., Pawellek F., Podlaha O.G., Strauss H. 1999. 87Sr/86Sr, β 13C and β 18O Evolution Phanerozoic seawater. *Chemical Geology*, **161**:59-88.
- Wang W., Bolhar R., Zhou M., Zhao X. 2018. Enhanced terrestrial input into Paleoproterozoic to Mesoproterozoic carbonates in the southwestern South China Block during the fragmentation of the Columbia supercontinent. *Precambrian Research*, **313**:1-17. <https://doi.org/10.1016/j.precamres.2018.05.001>
- Webb G.E., Kamber B.S. 2000. Rare earth elements in Holocene reefal microbialites: A new shallow seawater proxy. *Geochimica et Cosmochimica Acta*, **64**(9):1557-1565. [https://doi.org/10.1016/S0016-7037\(99\)00400-7](https://doi.org/10.1016/S0016-7037(99)00400-7)
- Windley B.F. 1984. *The evolving continent*. 2. ed. Chichester: John Wiley & Sons, 391 p.
- Winkler H.G.F. 1979. *Petrogenesis of metamorphic rocks*. New York: Springer-Verlag, 348 p.
- Winter J.D. 2001. *An introduction to igneous and metamorphic petrology*. Upper Saddle River, Prentice Hall.

- Yardley B.W.D. 1989. *Introdução à Petrologia Metamórfica*. 2. ed. Brasília: Ed. UnB, p. 215-248.
- Zhao Y.Y., Zhao M-Y., Li S-Z. 2018. Evidences of hydrothermal fluids recorded in microfacies of the Ediacaran cap dolostone: Geochemical implications in South China. *Precambrian Research*, **306**:1-21. <https://doi.org/10.1016/j.precamres.2017.12.028>
- Zhao Y., Zheng Y. 2013. Geochemical constraints on the origin of post-depositional fluids in sedimentary carbonates of the Ediacaran system in South China. *Precambrian Research*, **224**:341-363. <https://doi.org/10.1016/j.precamres.2012.10.014>
- Zhao Y., Zheng Y., Chen F.K. 2009. Trace element and strontium isotopic constraints on sedimentary environment of Ediacaran carbonates in Southern Anhui, South China. *Chemical Geology*, **265**(3-4):345-362. <https://doi.org/10.1016/j.chemgeo.2009.04.015>
- Zhong S., Mucci A. 1995. Partitioning of rare earth elements (REEs) between calcite and seawater solutions at 25°C and 1 atm, and high dissolved REE concentrations. *Geochimica et Cosmochimica Acta*, **59**(3):443-453. [https://doi.org/10.1016/0016-7037\(94\)00381-U](https://doi.org/10.1016/0016-7037(94)00381-U)
- Zhu B., Jiang S.Y., Yang J.H., Pi D., Ling H.F., Chen Y.Q. 2014. Rare earth element and Sr-Nd isotope geochemistry of phosphate nodules from the lower Cambrian Niutitang Formation, NW Hunan Province, South China. *Palaeogeography, Palaeoclimatology, Palaeoecology*, **398**:132-143. <https://doi.org/10.1016/j.palaeo.2013.10.002>
- Zhu B., Jiang S.Y. 2017. A LA-ICP-MS analysis of rare earth elements on phosphatic grains of the Ediacaran Doushantuo phosphorite at Weng'an, South China: implication for depositional conditions and diagenetic processes. *Geological Magazine*, **154**(6):1-17. <https://doi.org/10.1017/S001675681700022X>

ARTIGO 2 - POSITIVE $\delta^{13}\text{C}_{\text{carb}}$ EXCURSIONS IN PALEOPROTEROZOIC MARBLES FROM THE NORTHEAST SÃO FRANCISCO CRATON, BRAZIL: A REVIEW, NEW DATA AND PHOSPHOGENETIC AND GEOTECTONIC IMPLICATIONS.

POSITIVE $\delta^{13}\text{C}_{\text{carb}}$ EXCURSIONS IN PALEOPROTEROZOIC MARBLES FROM THE NORTHEAST SÃO FRANCISCO CRATON, BRAZIL: A REVIEW, NEW DATA AND PHOSPHOGENETIC AND GEOTECTONIC IMPLICATIONS.

Tatiana Silva Ribeiro^a, Aroldo Misi^a, Luís Rodrigues dos Santos de Oliveira^a, Pedro Maciel de Paula Garcia^b, José Haroldo da Silva Sá^a, Débora Correia Rios^a, Alcides Nóbrega Sial^c, Ib Câmara^a.

^a Metallogenesis and Metallogenic Models Group, Institute of Geosciences, Federal University of Bahia, Salvador, Brazil. ^b Institute of Geosciences, Federal University of Bahia, Salvador, Brazil. ^c Federal University of Pernambuco, Recife, Brazil.

Abstract

In the Northeast Bahia, Paleoproterozoic metasedimentary successions deformed during the Rhyacian-Orisnian orogeny are found in the São Francisco Craton. They are metamorphosed bodies in the greenschist to granulite facies. The marbles, calcisilicates, graphite-schists and iron formations of the Tanque Novo Complex – Ipirá (TNIC) and the Jacurici Valley (JV) region, both in the Salvador – Curaçá Orogen and the Rio Salitre Complex (RSC) in the Gavião block. Marbles and calcisilicates are hosts for mineralization that reaches up to 11% P₂O₅, represented by fluorapatite and carbonate-fluorapatite. Despite metamorphism, it is possible to identify records of primary marine signatures, and the recognition of suboxic phosphate precipitation conditions. The TNIC and JV carbonate sequences occurred on the continental margin of a paleocean and in an open sea, both with continental inputs, coming from the margins or magmatic arcs. While in the RSC they are related to an open sea developed in continental rift, according to Ce /Ce*_x Pr/Tb_N, Eu/Eu*, Pr/Yb_N and Tb/Yb_N. The positive $\delta^{13}\text{C}$ excursions in marbles from TNIC (+6.13 to +9.69), RSC (+5.38 and +6.78%) and JV (+2.2 to 6.9%), are similar to marine carbonates formed during the global Lomagundi-Jatuli event (LJE~2.3 to 2.1 Ga). The isotopic data and the presence of P, Fe and C, attest that their carbonate protoliths were precipitated at the end of the Great Earth Oxygenation Event and the LJE, after the fourth and last (2.2 Ga) of a series of glaciations initiated at 2.42 Ga. The genetic relationship between phosphogenesis and LJE is related to global and local (facies-dependent) causes, mainly related to the increase in oceanic primary paleoproductivity and the burial of organic matter. The unprecedented occurrences of this work, together with those from Argentina and Uruguay, record the oldest phosphogenesis of the South American Platform.

KEYWORDS: Lomagundi -Jatuli Event; Phosphate; Marbles; São Francisco Craton.

1. Introduction

Neoproterozoic – Paleoproterozoic transition is marked by dramatic paleoenvironmental, paleoclimatic and paleogeographical induced by geotectonic changes. The initial breakup of the Kenorland supercontinent (2.5 – 2.4 Ga) (Bekker and Eriksson, 2003), after the first Huronian deglaciation formed the first sedimentary basins of Paleoproterozoic era. In this transition, the high photosynthetic production of cyanobacteria promoted an increase in oxygen content in the oceans and

atmosphere, called Great Earth Oxygenation Event (GOE) that enhanced in the formation of phosphate mineralization on a global scale (Nelson et al. 2010, Pufahl 2010, Pufahl and Hiatt 2012, Papineau et al. 2013).

Thus, Paleoproterozoic phosphate deposits are associated with these changes in the hydrosphere and atmosphere, where a sequence of glaciations and deglaciations, combined with the presence of oxygen, generated intense chemical weathering, thus increasing the supply of continental P-Fe rich sediments to the oceans. The action of anaerobic bacteria and the presence of organic matter helped to make phosphorus available and fixed in marine sediments under different oxygenation conditions (Papineau et al., 2010 and Nelson et al, 2010).

This period records important positive excursions of $\delta^{13}\text{C}$ between +5 and 10‰ (and higher) in marine carbonate units dozens to several hundred meters thick (Melezhik et al. 2007; Martin et al. 2013; Gumsley et al. 2017), characterizing the Lomagundi – Jatuli Event (LJE). The LJE represents an event whose magnitude and duration are unique in Earth history and developed on all continents after the Huronian glaciation (Kopp et al., 2005; Melezhik et al., 2005b) and it follows the initial accumulation of atmospheric O_2 (Bekker et al., 2004; Hannah et al., 2004). However, the LJE is still much debated regarding its origin, whether it is a global or local event (Hodgskiss et al., 2023, Prave et al., 2022, Eguchi et al., 2020 and 2022, Bekker and Holland, 2012).

In several continents, the Paleoproterozoic basins host the first records of phosphates with economic contents in the Earth's history (Heaman, 1997; Barley et al., 2005; Bekker et al., 2006; Halls et al., 2008, Papineau 2010). However, on the South American platform there is few data available in the literature on these occurrences in paleobasins of the same age, especially the LJE has already been recognized in some sequences: carbonates in the Craton Rio de La Plata, in the Paso Severino Formation in Uruguay (Maheshwari et al., 2010, Lajoinie et al., 2018) and in the Brazil there are also records of the LJE, in the Cercadinho and Fecho do Funil Formation of the Minas SuperGroup (Bekker et al., 2003, Maheshwari et al., 2010), Crixás Greenstone Belt (Santos et al., 2008), in the Greenstone Belt of the Itapicuru River, located in the northeast of the São Francisco Craton (Maheshwari et al., 2010) and in the northeast of the Salvador – Curaçá Orogen, associated with the marbles located in the mafic body – ultramafic of Ipueira-Medrado, in the Jacurici Valley (Maheshwari et al., 2010).

In the Salvador-Curaçá Orogen, phosphate mineralization are known in the following metasedimentary successions in the north of the Itabuna-Salvador-Curaçá Orogen: in the Tanque Novo – Ipirá Complex (Ribeiro, 2016; Ribeiro, 2017 and Ribeiro et al, 2021) and metasediments in the Jacurici Valley (Gama, 2014, Gama et al, 2021), and in the northern region of the Gavião Block, in the Rio Salitre Complex (Sá, 1982; Sá, 1984; Leite, 1983; Leite, 1984, Oliveira, 2016). They are calcisilicate rocks, marbles, iron formations, quartzites, graphite-schists and metamorphosed

paragneisses in the high amphibolite to granulite facies and in the greenschist facies. The Tanque Novo – Ipirá and Salitre Complexes host primary phosphate mineralization in a disseminated form and P₂O₅ contents of up to 11% in marbles and calcisilicate rocks (Oliveira et al. 2017, Ribeiro, 2016, Ribeiro et al. 2017, Ribeiro et al. 2021). In the metasedimentary rocks of the Jacurici Valley, mineralization reach up to 4.56% in marbles and calcisilicate rocks (Gama et al., 2021).

The marbles, calcisilicates and iron formations of these metasedimentary rocks may indicate the paleoenvironmental conditions of their formation and combined with geological field observations are important in the interpretation of phosphate mineralization. The most effective geochemical tools for these purposes include studies of rare-earth elements and yttrium (REEY), stable isotopes (Carbon, Oxygen and Sulfur), ⁸⁷Sr/⁸⁶Sr isotopes in carbonate-fluorapatite or in whole rocks (Veizer et al. 1999, Bau 1993, Papineau 2010, Nelson et al 2010, Pufahl and Hiatt 2012, Swart 2015).

When normalized to the Post-Archaean Shale (PAAS) in Paleoproterozoic rocks such as La, Eu, Ce and Gd, the behavior pattern of these elements is very well known in the literature and seems remarkably consistent over geological time (Bolhar et al. 2004, Planavsky et al., 2010, Bolhar and Van Kranendonk 2007, Zhao et al. 2009, Johannesson et al. 2013; Joosu et al. 2016). Studies of well-preserved and even metamorphosed carbonates have provided valuable information about the biogeochemical cycle of carbon in the geological past (e.g. Schidlowski et al., 1976b; Knoll et al., 1986; Veizer and Hoefs, 1976; Derry et al., 1992; Kah et al., 1999; Maheshwari et al., 1999; Sreenivas et al., 2001; Bekker et al., 2003, 2008).

Therefore, in this paper we examine the records of phosphogenesis and LJE in supracrustal rocks northeast of the São Francisco Craton. Re-examine the marbles, related to the emplacements and hosts of phosphate mineralization, in order to understand the age of deposition, forms of mineralization and geochemical indicators of paleoenvironmental conditions. We also discuss the meaning of the new carbonate C and O isotope data from the Tanque Novo – Ipirá and Rio Salitre Complexes and its comparison with those from the Jacurici Valley and world basins. Furthermore, the depositional tectonic environments of these carbonate sequences are also demonstrated in this paper. Correlations between phosphorus and positive $\delta^{13}\text{C}$ values indicate genetic relationships between the mineralization study here and the alteration of the carbon cycle during the Lomagundi - Jatuli Event on Paleoproterozoic.

2. Regional Geology

The study phosphate mineralization are inserted in the South American Platform, in the northern São Francisco Craton (SFC), demonstrated in the figures 01 and 02. The SFC basement is made up of Archean paleocontinentes and magmatic arcs that collided during the Rhyacian-Orosinian

orogeny at the end of the Paleoproterozoic. It was partially reworked in the Neoproterozoic and Cambrian, during the Brazilian cycle (Alkmim et al. 1993, Barbosa and Sabaté 2003, Barbosa and Dominguez 2006). The Neoproterozoic orogens that border the craton are: Sergipana to the northeast, Riacho do Pontal to the north, Rio Preto to the northwest, Brasília to the west, and Orogen Araçuaí to the south-southeast (Alkmim et al., 1993; Barbosa et al. , 2012). The SFC extension, comprises almost the entire State of Bahia, extending to the neighboring regions of Minas Gerais, Sergipe, Pernambuco and Goiás (Fig. 01).

2.1 Salvador – Curaçá Orogen

The phosphate mineralizations of the Tanque Novo- Ipirá Complex (TNIC) and the Jacurici Valley are hosted by high-grade metamorphic rocks. It was formed over a period of about 200-300 million years, during the Paleoproterozoic, with collision of the block Gavião, Jequié and Serrinha, leading to the formation of an important mountain range in the Northeast of Bahia (Barbosa and Sabaté, 2003). The structuring of this orogen resulted from a complex system of polyphasic deformations, which caused crustal shortening that generated folding and refolding. The TNIC represents the axial zone of the transpressive structure in positive flower's, formed after collision and structuring of the orogen (Loureiro et al., 1991).

The Salvador-Curaçá Orogen can be subdivided into three main domains at northern segment (Melo et al., 1991): Caraíba Complex, São José do Jacuípe Suite and Tanque Novo-Ipirá Complex (Kosin et al., 2003). Several granite suites are present and classified according to the stages of deformation, in addition to the most recent rocks of Cenozoic age.

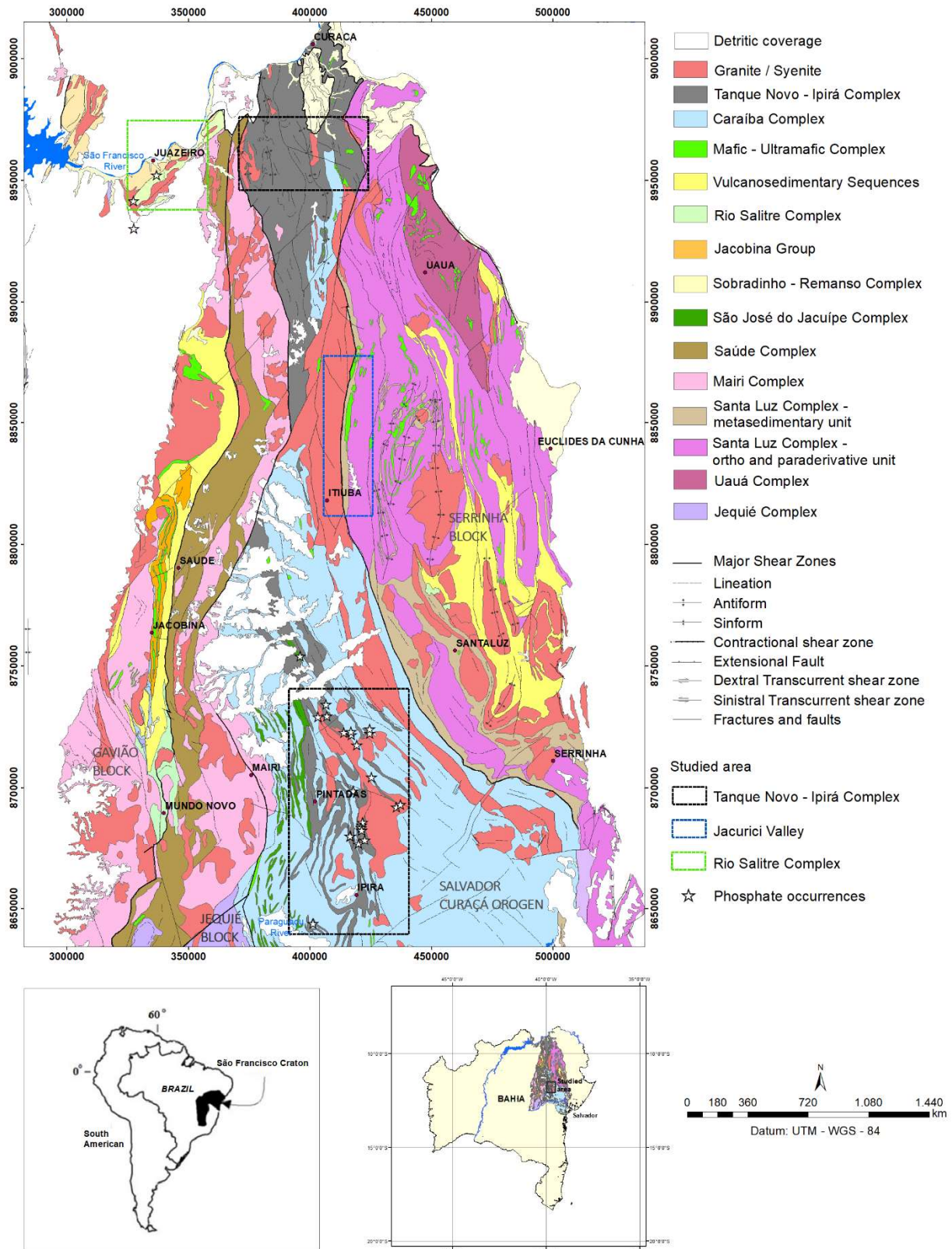


Fig. 1. Simplified regional geological map of the Salvador – Curaçá Orogen (after Oliveira et al. 2010), showing three study areas of the Tanque Novo Complex – Ipirá (north and south), and the phosphate mineralization and two other areas of phosphate occurrences in the São Francisco Craton – Vale metasediments of the Jacurici and Rio Salitre Complex.

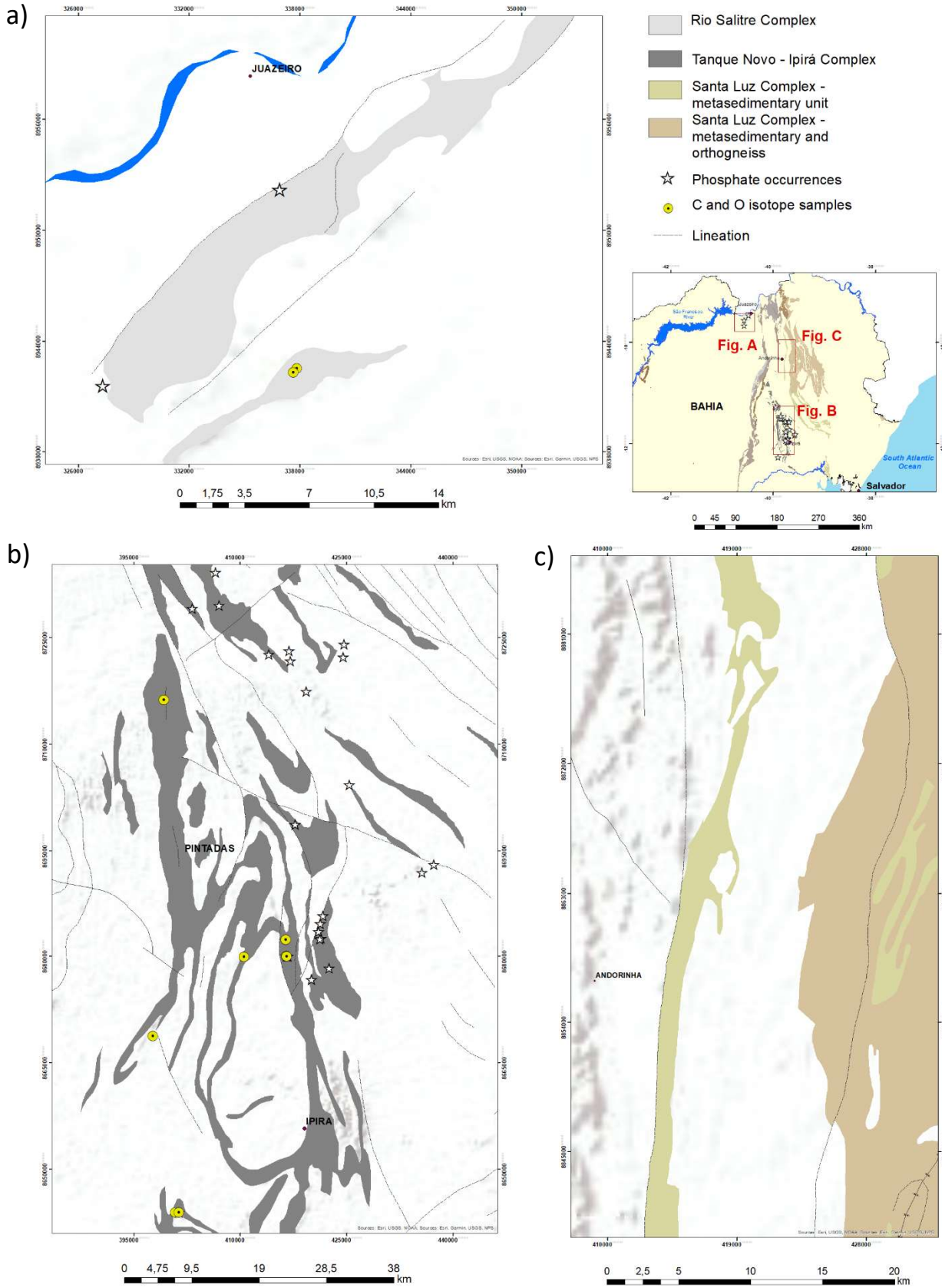


Fig. 2 - Geological map of the study areas, with emphasis on Paleoproterozoic metasedimentary rocks, and indication of sample points collected for isotopic studies in this work, from the Rio

Salitre Complex (a) and Tanque Novo-Ipirá (b) with the locations of phosphate occurrences. The metasedimentary rocks of the Jacurici Valley are represented in figure C.

2.1.1 *São José do Jacuípe Suite*

This suite occurs in the southwest part of the Salvador-Curaçá Orogen (Loureiro, 1991; Melo, 1991; Sampaio, 1992). It consists of a plutonic mafic-ultramafic association in the shape of lenses with directions ranging from N-S to NNW-SSE, forming tectonic imbrications with rocks of the Caraíba and Tanque Novo-Ipirá complexes.

The geochemistry of these rocks is of a tholeiitic lineage, similarly to rocks from the environment of the continent-ocean crust transition when a rift opened (Teixeira, 1997). Faced with this fact and the lack of truncation of the lithofacies of the São José do Jacuípe Suite with the rocks of the Caraíba and Ipirá complexes, Teixeira et al. (2000) suggested that this suite would correspond to remnants of an ancient oceanic crust. Oliveira et al., (2010) reports a zircon age (U/Pb) of 2584 ± 8 Ma for a suite leucogabbro, metamorphosed at 2082 ± 17 Ma. Koproski et al., (2023) show geochemical similarities of these rocks with ophiolites generated in suprasubduction environments, a possible source of the E-MORB type and U/Pb crystallization ages of 2549 ± 23 Ma and 2563 ± 13 Ma for gabbro-norites.

2.1.2 *Caraíba Complex*

It's the typical and most representative unit of the SCO. In the western part, it outcrops in the form of megalotopes that alternate with rocks from the São José do Jacuípe Suite, from the Tanque Novo-Ipirá Complex, and also intrusive granitoids, always with tectonic imbrications.

This complex corresponds to a bimodal suite of granulite facies, whose felsic pole is made up of orthogneisses that vary from enderbitic to charnoenderbitic and, rarely, charnockitic (Oliveira and Tarney, 1995; Teixeira, 1997; Kosin et al., 2003; Oliveira and others, 2004, 2010). For Teixeira (1997), the prototypes of these gray to greenish orthogneisses have a chemistry that can vary from juvenile calcium-alkaline with low potassium to calcium-alkaline, sometimes normal, sometimes high potassium. This complex is considered by this author to be the product of the fusion of a magmatic crust with a greater or lesser contribution of sedimentary material. It is worth noting that the basic pole of this complex is made up of gabbrodioritic lenses. Oliveira et al. (2010) suggest that the geochemical signature and positive $\epsilon\text{Nd}(T)$ values are characteristics of a juvenile (chondritic) source.

According to Souza et al., (2020) the igneous protoliths of the orthogneisses of the Caraíba Complex have U-Pb zircon between 2637 Ma and 2574 Ma. In the Caraíba mine area the U-Pb ages for felsic metaplutonic rocks are 2637 Ma, 2620 Ma, 2581 Ma, associated with a Neoproterozoic continental arc.

2.1.3 *Tanque Novo – Ipirá Complex (TNIC)*

The Tanque Novo – Ipirá Complex is a metavolcanosedimentary sequence, initially described by Melo et al, (1991) as the Ipirá Complex and is composed of five different units: Pintadas, Serra do Camisão, Juazeiro, Angico and Umbuzeiro.

The criterion used to separate the Pintadas and Serra do Camisão Unit was based on the large amount of calcisilicate rocks associated with apatite deposits at the Serra do Camisão Unit and the presence of aluminous paragneisses, only at the Pintadas Unit (Melo et al. 1991). Subsequently, Kosin et al. (2003) subdivided into six units, where marbles, calcisilicates, iron formations and graphite rocks are associated with quartzites, aluminous gneisses, kinzigites, metabasites and metaultrabasites.

The outcropping bodies of these rocks are discontinuous, with almond-shaped and lentiform or fusiform shapes, due to the intensity of the deformational processes occurring in the region. The general direction of these bodies is NNW-SSE, with azimuths N345° and N360° and subvertical dips. The supracrustal rocks are metamorphosed in the high amphibolite to granulite facies with temperatures between 710 and 810°C for progressive metamorphism and retrometamorphism around 500°C for serpentinization and between 350–450°C for talcification (Ribeiro, 2016). The aluminous, sapphirine-bearing granulites of this Complex achieved metamorphic retrograde conditions equilibrium at 900-950 C at pressures of 7.0-8.0 kbar (Leite et al. 2009), and are representatives of ultra-high temperature (UHT) metamorphism in the orogen.

According to Ribeiro et al., (2021) the geochronological data indicate a maximum deposition age of 2128 Ma in zircon U/Pb – LA-ICPMS in a study of quartzite from the upper metasedimentary sequence (Serra do Camisão Unit). Concord ages of 2595±18 Ma, with two populations with Neoproterozoic and Paleoproterozoic sources. TDM ages for aluminous gneisses indicate maximum ages of 2.6 Ga for sedimentation (Oliveira et al. 2002), and in the northern portion of the Orogen, Oliveira et al., (2010) obtained maximum Nd model ages between 2.6 and 2.7 for the deposition of protoliths. Leite et al., (2009) obtained in situ ages in monazite (EMP) of 2.08-2.05 Ga (Rhyacian) indicating UHT metamorphism. This age is associated with the formation of paragneisses of the Pintadas Formation, stratigraphically in the lower portion, of apatite-hosted carbonate metasedimentary rocks.

In the Salvador-Curaçá Orogen, several rocks are compatible with the ages of Neoproterozoic zircons, according to Ribeiro et al., (2021), the most prominent source rock is contemporary with the Caraíba norite — 2580 Ma (U-Pb SHRIMP; Oliveira et al. 2002). Zircon rims record a metamorphic event at 2082±14 Ma, interpreted as a reflection of the closure of the paleobasin and formation of the Salvador-Curaçá Orogen. This last event is related to the collision of the Archean Gavião and Serrinha block (Barbosa and Sabaté 2003b).

2.2 Serrinha Block

2.2.1 Jacurici Valley Terrain (JV)

The constituent lithologies of the Jacurici Valley (JV) region are positioned directly to the east of the Itiúba Sienite (Fig. 01), being composed of highly deformed, folded and faulted rocks, configured discontinuously in a megasyncline with predominant vergence to the east, in the N-S trend, along about 25 km. The supracrustal sequence described by Jardim de Sá (1983) and Marinho et al. (1986) consists of various metamorphosed lithotypes in high amphibolite to granulite and metasomatized facies (Del Lama et al., 2001), among them: diopsides, marbles, impure and metachert quartzites, iron formations, graphitites, paraderived and calcisilicate granulites. Marbles are well characterized by Del Lama et al., (2001), Maheshwari et al. (2010), Gama (2014), Blaskowski (2018) and Gama et al., (2021).

This set of rocks is directly intruded by stratified mafic-ultramafic bodies, of Paleoproterozoic age, mineralized in chromium (Marques and Ferreira Filho, 2003). In the supracrustal succession of the Vale do Jacurici, marbles and diopsides are the host rocks for phosphate mineralization. Marbles from this succession reach up to 30–40 m in thickness (Maheshwar et al., 2010).

According to Blaskowski (2018) and Gama et al., (2021) the marbles are magnesian and dolomitic and include serpentine (lizardite), olivine (forsterite), garnet, magnesian calcite, dolomite and apatite (Fig. 3C). The marbles range from serpentine-olivine marbles with or without garnets, serpentine-apatite marbles to pure marbles, with white to gray, greenish, sometimes orange coloring. According to Gama et al., (2021), phosphate mineralization are disseminated and P_2O_5 contents reach up to 4.56%, being in marbles (1.38 and 4.56%) and diopsidites (2.07 and 2.3%, Fig. 3j). They are represented by idiomorphic and subidiomorphic fluorapatites, colorless in marbles and diopsides.

The minimum deposition age is defined by the intrusive relationship of the Itiúba Sienite and the Vale do Jacurici Mafic-Ultramafic Complex that intrude the supracrustals. The Itiúba syenite of 2084 ± 9 Ma (U/Pb – SHRIMP) and the peridotite-noritic Jacurici Complex rich in chromite have 2099 ± 6 MA(LA-ICP-MS) metamorphic age (Dias et al., 2022) that intrude the supracrustal succession. Oliveira et al. 2004 and Silveira et al., suggest a Paleoproterozoic age for the succession of the JV.

2.2.2 Rio Itapicuru Greenstone Belt

The RIGB is a sequence of volcanic-sedimentary rocks affected by metamorphism, of Paleoproterozoic age, located in the Archean Serrinha Block in the northeast portion of the São Francisco Craton. RIGB is embedded in mafic schists within shear zones filled by quartz-carbonate veins and has an elongated shape in the north-south direction, 170 km long and 15 km wide, covering

an area of 7500 km² (Silva et al., 2001). The RIGB is limited in abrupt tectonic contact with Archean migmatites and gneisses of the Santa Luz Complex and metasedimentary rocks from Jacurici Valley.

The volcanic mafic unit, that represents the basal portion of the supracrustal sequence is composed of basaltic flows (sometimes pillow) with pelitic, chemical, and tuff sedimentary bodies (Rocha Neto and Pedreira, 1994). Mafic metatufos, iron formation, metacherts, marbles, and graphite phyllites are also present in this unit (Ruggiero and Oliveira, 2010).

2.3 Gavião Block

2.3.1 Rio Salitre Complex (RSC)

The RSC comprises supracrustal rocks of low metamorphic grade (greenschist to low amphibolite), divided into two units: (i) the Lower Unit composed of metabasalts (lava pillow) and metakomatiites with intercalations felsic metavolcanics, quartzite, metachert, phyllite and metacarbonate; and (ii) the Upper Unit, which mainly comprises pelitic and psammitic metasedimentary rocks, schists, meta-arkose, banded iron formations, phosphorites, marbles and calcisilicate rocks (Dalton de Souza et al., 1979; Dalton de Souza and Teixeira, 1981).

The phosphate mineralization of the Rio Salitre Complex were initially described by Leite (1983) and later by Oliveira (2016), as primary and secondary, located in Serrote da Batateira, Ilha do Fogo and Serra dos Espinhos, associated with Upper Unit.

According to Oliveira (2016), the primary host rocks include calcisilicate rocks, marbles (phlogopite-serpentine marble, diopside-apatite-tremolite-marble with phlogopite), schists and breccias with phosphatic oolites. Secondary mineralization is found in phosphate-foliated quartzite.

The primary mineralization is represented by carbonate-fluorapatite, which occurs in the form of lenses with polygonal crystals (Fig. 31) and in a disseminated form. In the secondary, is described the presence of variscite, crandalite, augelite and cyrovilite. In the Serrote da Batateira deposit, reserves were estimated at 660.000,00 tons with P₂O₅ contents varying from 8 to 11% in a layer approximately 12 m thick and extending around 600 m (Leite, 1983). For secondary mineralization, Oliveira (2016) recorded up to 25% P₂O₅.

Geochronological data with ϵ Nd values obtained in a banded iron formation, which contains host rocks for primary mineralization, range from -4.86 to -5.66, suggesting that the origin of the iron comes from a more differentiated crust. Sm-Nd geochronological data, in whole rock, indicate an age of 2021±97 Ma (Oliveira, 2016). Macedo et al., (2019) interpreted the RSC as Neoproterozoic, based on model ages Sm-Nd TDM – 2930 Ma and 2820 Ma, obtained from komatiites from the lower unit of the Complex. In contrast, Garcia et al., (2021) indicates a Paleoproterozoic age from U-Pb/SHRIMP dating of porphyritic rhyolite from the Rio Salitre Complex, indicating a concord age of 2161.1 ± 4 Ma.

3. Analytical methods

In this work, most of the marble samples geochemical studies from JV and TNIC were extracted from Gama et al., (2021) Ribeiro et al., (2021), respectively (appendix 1). The analytical results of all data are listed in table 1. The anomalies of Ce/Ce*, Pr/Pr* and Eu/Eu* were calculated according to the method of Bau & Dulski (1996): Ce/Ce*_{SN} [Ce_{SN}/(0.5 Pr_{SN} + 0.5La_{SN})], Pr/Pr*_{SN} [Pr_{SN}/(0.5 Ce_{SN} + 0.5 Nd_{SN})], Eu/Eu*_{SN} [Eu_{SN}/(0.67 Sm_{SN} + 0.33 Tb_{SN}).

These samples were collected carefully to be free from visible effects of weathering, hydrothermal alteration or late veins, the analytical methods were the same, so they can be compared. Colorimetric tests were carried out in the field to identify the presence of phosphorus, using ammonium molybdate and hydrochloric acid (10%). The yellow-green to green color is positive for phosphorus concentrations.

Whole rock litho-geochemical studies from all areas were prepared and analyzed at SGS Laboratório de Geosol in Belo Horizonte, Minas Gerais. 250g of marble crushed into 3mm particles were weighed, homogenized, quartered in Jones, and pulverized to 150 mesh.

Major elements abundances of major elements (SiO₂, Ti₂O, Al₂O₃, MgO, Fe₂O_{3t}, MnO, CaO, Na₂O, K₂O and P₂O₅) were obtained by X-ray fluorescence. In this analysis, 0.5 g of the samples was completely melt digested with lithium tetraborate in a Vulcan automatic machine at 1.000°C. The analysis was performed on a molten tablet by X-ray fluorescence spectrometry, Type WDXRF, simultaneous model PANalytical Axios Fast, obtaining results with a natural basis. Trace elements (Ba, Rb, Ga, Zr, Sr, Cr, Ni, Co and Y) and rare earth elements (REE) were determined by melt digestion in a muffle furnace at 950°C with lithium metaborate (LiBO₂), dissolving with an acidic solution of nitric acid and tartaric acid (HNO₃ and C₄H₆O₆). The trace elements were read by ICP-Optical Emission Spectrometry (ICP-OES), Model Optima 7300DV. This solution also quantified ETRs read by ICP-MS, model NexION 300X ICP-MS. REEY concentrations were normalized according to the average post-Archean Australian shale composition (PAAS) reported by McLennan (1989).

Petrographic studies were carried out with the Olympus machine, Microscope Petrographic microscope BX60 in the Microscopy Laboratory of the Institute of Geosciences of the Federal University of Bahia. Thin sections were also investigated with a JEOL JSM-6610LV Scanning Electron Microscope (SEM) at the Multiuser Laboratory of Electron Microscopy at the Federal University of Bahia (LAMUME); graphics were generated with the AZtec software.

Pure carbonates or those with a lower content of silicate minerals were selected for isotopic studies from TNIC and RSC. These rocks were crushed and subsequently, the calcite and dolomite crystals were manually separated from the other minerals present. Isotopic analyzes of C and O were carried out on carbonate samples (calcites and dolomites) at the Geochemical Studies Center – Stable

Isotopes Laboratory (NEG-LABISE) at the Federal University of Pernambuco and at the Stable Isotope Facility (SIF) Laboratory at the University of Exeter, England. For CO₂ gas extraction, approximately 20 mg of each sample (powder) was used. Each sample was diluted with orthophosphoric acid at 25°C to release CO₂. The CO₂ gas obtained from each sample was analyzed for O and C isotopes in a Thermofinnigan Delta V Advantage mass spectrometer. The results are expressed in the notation δ in permil (‰) relative to the standard in PDB (PeeDee Belemnite) and SMOW (Standard Mean Ocean Water), with precision better than $\pm 0.1\%$. The reference gas used was calibrated against the NBS-19 reference material (dolomite, Friedman et al., 1982). The NBS 19 is intended for the analysis of the ¹³C/¹²C and ¹⁸O/¹⁶O isotopic ratio of carbonates and is used to define the PDB scale (Hut, 1987). The SMOW values were calculated using the equation: $\delta^{18}\text{O}_{\text{SMOW}} = 1.03091 \times \delta^{18}\text{O}_{\text{PDB}} + 30,91$, from Hut (1987).

4. Mineralogical characterization of TNIC marbles and phosphate mineralization

The host rocks of phosphate mineralization are marbles and calcisilicate rocks. The marbles were interpreted as belonging to two distinct groups, one being calcitic (group 2), devoid of phosphorus and another dolomitic group of greenish white color, this last group hosting the mineralization (group 1). The mineral assembly of dolomitic marbles is formed by dolomite, calcite, olivine, serpentine, diopside, apatite, garnet, tremolite and talc (Fig. 3 a – j; m - o).

The calcisilicate rocks, the second host class in this area, are formed by diopside, tremolite, calcite, plagioclase, apatite, k-feldspars, quartz, biotite, titanite, biotite, hornblende and zircon. Structurally, they are banded rocks, where bands of diopside and/or tremolite and bands of quartz and feldspar compounds alternate, being called calcisilicate gneisses. They also occur massively, with a higher content of diopside, tremolite, calcite and apatite, called diopsidites (Figure 3 i) and diopsides with microcline.

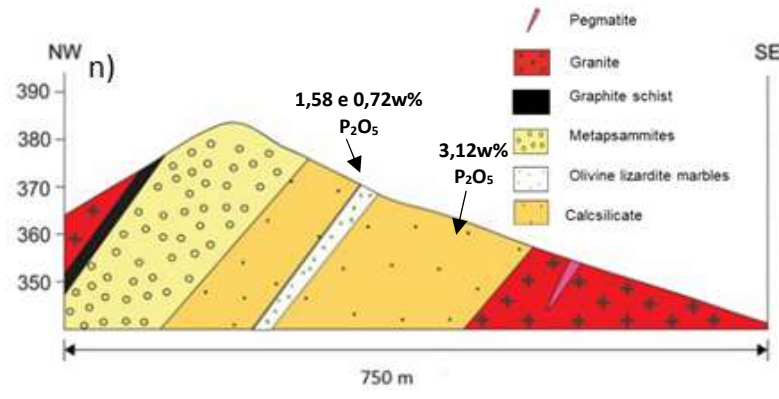
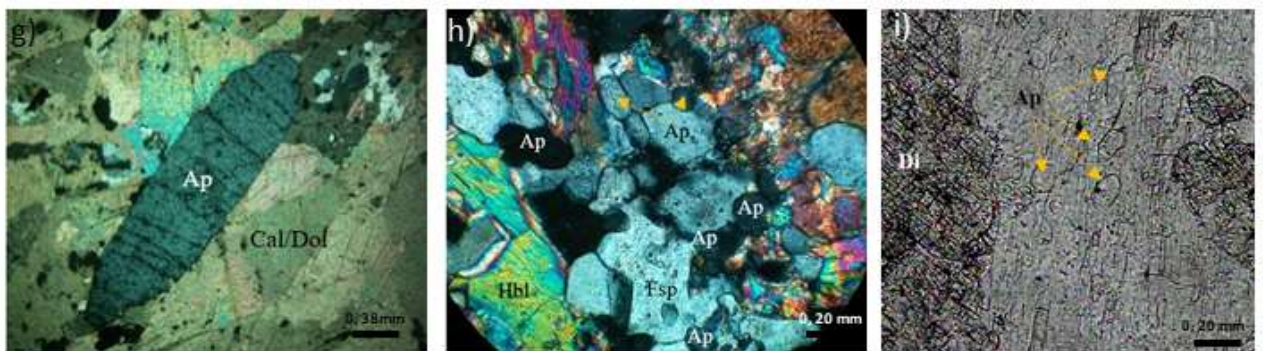
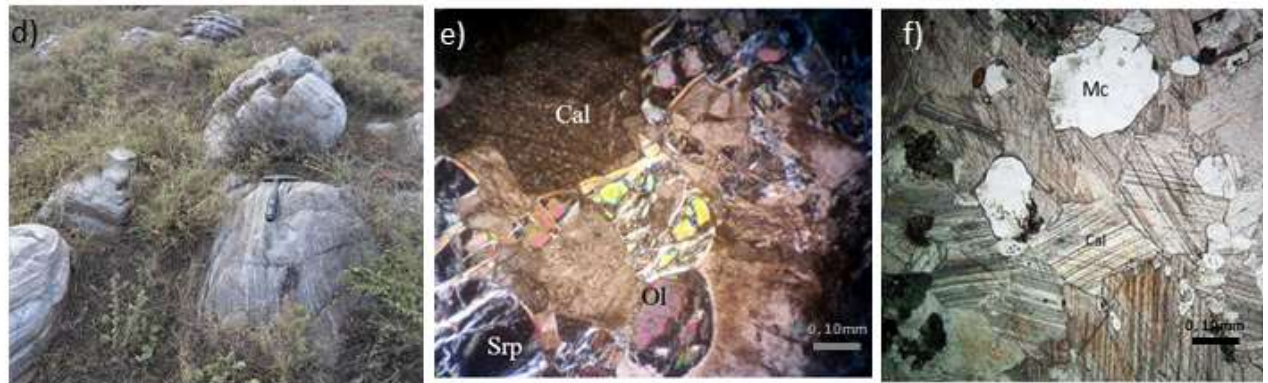


Fig. 3 – a) Dolomitic marble with serpentine; b) Calcite marble with orange calcite; c) Dolomitic marble indicating positive colorimetric test for phosphorus; d) Outcrop of calcisilicate gneisses; e) Relic olivine porphyroblasts (Ol) with mesh texture, evidenced by serpentinization in dolomitic marble (XPL); f) Calcite marbles with polygonal granoblastic texture in calcite crystals; g) Idioblast apatite crystal associated with calcite and dolomites in a contact zone with pegmatites; h) Prismatic apatite crystals in contact with hornblende and feldspar in calcisilicate rock; i) Subidiomorphic apatite oriented according to the foliation of the calcisilicate rock; j) Dolomitic marble with apatite from JV (Gama et al., 2021); l) Apatite crystals in RSC marbles (Oliveira, 2016); m) EDS image of phlogopite, chlorite, and calcite; n) Geological section of the TNIC showing intercalation between calcisilicate rocks, dolomitic marble and graphite-schist levels, and phosphorus concentration in dolomitic marbles (Group 1) and calcisilicate rocks, located west of the district of Bonfim de Ipirá; o) Backscattered electron image of calcite and lizardite.

5. Stable Isotopes C and O

Nine marble samples from the TNIC collected in the region between Ipirá – Pintadas, south of Ipirá and Tanque Novo (north of Bahia), and two marble samples from the Rio Salitre Complex, one stratigraphically located above the mineralized zone and other mineralized in phosphate, were analyzed for stable isotopes of carbon and oxygen. The isotopic ratios, expressed in per thousand (‰), according to the PDB and SMOW standards, are shown in Table 1. Furthermore, the results of $\delta^{13}\text{C PDB}\%$ and $\delta^{18}\text{O PDB}\%$ for marbles from the Vale do Jacurici and the Rio Itapicuru Greenstone Belt are listed (RIGB) – both also in the north of the São Francisco Craton (SFC), taken from Maheshwari et al. (2010) and used in the charts for regional comparison.

Three types of TNIC marbles were analyzed: group 2 calcitic marbles, group 1 dolomitic marbles and group 1 marbles in contact zones with pegmatites (skarnites, without lithogeochemical analyses). In the latter, the apatite crystals are well developed (idiomorphic) and truncate foliation, indicating input of late metasomatic fluids or post metamorphism of orogenic evolution.

Isotopic analyzes of C and O performed on carbonates from TNIC marbles show positive excursions of $\delta^{13}\text{C}_{\text{V-PDB}}$ between +6.13 to +9.69%, with most samples having a range of +6.13 to +7.36%, only two samples have values of +9.38% and 9.69% of $\delta^{13}\text{C}_{\text{V-PDB}}$, and negative $\delta^{13}\text{C}_{\text{V-PDB}}$ (-5.72) in squirrel. Concentrations of $\delta^{18}\text{O}_{\text{V-PDB}}$ range from -7.94 to -25.89%, while $\delta^{18}\text{O}_{\text{SMOW}}$ range from +16.96 to +22.67%, with one sample showing +4.18%. Those from RSC also show positive $\delta^{13}\text{C}_{\text{V-PDB}}$ excursions of +5.38 and 6.78%, with $\delta^{18}\text{O}_{\text{V-PDB}}$ concentrations of -8.29 and -11.96%.

Table 1

$\delta^{13}\text{C}$ and $\delta^{18}\text{O}$ ratios of marbles from the northeast of the São Francisco Craton. The SMOW values were calculated using the equation: $\delta^{18}\text{O}_{\text{SMOW}} = 1.03091 \times \delta^{18}\text{O}_{\text{PDB}} + 30.91$.

| Reference | Region | Sample | Lithology | $\delta^{13}\text{C}_{\text{PDB}}\text{‰}$ | $\delta^{18}\text{O}_{\text{PDB}}\text{‰}$ | $\delta^{18}\text{O}_{\text{SMOW}}\text{‰}$ |
|--------------------------|-------------------------------|----------------------------|----------------------------------|--|--|---|
| This paper | Tanque Novo-Ipirá Complex | MM-TR-293 | Calcitic marble | + 6.52 | -13.48 | 16.96 |
| | | MM-TR-299 | Calcitic marble | + 6.81 | -13.36 | 17.09 |
| | | MM-TR-275 | Dolomitic marble | + 9.38 | -15.89 | 14.53 |
| | | MM-TR-297 | Dolomitic marble | + 6.27 | -12.22 | 18.26 |
| | | MM-TR-302 | Dolomitic marble | + 6.13 | -12.73 | 17.73 |
| | | MM-TR-56A | Dolomitic marble | + 9.69 | -7.943 | 22.67 |
| | | MM-TR-69A | Dolomitic marble | + 7.36 | -10.69 | 19.84 |
| | | MM-TR-392 | Dolomitic marble - metasomatized | -5.72 | -18.38 | 11.91 |
| | | MM-TR-334 | Marble without chemical analysis | + 9.57 | -8.52 | 22.08 |
| | Rio Salitre Complex | MM-LR-64 | Marble | + 6.78 | -8.29 | 22.36 |
| MM-LR-378 | | Marble | + 5.38 | -11.96 | 18.58 | |
| Maheshwari et al. (2010) | Jacurici Valley | M2E 63-70 Ex 07 76 m | Marble | + 6.9 | -13.4 | 17.10 |
| | | M2E 63-70 Ex 07 72.8 m | Marble | + 5.8 | -13.8 | 16.68 |
| | | F5 14.90: C .77 289.2 m | Marble | + 2.2 | -16.3 | 14.11 |
| | Rio Itapicuru Greenstone Belt | RI-1 | Marble | + 8.4 | -13.1 | 17.41 |
| | | R1-2 | Marble | + 9 | -11.5 | 19.05 |
| | | R1-3 | Marble | + 5.5 | -14.3 | 16.17 |
| | | R1-4 | Marble | + 5.6 | -14 | 16.48 |

6. Discussion

6.1 Effect of diagenesis, metamorphism and preservation of TNIC, JV and RSC marbles

The geochemical and isotopic study to can demonstrate important evidences regarding the diagenetic and metamorphic processes in sedimentary rocks of Proterozoic age (Bau et al., 1999). Elements such as Mn, Sr, Fe, Ca and Mg are generally affected by post-depositional processes, and especially useful in the study of Proterozoic carbonates (Figure 3; Brand & Veizer, 1980; Veizer, 1983). The graph of the Ca/Mg ratio versus carbon and oxygen isotope values shows a low correlation (Figure 4a, b), indicating that TNIC carbonates consist of calcite and dolomite as main mineral phases and that the studied samples were weakly affected by diagenesis and metamorphism, as there is no change in the Ca/Mg ratio in relation to isotopic values (Mohanty et al., 2015).

The Mn/Sr ratio increases with decreasing $\delta^{13}\text{C}$ and $\delta^{18}\text{O}$ values because diagenesis of carbonate rocks leads to Mn enrichment and Sr depletion (Brand & Veizer, 1980; Veizer, 1983). The Mn/Sr and Fe/Sr ratios are relatively constant (Figure 4c, d and f). In graphs of Mn/Sr and Ca/Sr ratios versus $\delta^{13}\text{C}$ and $\delta^{18}\text{O}$ (Figs. 4 e - g), the results also show low correlations, implying limited effects of diagenesis and metamorphism.

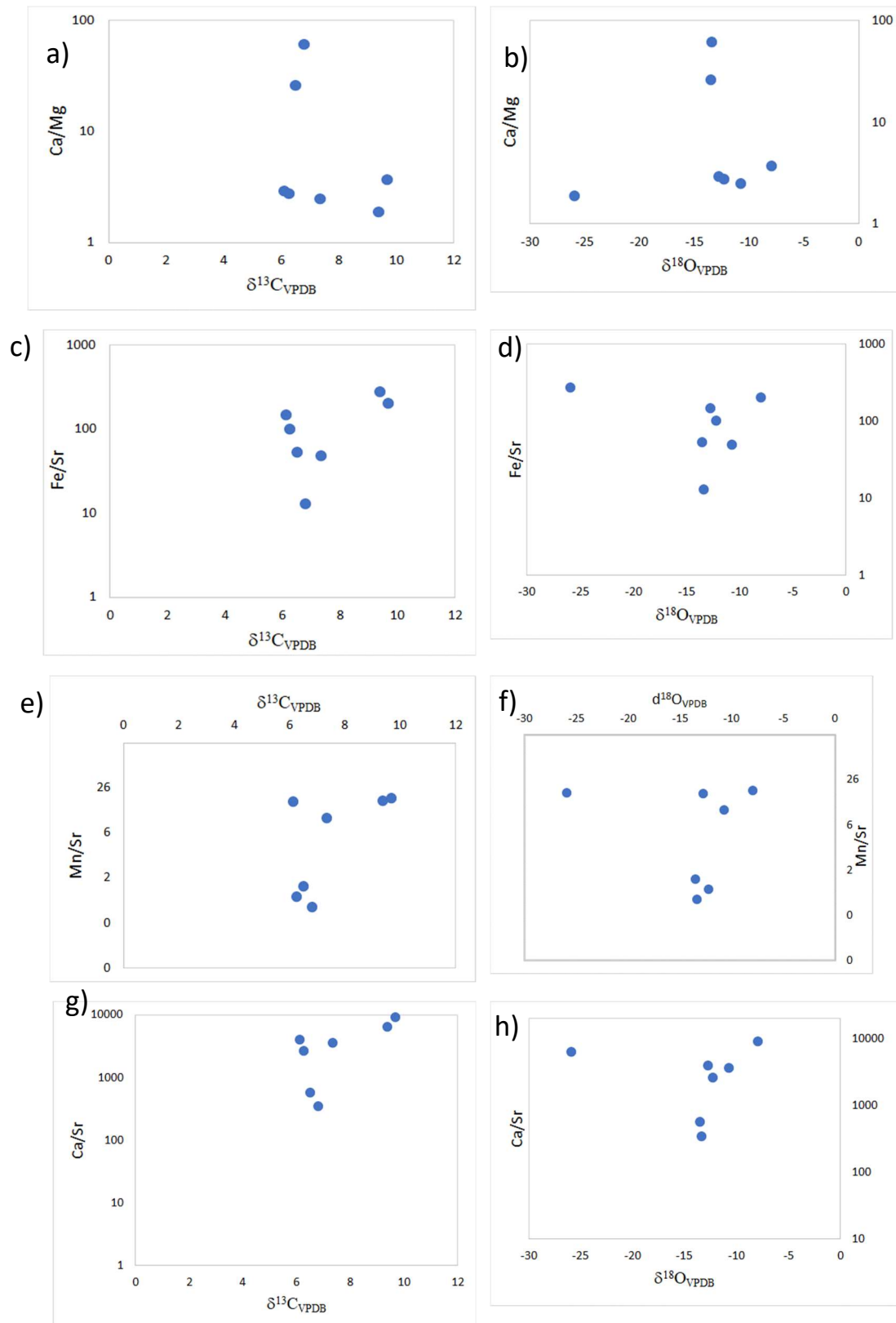


Fig. 4. Concentrations of trace elements versus isotopes of carbon and oxygen, such as (a) Ca/Mg versus $\delta^{13}\text{C}$; (b) Ca/Mg versus $\delta^{18}\text{O}$; (c) Ca/Sr versus $\delta^{13}\text{C}$; (d) Ca/Sr versus $\delta^{18}\text{O}$; (e) Mn/Sr versus $\delta^{13}\text{C}$; (f) Mn/Sr (g) Fe/Sr versus $\delta^{13}\text{C}$ and (h) Fe/Sr versus $\delta^{18}\text{O}$ to assess diagenetic and metamorphic effects.

Comparing data from the TNIC, JV and RSC marbles, these plot field of La anomaly and truly negative Ce anomalies. The La anomaly reflects its abundance in seawater and such an observation is also reported in ancient and recent marine sediments, as well as may come from hydrothermal fluids from mid-ocean ridges (Bau & Dulski, 1996, Planavsky et al., 2010).

The syn-depositional fluids associated with fumarole fluids are discarded by Ribeiro et al., (2021), Gama et al., (2021) and Oliveira (2016) for the interpretation of positive Eu anomalies, but they do not rule out the influence of post-depositional hydrothermal fluids.

Phosphate precipitation in the Paleoproterozoic paleobasin would have occurred under shallow, underoxygenated conditions, under the influence of detrital inflows. However, there is a greater interaction with sea water during the chemical precipitation of the apatite host rocks, as shown in figure 5a,b. At TNIC, samples with anomalous phosphorus exhibit Y/Ho ratios >30 and Ce/Ce* anomalies between 0.53 and 1.0, suggesting an environment ranging from suboxic to anoxic in the interstitial waters close to the water-sediment interface. However, in the RSC, Oliveira (2016) also presents mineralized pelitic rocks, originating from an anoxic environment, but here we will only discuss the carbonate sequence with phosphate, similar to the TNIC and JV environments.

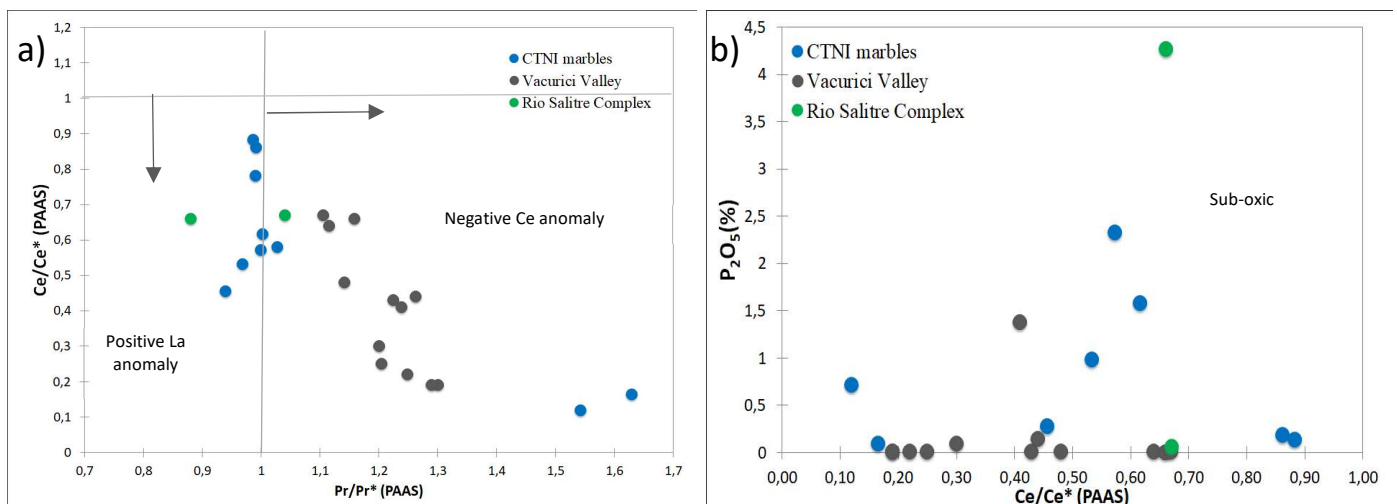


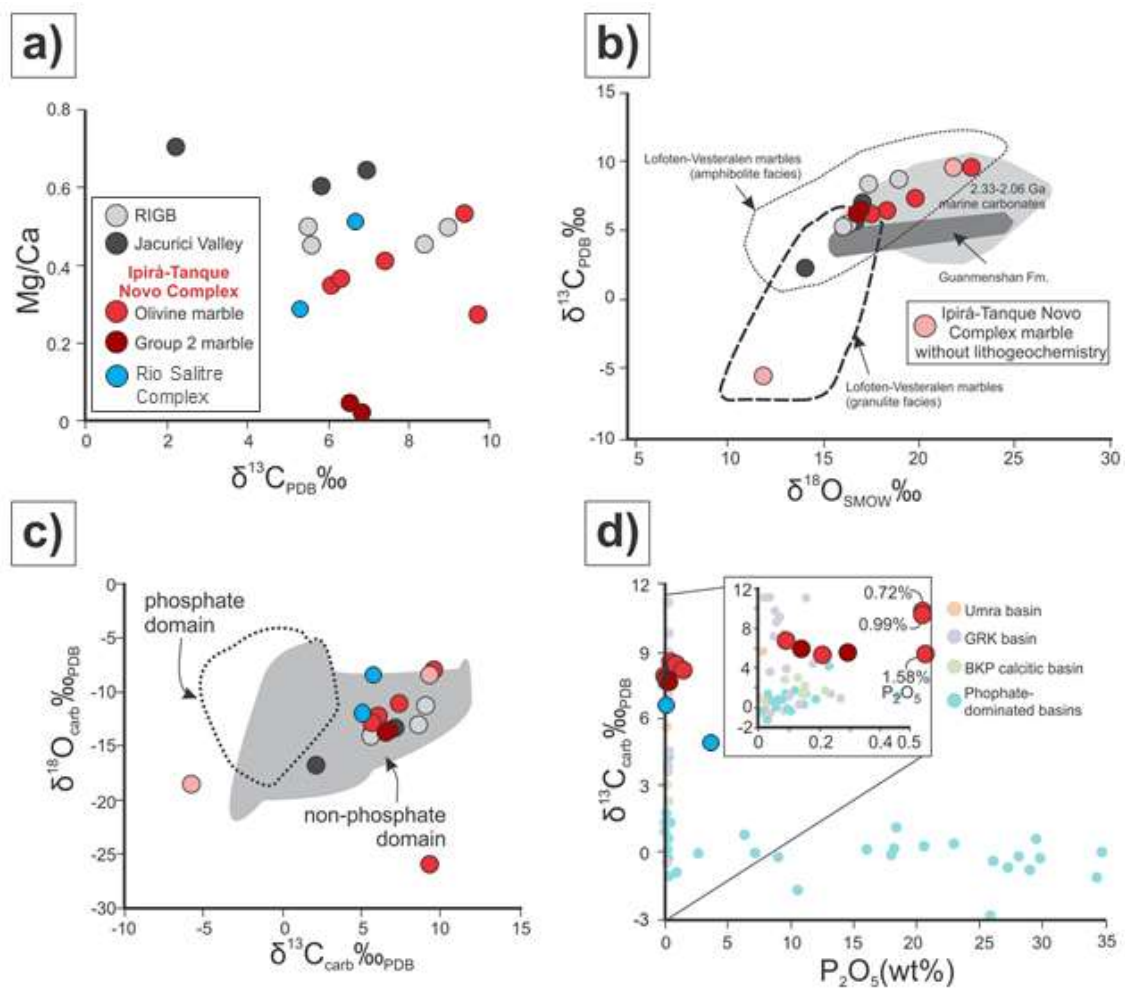
Fig 5. a) Behavior of rare earth elements in dolomitic and calcitic marbles from TNIC. B) PAAS-normalized diagram (Ce/Ce* vs. Pr/Pr*) indicating true negative Ce and positive La anomaly fields (Bau and Dulski 1996 modified by Webb and Kamber 2000); comparison of marine carbonate from Vale do Jacurici and RSC; PAAS: Post-Archaean Australian Shale. C) Y/Ho vs. P₂O₅ showing the highest phosphorus contents in marbles at TNIC and JV in a sub-oxic oceanic region. (Ce/Ce* concentrations normalized to PAAS below 1 ppm).

6.2 Stable isotope systematics of marbles

Considering the $\delta^{13}\text{C}$ and $\delta^{18}\text{O}$, the two marble samples in group 2 resulted in values compatible with each other: 6.52 and 6.81‰ of $\delta^{13}\text{C}_{\text{PDB}}$; -13.48 and -13.36‰ of $\delta^{18}\text{O}_{\text{PDB}}$. There are more samples (five in total), the dolomitic marbles (olivine marbles) provided a wider range of isotope ratios, with $\delta^{13}\text{C}_{\text{PDB}}$ values between 6.13 and 9.89‰ and $\delta^{18}\text{O}_{\text{PDB}}$ between -25.89 and -7, 94‰. The two samples without chemical analysis show contrasting results for the two isotopes, with

ratios of -5.72 (skarnite) and 9.57‰ (Group 1 dolomitic marble) for $\delta^{13}\text{C}_{\text{PDB}}$ and -18.38 and -8.52‰ for $\delta^{18}\text{O}_{\text{PDB}}$.

In addition to the variation in C and O isotopes, the analyzed marbles also have different chemical compositions. Marble samples from group 2 (calcitic marbles) have much lower Mg/Ca ratios, in addition to a more restricted isotopic variation, when compared to olivine-marbles samples (dolomitic marbles) (Figure 6a). In this comparison, the olivine marble from the Tanque Novo-Ipirá Complex, present similar data to the RIGB and RSC samples and contrast with those from the Jacurici Valley, with lower $\delta^{13}\text{C}$ (Maheshwari et al., 2010).



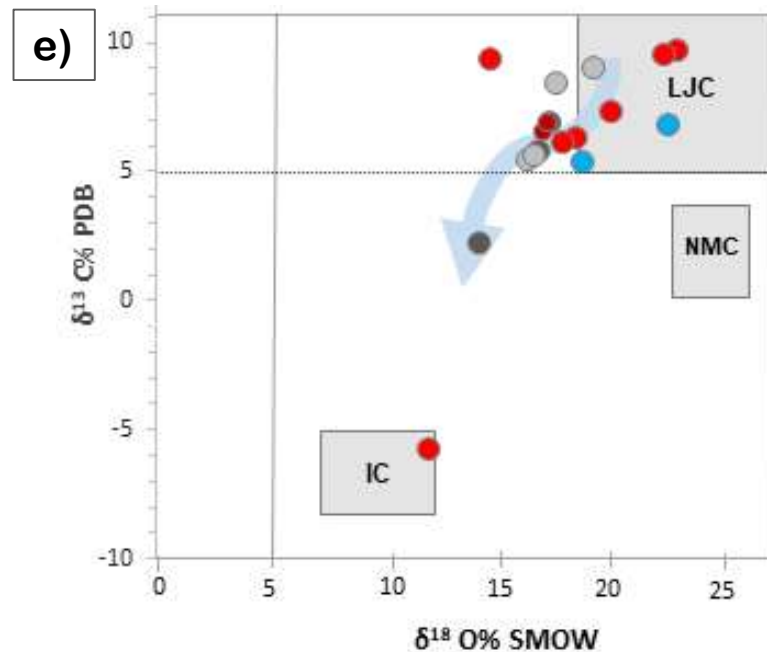


Fig 6. Stable isotope diagrams of C and O for samples of Paleoproterozoic marbles from the northern São Francisco Craton. Data from the Tanque Novo-Ipirá Complex produced by this research and from the Jacurici Valley and the RIGB by Maheshwari et al. (2010). a) Graph $\delta^{13}\text{C}_{\text{PDB}}\text{‰}$ versus Mg/Ca ratio. b) $\delta^{18}\text{O}_{\text{SMOW}}\text{‰}$ by $\delta^{13}\text{C}_{\text{PDB}}\text{‰}$ diagram with sample fields of Paleoproterozoic carbonates and metacarbonates (modified from Tang et al., 2013). c) $\delta^{13}\text{C}_{\text{PDB}}\text{‰}$ x $\delta^{18}\text{O}_{\text{PDB}}\text{‰}$ plot of samples of carbonates from domains with and without phosphate (modified from Papineau et al., 2013). D) P_2O_5 diagram (wt%) by $\delta^{13}\text{C}_{\text{PDB}}\text{‰}$ with samples of Paleoproterozoic carbonates from basins with and without phosphate (according to Papineau et al., 2013). E) D-Values of $\delta^{18}\text{O}$ vs. $\delta^{13}\text{C}$. The boxes correspond to typical values of: Lomagundi-Jatuli carbonates (LJC, Martin et al., 2013), normal marine carbonates (NMC) and igneous calcites (IC), according to Bowman(1998), modified from Lajoinie et al, (2018).

The $\delta^{13}\text{C}_{\text{PDB}}$ and $\delta^{18}\text{O}_{\text{SMOW}}$ isotopic ratios of the northern SFC marbles resemble those observed in amphibolite facies marbles from Lofoten-Vesteralen, especially when intersecting marine carbonate values from 2.33 to 2.06 Ga (Figure 6 b; Tang et al., 2013). The marble sample without chemical analysis with anomalous (extremely low) values of $\delta^{13}\text{C}$ and $\delta^{18}\text{O}$ is correlated with marbles from the granulite facies of the same region.

Values plotted on a $\delta^{13}\text{C}_{\text{PDB}}$ vs. $\delta^{18}\text{O}_{\text{SMOW}}$ (Fig. 6 E) shows the evolution of the fluid in isotopic equilibrium with calcite and correlation of marbles from TNIC with carbonates from Lomagundi-Jatuli (LJC, Martin et al., 2013) and carbonates extracted from marbles metamorphosed in the amphibolite facies high to granulite from the Rio de La Plata Craton (Lajoinie et al., 2018, 2019). While the marbles with negative $\delta^{13}\text{C}$ are plotted in the field of igneous carbonates or outside the two fields, like the marble in the skar zone of the TNIC.

The correlation shows that the more positive values of $\delta^{13}\text{C}_{\text{PDB}}$ and $\delta^{18}\text{O}_{\text{SMOW}}$ that the SFC carbonates are associated with those deposited during the Lomagundi-Jatuli event. The evolution of the interaction of carbonates with hydrothermal fluids is evidenced with the reduction in ^{13}C values,

as occurs with carbonate extracted from skarnite zones, plotted on igneous carbonates (Fig. 6e). Thus, the most preserved marble samples show $\delta^{13}\text{C}$ similar to LJE carbonates, while the negative values of $\delta^{13}\text{C}$ and the simultaneous decrease of C and O may be due to metamorphism, accompanied by devolatilization of CO_2 or interaction with meteoric fluids at high temperatures. The first case is the probable one, due to the geological context in skarn zones, therefore, the removal of carbon and oxygen causes the values of $\delta^{13}\text{C}$ and $\delta^{18}\text{O}$ be reduced during the decarbonation process, the magnitude of this variation being dependent on the temperature and the form of CO_2 release (Chacko et al., 1991, Valley et al. 1986, Yuanlin et al., 2023).

6.3 Deposition Age of protoliths and paleogeography of the TNIC paleobasin

Comparing the isotopic data, especially the carbon ones, from the analyzed TNIC samples with geochronological studies and with the regional tectonic context, it is possible to establish some inferences regarding the genesis and evolution of the protoliths of these marbles. Next, discussions are presented involving, initially, the age of deposition of the protoliths, the Paleogeography of the TNIC and RSC basin, and implications for the geotectonic configuration and metallogenesis in the northeast of the São Francisco Craton.

6.3.1 Deposition Age

The nine marble samples analyzed by the TNIC, eight have high $\delta^{13}\text{C}$ ratios (between 6.13 and 9.69‰) and the two RSC samples also have positive excursions. Although some authors understand this set of metasedimentary lithotypes as being of Mesoarchean age (Barbosa et al., 2012 and cited references, Macedo et al., 2019), recent studies have shown that the deposition of protoliths occurred in the Paleoproterozoic (Ribeiro et al., 2021, Garcia et al., 2021, Oliveira, 2016).

In the context of this era, the isotopic signatures obtained are compatible with the global Great Oxygenation Event (GOE) and are referred to as Lomagundi-Jatuli isotopic excursion or Lomagundi-Jatuli event (Figure 10a; Melezhik et al., 1999, 2007; Maheshwari et al., 2010; Bekker and Holland, 2012; Papineau et al., 2013). The general context of the GOE follows the fragmentation of the first supercratons and, possibly, supercontinents (such as Kenorland), in a series of glaciations and deglaciations, which ended with the amalgamation of a supercontinent at the end of the Paleoproterozoic – Nuna, Atlântica, Columbia or the Block from Central Africa (Sial et al., 2015; Hasui, 2012; Teixeira et al., 2007; Garcia et al., 2021). This cycle of glaciations and deglaciations, with formation of iron formations (and less commonly of phosphorites), is one of the factors that results in the pattern of peaks and valleys of $\delta^{13}\text{C}$ observed in the Lomagundi-Jatuli excursion (Bekker and Holland, 2012). There are several proposals for curves for C isotopes around the GOE, which present modifications in terms of isotopic ratios, general duration of the event, number and duration

of peaks, which can generate multiple interpretations for the TNIC samples (Figure 7 b). These variations also imply different age estimates for the marbles studied here.

To estimate the deposition interval of carbonate protoliths in the TNIC, we used the confluence between the $\delta^{13}\text{C}$ ratios and the maximum age of deposition, estimated by Ribeiro et al. (2021) at 2.128 Ga. Considering all the works consulted, the age range would be restricted between 2.218 and 2.072 Ga (Figure 7b; Karhu and Holland, 1996; Melezhik et al., 1999; Maheshwari et al., 2012; Bekker and Holland, 2012; Ribeiro et al., 2021).

The analysis of the curves from each study highlights other possible ages for the marbles from the Tanque Novo-Ipirá Complex studied here. Melezhik et al. (1999), who superimposed their graph on that of Karhu and Holland (1996), propose a curve with four distinct $\delta^{13}\text{C}$ peaks above 6‰, two of them younger than 2.128 Ga. These curves are those that cover the largest time interval in the Paleoproterozoic. From this perspective, there would still be the possibility of coincidence with the youngest peak, between 1.920 and 1.882 Ga. This possibility, however, must be ruled out since the metamorphism peak of the North Itabuna-Salvador-Curaçá Orogen is estimated around 2.08 Ga (Leite, 2002 and Leite et al., 2009), with final collapse and exhumation events at 2.04 and 1.95 -1.92 Ga, respectively (Garcia et al., 2018).

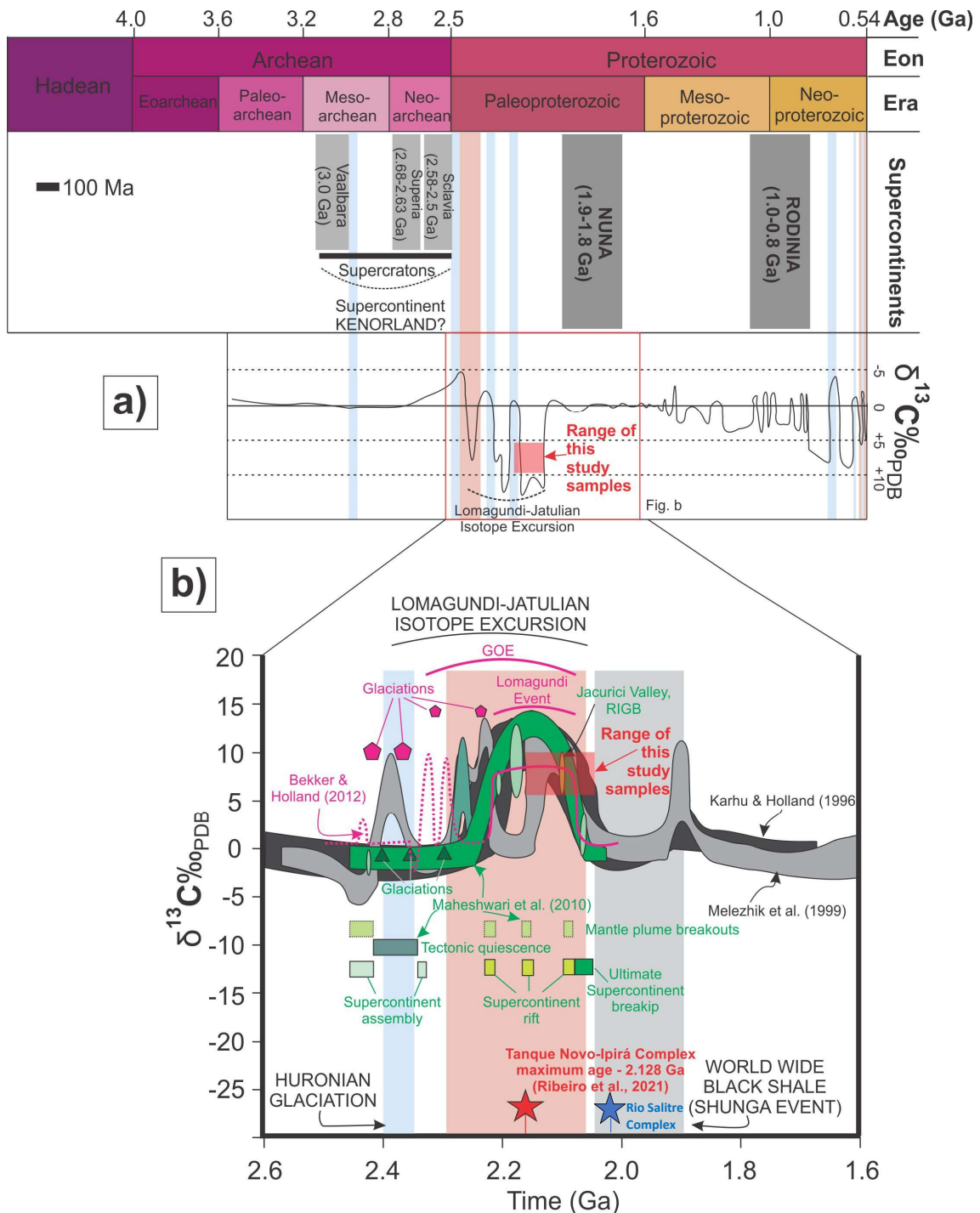


Fig. 7. Variation curves of $\delta^{13}\text{C}_{\text{PDB}}\text{‰}$ throughout Earth's history. a) Variation of $\delta^{13}\text{C}_{\text{PDB}}\text{‰}$ in the Precambrian, with emphasis on the position of the samples from the Tanque Novo-Ipirá Complex in the context of the Lomagundi-Jatuli isotopic excursion (Sial et al., 2015). There are data on glaciations (blue), global oxygenation events (red) and the formation of supercontinents (gray). b) Samples from the Tanque Novo-Ipirá Complex in the context of the global variation of $\delta^{13}\text{C}_{\text{PDB}}\text{‰}$ of sedimentary and diagenetic carbonates throughout the Paleoproterozoic, according to Melezhik et al. (1999), comparing with the curve of Karhu and Holland (1996). It contains data on global events of redbed formation (red), black shales (grey) and glaciation (blue). The curve and glaciations proposed by Bekker and Holland (2012) and the curve, superplume events, merger and fission of supercontinents, according to Maheshwari et al. (2010). The latest authors also contain data on Paleoproterozoic marbles, including those from the north of the SFC (Jacurici Valley and RIGB). The age range of samples from the Tanque Novo-Ipirá and Rio Salitre Complex were determined determined by combining $\delta^{13}\text{C}$ signatures and the maximum deposition age proposed by Ribeiro et al. (2021) and Garcia et al., (2021).

Still from the perspective of Melezhik et al. (1999), it is possible to consider that the oldest and most probable age interval (2.128-2.074 Ga) corresponds to the end of the GOE and the Lomagundi-Jatuli event, in addition to preceding the Schunga event, responsible for the global deposition of a level of black shale between 2.046 and 1.896 Ga. Câmara (2021) studied graphite-rich rocks at TNIC, in the same region of the study area, and proposed that the origin of these lithotypes would be linked to the increase in organic paleoproductivity that followed the GOE. However, it should be noted that the organic matter deposition event in the north of the SFC must be older, possibly overlapping with the beginning of the Schunga event, considering the estimated ages for the metamorphism of the region.

The carbon isotope curves for the Paleoproterozoic proposed by other authors are encompassed in a more restricted temporal interval, between about 2.4 and 2.0 Ga. According to values compiled by Bekker and Holland (2012), the results from the TNIC samples correspond to ages up to 2.077 Ga. It should be noted, however, that the $\delta^{13}\text{C}$ values considered by the authors do not reach values as high as those of the present study, reaching up to 8.55‰. As part of the reconstruction of these authors, the TNIC marbles were deposited at the end of the Lomagundi and GOE events, after the fourth and last (2.228 Ga) of a series of glaciations that began at 2.42 Ga.

These age estimates are very close to those obtained by the curve of Maheshwari et al. (2010). Based on what the last authors propose, the TNIC marbles have 2.072 Ga, as the minimum age of deposition. In the same graph, the rocks from the Vale do Jacurici and the RIGB have their protolith deposition ages estimated at 2.098 Ga. According to the study's conclusions, the carbonate protoliths, which have isotopic signatures similar to those of the TNIC, were deposited at the end of the Lomagundi event, which began after a series of three glaciations (2.4, 2.352 and 2.297Ga).

Maheshwari et al. (2010) also present a series of information on the global tectonic framework at this point in the Paleoproterozoic. Here, data on mantle plume events, tectonic quiescence, agglutination and fragmentation of supercontinents were highlighted (Figure 7 b). By comparing them with the signatures of samples from the north of the São Francisco Craton, it is possible to infer that they were deposited in the context of the last of three supercontinental breaks associated with mantle plumes in the Paleoproterozoic.

It should be noted that a marble sample without chemical analysis showed a negative $\delta^{13}\text{C}$ ratio (-5.72‰). This value is compatible, among the graphs analyzed, only with signatures of around 2.44 Ga, according to the curve proposed by Melezhik et al. (1999). However, this explanation is less plausible than the negative reason being explained by the metamorphism of the granulite facies that affected the sample (Figure 6b; Tang et al., 2013).

Considering the isotopic curve of Maheshwari et al. (2010), the ages obtained between 2.2 and 2.02 Ga (Oliveira, 2016 and Garcia et al., 2021) and the ^{13}C excursions between approximately 5 – 6%, the minimum deposition age would be prior to the Shunga Event and concordant with the formation period of the TNIC protoliths, around 2.068 Ga.

In the Jacurici Valley, in the Ipueira-Medrado terrain, Gama et al. (2021) obtained the minimum age of deposition is defined by the intrusive relationship of the Itiúba Sienite and the Vale do Jacurici Mafic-ultramafic Complex that intrude the supracrustals. The Itiúba syenite of 2084 ± 9 Ma (U/Pb – SHRIMP, Oliveira et al., 2004) and the peridotite-noritic Complex containing 2099 ± 6 Ma chromite (U/Pb – SHRIMP, Dias et al., 2022) that intrude the supracrustal succession. These authors suggest a Paleoproterozoic age for the succession of the JV.

6.3.2 Paleogeography of the TNIC paleobasin and implications for geotectonic configuration and metallogenesis in the northern São Francisco Craton.

Recent studies demonstrate that the protoliths of marbles, calcisilicates and phosphorites from the northern units of the São Francisco Craton were deposited in the Paleoproterozoic, in shallow to deep marine environments (Maheshwari et al., 2010; Oliveira, 2016; Ribeiro, 2017; Ribeiro et al., 2021; Gama et al., 2021). The largest metasedimentary unit among these, the Tanque Novo-Ipirá Complex extends to the extreme north of the Itabuna-Salvador-Curaçá orogen, outcropping along the Curaçá Valley in the form of paragneisses, calcisilicates, marbles and diopsidites (Kosin et al., 2003; Garcia et al., 2018).

Considering the current configuration, it is possible to deduce that the Tanque Novo-Ipirá Complex was deposited in a sea that extended throughout the Itabuna-Salvador-Curaçá North Orogen, bordered by Archean gneisses and Paleoproterozoic meta-volcanosedimentary sequences, among them the Saúde Complex, also of Paleoproterozoic age (2.06 and 2. Ga to 2.50 and 2.68 Ga, Zincone et al., 2017). It is considered here that it was a sea, since there is no evidence of the formation of Paleoproterozoic oceanic crust in the north of the SFC (Barbosa et al., 2012), however, this hypothesis cannot be discarded, requiring more detailed studies. However, due to the shortening resulting from the Paleoproterozoic orogeny, it is not possible to measure the extent of this paleobasin.

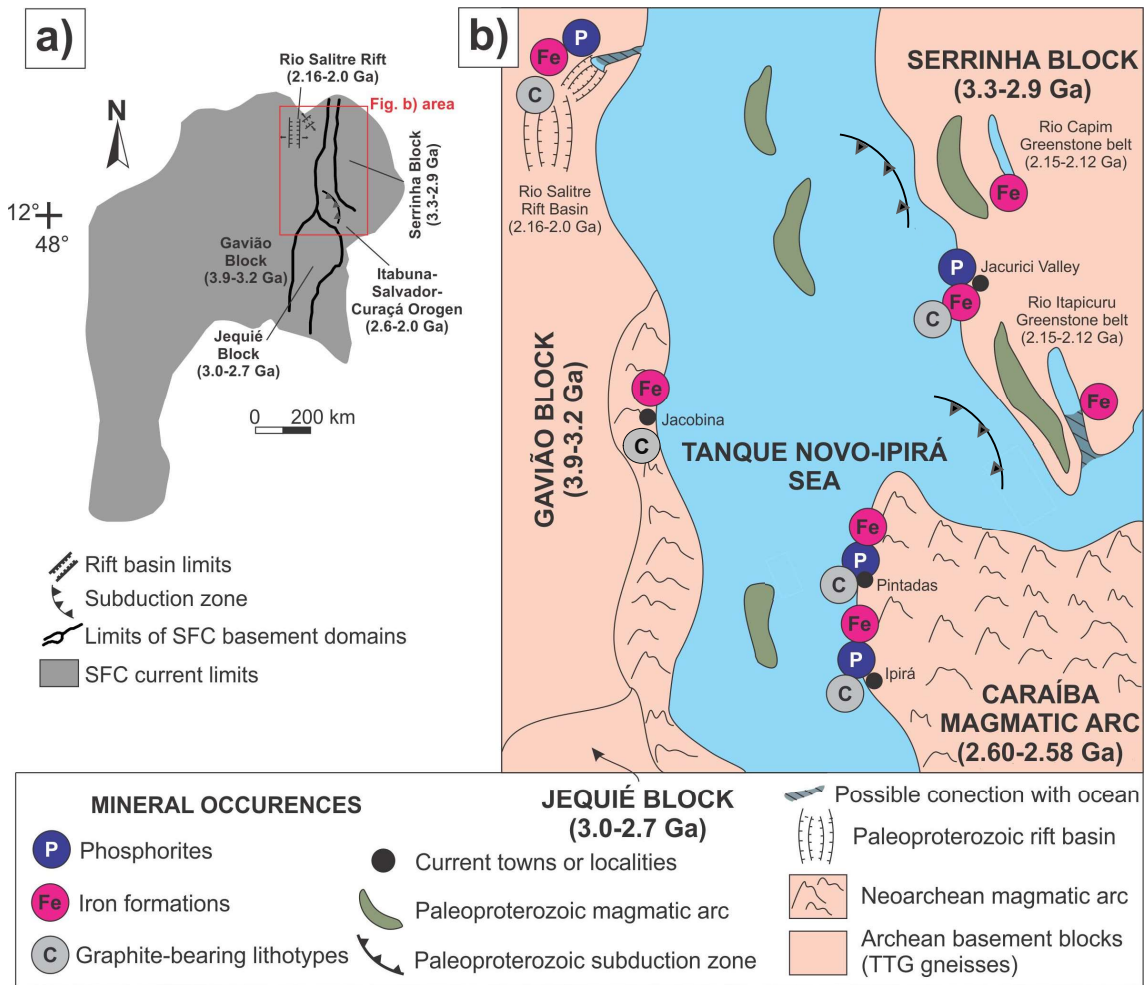


Fig 8. Reconstitution of the tectonic context of the protoliths of the Paleoproterozoic marbles from the north of the São Francisco Craton. a) Current tectonic boundaries of the São Francisco Craton, with emphasis to the north of the Itabuna Salvador Curaçá Orogen and adjacent terrains (modified from Garcia et al., 2021). b) Proposal for the paleogeographic reconstitution of the deposition environment of the protoliths of the Paleoproterozoic marbles from the north of the SFC, with emphasis on the Tanque-Novo Ipirá Mar, between 2.15 and 2.02 Ga. Occurrences of phosphorites, iron formations and rocks with graphite are contextualized. Age information extracted from Oliveira et al. (2004a,b), Barbosa et al. (2012), Oliveira (2016), Garcia et al. (2018, 2021) and Ribeiro et al. (2021).

According to Zhang et al., (2017 and citation present therein), the relationship between geochemistry of carbonate rocks and tectonic plates provide criteria for the recognition of tectonic environments. This fact becomes interesting in a complex tectonic context, such as the formation of Orogens, which involves subduction, shortening and stripping and, where the primary information about the stratigraphy may have been obscured, or with primary textures obliterated by the intense deformation during the formation of metamorphosed carbonates (eg Tarduno et al., 1985; Zhang et al. 2014, Satish-Kumar et al., 2021).

Based on this, when correlated Ce/Ce^* anomalies with $(Pr/Yb)_{SN}$ ($Pr/Tb)_{SN}$ and $(Tb/Yb)_{SN}$ ratios in TNIC and JV marbles are plotted in two fields related to open sea and continental margin (Figures 9a–c). Therefore, it is possible that deposition occurred on the continental margins of a paleo ocean and in the open sea with continental inputs, coming from continental margins or magmatic arcs. Such a geotectonic configuration was also demonstrated by Zhang et al., (2017) and Satish-Kumar et al., (2021). Thus, if there is continental input from magmatic arcs, the carbonates were formed in periods of tectonic and volcanic quiescence. Carbonates develop best in passive margins that favor chemical activity, whether allochemical or biochemical.

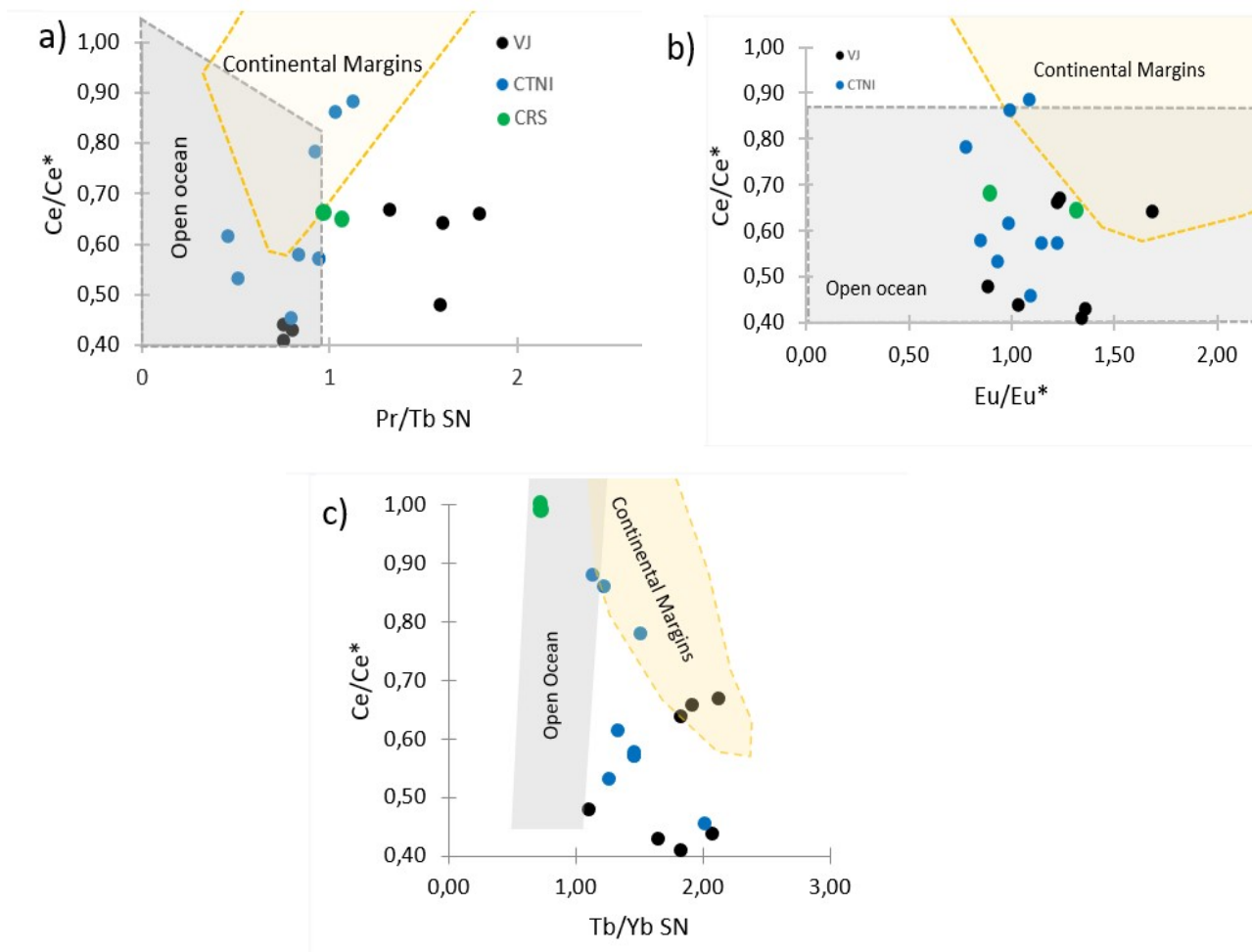


Figura 9- Plots of various proportions of rare earth elements in TNIC metacarbonate rocks. a) Graph Ce/Ce^* vs. normalized shale (Pr/Tb) showing the LREE distribution in terms of a Ce anomaly. b) Cross plot Ce/Ce^* vs. Eu/Eu^* with samples associated with an open sea and continental margin environment. c) Ce/Ce^* vs. Shale normalized graph (Tb/Yb) showing variations in HREE contents in relation to Ce anomalies. The areas marked as continental margins and open ocean are from Zhang et al., (2017), later reproduced by Satish-Kumar et al., (2021).

The Tanque Novo-Ipirá sea presents several granitoids of paleoproterozoic age, syn to post tectonics in the Curaçá Valley, such as Riacho da Onça (Sobrinho et al., 2015; Garcia et al., 2018), in the central and southern sector of the Orogen as Itiúba syenite, São Félix, Santanópolis, Bravo

granite, Capela de Alto Alegre monzonite (Barbosa et al., 2008, Oliveira et al., 2010, Melo, 1991, Conceição, 1993) and 2.1 Ga detrital zircons found in quartzites from the TNIC (Ribeiro et al., 2021) that demonstrate the existence of fragments of Paleoproterozoic magmatic arcs in the TNIC. These geological and geochronological data corroborate the paleogeographic model suggested by the geochemical correlations. Other magmatic arcs are associated with the Serrinha Block, in which the protoliths of the metasedimentary rocks of the southwest margin of this Block are associated with the Greenstone Belt of the Itapicuru River, which was deposited in a Paleoproterozoic back-arc basin (Silva, 1992), as well as the Capim River, its correlate more metamorphized (Oliveira et al. 2004a,b).

On the geotectonic reconstitution of the area, the unit that records the Neoproterozoic tectonic cycle in the northern OISC is the Caraíba Complex, which includes 2.6 Ga magmatic arc orthogneisses and 2.58 Ga ultramafic intrusions (Kosin et al., 2003; Oliveira et al., 2004a; Garcia et al., 2018). Observing the current configuration, with domains interspersed between this unit and the metacarbonates, it is possible to infer that, in the region of Pintadas and Ipirá, the Tanque-Novo Ipirá sea was deposited amidst the orthogneisses of the Caraíba arc, rifted in the Paleoproterozoic. This deduction is corroborated by the presence of zircons with ages compatible with those of the Caraíba Complex in the TNIC (Ribeiro et al., 2021). There is a consensus that the Neoproterozoic Caraíba Arc collided from Gavião and Serrinha block during the Paleoproterozoic (Barbosa and Sabaté 2002), however there are many discussions about the direction of subduction.

Further north, in the Jacurici Valley and in the Rio Salitre rift, the supracrustal sequences were deposited on gneisses of the Archean block that make up, together with the OISC, the high-grade metamorphic basement of the CSF (Barbosa et al., 2012).

The paleogeographic model proposed here, according to the references consulted, points to the existence of occurrences of rocks rich in phosphate, graphite and iron formations on the eastern margin of the Tanque-Novo Ipirá paleo-ocean (Figure 8). Phosphate and iron depositions are associated, as a record of moments with greater oxygenation and biogenic activity and are compatible with the paleoclimatic changes that occurred during the Lomagundi-Jatuli event. Lithotypes rich in organic carbon – protoliths of graphite-rich rocks, in contrast, tend to be deposited in low-oxygen environments.

The C-Fe-P association may indicate moments close to, but distinct from, the basin, or contemporary facies deposited at different depths. As proposed by Maheshwari et al. (2010) for the RIGB black shale-marble association, it is possible that the lithotypes with graphite from the TNIC and JV correspond to facies deposited in deeper environments during the Lomagundi-Jatuli event.

There is a possibility that the Tanque Novo-Ipirá paleo-ocean was connected to the RIGB and the Rio Salitre rift, considering the similarities of the observed depositional and geochronological contexts. It is more likely that the connection occurred with the RIGB, based on the geochronological

proximity between the two sequences (RIGB – 2.15-2.12 Ga and TNIC – 2.128 and 2.08 Ga). Although the Rio Salitre rift has its evolution considered between 2.2 and 2.0 Ga, the deposition of the chemical sedimentary unit is estimated at 2.02 Ga (Oliveira, 2016; Garcia et al., 2021). However, this weighting is based on an age with a high error (2021 ± 96 Ma), which leaves open the possibility of an older deposition for the upper unit of the Rio Salitre Complex. Therefore, it is possible to assume that the rocks analyzed here, with ages estimated between 2.16 and 2.08 (considering the peak of OISC Norte metamorphism) are the diachronic and youngest representatives of the phosphogenesis recorded in the Rio Salitre rift.

6.4 Correlations with Paleoproterozoic world basins, control of mineralization, and genetic implications between the LJE and Phosphogenesis.

In the Paleoproterozoic there are records of basins mineralized with phosphorus in several cratons worldwide. The best-known ones stand out, such as deposits and/or occurrences in Russia, China, North America, Finland, North Korea, Africa and India. The largest reserves are found in: Sinpkhup, Singpung and Yongby, North Korea estimated at 100Mt of P_2O_5 , Jhamarkotra Formation, Aravalli Supergroup in India, with 70Mt, Russia with 50Mt and in Finland the Jatuli Formation of 50Mt also hosted in marbles and gneisses graffiti (Banerjee 1999, Papineau, 2010, Pufahl & Groat, 2017). There is only one deposit in Brazil with a measured reserve of 660,000t in the RSC (Leite, 1983).

There are few studies on the South American platform that indicate the scope of Paleoproterozoic phosphogenesis in South America. However, there is evidence of phosphorus in the Amazon Craton (Paleoproterozoic Guiana Shield) associated with the Bakhuis Granulitic Belt (BGC) and in the Rio de La Plata Craton, in Pedra Alta Terrano (Fig.10). In the CGB, mineralization is related to calcisilicate granulites and P_2O_5 abundances are above 14.4 wt% (Patendie et al., 2019). According to Keersemaaker (2020), the apatite lenses are probably metamorphic sedimentary phosphorites. In the Rio de La Plata Craton, in the Paso Severino Formation, P_2O_5 levels reach 2% in carbonate breccias, with positive ^{13}C values of +3.5 to +11.6‰ V-PDB (Maheshwari et al, 2010, Oyhantcabal et al, 2011) and deposition age estimated by Santos et al., (2003) of 2146 ± 7 Ma (U-Pb SHRIMP).

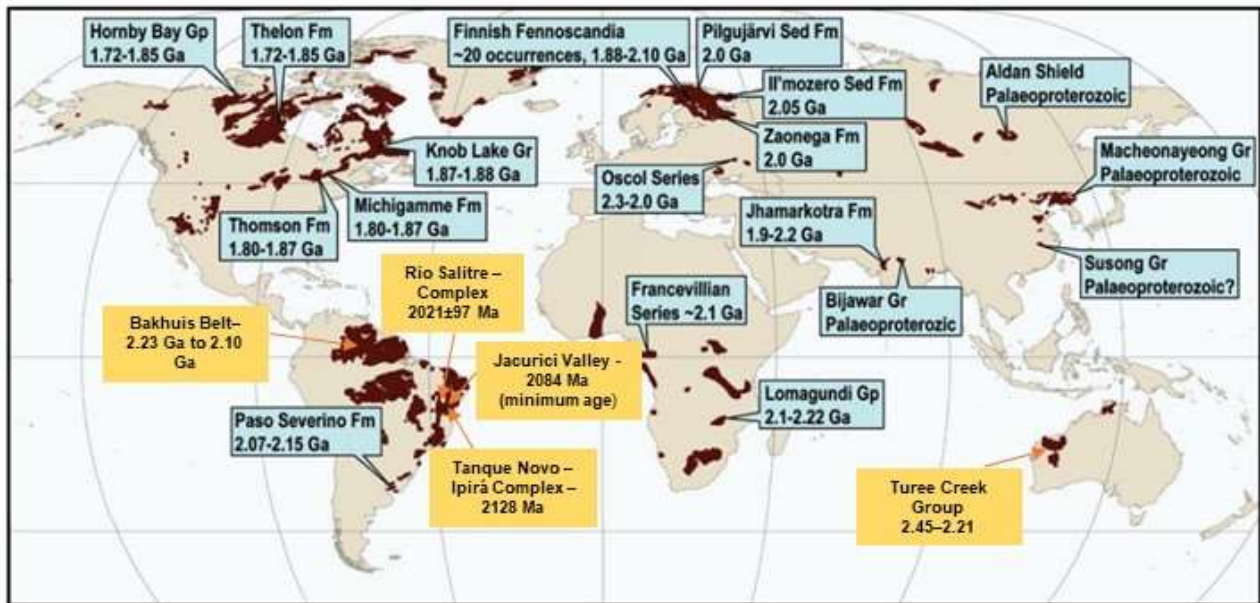


Fig 10. Distribution of phosphate mineralization in Paleoproterozoic basins worldwide. Highlighting new occurrences on the South American platform such as the Rio Salitre Complex, Jacurici Valley, Tanque Novo – Ipirá Complex and Bakhuis Belt, in the Amazon and São Francisco Cratons. Modified from Lepland et al., (2013).

Based on isotopic and geochronological data, it is estimated that there is a temporal correlation in the mineralizing event between the São Francisco, Rio de La Plata and Amazonian cratons on the South American platform. The carbonates of the Paso Severino Formation were deposited in the middle of the Lomagundi-Jatuli excursion, while those of the TNIC, JV, RSC and RIGB were deposited at the end. As for the BGC carbonates, there are no data available on the C and O isotopes, but the ages suggest that they belong to the same event.

When we compare the carbon and oxygen isotopic ratios of the paleoproterozoic basins of the Aravalli Group, the high $\delta^{13}\text{C}$ values constitute the main distinction between samples from the São Francisco Craton and those collected in phosphate-rich domains. The same diagnosis can be reached when comparing $\delta^{13}\text{C}$ ratios with P_2O_5 contents: the TNIC, RSC and JV samples analyzed here are not compatible with those from phosphate-dominated basins (Figure 6c; Papineau et al., 2013). Three samples of marble olivine have P_2O_5 contents above 0.5%, therefore they do not appear in the detailed graph. These samples present results of $\delta^{13}\text{C}_{\text{PDB}}$, $\delta^{18}\text{O}_{\text{PDB}}$ and P_2O_5 , respectively, of 9.69‰, -7.943‰, 0.72%; 9.38‰, 25.89‰, 0.99%; 6.13‰, -12.73‰, 1.58%. In the RSC, a sample presents P_2O_5 levels of 4.5% and $\delta^{13}\text{C}_{\text{PDB}}$ of 5.38‰.

Thus, Papineau et al. (2013) concluded that the host basins of phosphate deposits in the lower Aravalli Group have carbonates with $\delta^{13}\text{C}$ close to zero. On the other hand, basins without known phosphate deposits (Umra, GRK and BKP) also in the same Aravalli Sea show positive $\delta^{13}\text{C}$ excursions, with values up to 11.2‰. Although the Aravalli Group carbonates with positive $\delta^{13}\text{C}$ excursions are not

mineralized, it is not possible to rule out a temporal relationship and the possibility of a genetic relationship between LJE and phosphogenesis. Therefore, to better understand the subject, a survey of the geological profiles of several basins with phosphate occurrence and positive $\delta^{13}\text{C}$ excursions was carried out, presented in table 2.

In the LJE period there are 3 distinct moments in which there is an intimate temporal relationship with mineralization in shallow environments, namely at the beginning (2.26 - 2.200 Ga), middle (2146 - 2128 Ma) and at the end (2021 Ma - 1087 Ma) .) and 2 distinct moments associated with deposition in deep environments: in the middle (2146 Ma – 2.22Ga) and final (2051 Ma – 1.98 Ga).

Regardless of the depositional environment, there is a possible genetic relationship between Paleoproterozoic phosphogenesis and the LJE. Hodgskiss et al., (2023) discuss whether the cause of LJE is global or local, there are several models that try to explain, including the canonical ones (Bekker and Holland, 2012), changes associated with C recycling (Eguchi et al., 2020, 2022), methanogenesis in the sediment column (Birgel et al., 2015) and facies-dependent (Melenzki, 1999 and Prave et al., 2022).

According to Holland (2006) and Bekker and Holland, (2012), in the canonical model, the increase in phosphate availability would be caused by weathering and decomposition of pyrite during the GOE, which resulted in an increase in the flow of P into the interior of the oceans, and consequent increase in cyanobacterial activity and accumulation of organic matter.

Furthermore, Lepland et al, (2013) and Papineu (2010) demonstrate that phosphogenesis is not restricted to the oxic-suboxic zone, but also occurs in a reductive/sulfidic diagenetic environment of sediments rich in organic matter, where a variety of microorganisms , including sulfate-reducing and sulfide-oxidizing bacteria, decompose organic matter and control the absorption and release of phosphate (Burnett 1977; Schulz and Schulz 2005; Bailey et al. 2007; Arning et al. 2009; Tribovillard et al. 2010) . When phosphorus remains buried in facies rich in organic matter, these constitute the main host group.

The cause of the efficiency of the burial of organic matter is still under debate, however (Playter et al., 2017 and Hao et al., 2022) emphasizes the contribution of clay minerals, with sealing power in preserving organic matter in an oxygenated environment. Once this organic matter was preserved in the anoxide sediments, the metabolic action of microorganisms used the ^{12}C carbon isotopes in biological processes and released the heavier ^{13}C isotopes into the water, which were precipitated in the seawater, often together with the phosphorus that was remineralized during diagenesis. (Follmi, 1996; Ruttenger and Dyrman, 2005; Coleman et al., 2005).

That phosphorus that was remineralized in marine waters, and can even reach shallower levels, which, when saturated in porous waters, can precipitate as Carbonate-fluorapatite in the more proximal lithofacies, as carbonates.

The phosphogenesis recorded in these carbonate sequences would have occurred in a coastal environment associated with the marine platform, under the influence of continental waters. Therefore, during the LJE it was possible to deposit phosphate associated with shallow facies such as carbonates and siliciclasts.

Nelson et al., (2010) demonstrates that phosphate precipitation would occur in the oxic-suboxic zones of the paleocean. Furthermore, the phosphogenesis recorded in marbles and calcisilicate rocks, associated with graphite-schists and iron formations in CTNI, VJ and CRS would have occurred in a coastal environment associated with a marine platform, under the influence of continental waters, consistent with a model-dependent facies de Prave et al., (2022), which associates the LJE with local events.

Therefore, the association of these mineralized lithofacies with graphite from the metamorphism of sediments rich in organic matter (Ribeiro, 2016, Câmara, 2021, Jardim de Sá, 1983, Marinho et al., 1986) and BIFS, may indicate this increase in organic matter paleoproductivity in the northeast of the SFC, during lithofacies deposition in the LJE. It is also known that there are extensive Paleoproterozoic graphite deposits in the North and South China Cratons and other parts of the world, indicating that globally the burial of ^{12}C -enriched organic carbon has resulted in the global enrichment of ^{13}C in atmospheric and oceanic CO_2 , which is recorded in marine carbonate rocks from this period (Li et al., 2022).

In this sense, the combination of some factors such as the entry of detrital sediments into the paleobasin containing P and Fe, but mainly the presence of graphite from a sedimentary protolith rich in organic matter, are possibly responsible for the enrichment of phosphorus in the SFC. This fact may explain the absence of other occurrences of phosphorus in other places in the São Francisco Craton where there is no occurrence of graphite.

Furthermore, the higher concentrations of phosphorus in the supracrustal rocks of the RSC may have been a consequence of the greater primary productivity and high oxygenation rates in this sector, since the Salitre rift is smaller in extension when compared to the Tanque Novo – Ipirá paleobasin. He suggested that this fact facilitated cyanobacterial activity on a smaller, restricted platform in the Salitre rift.

It is observed that although the first appearance of phosphorite during the Paleoproterozoic was at the beginning of the ^{13}C excursion, the most frequent and economically important deposits are found at the end of the excursion. This fact may be related to a higher rate of burial of organic matter at the end of the Lomagundi excursion and, relatively, to a greater release of phosphate.

After the end of the LJE, reappearance of sedimentary phosphate mineralization occur in the Neoproterozoic, during and after excursions of positive carbon isotopes in seawater composition, similar to Paleoproterozoic phosphogenesis, Neoproterozoic phosphorites appear after glaciations in association with a greater oxygenation rate in the atmosphere-ocean system (Bekker & Holland, 2012), such as the Neoproterozoic phosphorites from the Irecê Basin in the São Francisco Craton (Misi et al., 2010, Misi et al., 2011, Sanches et al., 2007 , Sanches, 2012).

Table 2
Paleoproterozoic supracrustal rocks mineralized in phosphate and relationship with ¹³C.

| Geographic and geological location | Age constraints | Hosted rocks | Associated metasedimentary rocks | Phosphate occurrences | P ₂ O ₅ range (%) | Estimated P ₂ O ₅ reserve | Metamorphism | ¹³ C _{carb} variation (‰) | Conditions Paleoenvironment | References |
|--|---|---|--|---|---|---|--------------------------------|---|-----------------------------|--|
| <i>South America</i> | | | | | | | | | | |
| São Francisco Craton, Brazil. Salvador - Curaçá Orógen. North and South region Tanque Novo - Ipirá Complex. | 2128 Ma zircon U/Pb – LA-ICPMS | Dolomitic marbles, Calcisilicate rocks (diopsidites and gneiss) | Metapsamites, banded iron formation ferruginous quartzites ferruginosos, grafite schists, aluminous gneiss, quartzites | Fluorapatite | 0.7 - 3.2 | -- | High Amphibloite to granulite | +6,13 to +9,69 (This study) | Shallow marine | This paper, Ribeiro et al.,(2021), Ribeiro (2016), Kosin et al., (2001), Melo et al., (1991). |
| Salvador Curaçá Orogen. Ipueira – Medrado region Jacurici Valley. | 2084 Ma (minimum age) | Dolomitic marbles, Calcisilicate rocks (diopsidites, and gneiss) | Calcisilicate gneiss, iron formations, graphite-schists | Fluorapatite | 1.38 - 4.56 | -- | High Amphibloite to granulite | +5.8 to 6.9 | Shallow marine | Gama et al., (2021), Dias et al., (2022), Maheshwari et al., (2010), Silveira et al., (2015), Oliveira et al., (2004), Marques et al., (2003) Del Lama et al., (2001). |
| Gavião Block. Juazeiro region. Rio Salitre Complex. | 2021±97 Ma Sm/Nd in banded iron formation. 2161,1 ± 4 Ma U/Pb (SHRIMP) in rhyolite. | Calcisilicate rocks, marbles, grafite schist, phosphatic oolite, kyanite schist, quartzite. | Iron formations, ferruginous quartzites, quartzites, graphite-schists | Carbonate-fluorapatite in lenses or disseminated. Variscite, crandalite, augelite and cyrovilite in intraclasts, cement or crystalline microphosphorites. | 5.3 a 25 | 660.000 t | Low amphibolite to greenschist | +5.38 and 6.78 | Shallow and deep marine | Oliveira, (2016) e Garcia et al.,(2021). |
| Rio de La Plata Craton Uruguai. Formation Paso Severino / | 2146 ± 7 Ma U/Pb SIMS | Carbonate breccias | Dolomitic calcarenites, dolostones, | Phosphate matrix breccias | 2 | -- | Greenschist | +3,5 to +11,6 V-PDB | Deep marine | Santos et al., (2003) apud Martins et al., |

| | | | | | | | | | | |
|---|--|--|--|---|--------|--------|-------------------------------|-------------------|-------------------|--|
| São José Greenstone Belt | in dacite - rhyolite | | calcsilicate rocks | | | | | | | (2013),Maheshwari et al., (2010). |
| Amazônico Craton - Suriname. Bakhuis Granulite Belt | 2.23 Ga - 2.10 Ga in metapelites. 2.26 Ga in intermediate granulite | Paraderivative migmatitic and calcsilicate granulites | Metapelites, quartzites, greywacks | Fluorapatite lens, disseminated fluorapatite and lateritic crust containing wavellite | > 14.4 | -- | Granulite | No data available | No data available | Beunk et al., (2021), Keersemaker (2020), Kronenberg (2019), Patadien (2019), de Roever et al., (2019), de Roever et a.,l (2003), Dahlberg (1982, 1987). |
| <i>North America</i> | | | | | | | | | | |
| Michigamme Fm., Baraga Group, Michigan | 1.80-1.87 Ga | Cherty dolomite with pyrite and argillite beds | Argillite | Carbonate fluorapatite nodules, thin beds, and possibly stromatolites | 15 | -- | Greenschist | - 3.1 ± 0.9 | Shallow marine | Papineu (2010), Papineu et al., (2017), Martins et al., (2013). |
| <i>Russia</i> | | | | | | | | | | |
| Karelia Craton. Ludikovi Group, Zaonega Formation, Onega Basin, NW Russia | 1.98–2.06 Ga | Organic-rich greywacke with pyrite and stromatolitic dolomite with magnesite bands | Turbidite, cherts, banded iron formation | Phosphate nodules and clasts | -- | -- | Greenschist to amphibolite | - 6,13 to + 10 | Deep marine | Papineu (2010), Martins et al., (2013), Melezhik et al, (1999), Ojakangas etal., (2001). |
| Karelia Craton. Jatuli-type formations | 2.06–2.10 Ga | Carbonate marbles | Graphitic gneisses, skarn rocks, banded iron formation | Uraniferous phosphorite bands, lenses, and fine disseminations | 3–19 | >50 Mt | Greenschist to amphibolite | + 3,5 to + 17.2 | Shallow marine | Papineu (2010), Martins et al., (2013),Ojakangas etal., (2001). |
| Slyudyanka cristaline Complex, Siberia, Russia | 2200 Ma | Carbonates (dolomites) and skarn rocks, | Quartzites, shale, shale with graphite | Fluoroapatite beds | 1–20 | 50 Mt | High amphibolite to granulite | No data available | Shallow marine? | Yudin (1996), Bushinskii (1966) apud Papineu (2010), Reznitskii et |

| | | | | | | | | | | |
|---|--|--|--|---|-----------|----|-------------------------------|----------------------|---|--|
| | | sandstone rich phosphate | | | | | | | | al., (1998), Volkov et al., (1972). |
| Imandra/Varzuga Greenstone Belt, Il'mozero Sedimentary Formation, Kola Peninsula, Russia | 2051 Ma | Siltstones and Graywacke | Carbonates, limestones | Phosphate and calcite - bearing concretions | >1.2 | -- | Greenschist | - 0,83 to + 2.36% | Deep marine | Bekker et al., (2013), Martin et al., (2010), Lepland et al., (2013), Soomer et al., (2022), Martin et al., (2013). |
| Pechenga Greenstone Belt, Pilgularvi Sedimentary Formation, Kola Peninsula, Russia | 1922.8 ± 1.6 Ma and 1919.2 ± 1.3 Ma | Tuffitic schist, sandstones with graphite and sulfites, gritstones | -- | Carbonate-fluorapatite beds, lenses, small- scale channels, Carbonate fluorapatite nodules, concretions, stromatolites, and oolites | 2–11 | -- | Greenschist | No data available | Deltaic or deep- water continental slope turbidite | Lepland et al., (2013), Papineu (2010), Martin et al., (2015), Jossu et al., (2015b). |
| <i>Africa</i> | | | | | | | | | | |
| Zimbabwe Craton. Magondi Mobile Belt Upper Lomagundi/Piriwiri Group. | 2.1–2.22 Ga | Shales | Graphitic slates, banded iron formation, metapelites, Conglomerates, arkosic arenites, quartz arenites, stromatolitic dolomites | Phosphate beds. Collophanite (fluorapatite and quartz) | -- | -- | Greenschist to amphibolite | + 7.1 to + 11.9 | Deep marine | Papineu (2010), Master et al., (2010), Bekker et al., (2003), Bekker et al., (2001), Master (1991). |
| Gabon Franceville Basin. FB Formation, Francevillian Supergroup | ca. 2.0 Ga | Black shales, cherts, and Fe- Mn formation | Sandstones, siltstones | Apatite nodules with silicified rims | Up to 2.5 | -- | Greenschist | - 5.2 to + 6.5 | Shallow marine | Mossman et al. (2005), Papineu (2010), Martins et al., (2013), Ossa et al., (2013), Aubineau et al., (2018). |

| <i>Asia</i> | | | | | | | | | | |
|---|--------------|---|--|---|----------------|-----------|-------------|----------------------|--|---|
| Jhamarkotra Fm., Aravalli Supergroup, India | 1.9–2.2 Ga | Dolomite and ferruginous carbonate* | -- | Stromatolitic and amorphous carbonate fluorapatite | 10–37 | >65 Mt | | | | Banerjee (1971), Chauhan (1979) apud Papineu (2010). |
| Liuping Fm., Susong Group, China | 1.90–1.85 Ga | Dolomite, graphitic schist, and chert* | Graphitic bearing quartz mica schist, marbles | Phosphorite beds and lenses | 7–26 | -- | Amphibolite | No data available | Ocean current sediment ation | Longkang and Zhendong (1988), Papineu (2010), Wang et al., (2021). |
| <i>Australia</i> | | | | | | | | | | |
| Turee Creek Group, Kungarra and Kazput Formation | 2.45–2.21 | Dolomitic carbonates | Limestone, sandstone, shale/argilite | Stromatolitic, phosphatic peloids and clasts, apatite | 37.4 - 40.3 | -- | Greenschist | –2 to +1.5 | Shallow marine (interdita l zone) | Soares et al., (2019), Martindale et al., (2015), Martin et al., (2000), Thorne et al., (1991). |

7. Conclusions

The supracrustal rocks of the northeast of the São Francisco Craton in the areas of the Tanque Novo – Ipirá Complex, Jacurici Valley and Rio Salitre Complex are marbles, calcisilicate rocks, quartzites, graphite-schists, iron formations and aluminous gneisses. These lithofacies are derived from the regional metamorphism of carbonate, siliciclastic, carbonaceous and aluminous sediments, in different degrees (high amphibolite to granulite in the southern sector of the Craton and greenschist to low amphibolite in the northern sector, associado ao RSC).

The paleoenvironmental conditions of oxygenation are suggestive of the predominance of oxygenated environments, although several lithofacies from the 3 areas indicate a low oxygenated environment, according to true anomalies of Ce. The high content of P_2O_5 is verified in lithofacies deposited in a sub-oxic environment, with greater influences of sea water.

Phosphate mineralization in TNIC, RSC and JV is compatible with the model of shallow, peritidal deposition in association with burial of organic matter. While in the RSC, there are also hosts of aluminous and siliceous origin. The P-Fe-C association is an indicator of primary oceanic paleoproductivity in the Tanque Novo - Ipirá paleobasin, this association registers moments of greater oxygenation of the atmosphere and are correlated with the paleoclimatic changes that occurred during the Lomagundi-Jatuli event.

Due to the regional geological and geochronological context, it is possible that the JV carbonates were deposited in the same paleo-ocean of Tanque Novo – Ipirá, after the Paleoproterozoic collision, which resulted in the formation of the Salvador – Curaçá Orogen, it is suggested that these lithologies were placed on the Serrinha Block, in the well-known structure of the region in positive bloom. There is a possibility that the Tanque Novo-Ipirá paleo-ocean could be connected geographically and temporally to the RIGB paleo-ocean, in this way, the supracrustal rocks would have precipitated over the RIGB.

The Paleoproterozoic phosphogenetic event on a global scale includes phosphate mineralization of the NE SFC and can be correlated with other basins around the world. During this period, increased oxygenation, primary productivity and burial of organic matter enabled phosphorus precipitation in shallow and deep marine environments. CSF also demonstrates local oxygenation and ^{13}C enrichment events, suggesting a possible local and/or faciological control for phosphogenesis.

On the contrary the mineralized samples from the Aravalli Group, the samples analyzed here show a certain correlation between P_2O_5 levels and $\delta^{13}C$ ratios that suggest a genetic relationship between precipitated phosphates and positive $\delta^{13}C$ ratios. Furthermore, the coexistence of positive $\delta^{13}C$ excursion values in mineralized geological profiles in several basins of the same age corroborates the hypothesis of a genetic relationship between Paleoproterozoic phosphogenesis and the LJE.

The positive excursion of ^{13}C in South America is demonstrated in the northeastern portion of the basement of the São Francisco Craton (JV, RSC and TNIC) and in the Rio de La Plata Craton. Isotopic studies in the Suriname Craton are necessary in order to obtain a better confirmation of the LJE, although geological, geochemical and geochronological data of the host rocks of the mineralization prove an intrinsic relationship with the event on a global and/or local scale.

APPENDIX 1

| Sample | MM-TR-69A | MM-TR-275 | MM-TR-297 | MM-TR-302 | MM-KP-49 | MM-TR-56A | MM-TR-293 | MM-TR-299 | MM-KP-54 | MM-KP-72 | TAJ-18A | TAJ-22A | TAJ-24A | TAJ-25A | TAJ-38A | TAJ-51A | MI-01 | MI-07 | MPD-01 | MPD-02 | MPD-04 | MPD-05 | MM-TR-64 | MM-TR-378 | |
|------------------------------------|---|-----------|-----------|-----------|----------|-----------|-----------|-----------|----------|----------|-------------------------------------|---------|---------|---------|---------|---------|-------|--------|--------|--------|---------------------|--------|----------|-----------|------|
| | Tanque Novo - Ipirá Complex (Ribeiro et al., 2021 and this paper) | | | | | | | | | | Jacurici Valley (Gama et al., 2021) | | | | | | | | | | Rio Salitre Complex | | | | |
| SiO ₂ wt (%) | 10.95 | 11.13 | 12.12 | 11.01 | 12.99 | 9.5 | 21.21 | 14.05 | 6.29 | 11.77 | 17.25 | 19.01 | 14.11 | 11.89 | 16.47 | 15.64 | 12.29 | 16.33 | 8.72 | 12.52 | 14.88 | 9.81 | 8.39 | 35.15 | |
| TiO ₂ | <0.01 | 0.06 | 0.05 | 0.08 | 0.12 | 0.03 | 0.31 | 0.09 | 0.07 | 0.17 | <0.01 | 0.01 | <0.01 | 0.01 | 0.07 | 0.04 | 0.01 | <0.01 | 0.02 | <0.01 | <0.01 | <0.01 | <0.01 | 0.05 | 0.03 |
| Al ₂ O ₃ | 0.65 | 1.44 | 0.67 | 1.2 | 1.00 | 1.12 | 7.14 | 4.38 | 1.11 | 3.46 | 0.13 | 1.26 | 0.81 | 1.09 | 1.22 | 0.16 | 0.98 | 0.5 | 0.52 | 2.22 | 0.24 | 0.44 | 0.94 | 0.68 | |
| Fe ₂ O ₃ (t) | 0.48 | 1.24 | 1.24 | 1.36 | 0.96 | 0.85 | 3.85 | 1.54 | 0.75 | 1.62 | 1.5 | 1.6 | 0.81 | 0.9 | 1.07 | 0.62 | 1.18 | 0.72 | 0.7 | 0.97 | 0.56 | 0.62 | 0.52 | 0.77 | |
| MnO | 0.09 | 0.07 | <0.01 | 0.14 | 0.04 | 0.07 | 0.08 | 0.07 | 0.1 | 0.08 | 0.1 | 0.1 | 0.09 | 0.09 | 0.15 | 0.12 | 0.06 | 0.04 | 0.04 | 0.09 | 0.11 | 0.11 | 0.05 | 0.18 | |
| MgO | 16.88 | 18.04 | 13.95 | 15.00 | 17.65 | 12.38 | 1.84 | 0.79 | 21.17 | 1.75 | 27.98 | 24.93 | 18.99 | 16.78 | 16.61 | 19.02 | 14.31 | 15.75 | 19.64 | 20.3 | 21.46 | 18.7 | 19.2 | 25.45 | |
| CaO | 34.93 | 28.33 | 32.1 | 36.52 | 29.58 | 38.21 | 39.93 | 40.39 | 34.27 | 47.16 | 18.15 | 18.37 | 28.93 | 29.96 | 32.63 | 28.3 | 32.9 | 34.08 | 30.21 | 30.96 | 27.75 | 30.31 | 41.5 | 16.64 | |
| K ₂ O | 0.04 | 0.07 | 0.08 | 0.11 | 0.11 | 0.05 | 2.4 | 1.38 | 0.11 | 0.31 | 0.01 | 0.36 | <0.01 | 0.34 | 0.01 | <0.01 | 0.02 | <0.01 | <0.01 | <0.01 | 0.02 | <0.01 | <0.1 | 0.06 | |
| Na ₂ O | <0.01 | <0.01 | <0.01 | 0.11 | 0.12 | 0.02 | 0.2 | 0.07 | 0.09 | 0.91 | 0.02 | 0.08 | 0.02 | 0.03 | 0.11 | 0.02 | 0.03 | 0.02 | 0.01 | 0.02 | 0.06 | 0.03 | 0.01 | 0.03 | |
| P ₂ O ₅ | 0.1 | 0.28 | 0.99 | 1.58 | 2.33 | 0.72 | 0.14 | 0.19 | 0.24 | 0.12 | <0.01 | <0.01 | <0.01 | <0.01 | 0.14 | 1.38 | <0.01 | 0.09 | <0.01 | <0.01 | <0.01 | <0.01 | 0.157 | 4.27 | |
| LOI | 35.8 | 34.65 | 34.44 | 34.43 | 33.3 | 36.42 | 27.33 | 32.89 | 34.66 | 32.25 | 35.16 | 32.01 | 33.07 | 35.42 | 31.07 | 30.66 | 35.23 | 32.68 | 38.28 | 33.49 | 33.54 | 38.38 | 24 | 13.54 | |
| Sum | 99.92 | 95.31 | 95.64 | 101.54 | 94.9 | 99.37 | 104.43 | 95.84 | 98.86 | 99.6 | 100.3 | 97.73 | 96.83 | 96.51 | 99.55 | 95.96 | 97.01 | 100.21 | 98.14 | 100.57 | 98.62 | 98.4 | 94.8 | 96.8 | |
| Sr | 70.00 | 32.00 | 88.00 | 66.00 | 46.00 | 30.00 | 510.00 | 852.00 | 56 | 706 | 38 | 39 | 239 | 266 | 240 | 88 | 155 | 66 | 42 | 48 | 55 | 64 | 49 | 67 | |
| Y | 12.68 | 3.09 | 11.95 | 17.98 | 3.58 | 5.1 | 11.66 | 9.01 | 3.11 | 7.08 | 13.69 | 13.74 | 14.45 | 17.06 | 24.43 | 13.31 | 22.54 | 16.11 | 17.35 | 10.17 | 15.17 | 14.01 | 1.5 | 1.69 | |
| La | 39.00 | 16.3 | 19.6 | 12.00 | 9.7 | 51.9 | 29.5 | 22.5 | 8.3 | 19.00 | 20.1 | 15.5 | 23.6 | 25.7 | 20.1 | 10.2 | 27.5 | 17.2 | 13.2 | 15.5 | 14.7 | 11.5 | 4.5 | 7.2 | |
| Ce | 10.5 | 9.8 | 15.2 | 11.9 | 8.00 | 7.1 | 46.00 | 33.9 | 7.00 | 24.7 | 21.2 | 10.2 | 29.00 | 31.2 | 15.00 | 6.8 | 21.8 | 7.7 | 3.7 | 5.6 | 4.00 | 3.6 | 4.8 | 6.7 | |
| Pr | 5.13 | 1.00 | 1.8 | 1.51 | 0.86 | 1.23 | 4.74 | 3.53 | 0.76 | 2.62 | 2.75 | 1.65 | 4.31 | 4.36 | 2.91 | 1.29 | 3.82 | 1.67 | 1.25 | 1.3 | 1.21 | 1.03 | 0.55 | 0.6 | |
| Nd | 19.7 | 4.00 | 7.8 | 6.5 | 3.2 | 3.1 | 17.3 | 12.9 | 2.7 | 9.8 | 9.9 | 6.00 | 16.2 | 17.00 | 11.3 | 5.1 | 16.4 | 7.4 | 5.8 | 5.9 | 5.5 | 4.8 | 2 | 2.4 | |
| Sm | 3.00 | 0.6 | 1.8 | 1.4 | 0.6 | 0.5 | 2.8 | 2.2 | 0.5 | 1.6 | 1.00 | 1.1 | 2.4 | 2.4 | 2.1 | 0.8 | 2.3 | 1.00 | 0.8 | 0.7 | 0.7 | 0.7 | 0.3 | 0.4 | |
| Eu | 0.63 | 0.14 | 0.35 | 0.31 | 0.14 | 0.22 | 0.58 | 0.42 | 0.1 | 0.27 | 0.37 | 0.33 | 0.55 | 0.64 | 0.5 | 0.27 | 0.45 | 0.19 | 0.16 | 0.1 | 0.13 | 0.12 | 0.07 | 0.1 | |
| Gd | 2.61 | 0.74 | 2.06 | 1.9 | 0.55 | 0.71 | 2.67 | 2.02 | 0.6 | 1.67 | 1.06 | 1.17 | 1.88 | 2.46 | 2.41 | 1.07 | 2.5 | 1.33 | 1.3 | 0.91 | 1.22 | 1.06 | 0.37 | 0.42 | |
| Tb | 0.41 | 0.11 | 0.31 | 0.29 | 0.08 | 0.12 | 0.37 | 0.3 | 0.08 | 0.24 | 0.15 | 0.18 | 0.21 | 0.29 | 0.34 | 0.15 | 0.21 | 0.07 | 0.1 | 0.05 | 0.07 | 0.05 | 0.05 | <0.05 | |
| Dy | 1.81 | 0.56 | 1.85 | 1.98 | 0.48 | 0.58 | 2.12 | 1.63 | 0.44 | 1.24 | 1.03 | 1.12 | 1.35 | 1.65 | 2.02 | 0.86 | 1.84 | 1.17 | 1.18 | 0.69 | 0.97 | 0.88 | 0.29 | 0.29 | |
| Ho | 0.38 | 0.11 | 0.41 | 0.45 | 0.1 | 0.15 | 0.45 | 0.33 | 0.08 | 0.24 | 0.22 | 0.26 | 0.3 | 0.35 | 0.43 | 0.22 | 0.3 | 0.18 | 0.19 | 0.07 | 0.16 | 0.14 | 0.05 | 0.05 | |
| Er | 0.91 | 0.32 | 1.25 | 1.26 | 0.27 | 0.35 | 1.33 | 0.98 | 0.28 | 0.68 | 0.64 | 0.65 | 0.84 | 0.88 | 1.11 | 0.7 | 1.09 | 0.73 | 0.72 | 0.41 | 0.65 | 0.59 | 0.13 | 0.19 | |
| Tm | 0.12 | 0.05 | 0.16 | 0.17 | 0.05 | 0.06 | 0.18 | 0.13 | 0.05 | 0.1 | 0.08 | 0.09 | 0.14 | 0.14 | 0.14 | 0.06 | <0.05 | <0.05 | <0.05 | <0.05 | <0.05 | <0.05 | 0.05 | <0.05 | |
| Yb | 0.6 | 0.2 | 0.9 | 0.8 | 0.2 | 0.3 | 1.2 | 0.9 | 0.2 | 0.6 | 0.3 | 0.4 | 0.4 | 0.5 | 0.6 | 0.3 | 0.7 | 0.4 | 0.4 | 0.2 | 0.3 | 0.3 | 0.2 | 0.2 | |
| Lu | 0.08 | 0.05 | 0.14 | 0.11 | 0.05 | 0.06 | 0.18 | 0.12 | 0.05 | 0.1 | <0.05 | 0.07 | 0.05 | 0.08 | 0.08 | 0.05 | <0.05 | <0.05 | <0.05 | <0.05 | <0.05 | <0.05 | 0.05 | <0.05 | |
| Ce/Ce* | 0.16 | 0.46 | 0.53 | 0.62 | 0.57 | 0.12 | 0.88 | 0.86 | 0.58 | 0.78 | 0.64 | 0.43 | 0.66 | 0.67 | 0.44 | 0.41 | 0.48 | 0.3 | 0.19 | 0.25 | 0.19 | 0.22 | 0.67 | 0.66 | |
| Pr/Pr* | 1.63 | 0.94 | 0.97 | 1.00 | 1.00 | 1.54 | 0.99 | 0.99 | 1.03 | 0.99 | 1.12 | 1.22 | 1.16 | 1.11 | 1.26 | 1.24 | 1.14 | 1.20 | 1.30 | 1.20 | 1.29 | 1.25 | 1.04 | 0.88 | |
| Y/Ho | 33.67 | 28.09 | 29.15 | 39.96 | 35.80 | 34.00 | 25.91 | 27.30 | 38.88 | 29.50 | 62.23 | 52.85 | 48.17 | 48.74 | 56.81 | 60.50 | 75.13 | 89.50 | 91.32 | 145.29 | 94.81 | 100.07 | 56.00 | 33.80 | |
| Eu/Eu* | 1.09 | 1.09 | 0.93 | 0.98 | 1.22 | 1.83 | 1.08 | 0.99 | 0.85 | 0.77 | 1.68 | 1.36 | 1.22 | 1.23 | 1.03 | 1.34 | 0.88 | 0.76 | 0.7 | 0.58 | 0.62 | 0.63 | 0.97 | 1.30 | |

References

- Alexander, B. W. et al. Continentially-derived solutes in shallow Archean seawater: rare earth element and Nd isotope evidence in iron formation from the 2.9 Ga Pongola Supergroup, South Africa. *Geochimica et Cosmochimica Acta*, London, v. 72, n. 2, p. 378-394, Jan. 2008.
- Alkmim F. 2004. O que faz de um cráton um cráton ? O Cráton do São Francisco e as revelações Almeidianas ao delimita-lo. In: Mantesso-Neto et al. (eds) *Geologia do Continente SulAmericano. Evolução da obra de Fernando Flávio Marques de Almeida*. Becca, pp.: 17-35.
- Angelim, L. AA.(org.). 1997. *Geologia-Petrolina-PLGB-CPRM-Folha SC24-VC. Projeto Mapas Metalogenéticos e de Previsão de Recursos Minerais. Programa Levantamentos Geológicos Básicos do Brasil. Companhia Pesquisa e Recursos Minerais (CPRM), 1997.*
- Almeida F.F.M. 1977. O Cráton do São Francisco. *Revista Brasileira de Geociências.*, 7: 285-295.
- Aubineau.J., Albani, A.E., Fru, E.F., Gingras. M., et al. Unusual microbial mat-related structural diversity 2.1 billion Years ago and implications for the Francevillian biota.2018 *Geobiology*, Sep;16(5):476-497. doi: 10.1111/gbi.12296.
- Barbosa J.S.F., Sabaté P. 2003a. Marinho, M. M. O Cráton do São Francisco na Bahia: uma síntese. *Revista Brasileira de Geociências*, 33:3-6.
- Barbosa, J.S.F., Mascarenhas, J.F., Gomes, L.C.C., Dominguez, J.M.L. 2012, *Geologia da Bahia - Pesquisa e Atualização, Edição 1*, Editora Sooffset Gráfica.
- Barley, M.E., Bekker, A., and Krapez, B. (2005) Late Archean to early Paleoproterozoic global tectonics, environmental change and the rise of atmospheric oxygen. *Earth Planet. Sci. Lett.* 238:156–171.
- Bau M. 1991. Rare-earth element mobility during hydrothermal and metamorphic fluid - rock interaction and the significance of the oxidation state of europium. *Chemical Geology*, 93(3-4):219-230. [https://doi.org/10.1016/0009-2541\(91\)90115-8](https://doi.org/10.1016/0009-2541(91)90115-8).
- Bau M. 1993. Effects of syn-depositional and postdepositional processes on the rare-earth element distribution in Precambrian iron-formations. *European Journal of Mineralogy*, 5(2):257-267.
- Blaskowski, A. E. (2018). *Caracterização petrográfica e química das rochas de rejeito da mina Ipueira e seu potencial agromineral. Dissertação (Mestrado)*. Salvador: Instituto de Geociências - UFBA.
- Bau, M.; Dulski, P. Distribution of yttrium and rare-earth elements in the Penge and Kuruman iron-formations, Transvaal Supergroup, South Africa. *Precambrian Research*, Amsterdam, v. 79, n. 1-2, p. 37-55, July 1996.
- Bau, M. (1999). Scavenging of dissolved yttrium and rare earths by precipitating iron oxyhydroxide: experimental evidence for Ce oxidation, Y-Ho fractionation, and lanthanide tetrad effect. *Geochimica et Cosmochimica Acta*, 63(1), 67-77. [https://doi.org/10.1016/S0016-7037\(99\)00014-9](https://doi.org/10.1016/S0016-7037(99)00014-9)
- Bekker, A., Karhu, J.A., and Kaufman, A.J. (2006) Carbon isotope record for the onset of the Lomagundi carbon isotope excursion in the Great Lakes area, North America. *Earth Planet. Sci. Lett.* 148:145–180. <https://doi.org/10.1016/j.precamres.2006.03.008>..
- Bekker e Holland (2012) – Oxygen overshoot and recovery during the early Paleoproterozoic. *Earth and Planetary Science Letters* 317-318 (2012) 295–304. doi:10.1016/j.epsl.2011.12.012.

- Birgel D, Meister P, Lundberg R, Horath TD, Bontognali TRR, et al. 2015. Methanogenesis produces strong ^{13}C enrichment in stromatolites of Lagoa Salgada, Brazil: a modern analogue for Palaeo-/Neoproterozoic stromatolites? *Geobiology* 13(3):245–66.
- Bolhar R., Kamber B.S., Moorbath S., Fedo C.M., Whitehouse M.J. 2004. Characterisation of early Archaean chemical sediments by trace element signatures. *Earth and Planetary Science Letters*, 222(1):43-60. <https://doi.org/10.1016/j.epsl.2004.02.016>
- Bolhar R., Van Kranendonk M.J. 2007. A non-marine depositional setting for the northern Fortescue Group, Pilbara Craton, inferred from trace element geochemistry of stromatolitic carbonates. *Precambrian Research*, 155(3-4):229-250. <https://doi.org/10.1016/j.precamres.2007.02.002>.
- Brand, U., & Veizer, J. (1980). Chemical diagenesis of a multicomponent carbonate system; 1, trace elements. *Journal of Sedimentary Research*, 50(4), 1219–1236.
- Câmara, I.S. 2021. Ocorrências de grafita no Complexo Tanque Novo – Ipirá, Nordeste do Cráton do São Francisco, Bahia, Brasil: Caracterização e potencial metalogenético. Dissertação de mestrado (UFBA), 2021, p. 71.
- Chao M., Yanjie Tang, Jifeng Ying, Global tectonics and oxygenation events drove the Earth-scale phosphorus cycle, *Earth-Science Reviews*, Vol 233, 2022, 104166, ISSN 0012-8252, <https://doi.org/10.1016/j.earscirev.2022.104166>.
- Conceição, H., Rosa, M.L.S., Oberli, F., Rios, D.C. 2007. Idade U-Pb do dique sienítico Anurí, sul da Bahia: magmatismo alcalino-potássico paleoproterozoico e sua implicação para a orogenia transamazônica no Cráton do São Francisco. *Revista Brasileira de Geociências*, vol 37 (4), p. 61-69.
- Cox G.M. et al. 2018. Linking the rise of atmospheric oxygen to growth in the continental phosphorus inventory. *Earth and Planetary Science Letters*. vol 489, 1 May 2018, p. 28-36.
- Dalton de Souza., Teixeira – Prospecto Rio Salitre. Relatório final: Geologia e prospecção geoquímica preliminar do Complexo Rio Salitre. Escala 1:50.000. Brasília: CPRM, 1981.
- Dalton de Souza, J., Teixeira, L.R., Figueiroa, I., Azevedo, R.R., Barral, W.M., Costa, I.V.G., Filho, E.L.A., Oliveira, R.B.A., Lopes, J.N., 1979. Projeto Colomi. Relatório final: Geologia e Prospecção Geoquímica da Região de Remanso – Santo Sé. CPRM.
- De Baar H.J.W., Schijf J., Byrne R.H. 1991. Solution chemistry of the rare earth elements in seawater. *European Journal of Solid State and Inorganic Chemistry*, 28(Suppl.):357-373.
- Del Lama, E. A., Candia, M. A. F., Szabó, G. A. J. (2001). Petrography and Metamorphism of the Metasedimentary Country-Rocks of the Jacurici Valley Chromitite-Hosting Mafic-Ultramafic Complexes, Bahia, Northeastern Brazil. *Geologia USP. Série Científica*, 1, 1-15. <https://doi.org/10.5327/S1519-874X2001000100002>.
- Dias, J.R.V., Marques, J.C., Bertolini, G., Frantz, J.C., Friedrich, B., Paim, J.C.S., Silveira, C.J.S., Queiroz, W.J.A. 2022. Regional high-grade metamorphic peak imprint in zircons from the mafic-ultramafic Jacurici Complex, São Francisco Craton, Brazil, *Braz. J. Geol.* 52 (1), <https://doi.org/10.1590/2317-4889202120210007>.
- Eguchi J, Diamond CW, Lyons TW. 2022. Proterozoic supercontinent break-up as a driver for oxygenation events and subsequent carbon isotope excursions. *PNAS Nexus* 1(2):pgac036.
- Eguchi J, Seales J, Dasgupta R. 2020. Great Oxidation and Lomagundi events linked by deep cycling and enhanced degassing of carbon. *Nat. Geosci.* 13(1):71–76.

Föllmi, K.B., 1996. The phosphorus cycle, phosphogenesis and marine phosphate rich deposits. *Earth Sci. Rev.* 40, 55–124.

Friedman, I., O'Neil, J., Cebula, G., Two new carbonate stable isotope standards, *Geostandards Newsletter* 6 1 (1982) 11-12.

Gaertner, C., Broecker, M., Strauss, H., Farber, K. (2011). Strontium-, carbon- and oxygen-isotope compositions of marbles from the Cycladic blueschist belt. *Greece Geology*, 148, 511-528. <https://doi.org/10.1017/S001675681100001X>

Gama, M. (2014). Caracterização petrográfica e litogeoquímica das rochas metacarbonáticas e calcissilicáticas do Vale do Rio Jacurici, Bahia. Trabalho de Conclusão de Curso. Bahia: Instituto de Geociências – UFBA.

Gama M. A., Misi A., Sá J.H.S., Oliveira L.R.S.S., Ribeiro T.S (2021). Caracterização petrográfica e litogeoquímica dos mármore e rochas calcissilicáticas do Vale do Jacurici, Bahia: condições paleoambientais e processos fosfogenéticos. *Geologia USP, Série Científica*, São Paulo, v. 21, n. 2, p. 12-143. <https://doi.org/10.11606/issn.2316-9095.v21-161794>

Garcia et al. 2018 – Tectonic and metallogenic evolution of the Curaçá Valley Copper Province, Bahia, Brazil: A review based on new SHRIMP zircon U-Pb dating and sulfur isotope geochemistry. *Ore Geology Reviews*, Volume 93, February 2018, Pages 361-381. Doi: <https://doi.org/10.1016/j.oregeorev.2018.01.007>.

Garcia et al. 2021. Geology, petrogenesis, and geochronology of the Rio Salitre Complex: Implications for the Paleoproterozoic evolution of the northern São Francisco Craton, Brazil. *Journal of South American Earth Sciences*, Volume 107, April 2021, 103112. Doi: <https://doi.org/10.1016/j.jsames.2020.103112>.

Glenn, C.R., Föllmi, K.B., Riggs, S.R., Baturin, G.N., Grimm, K.A., Trappe, J., Abed, A.M., Galli-Olivier, C., Garrison, R.E., Ilyin, A.V., Jehl, C., Rohrllich, V., Sadaqah, R.M.Y., Schidlowski, M., Sheldon, R.E., Siegmund, H., (1994). Phosphorus and phosphorites: sedimentology and environments of formation. *Eclogae Geologicae Helveticae* 87, 747–788.

Gumsley, A.P., Chamberlain, K.R., Bleeker, W., Bekker, A., 2017 Timing and tempo of the Great Oxidation Event. *Earth, Atmospheric, and Planetary Sciences* 114 (8), 1811-18816. DOI: <https://doi.org/10.1073/pnas.1608824114>.

Halls, H.C., Davis, D.W., Stott, G.M., Ernst, R.E., and Hamilton, M.A. (2008) The Paleoproterozoic Marathon Large Igneous Province: new evidence for a 2.1 Ga long-lived mantle plume event along the southern margin of the North American Superior Province. *Precambrian Res.* 162:327–353.

Hannah, J.L., Bekker, A., Stein, H.J., Markey, R.J., and Holland, H.D., 2004, Primitive Os and 2316 Ma age for marine shale: Implications for Paleoproterozoic glacial events and the rise of atmospheric oxygen: *Earth and Planetary Science Letters*, v. 225, p. 43–52, doi: 10.1016/j.epsl.2004.06.013.

Hao, J et al. 2020. Cycling phosphorus on the Archean Earth: Part I. Continental weathering and riverine transport of phosphorus. *Geochimica et Cosmochimica Acta*, vol 273, 15, p.70-84.

Hao, W., Chen, N., Sun, W., Mand, K., Kirsimäe, K., Teitler, Y., Somelar, P., Robbins, L.J., Babechuk, M.G., Planavsky, J.N., Alessi, D.S., Konhauser, K.O. 2022. Binding and transport of Cr(III) by clay minerals during the Great Oxidation Event, *Earth and Planetary Science Letters*, vol 584, 117503, DOI: <https://doi.org/10.1016/j.epsl.2022.117503>.

- Hasui, Y. 2012. Livro Geologia do Brasil, Editora Beca, ISBN: 987-85-62768-10-1, 900p.
- Heaman, L.M. 1997. Global magmatism at 2.45 Ga: remnants of an ancient large igneous province? *Geology* 25:299–302.
- Hodgskiss, M.S.W., Crockford, P.W., Turchyn, A.V. 2023. Deconstructing the Lomagundi-Jatuli Carbon Isotope Excursion. *Annual Review of Earth and Planetary Sciences*, 51:301–30. <https://doi.org/10.1146/annurev-earth-031621-071250>.
- Hut, G., Consultants' group meeting on stable isotope reference samples for geochemical and hydrological investigations, Report to the Director General, International Atomic Energy Agency, Vienna, Austria (1987).
- Kamber B.S., Webb G.E. 2001. The geochemistry of late Archean microbial carbonate: implications for ocean chemistry and continental erosion history. *Geochimica et Cosmochimica Acta*, 65(15):2509-2525. [https://doi.org/10.1016/S0016-7037\(01\)00613-5](https://doi.org/10.1016/S0016-7037(01)00613-5).
- Kamber B.S., Bolhar R., Webb G.E. 2004. Geochemistry of late Archaean stromatolites from Zimbabwe: evidence for microbial life in restricted epicontinental seas. *Precambrian Research*, 132(4):379-399. <https://doi.org/10.1016/j.precamres.2004.03.006>
- Karhu, J.A., Holland, H.D., 1996. Carbon isotopes and rise of atmospheric oxygen. *Geology* 24, 867–879.
- Kosin M.D., Melo R.C., Souza J.D., Oliveira E.P., Carvalho M.J., Leite C.M.M. 2003. Geologia do segmento norte do Orógeno Itabuna-SalvadorCuraçá e guia de excursão. *Revista Brasileira de Geociências*, São Paulo, v 33(1):15-26.
- Kopp, R.E., Kirschvink, J.L., Hilburn, I.A., and Nash, C.Z., 2005, The Paleoproterozoic snowball Earth: A climatic disaster triggered by the evolution of oxygenic photosynthesis: *Proceedings of the National Academy of Sciences*, v. 102, p. 11,131– 11,136, doi: 10.1073/pnas.0504878102.
- Koproski, L.M , Barbosa, n., Debruyne, D., Oliveira, E.P., Barbosa, N.S., Moraes, A.M.V., Lau, A.M.P., Santos, R.P.Z, 2023. The Neoproterozoic mafic-ultramafic São José do Jacuípe Suite in the Itabuna-Salvador-Curaçá orogen, Brazil: New U-Pb ages and geochemical data. *Lithos*, 462-463, vol 10747. Doi: <https://doi.org/10.1016/j.lithos.2023.107407>.
- Jardim de Sá, E. F. (1982). Nota sobre o estilo estrutural e relações gnaisses supracrustais no “greenstone belt” de Serrinha (Bahia). *Revista Ciências da Terra*, 2, 8-126.
- Johannesson K.H., Telfeyan K., Chevis D.A., Rosenheim B.E., Leybourne M.I. 2014. Rare Earth elements in stromatolites – 1. Evidence that modern terrestrial stromatolites fractionate rare Earth elements during incorporation from ambient Waters. *Evolution of Archean Crust and Early Life*, 385-411.
- Joosu L., Lepland A., Kirsimäe K., Romashkin A.E., Roberts N.M.W., Martin A.P., C̃rne A.E. 2015. The REE-composition and petrography of apatite in 2 Ga Zaonega Formation, Russia: The environmental setting for phosphogenesis. *Chemical Geology*, 395:88-107. <https://doi.org/10.1016/j.chemgeo.2014.11.013>
- Joosu L., Lepland A., Kreitsmann T., Upraus K., Roberts N.M.W., Paiste P., Martin A.P., Kirsimäe K. 2016. Petrography and the REE-composition of apatite in the Paleoproterozoic Pilgumarj Sedimentary Formation, Pechenga Greenstone Belt, Russia. *Geochimica et Cosmochimica Acta*, 186:135-153. <https://doi.org/10.1016/j.gca.2016.04.043>.

- Khelen, A., Manikyamba, C., Subramanyam, K.S.V., Raza, W. 2022. Geochemistry of the Neoproterozoic carbonates of Chitradurga greenstone belt, Dharwar Craton, India: Implications on depositional environment. *Geological Journal*, vol 58(6), DOI: 10.1002/gj.4616.
- Lajoinie, M.F., Lanfranchini, M.E., Recio, C., Sial, A.N., Cingolani, C.A., Ballivián Justiniano, C.A., Etcheverry, R.O., 2018. The Lomagundi-Jatuli carbon isotopic event recorded in the marble basement of the Tandilia System basement, Río de la Plata Craton. *Precamb. Res.* <https://doi.org/10.1016/j.precamres.2018.03.012>.
- Lajoinie, M.F., Sial, A.N., Justiniano, C.A.B, Cingolani, C.A., Recio, C., Etcheverry, R.O., Miguel Basei, M., Lanfranchini, M.E. 2019. First geochronological constraint for the Palaeoproterozoic Lomagundi-Jatuli $\delta^{13}\text{C}$ anomaly in the Tandilia Belt basement (Argentina), Río de la Plata Craton.
- Lawrence M.G., Greig M., Collerson K.D., Kamber B.S. 2006. Rare Earth element and yttrium variability in South East Queensland waterways. *Aquatic Geochemistry*, 12:39-72. <https://doi.org/10.1007/s10498-005-4471-8>.
- Leiming Yin, Fanwei Meng, Fanfan Kong, Changtai Niu, Microfossils from the Paleoproterozoic Hutuo Group, Shanxi, North China: Early evidence for eukaryotic metabolism, *Precambrian Research*, Volume 342, 2020, 105650. Doi: <https://doi.org/10.1016/j.precamres.2020.105650>.
- Leite, C.M.M-1983- “Projeto Serrote da Batateira”, Estado da Bahia, Convênio SME/CBPM, Salvador.
- Leite, C.M.M-1984- “Projeto Juazeiro”, Estado da Bahia, Convênio SME/CBPM, Salvador.
- Leite, C. M. M. 2002. A evolução geodinâmica da orogênese paleoproterozoica nas regiões de Capim Grosso– Jacobina e Pintadas–Mundo Novo (Bahia, Brasil): Metamorfismo, anatexia crustal e tectônica. PhD thesis, Instituto de Geociências, Universidade Federal da Bahia, Salvador
- Leite, C. M. M., Barbosa, J. S. F., Goncalves, P., Nicollet, C. & Sabate', P. 2009. Petrological evolution of silica-undersaturated sapphirine-bearing granulite in the Paleoproterozoic Salvador–Curaçá Belt, Bahia, Brazil. *Gondwana Research*, 15, 49–70.
- Lepland, A., Melezhik, V.A., Papineau, D., Alexander E., Jossu, L., 2013. The Earliest Phosphorites: Radical Change in the Phosphorus Cycle During the Palaeoproterozoic. *Frontiers in Earth Sciences in earth's oxygenation book: Volume 3: Global Events and the Fennoscandian Arctic Russia - Drilling Early Earth Project*, p.1275-1296, DOI: http://dx.doi.org/10.1007/978-3-642-29670-3_7.
- Li, Y., Satish-Kumar, M., Kiran S., Wan, C., Zheng, J. 2022. 2.0 Ga orogenic graphite deposits and associated ^{13}C -enriched meta-carbonate rocks from South China Craton: Implications for global Lomagundi event. *Geoscience Frontiers*, vol 13, Issue 4, 101409, DOI: <https://doi.org/10.1016/j.gsf.2022.101409>.
- Ling H., Chen X., Li D., Wang D., Shields-Zhou G., Zhu M. 2013. Cerium anomaly variations in Ediacaran – earliest Cambrian carbonates from the Yangtze Gorges area, South China: Implications for oxygenation of coeval shallow seawater. *Precambrian Research*, 225:110-127. <https://doi.org/10.1016/j.precamres.2011.10.011>.
- Macedo, E.P., Neves, J.P., Pereira, L.H.M., Macêdo, L.L., Mota, E.L., 2019. Mapa Geológico da Folha Campo dos Cavalos (SC.24-V-C-VI). CPRM, escala 1. 100,000.
- Marques, J. C., Ferreira Filho, C. F. (2003). The chromite deposits of the Ipueira Medrado Sill, Bahia, Brazil. *Economic Geology*, 98(1), 87-108. <https://doi.org/10.2113/98.1.87>

- Maheshwari et al. (2010) – Global nature of the Paleoproterozoic Lomagundi carbon isotope excursion: A review of occurrences in Brazil, India, and Uruguay. *Precambrian Research* 182 (2010) 274–299.
- Marinho, M. M., Rocha, G. F., Deus, P. B., Viana, J. S. (1986). Geologia e potencial cromitífero do Vale do Jacurici, Bahia: XXXIV Congresso Brasileiro de Geologia, 5, 2074– 2088. Goiânia, SBG.
- Martin, D.McB., Powell, C.McA., George, A.D., 2000. Stratigraphic architecture and Evolution of the Early Paleoproterozoic McGrath Trough, Western Australia. *Precambrian Research*, vol 99, p. 33-64. DOI: [https://doi.org/10.1016/S0301-9268\(99\)00053-4](https://doi.org/10.1016/S0301-9268(99)00053-4).
- Martin, A.P., Condon, S.J., Prave, A.R., Lepland, A., 2013. A review of temporal constraints for the Palaeoproterozoic large, positive carbonate isotope excursion (the Lomagundi-Jatuli Event). *Earth Sci. Rev.* 127, 242–261.
- Melezhik , V.A., Fallick,A.E., Medvedev, P.V, 1999. Extreme $^{13}\text{C}_{\text{carb}}$ enrichment in ca. 2.0 Ga magnesite–stromatolite–dolomite–‘red beds’ association in a global context: a case for the world-wide signal enhanced by a local environment. *Earth-Science Reviews* 48 1999 71–120
- Melezhik, V.A., Fallick, A.E., Hanski, E.J., Kump, L.R., Lepland, A., Prave, A.R., and Strauss, H., 2005a, Emergence of the aerobic biosphere during the Archean-Proterozoic transition: Challenges of future research: *GSA Today*, v. 15, no. 11, p. 4–11, doi: 10.1130/1052-5173 (2005)015[4:EOAABD]2.0.CO;2.
- Melezhik, V.A., Fallick, A.E., Rychanchik, D.V., and Kuznetsov, A.B., 2005b, Palaeoproterozoic evaporites in Fennoscandia: Implications for seawater sulphate, $\delta^{13}\text{C}$ excursions and the rise of atmospheric oxygen: *Terra Nova*, v. 17, p. 141– 148, doi: 10.1111/j.1365-3121.2005.00600.x.
- Melo R.C. de (ed.). 1991. Pintadas, folha SC.24-Y-D-V: Estado da Bahia: texto explicativo. Salvador: CPRM. Programa Levantamentos Geológicos Básicos do Brasil, 96 p.
- Misi, A., Azmy,K., Kaufman, A.J., Oliveira, T.F., Sanches, A.L., 2010. Metallogenic and phosphogenic events in the intracratonic and passive-margin Proterozoic basins of the São Francisco Craton: The Bambuí/Una and Vazante Groups. In: VII South American Symposium on Isotope Geology, Brasília, DF., VII SSAGI, 2010.
- Misi, A., Kaufman, A.J., Azmy,K., Dardenne, M.A., Sial, A.N., De Oliveira, T.F. 2011. Neoproterozoic successions of the São Francisco Craton, Brazil: The Bambuí, Una, Vazante and Vaza Barris/Miaba Groups and their glaciogenic deposits. *Geological Society, London, Memoirs*, v. 36, p. 509-522.
- Mohanty S.P., Barik A., Sarangi S., Sarkar A. 2015. Carbon and oxygen isotope systematics of a Paleoproterozoic cap-carbonate sequence from the Sausar Group, Central India. *Palaeogeography, Palaeoclimatology and Palaeoecology*, 417:195-209. <http://dx.doi.org/10.1016/j.palaeo.2014.10.036si>.
- Nelson, G.J., Pufahl, P.K., Hiatt, E.E., 2010. Paleooceanographic constraints on Precambrian phosphorite accumulation, Baraga Group, Michigan, USA. *Sedimentary Geology* 226, 9–21
- Northdurft L.D, Webb G.E, Kamber B.S. 2004. Rare earth element geochemistry of Late Devonian reefal carbonates, Canning Basin Western Australia: confirmation of a seawater REE proxy in ancient limestones. *Geochimica et Cosmochimica Acta*, 68(2):263-283. [https://doi.org/10.1016/S0016-7037\(03\)00422-8](https://doi.org/10.1016/S0016-7037(03)00422-8).

Nozaki Y., Zhang J., Amakawa H. 1997. The fractionation between Y and Ho in the marine environment. *Earth and Planetary Science Letters*, 148(1- 2):329-340. [https://doi.org/10.1016/S0012-821X\(97\)00034-4](https://doi.org/10.1016/S0012-821X(97)00034-4).

Oliveira E.P., Carvalho, M.J., Mcnaughton, N.J. Evolução do Segmento Norte do Orógeno Itabuna-Salvador-Curaçá: Cronologia da Acresção de Arcos, Colisão Continental e Escape de Terrenos. *Geol. USP Sér. Cient.*, São Paulo.,v. 4., n,1, p. 41-53. abr, 2004a.

Oliveira M. A. J. & Sighinolfi G.P. 1983. Geochemistry of Precambrian phosphate-carbonate intrusives from Bahia (Brazil). *Geochemical Journal*, 17:277-287. https://www.jstage.jst.go.jp/article/geochemj1966/17/6/17_6_277/_pdf

Oliveira, E. P., Windley, B., McNaughton, N.J., Pimental, M. 2004. Contrasting copper and chromium metallogenic evolution of terranes in the Paleoproterozoic Itabuna-Salvador-Curaçá orogeny, São Francisco craton, Brazil: new zircon (SHRIMP) and Sm-Nd (model) ages and their significance for orogeny parallel escape tectonics. *Precambrian Research*, v. 128, p. 143-165.

Oliveira, L. O. 2016. Fosforitos da Região de Juazeiro, Bahia: Paleoambientes, Geocronologia, Controles da Mineralização e Correlações Estratigráficas. Dissertação de Mestrado, Universidade Federal da Bahia, Salvador, 195 p.

Oyhantçabal. P, Siegesmund. S, Wemmer K.2011. The Río de la Plata Craton: a review of units, boundaries, ages and isotopic signature. *Int J Earth Sci (Geol Rundsch)* (2011) 100:201–220. DOI 10.1007/s00531-010-0580-8.

Ossa, O.F., Albani, A.E., Hofmann, A., Bekker, A., Lafaye, F.G., et al.,. 2013. Exceptional preservation of expandable clay minerals in the ca. 2.1 Ga black shales of the Francevillian basin, Gabon and its implication for atmospheric oxygen accumulation. *Chemical Geology*, Vol 362, p. 181-192. DOI: <https://doi.org/10.1016/j.chemgeo.2013.08.011>.

Papineau, D., 2010. Global biogeochemical changes at both ends of the Proterozoic: insights from phosphorites. *Astrobiology* 10, 165–181.

Papineau et al. (2013) – High phosphate availability as a possible cause for massive cyanobacterial production of oxygen in the Paleoproterozoic atmosphere. *Earth and Planetary Science Letters* 362 (2013) 225–236. Doi: <http://dx.doi.org/10.1016/j.epsl.2012.11.050>.

Patadien, Raysree., La Point. D., De Roeveer, Emond. 2019. The K3 Copper Deposit in the Bakhuis Granulite Belt, W Suriname. SAXI- XI Interguiana Geological Conference 2019: Paramaribo, Suriname

Planavsky N., Bekker A., Rouxel O.J., Kamber B., Hofmann A., Knudsen A., Lyons T.W. 2010. Rare earth element and yttrium compositions of Archean and Paleoproterozoic Fe formations revisited: new perspectives on the significance and mechanisms of deposition. *Geochimica et Cosmochimica*, 74(22):6387-6405. <https://doi.org/10.1016/j.gca.2010.07.021>.

Playter, T., Konhauser, k., Owttrim, G., Hodgson, C., Warchola, T., Mloszewska, A.M., Sutherland, B., Bekker, A., Zonneeld, J.P., Pemberton, S.G., Gingras, M. 2017. Microbe—clay as a mechanism for the preservation of organic matter and trace metal biosignatures in black shales. *Chemical Geology*, vol 459, p. 75-90.

Prave AR, Kirsimäe K, Lepland A, Fallick AE, Kreitsmann T, et al. 2022. The grandest of them all: the Lomagundi–Jatuli Event and Earth’s oxygenation. *J. Geol. Soc. Lond.* 179(1):jgs2021-036.

Piper D.Z., Bau M. 2013. Normalized Rare Earth Elements in Water, Sediments, and Wine: Identifying Sources and Environmental Redox Conditions. *American Journal of Analytical Chemistry*, 4(10A):69-83. <http://dx.doi.org/10.4236/ajac.2013.410A1009>

Pufahl, P.K., Hiatt, E.E., 2012. Oxygenation of the Earth's atmosphere–ocean system: a review of physical and chemical sedimentologic responses. *Marine and Petroleum Geology* 32, 1–20.

Pufahl P.K., Groat L.A. 2017. Sedimentary and Igneous Phosphate Deposits: Formation and Exploration an invited paper. *Economic Geology*, 112(3):483-516. <https://doi.org/10.2113/econgeo.112.3.483>.

Ruttenberg, K.C., Dyrhman, S.T., 2005. Temporal and spatial variability of dissolved organic and inorganic phosphorus, and metrics of phosphorus bioavailability in an upwelling-dominated coastal system. *Journal of Geophysical Research Oceans*, vol 110, C10. DOI: <https://doi.org/10.1029/2004JC002837>.

Reinhard, C.T., Planavsky, N.J., Gill, B.C., Ozaki, K., Robbins, L.J., Lyons, T.W., Fischer, W.W., Wang, C., Cole, D.B., Konhauser, K.O., 2017. Evolution of the global phosphorus cycle. *Nature* 541, 386–389. doi:10.1038/nature20772

Reznitskii, L.Z Fefelov, N.N. Vasilyev, Y.P., Zarudneva, N.V., Nekrasova, E.A. 1998. Isotopic composition of lead from metaphosphorites and problem of the Slyudyanka Group age, the Southern Baikal western Khamar Daban region. *Lithology and Mineral Resources*, vol 33 (55), p. 432-442.

Ribeiro T.S. 2016. Caracterização Geológica das Rochas Calcissilicáticas e Metacarbonáticas do Complexo Tanque Novo- Ipirá na Folha Pintadas-Ba: Potencial Metalogenético para Fosfato, Salvador. MS Dissertation, Instituto de Geociências, Universidade Federal de Bahia, Salvador, 181 p.

Ribeiro T. S. (2017). Complexo Tanque Novo-Ipirá: Geologia e potencialidade para fosfato na folha Pintadas, Bahia. CBPM. Série Arquivos Abertos, 42.

Ribeiro T.S., Misi A., Oliveira., L.R.S.S., Sá J.H.S., Debruyne. D., Câmara I. Evidence of Paleoproterozoic phosphogenesis in the Salvador-Curaçá Orogen (Tanque Novo-Ipirá Complex), northeastern São Francisco Craton, Brazil. (2021). *Brazilian Journal of Geology*, 51(3): <https://doi.org/10.1590/2317-4889202120190137>.

Rocha Neto, M.B., Pedreira, A.J., 1994. Geologia e recursos minerais do Greenstone Belt do Rio Itapicuru, Bahia. Companhia Baiana de Pesquisa Mineral, Salvador.

Ruggiero, A., Oliveira, E.P., 2010. Caracterização de vulcânicas adakíticas e cálcio-alcalinas no greenstone belt do rio Itapicuru, Bahia: petrogênese e implicações geodinâmicas. *Rev. Bras. Ciênc. Solo* 40, 01–18.

Sá, J. H. S. e Oliveira, N. P. – 1982- “Relatório sobre os levantamentos Realizados na Ilha do Fogo e Serrote da Batateira, Juazeiro-Bahia”. CPM/SME, Relatório Interno, 5 p. ilustr., Salvador.

Sá, J. H. S.; Leite, C. M. M.; Conceição V. M.; Oliveira, N. P., 1984. Depósitos de rochas fosfáticas no município de Juazeiro, Bahia. In: XXXIII Congresso Brasileiro de Geologia, 1984. Anais... Rio de Janeiro, SBG.

Sanches, A.L., Misi, A., Kaufman, A.J., Azmy, K. (2007) – As sucessões carbonáticas neoproterozóicas do Cráton do São Francisco e os depósitos de fosfato: correlações e fosfogênese. *Revista Brasileira de Geociências* 37(4):182. DOI:10.25249/0375-7536.200737S4182194.

Santos, R.V., de Oliveira, C.G., de Sousa, V.H.V., de Carvalho, M.J., Andrade, T.V., de Azevedo e Souza, H.G., 2008. Correlação isotópica baseada em isótopos de carbono entre os greenstone belts de Goiás. In: 44º Congresso Brasileiro de Geologia, Curitiba, Sociedade Brasileira de Geologia. (CD-ROM)

Satish-Kumar, M., Shirakawa, M., Imura, A., Otsuji-Makino N., Imanaka-Nohara, R., Malaviarachchi, S.P.K., Fitzsimons, I.C.W., Sajeev, K., Grantham G.H., Windley, B.F., Hokada, T., Takahashi, T., Shimoda, G., Goto, K.T. 2021. A geochemical and isotopic perspective on tectonic setting and depositional environment of Precambrian meta-carbonate rocks in collisional orogenic belts. *Gondwana Research*, vol 96, p. 163-204, DOI: <https://doi.org/10.1016/j.gr.2021.03.013>.

Sial, Alcides N et al., (2015). Isotope and Elemental. *Chemostratigraphy*. 23–64. doi:10.1016/B978-0-12-419968-2.00002-9, 136p.

Silva, M.G. 1992. O Greenstone belt do Rio Itapicuru: uma bacia do tipo back-arc fóssil. *Revista Brasileira de Geociências*. 22(2):157-166.

Silva, M. da G., Silva Coelho, C.E., Teixeira, J.B.G., da Silva, F.C.A., Silva, R.A., de Souza, J.A.B., 2001. The Rio Itapicuru greenstone belt, Bahia, Brazil: geologic evolution and review of gold mineralization. *Mineral Deposits* 36:345–357. <http://dx.doi.org/10.1007/s001260100173>.

Silveira, C.J.S. Geocronologia U-Pb em zircão de rochas intrusivas e de embasamento na região do Vale do Jacurici, Craton do São Francisco, Bahia. *Brazilian Journal of Geology*, São Paulo, v. 45, n. 3, p. 453-474, 2015b.

Singh A.K., Tewari V.C., Sial A.N., Khanna P.P., Singh N.I. 2015. Rare earth elements and stable isotope geochemistry of carbonates from the mélange zone of Manipur ophiolitic Complex, Indo-Myanmar Orogenic Belt, Northeast India. *Carbonates and Evaporites*, 31:139-151. <https://doi.org/10.1007/s13146-015-0249-2>.

Sobrinho, V. R. S. et al. Programa Geologia do Brasil - PGB. Pinhões. Folha SC.24-D-V. Estados da Bahia. Mapa Geológico. Salvador: CPRM, 2015. Escala - 1:100.000.

Souza, D. F. M., Oliveira, E.P., Amaral, W.S., Baldim, M.R. 2020. The Itabuna – Salvador – Curaçá Orogen revisited, São Francisco Craton, Brazil: New zircon U-Pb ages and Hf data support Evolution from archaic continental arc to paleoproterozoic crustal reworking during block collision. *Journal of South American Earth Sciences*, vol 104, 102826. DOI: <https://doi.org/10.1016/j.jsames.2020.102826>.

Soomer S., Peeter. S., Mänd. K., Lepland.A., Kirsimäe. 2022. Geochemistry and mineralogy of Paleoproterozoic metasediments in the Imandra-Varzuga Greenstone Belt: Implications for sediment provenance tectonic settings and weathering intensity at the transition to oxygenated surface environments. *Precambrian Research*, vol 171, 106578. DOI: <https://doi.org/10.1016/j.precamres.2022.106578>.

Swart P.K. 2015. The geochemistry of carbonates diagenesis: The past, present and future. *Sedimentology*, 62(5):1233-1304. <https://doi.org/10.1111/sed.12205>.

Tang et al. (2013) – C-O isotope geochemistry of the Dashiqiao magnesite belt, North China Craton: Implications for the Great Oxidation Event and ore genesis

Tang L., Santosh M., Tsunogae T., Maruoka T. 2016. Paleoproterozoic meta-carbonates from the central segment of the Trans-North China Orogen: Zircon U-Pb geochronology, geochemistry, and

carbon and oxygen isotopes. *Precambrian Research*, 284:14-29. <https://doi.org/10.1016/j.precamres.2016.08.001>.

Tarduno, J.A., McWilliams, M., Debiche, M.G., Sliter, W.V., Blake Jr., M.C., 1985. Franciscan Complex Calera limestones: Accreted remnants of Farallon Plate oceanic plateau. *Nature* 317, 345–347.

Teixeira, J. B. G., Misi, A. Silva, M. G. Supercontinent evolution and the Proterozoic metallogeny of South America. *Gondwana Research*, v.11, p. 346–361, 2007.

Tostevin R., Shields G.A., Tarbuck G.M., He T., Clarkson M.O, Wood R.A. 2016. Effective use of cerium anomalies as a redox proxy in carbonatedominated marine settings. *Chemical Geology*, 438:146-162. <https://doi.org/10.1016/j.chemgeo.2016.06.027>

Veizer, J. (1983). Chemical diagenesis of carbonates: Theory and application of trace element technique. In M. A. Arthur, T. F. Anderson, I. R. Kaplan, J. Veizer, & L. S. Land (Eds.), *Stable isotopes in sedimentary geology* Society of Economic Paleontologists and Mineralogists (SEPM) short course notes (Vol. 10, pp. I–III). SEPM Society for Sedimentary Geology.

Veizer, J., & Hoefs, J. (1976). The nature of $^{18}\text{O}/^{16}\text{O}$ and $^{13}\text{C}/^{12}\text{C}$ secular trends in sedimentary carbonate rocks. *Geochimica et Cosmochimica Acta*, 40, 1387–1395

Wang, X., Guo, J., Tao, L., Deng, J., Ma, C. 2021. Paleoproterozoic tectonic Evolution of the Yangtze Craton: Evidence from magmatism and sedimentation in the Susong area, South China. *Precambrian Research*, 365, 106390. DOI:<https://doi.org/10.1016/j.precamres.2021.106390>.

Yuanlin, C., Huan, L, Shangyi, G., Gary, G.L, Chaoyang, Z., Shige.C., Dadou, L., Safiyanu, M., Liuan, D. 2023. Marble trace element and C-O isotope geochemistry of the Paleoproterozoic Jingshan Group, North China: Insights into BIF formation during the Lomagundi-Jatuli Event. *Precambrian Research*, vol 395, 107152. DOI: <https://doi.org/10.1016/j.precamres.2023.107152>.

Zhang, K.J., Li, Q.H., L.L., Zeng, L., Lu, L., Zhang, Y.X., Hui, J., Jin, X., Tang, X.C., 2017. Geochemistry of limestone deposited in various plate tectonic settings. *Earth Science Review*, vol 167, p. 27-46. DOI: <https://doi.org/10.1016/j.earscirev.2017.02.003>.

Zhang, K.J., Xia, B., Zhang, Y.X., Liu, W.L., Zeng, L., Li, J.F., Xu, L.F., 2014. Central Tibetan Meso-Tethyan oceanic plateau. *Lithos* 210–211, 278–288.

Zhao Y., Zheng Y., Chen F.K. 2009. Trace element and strontium isotopic constraints on sedimentary environment of Ediacaran carbonates in Southern Anhui, South China. *Chemical Geology*, 265(3-4):345-362. <https://doi.org/10.1016/j.chemgeo.2009.04.015>.

Zhao Y., Zheng Y. 2013. Geochemical constraints on the origin of postdepositional fluids in sedimentary carbonates of the Ediacaran system in South China. *Precambrian Research*, 224:341-363. <https://doi.org/10.1016/j.precamres.2012.10.014>.

Zhong S., Mucci A. 1995. Partitioning of rare earth elements (REEs) between calcite and seawater solutions at 25°C and 1 atm, and high dissolved REE concentrations. *Geochimica et Cosmochimica Acta*, 59(3):443-453. [https://doi.org/10.1016/0016-7037\(94\)00381-U](https://doi.org/10.1016/0016-7037(94)00381-U).

Zhu B., Jiang S.Y. 2017. A LA-ICP-MS analysis of rare earth elements on phosphatic grains of the Ediacaran Doushantuo phosphorite at Weng'an, South China: implication for depositional conditions and diagenetic processes. *Geological Magazine*, 154(6):1-17. <https://doi.org/10.1017/S001675681700022X>.

As mineralizações de fosfatos estudadas neste trabalho estão associadas com rochas calcissilicáticas e mármore, formadas em uma paleobacia durante a geração de arcos magmáticos, na colagem paleoproterozoica das blocos que compõem o Cráton do São Francisco, impulsionado pelo aumento do conteúdo de oxigenação da Terra, assim como do intemperismo, o aporte de sedimentos terrígenos e soterramento da matéria orgânica.

O capítulo 2 mostra que as rochas hospedeiras estão metamorfizadas nas fácies anfibolito alto a granulito e possuem uma assembleia prógrada composta por olivina + diopsídio + granada + calcita, enquanto a assembleia retrógrada compreende serpentina + tremolita + microclina + biotita + hornblenda + talco + sericita.

A mineralização é caracterizada pela fluorapatita em concentrações de até 10% em volume modal nos mármore e calcissilicáticas, encontrada de forma disseminada e orientada de acordo com a foliação das rochas, demonstrando que ela foi reconcentrada durante a deformação. Nos dois tipos de mármore verificados (calcíticos e dolomíticos), a sua ocorrência está associada aos dolomíticos, em associação com calcita e diopsídio. Os teores de P_2O_5 alcançam até 3,4%.

A intensa deformação e metamorfismo dificultaram a reconstrução da sucessão metassedimentar do Complexo Tanque Novo-Ipirá. Estruturas sedimentares primárias foram obliteradas, dificultando a interpretação do ambiente deposicional, mas as correlações entre os elementos e padrões geoquímicos, especialmente assinaturas elementos terras-raras e ítrio (ETRY), forneceram informações sobre sua origem e possíveis condições paleoambientais durante e após a sedimentação.

A evidência de um protólito marinho-sedimentar é claro através da interpretação das características mineralógicas, geológicas e dos padrões geoquímicos de ETRY, com verdadeiras anomalias negativas características de Ce e anomalias positivas de Y e Gd, que indicam condições de oxigenações locais. Além disso, é possível restringir que as faixas mineralizadas encontram-se em litofácies com Ce/Ce* entre 0,53 e 1,0, o que atesta um ambiente subóxico, favorável à precipitação de fosfato.

Foi demonstrado a presença de *inputs* terrígenos no ambiente marinho, que geraram baixas razões Y/Ho e maiores concentrações de Al e Zr nos mármore calcíticos (sem mineralizações) e em grande parte das rochas calcissilicáticas. Portanto, gerando uma mistura rochas químicas/carbonáticas com siliciclásticas, pelíticas, siliciclásticas e químicas/carbonáticas com maior contribuição marinha e carbonosas em uma plataforma continental.

Os dados geocronológicos indicam uma idade máxima de 2.128 Ma (zircão mais jovem) para deposição de rochas metassedimentares. No entanto, a idade concordante do núcleo de zircão U-Pb de 2595 ± 18 Ma obtida para este Complexo sugere que esta sucessão possui fontes Paleoproterozóicas e Neoarqueanas. Os sedimentos depositados na paleobacia podem ter originados da erosão de terrenos arqueanos ou de um terreno com herança arqueana. A população arqueana mostram núcleos de zircão na faixa de 2.573–2.736 Ma. Outra população possui núcleo de zircão herdado do Paleoproterozóico, entre 2.453 e 2.128 Ma.

Esses resultados são correlacionados com o início da oxigenação da atmosfera e da superfície oceânica, compatível com modelos fosfogenéticos de águas rasas em ambientes peritidais, onde a fonte do fósforo seriam provenientes do intenso intemperismo químico, causado pela deglaciação Huroniana, alcançando os oceanos através de inputs detríticos. Neste ambiente, a disponibilização do P ocorreria em regiões mais profundas da paleobacia, a partir da sintetização de bactérias anaeróbicas, gerando P solúvel na coluna d'água, desta maneira, precipitando-se nas zonas sub-óxicas, associados com calcários dolomíticos e rochas mistas carbonáticas e siliciclásticas mais distais da região plataformal, sob maiores influências marinhas, do que continentais.

O capítulo 3 demonstra as assinaturas isotópicas de C e O nos mármore dolomíticos e calcíticos do TNIC e mármore do RSC, e compara com valores encontrados na literatura do JV, discutindo a implicação metalogenética e tectônica destes resultados com a associação de C-P-Fe nas paleobacias paleoproterozoicas. As variações de ^{13}C , ^{18}O versus Mn/Sr, Fe/Sr, Ca/Sr e Ca/Mg demonstram que as litofácies selecionadas exibem efeitos limitados de diagênese e metamorfismo, sendo possível considerar os valores isotópicos encontrados.

Analisando os mármore das sequências carbonáticas estudadas, todas as ocorrências de fosfato estão relacionadas com um ambiente subóxico e que há uma intrínseca correlação entre o ambiente deposicional.

As análises isotópicas de C e O realizadas em carbonatos dos mármore do TNIC e RSC são associados com carbonatos marinhos e com aqueles formados no Evento Lomagundi-Jatuli, apresentando excursões positivas de $\delta^{13}\text{C}_{\text{V-PDB}}$ entre +6,13 a + 9,69%, sendo que a maioria das amostras apresentam um intervalo de + 6,13 a +7,36% no TNIC e de 5.38 e 6.78% no RSC. No TNIC os valores reduzidos verificados em zona escarnítica, com $\delta^{13}\text{C}_{\text{V-PDB}}$, (-5,72) demonstra o efeito da alta razão fluido/rocha.

As estimativas de idade mínima de deposição dos mármore do TNIC é de 2.072 Ga e no RSC é de 2.068 Ga. Enquanto do JV, assim como do Greentone Belt do Rio Itapicuru têm as idades de formação de seus protólitos estimadas em 2,098 Ga. Os seus protólitos carbonáticos, que possuem assinaturas isotópicas similares às do TNIC, foram depositados no final do evento Lomagundi, que teve seu início após uma série de três glaciações (2,4, 2,352 e 2,297Ga).

A sequência carbonática do TNIC foi precipitada em um oceano que se estendeu por toda a extensão nordeste do Cráton do São Francisco, onde posteriormente, seria formado após a colisão dos blocos que o compõem, o Orógeno Itabuna-Salvador-Curaçá Norte, margeado por gnaisses arqueanos e sequências meta-vulcanossedimentares paleoproterozoica, dentre elas o Complexo Saúde, também de idade paleoproterozoica. A abertura desse oceano seguiu a fissão do supercontinente Kenorland ou dos primeiros supercrátons, representados no norte do SFC pelo Ciclo Jequié. Não há evidência até o presente, de uma crosta, entretanto, esta hipótese não pode ser descartada, sendo necessário mais investigações sobre o tema.

As assinaturas $(Pr/Yb)_{SN}$ $(Pr/Tb)_{SN}$ e $(Tb/Yb)_{SN}$ do TNIC e JV demonstram a deposição em uma margem continental e em mar aberto, sob influência de *inputs* continentais, provenientes das margens ou de arcos magmáticos. O arco magmático neoarqueano do Complexo Caraíba é o mais provável, de acordo com os dados de zircão apresentados no capítulo 2.

Quanto a formação da sequência do JV é possível que tenha ocorrido sobre a bloco Serrinha ou faça parte da mesma paleobacia do TNIC, nas margens da bloco Serrinha, em uma bacia de margem passiva, retroarco, sendo posteriormente, colocada tectonicamente sobre este. Para confirmar essa hipótese, é preciso trabalhos mais detalhados envolvendo a proveniência dos zircões detríticos nas rochas calcissilicáticas desta sequência. As espessas camadas de mármore do JV em comparação ao TNIC podem indicar que o JV compreende a região plataformal mais distal (com maiores razões Y/Ho), e/ou que esta foi depositada em uma bacia retroarco, facilitando a precipitação de carbonatos.

No RSC a precipitação dos carbonatos está associada com a abertura do *rifte* Salitre, em condições de mar aberto, na Bloco Gavião, provavelmente, sem conexão com o paleobacia do TNIC e JV, mas contemporâneo em termos de idade e de evolução atmosférica e oceânica, na qual as paleobacias foram submetidas no paleoproterozoico, por isso são constatadas também excursões positivas de ^{13}C e presença de fosfato.

Em relação à fosfogênese do SFC com bacias mundiais, observou-se que há uma correlação temporal (isotópica e geocronológica) no evento mineralizante com os Cratons Rio de La Plata e Amazônico na plataforma sulamericana. Com a revisão das mineralizações de fosfatos em bacias mundiais e assinaturas isotópicas de C e O constatou-se que há 3 momentos distintos durante o evento Lomangudi-Jatuli em que há uma íntima relação temporal com as mineralizações em ambientes rasos, sendo eles no início (2.26 – 2.200 Ga), meio (2146 - 2128 Ma) e no final (2021 Ma – 1087) e 2 momentos distintos associados com deposição em ambientes profundos: no meio (2146 Ma – 2.22Ga) e fim (2051 Ma – 1.98 Ga).

A alta produtividade primária deste período associado com o acúmulo de sedimentos ricos em matéria orgânica nas plataformas e encostas continentais, estuários e ambientes deltaicos, foram, portanto os locais preferidos da fosfogênese e configura um esboço regional durante o início do

paleoproterozoico. Desta forma, a associação de rochas carbonáticas e grafitosas no Orógeno Salvador – Curaçá podem ser bons rastreadores metalogenéticos para o fosfato.

Portanto, as mineralizações de fosfatos das litofácies estudadas, estão intimamente conectada com as mudanças drásticas que ocorreram na atmosfera e hidrosfera durante o início do paleoproterozoico. Tendo como fontes os sedimentos ricos em P e Fe continentais provenientes do intemperismo, em períodos pós-glaciais e o soterramento da matéria orgânica e argilominerais associado com ambientes plataformais rasos (TNIC, RSC e JV) e zonas profundas (RSC), conforme o modelo global canônico que explica o Evento. Além disso, apresenta controle faciológico associado principalmente, às fácies rasas, carbonáticas e mistura de carbonatos e siliciclásticos, que configura um controle local, dependente de fácies.

Do ponto de vista científico, é preciso desenvolver estudos mais detalhados no TNIC para investigar a presença de crosta oceânica e de fosfato associado com as litofácies aluminosas, mais profundas da Unidade Pintadas. No JV são necessários dados geocronológicos mais detalhados nesta sequência. Do ponto de vista de exploração mineral, as rochas calcissilicáticas e mármore apresentam grande potencial para agrominerais silicáticos, visto que o P é um macronutriente essencial para as plantas. Além disso, apresentam também altas concentração das bases Ca, Mg e K e, presença de elementos benéficos como o Si. Entretanto, investigações direcionadas à essa pesquisa devem ser feitas, como ensaios agronômicos. Não se descarta a possibilidade de prospectar áreas com maiores concentrações de fósforo e seu uso como fertilizantes tradicionais.

APÊNDICE A – JUSTIFICATIVA DA PARTICIPAÇÃO DOS CO-AUTORES

1. Aroldo Misi (Orientador)

Professor colaborador do Curso de Pós-Graduação em Geologia do IGEO/UFBA, Pesquisador do CPGG/UFBA, desde 1979, fundador e líder do Grupo de Metalogênese e Modelos Metalogenéticos. Possui graduação em Geologia, Doutor em Geologia, Livre-Docente em Geologia Econômica e Metalogênese. Possui diversos trabalhos publicados em periódicos internacionais e nacionais, sobre Ambientes sedimentares e Metalogênese, dentre elas fosfogênese neoproterozoica.

Contribuiu na execução desta pesquisa com orientação, sugestões no que tange à dinâmica de bacias e dos modelos de fosfogênese, sugestões de leitura, correções dos textos e apoio nas resoluções das adversidades ao longo da construção dos artigos.

2. José Haroldo da Silva Sá

Possui graduação em Geologia pela Universidade Federal do Rio de Janeiro (1967), mestrado em Geologia pela Universidade Federal do Rio de Janeiro (1970) e doutorado em Geociências (Recursos Minerais e Hidrogeologia) pela Universidade de São Paulo (1976). Atualmente é consultor do Governo do Estado da Bahia. Tem experiência na área de Geociências, com ênfase em Prospecção Mineral. Contribuiu com dados da Geologia regional, auxiliou nos trabalhos de campos, nas discussões dos dados e com o manuscrito.

3. Luís Rodrigues dos Santos de Oliveira

Possui graduação em Geologia pela UFBA, mestrado em Geologia com pesquisa de fosfogênese paleoproterozoica no Cráton do São Francisco (Complexo Salitre). Já atuou como professor substituto da UFBA nas disciplinas de Geofísica, Geologia de Campo, Geofísica aplicada a geotecnia, Minerais e Rochas industriais. Atua com pesquisas relacionadas a dinâmica evolutiva de bacias Sedimentares e metalogênese.

Contribuiu na execução desta pesquisa com sugestões no que tange a metodologia aplicada, sugestões de leitura, correções e revisões dos manuscritos, reuniões para discussão dos dados obtidos, auxílio na condução da pesquisa, e nas resoluções das adversidades ao longo da construção dos artigos.

4. Pedro Maciel de Paula Garcia

Professor Adjunto/DE de Geologia Econômica da Faculdade de Geociências (FAGEO) da Universidade Federal de Mato Grosso (UFMT), em Cuiabá. Editor da série de livros "SpringerBriefs in Earth Sciences" da Springer Nature. Geólogo (2011), Mestre (2013) e Doutor (2017) em Geologia

pela Universidade Federal da Bahia (UFBA). Docente colaborador do Programa de Pós-Graduação em Geologia da UFBA. Atuou como Coordenador do Programa de Pós-Graduação em Geociências da FAGEO/UFMT entre 2020 e 2023. Desenvolve pesquisas em ambientes metalogenéticos e mineralizações de naturezas variadas (Au, Cu-Au, Pb-Zn, Ni laterítico, diamante, fosfato, Al-ETR, Li, entre outras). Contribui com a confecção de gráficos e mapas, com texto do manuscrito, além de correções e revisões.

5. Ib Câmara

Possui graduação em Geologia e mestrado em pesquisa de grafita do Complexo Tanque Novo-Ipirá. Faz parte do Grupo de Metalogênese e Modelos metalogenéticos da UFA. Tem experiência na área de Geociências com ênfase em Prospecção Mineral e Geologia Ambiental, atuando principalmente nos seguintes temas: mapeamento geológico, geologia estrutural, geoquímica, geofísica, avaliação de impacto ambiental e geoprocessamento. Contribuiu nessa pesquisa com a confecção e edição de figuras temáticas para exposição dos dados.

6. Alcides Nóbrega Sial

Professor titular no Dept. de Geologia da UFPE, em Recife. Geólogo (1966, UFPE), Ph.D. pela Univ. California, Davis, EUA (1974), pós-doutorados nos EUA (Austin, Texas, 09/1977-09/1978; Athens, Georgia, 01/1983-12/1983; Athens, Georgia, 01/1988 a 12/1988) e estágio pós-doutoral na Univ. de Wisconsin, Madison (01-03/2001). Fundador do Laboratório de Isótopos Estáveis (LABISE-UFPE). Um dos primeiros no País na utilização da quimioestratigrafia isotópica na resolução de problemas estratigráficos (Brasil, Argentina, Chile, Uruguai, Colombia, Índia, China). Um dos professores da UFPE mais influentes no mundo em sua área de atuação (PLOS BIOLOGY, 2019, 2020); entre os melhores 36 geocient. bras. (Research.com ranking, 2022).

Contribuiu nessa pesquisa com a análise de isótopos estáveis de C e O em carbonatos e disponibilização desses dados.

7. Débora Correia Rios

Professora no Departamento de Geoquímica da UFBA (2001-2010), tendo lecionado cursos introdutórios e avançados de alunos de graduação e pós-graduação. Atua em pesquisas relacionadas a petrologia ígnea, abrangendo aplicações das ferramentas da geocronologia e geoquímica em amostras de rochas terrestres e extra-terrestres, mas também envolvendo ciência aplicada (ex. rochas ornamentais) e trabalhos com a comunidade para a divulgação científica e o progresso da ciência.

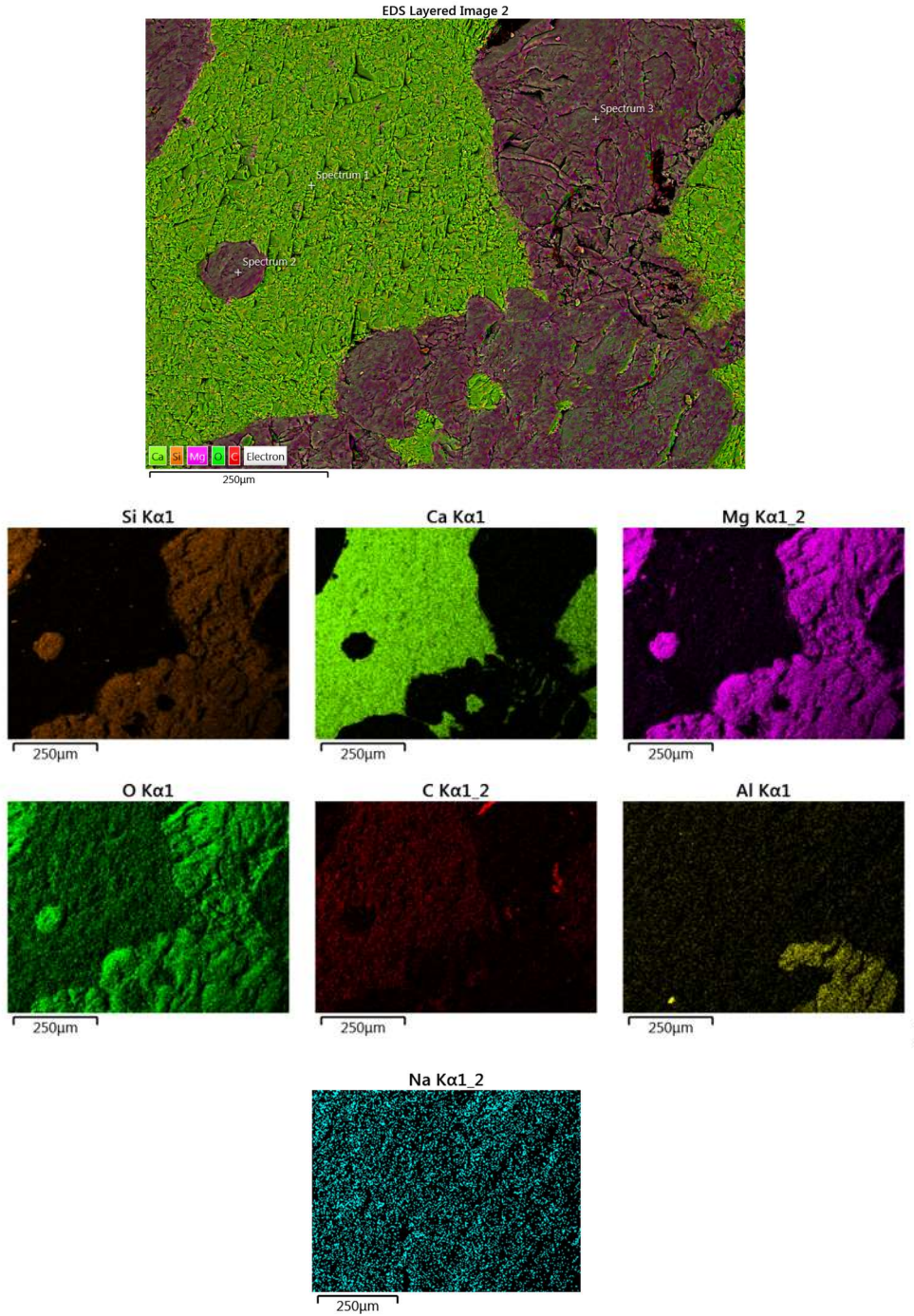
Contribuiu nessa pesquisa com a análise de isótopos estáveis de C e O em carbonatos, disponibilização dos dados e orientação durante as fases iniciais da pesquisa.

8. David Debruyne

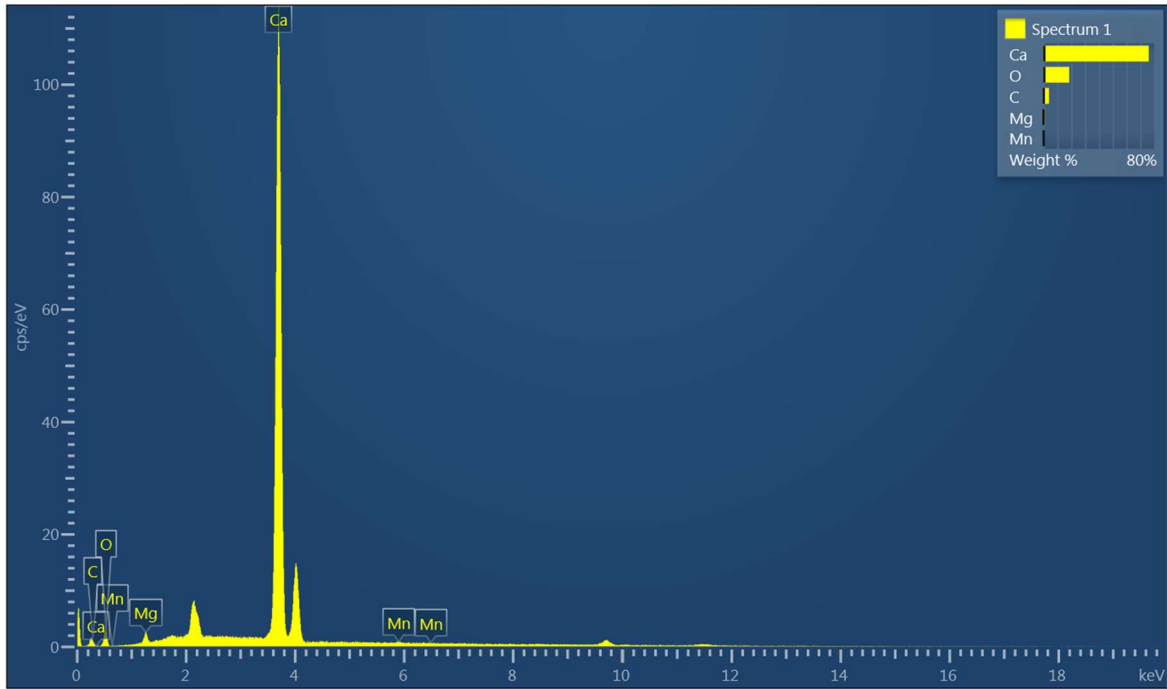
Bacharel e Mestre em Geologia pela Universidade de Ghent (2009). Pós-doutorado na UNICAMP sobre datação de minerais detríticos de sedimentos Proterozóicos em bacias intracontinentais no Cráton do Congo. Foi 2x professor substituto na engenharia geológica (UFPEL) ministrando as seguintes disciplinas: cristalografia, mineralogia, petrologia metamórfica, geomorfologia e geodiversidade, geoquímica e prospecção geoquímica como professor responsável; e professor-colaborador na disciplina de mapeamento geológico. Professor na UNICAMP desde 06/2023 atuando na linha de pesquisa sobre Evolução Crustal e Metalogênese e ministrando Geologia de Campo (I,II), Mineralogia e colaborando na disciplina de Geologia Econômica. Contribui com a pesquisa com a revisão dos dados geocronológicos, litogeoquímicos e com a revisão do inglês no primeiro artigo.

APÊNDICE B – MICROSCOPIA ELETRÔNICA DE VARREDURA

Amostra MM-TR-302 – Mármore dolomítico. Sítio 1 (Cristal 1 e 2)

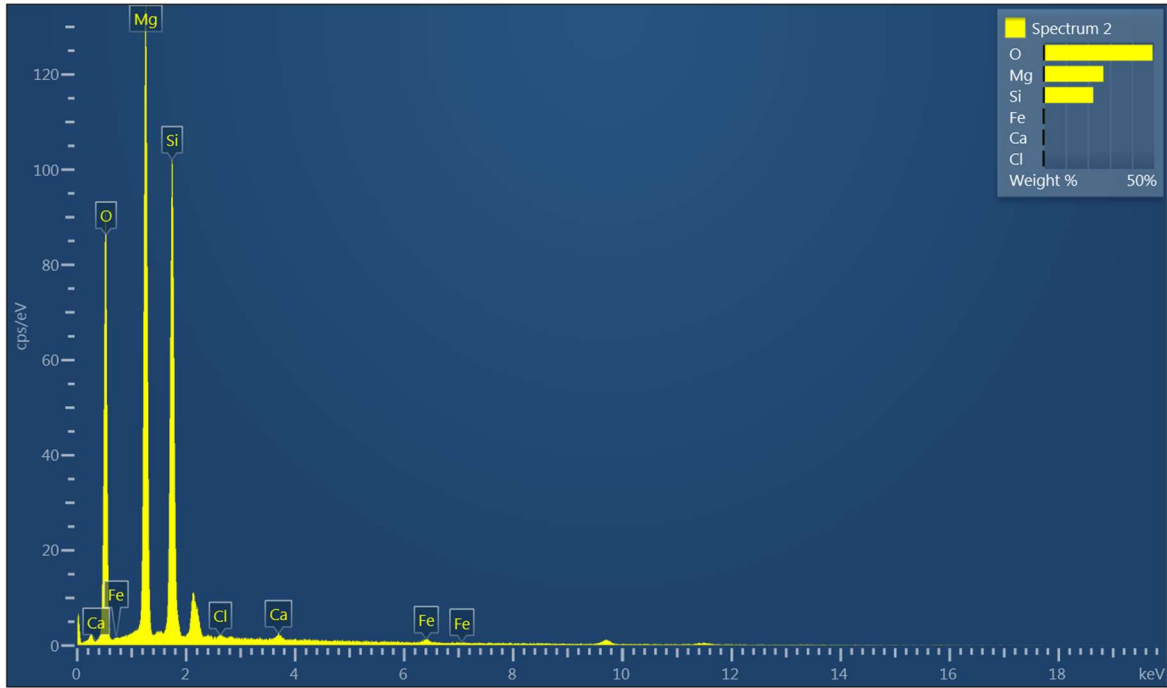


Análise Pontual 1



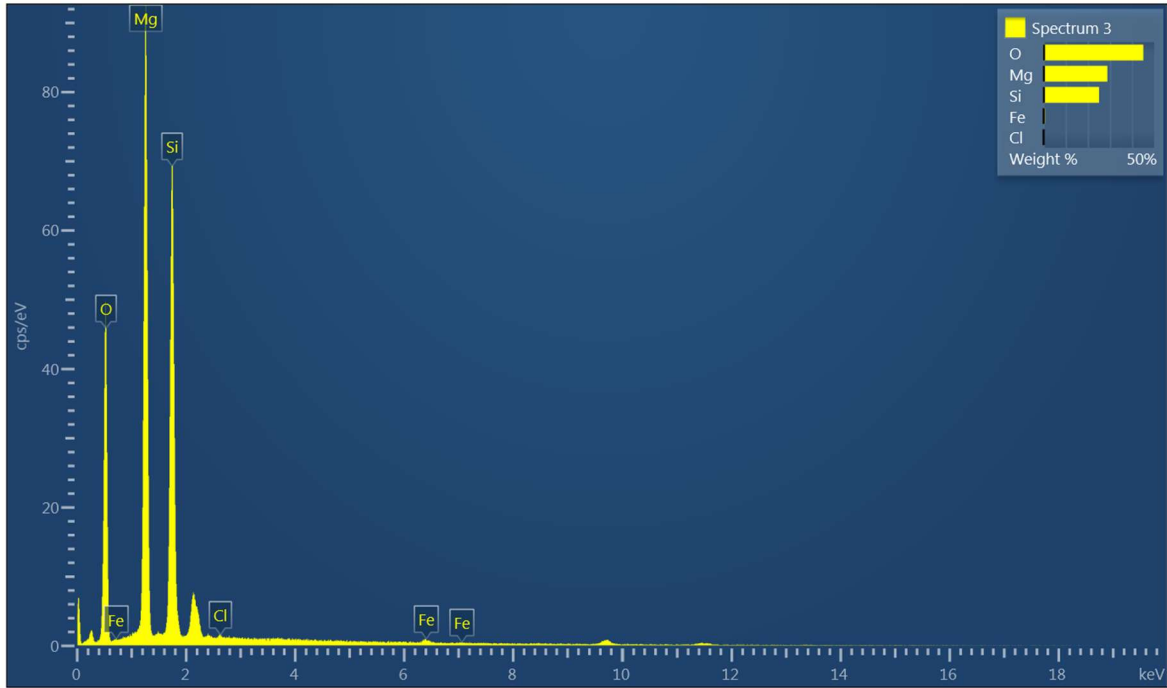
| Element | Line Type | Apparent Concentration | k Ratio | Wt% | Wt% Sigma | Atomic % | Standard Label | Factory Standard | Standard Calibration Date |
|---------|-----------|------------------------|---------|--------|-----------|----------|----------------|------------------|---------------------------|
| C | K series | 0.30 | 0.00301 | 3.94 | 0.25 | 9.56 | C Vit | Yes | |
| O | K series | 0.92 | 0.00310 | 18.53 | 0.58 | 33.72 | SiO2 | Yes | |
| Mg | K series | 0.20 | 0.00130 | 1.03 | 0.06 | 1.24 | MgO | Yes | |
| Ca | K series | 24.54 | 0.21930 | 76.15 | 0.58 | 55.30 | Wollastonite | Yes | |
| Mn | K series | 0.08 | 0.00081 | 0.34 | 0.11 | 0.18 | Mn | Yes | |
| Total: | | | | 100.00 | | 100.00 | | | |

Análise Pontual 2



| Element | Line Type | Apparent Concentration | k Ratio | Wt% | Wt% Sigma | Atomic % | Standard Label | Factory Standard | Standard Calibration Date |
|---------|-----------|------------------------|---------|--------|-----------|----------|----------------|------------------|---------------------------|
| O | K series | 26.77 | 0.09010 | 49.29 | 0.23 | 61.37 | SiO2 | Yes | |
| Mg | K series | 14.44 | 0.09576 | 27.08 | 0.16 | 22.19 | MgO | Yes | |
| Si | K series | 10.72 | 0.08493 | 22.48 | 0.15 | 15.94 | SiO2 | Yes | |
| Cl | K series | 0.10 | 0.00083 | 0.20 | 0.04 | 0.11 | NaCl | Yes | |
| Ca | K series | 0.22 | 0.00195 | 0.36 | 0.04 | 0.18 | Wollastonite | Yes | |
| Fe | K series | 0.32 | 0.00323 | 0.59 | 0.07 | 0.21 | Fe | Yes | |
| Total: | | | | 100.00 | | 100.00 | | | |

Análise Pontual 3



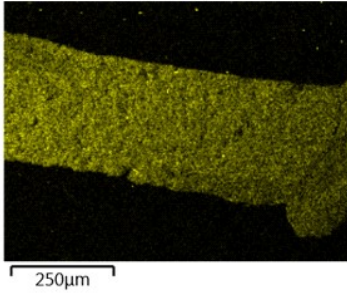
| Element | Line Type | Apparent Concentration | k Ratio | Wt% | Wt% Sigma | Atomic % | Standard Label | Factory Standard | Standard Calibration Date |
|---------|-----------|------------------------|---------|--------|-----------|----------|----------------|------------------|---------------------------|
| O | K series | 14.42 | 0.04852 | 45.14 | 0.25 | 57.34 | SiO2 | Yes | |
| Mg | K series | 9.79 | 0.06492 | 28.84 | 0.18 | 24.11 | MgO | Yes | |
| Si | K series | 7.35 | 0.05824 | 25.13 | 0.17 | 18.18 | SiO2 | Yes | |
| Cl | K series | 0.06 | 0.00051 | 0.20 | 0.04 | 0.11 | NaCl | Yes | |
| Fe | K series | 0.23 | 0.00233 | 0.69 | 0.08 | 0.25 | Fe | Yes | |
| Total: | | | | 100.00 | | 100.00 | | | |

MM-TR-302 - Sítio 2 (CRISTAIS 2 E 3)

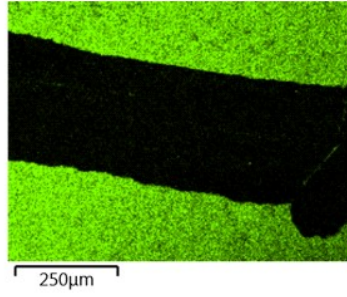
EDS Layered Image 3



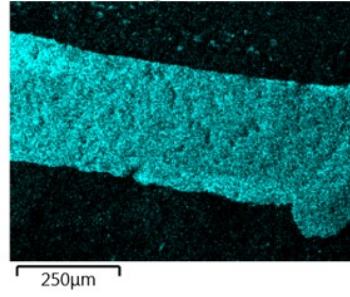
Si Kα1



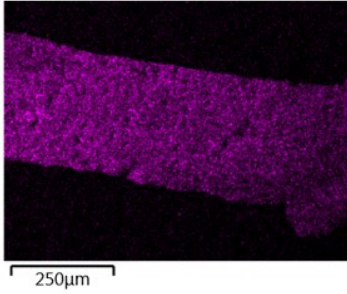
Ca Kα1



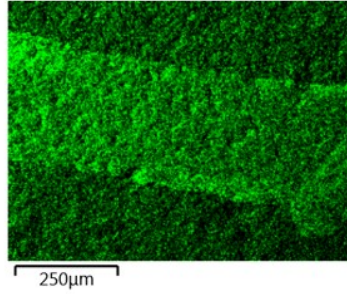
Mg Kα1_2



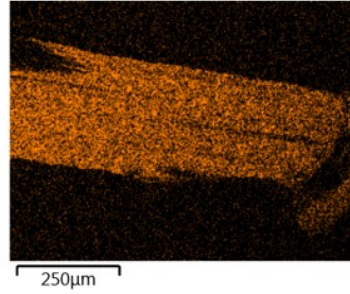
Al Kα1



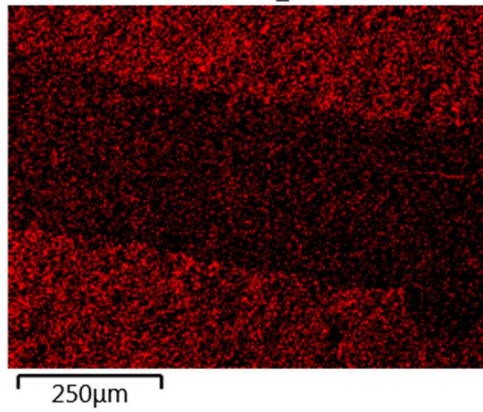
O Kα1



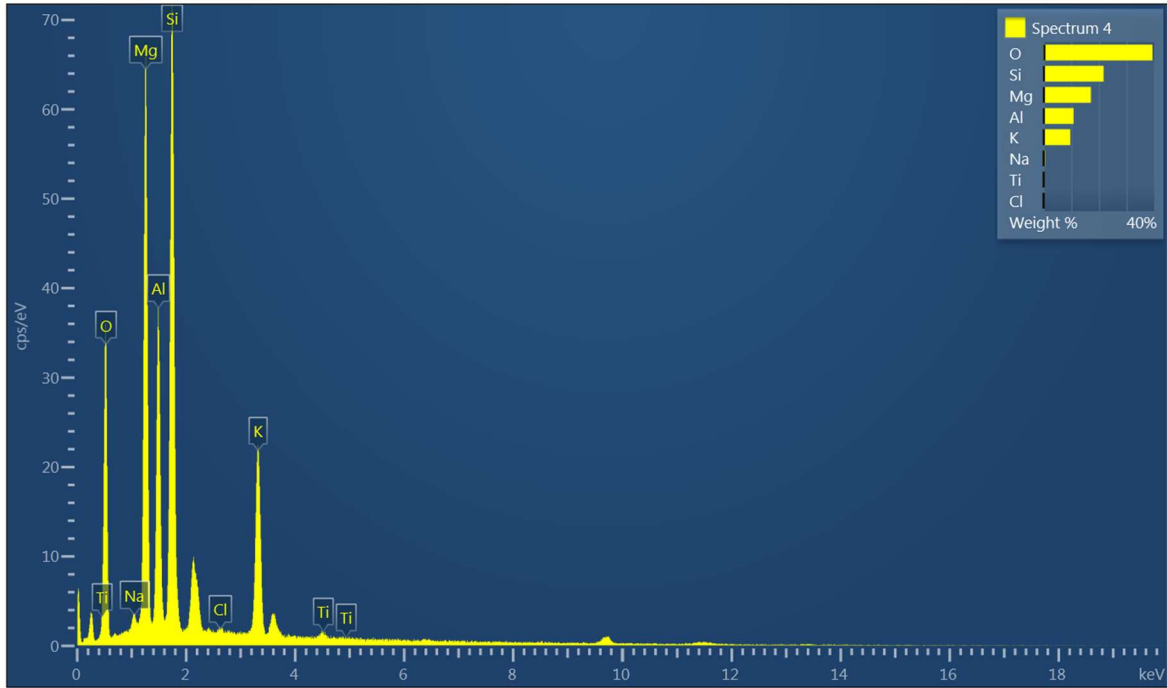
K Kα1



C Kα1_2



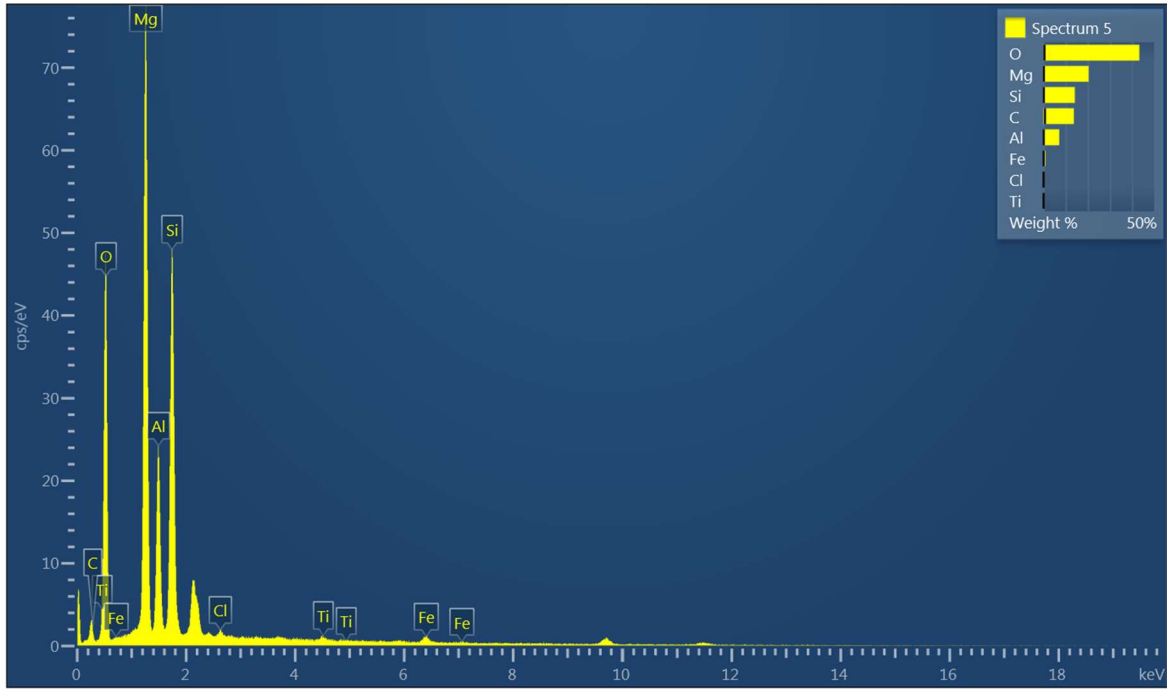
Análise Pontual 4



| Element | Line Type | Apparent Concentration | k Ratio | Wt% | Wt% Sigma | Atomic % | Standard Label | Factory Standard | Standard Calibration Date |
|---------|-----------|------------------------|---------|-------|-----------|----------|----------------|------------------|---------------------------|
| O | K series | 10.33 | 0.03475 | 39.39 | 0.32 | 53.16 | SiO2 | Yes | |
| Na | K series | 0.26 | 0.00111 | 0.60 | 0.07 | 0.56 | Albite | Yes | |
| Mg | K series | 6.84 | 0.04537 | 17.15 | 0.15 | 15.23 | MgO | Yes | |
| Al | K series | 3.72 | 0.02674 | 10.85 | 0.13 | 8.69 | Al2O3 | Yes | |
| Si | K series | 7.50 | 0.05943 | 21.72 | 0.17 | 16.70 | SiO2 | Yes | |
| Cl | K series | 0.07 | 0.00062 | 0.20 | 0.05 | 0.12 | NaCl | Yes | |
| K | K series | 4.24 | 0.03591 | 9.67 | 0.11 | 5.34 | KBr | Yes | |
| Ti | K series | 0.16 | 0.00162 | 0.43 | 0.06 | 0.19 | Ti | Yes | |

| | | | | | | | | | |
|--------|--|--|--|--------|--|--------|--|--|--|
| Total: | | | | 100.00 | | 100.00 | | | |
|--------|--|--|--|--------|--|--------|--|--|--|

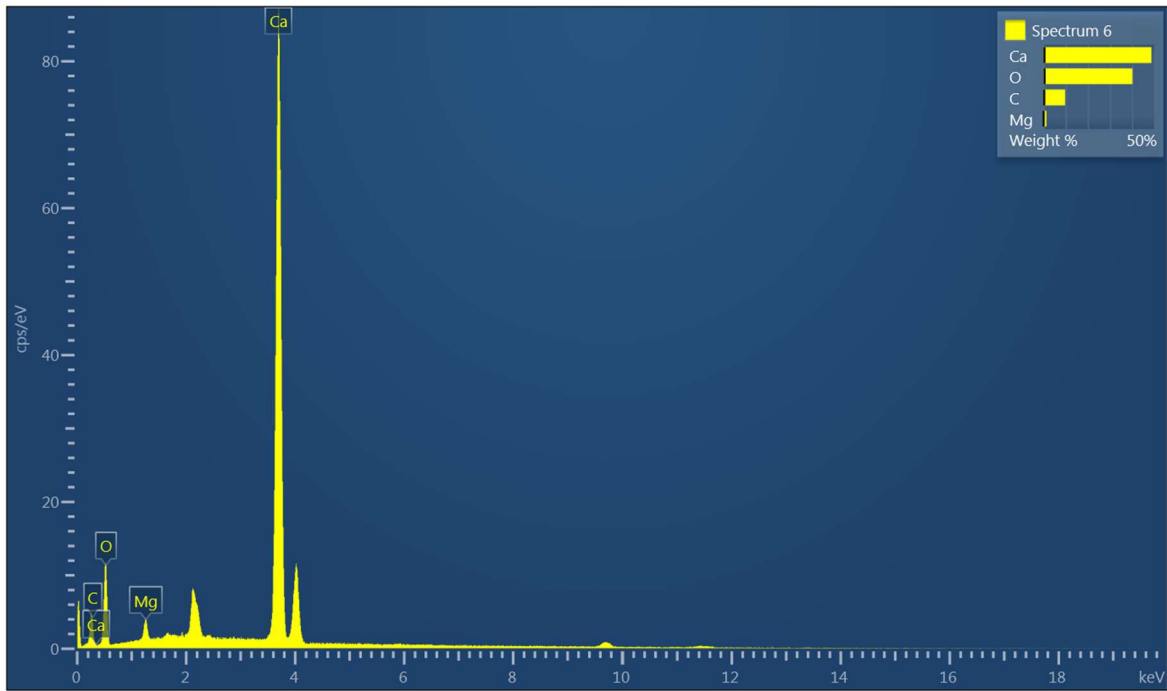
Análise Pontual 5



| Element | Line Type | Apparent Concentration | k Ratio | Wt% | Wt% Sigma | Atomic % | Standard Label | Factory Standard | Standard Calibration Date |
|---------|-----------|------------------------|---------|-------|-----------|----------|----------------|------------------|---------------------------|
| C | K series | 0.52 | 0.00516 | 13.70 | 0.69 | 20.82 | C Vit | Yes | |
| O | K series | 13.80 | 0.04645 | 43.29 | 0.42 | 49.38 | SiO2 | Yes | |
| Mg | K series | 8.16 | 0.05413 | 20.37 | 0.21 | 15.29 | MgO | Yes | |
| Al | K series | 2.32 | 0.01666 | 7.08 | 0.11 | 4.79 | Al2O3 | Yes | |
| Si | K series | 4.96 | 0.03927 | 14.15 | 0.16 | 9.20 | SiO2 | Yes | |
| Cl | K series | 0.11 | 0.00096 | 0.29 | 0.04 | 0.15 | NaCl | Yes | |
| Ti | K series | 0.10 | 0.00101 | 0.25 | 0.04 | 0.10 | Ti | Yes | |

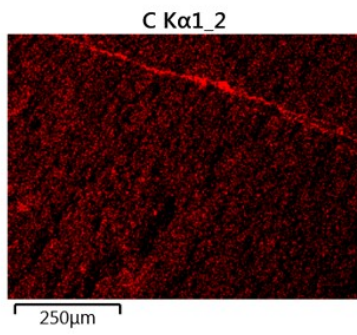
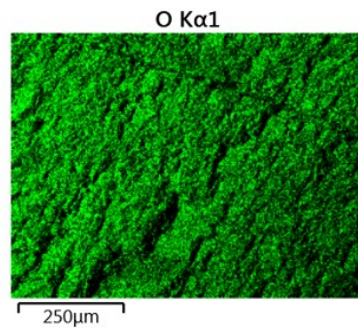
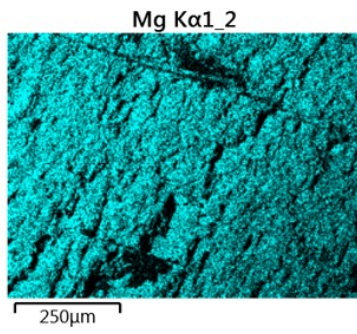
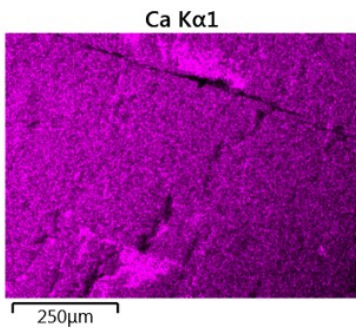
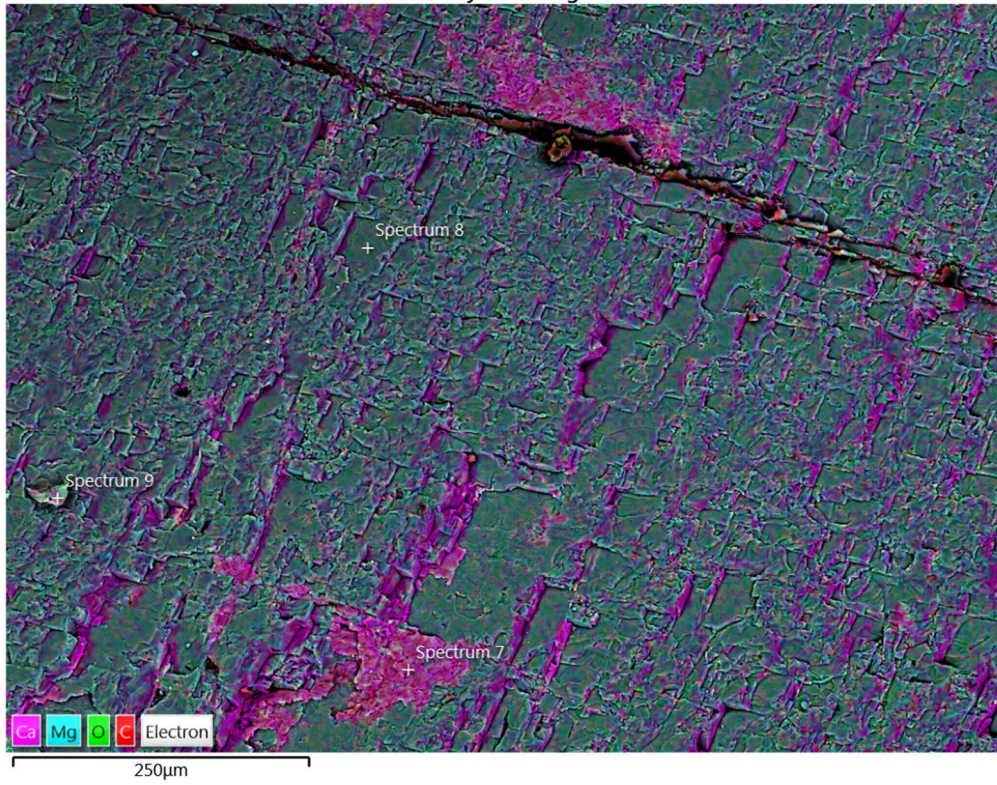
| | | | | | | | | | |
|--------|----------|------|---------|--------|------|--------|----|-----|--|
| Fe | K series | 0.35 | 0.00354 | 0.87 | 0.07 | 0.28 | Fe | Yes | |
| Total: | | | | 100.00 | | 100.00 | | | |

Análise Pontual 6

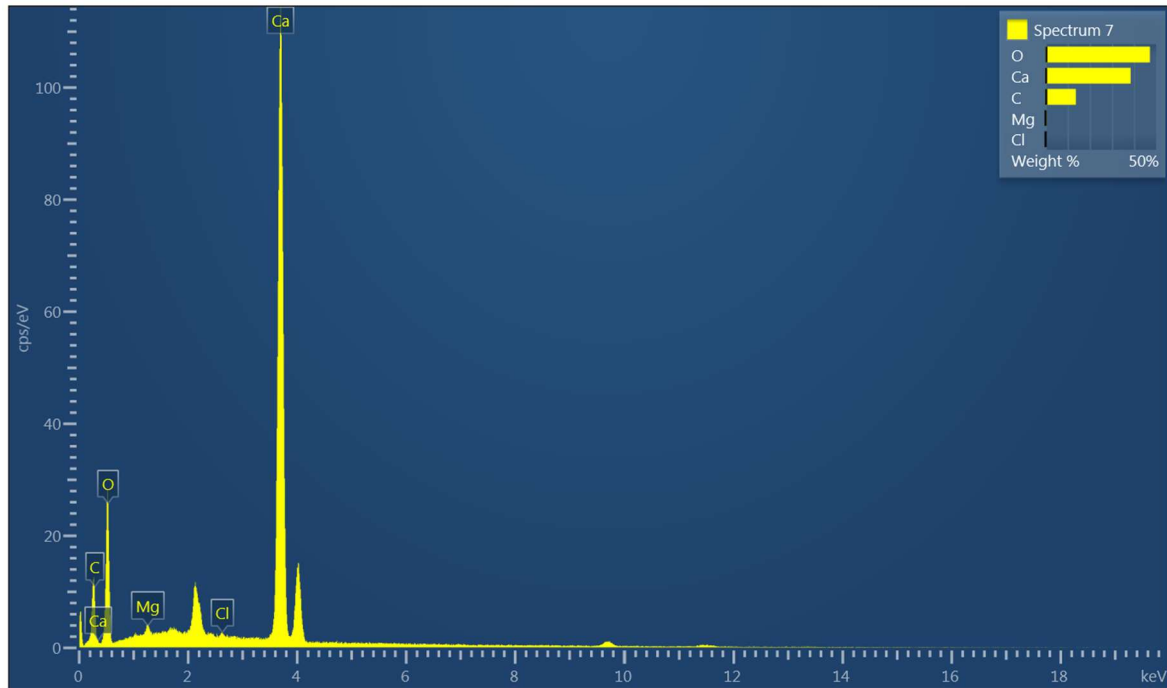


| Element | Line Type | Apparent Concentration | k Ratio | Wt% | Wt% Sigma | Atomic % | Standard Label | Factory Standard | Standard Calibration Date |
|---------|-----------|------------------------|---------|--------|-----------|----------|----------------|------------------|---------------------------|
| C | K series | 0.90 | 0.00904 | 9.73 | 0.32 | 17.64 | C Vit | Yes | |
| O | K series | 3.43 | 0.01156 | 40.19 | 0.46 | 54.69 | SiO2 | Yes | |
| Mg | K series | 0.30 | 0.00200 | 1.30 | 0.06 | 1.16 | MgO | Yes | |
| Ca | K series | 18.72 | 0.16727 | 48.79 | 0.41 | 26.51 | Wollastonite | Yes | |
| Total: | | | | 100.00 | | 100.00 | | | |

EDS Layered Image 4

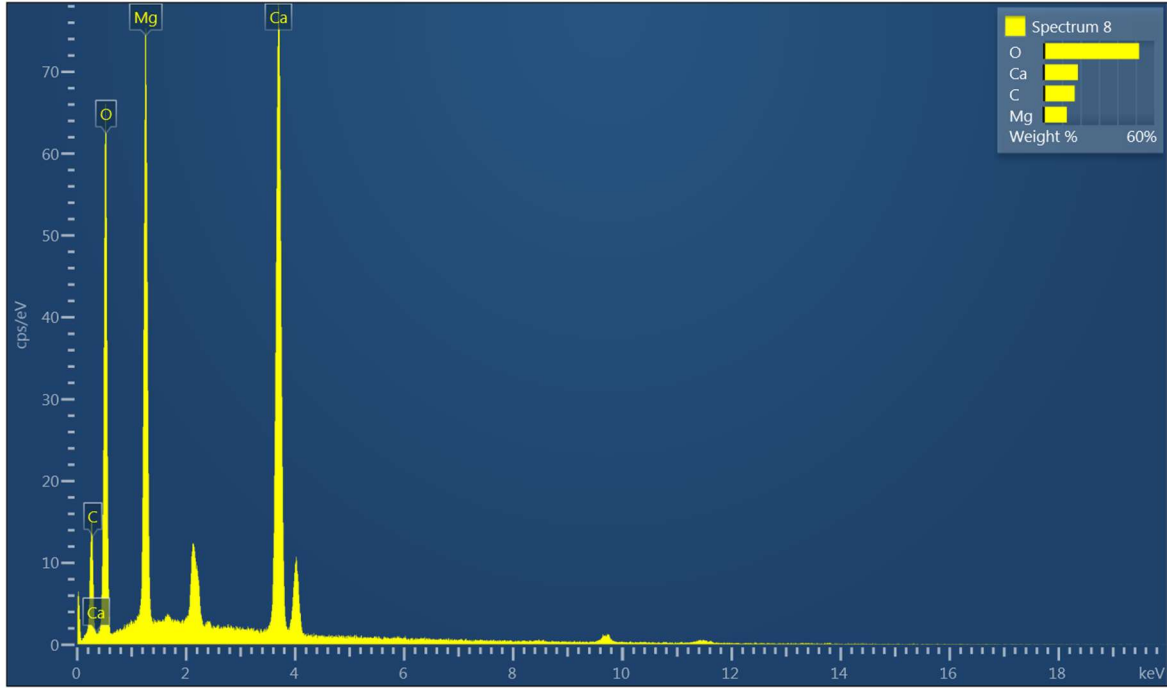


Análise Pontual 7



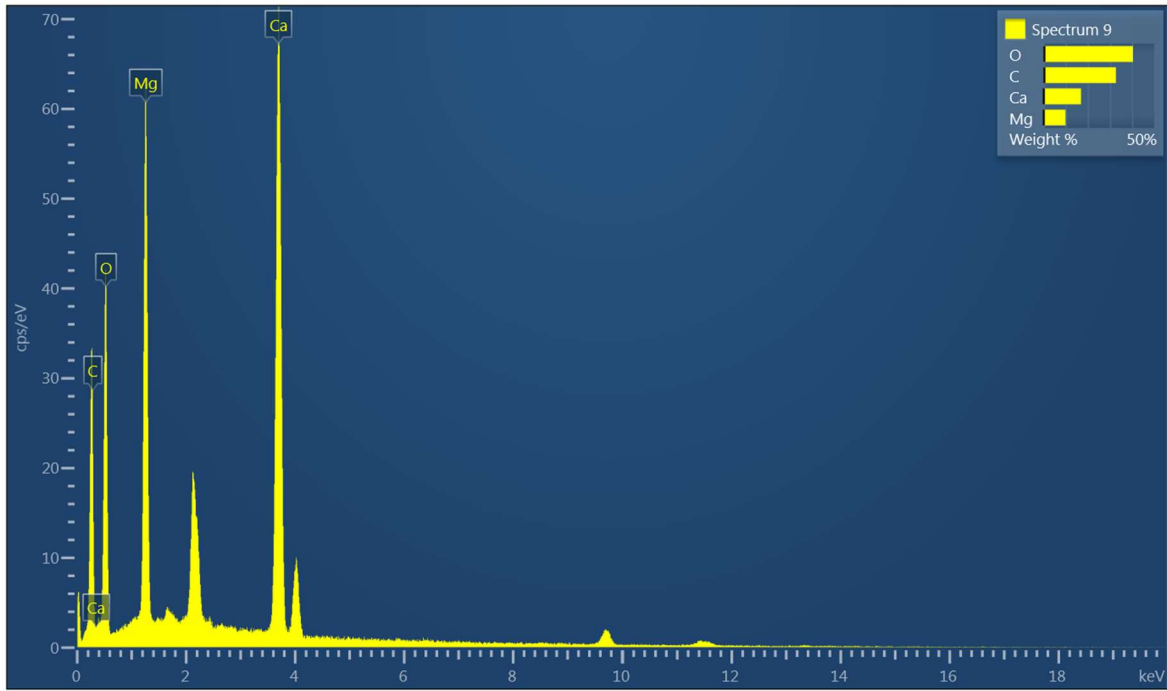
| Element | Line Type | Apparent Concentration | k Ratio | Wt% | Wt% Sigma | Atomic % | Standard Label | Factory Standard | Standard Calibration Date |
|---------|-----------|------------------------|---------|--------|-----------|----------|----------------|------------------|---------------------------|
| C | K series | 2.20 | 0.02198 | 13.71 | 0.34 | 22.50 | C Vit | Yes | |
| O | K series | 7.95 | 0.02677 | 47.18 | 0.40 | 58.11 | SiO2 | Yes | |
| Mg | K series | 0.19 | 0.00123 | 0.47 | 0.05 | 0.38 | MgO | Yes | |
| Cl | K series | 0.09 | 0.00083 | 0.16 | 0.03 | 0.09 | NaCl | Yes | |
| Ca | K series | 24.67 | 0.22040 | 38.48 | 0.31 | 18.92 | Wollastonite | Yes | |
| Total: | | | | 100.00 | | 100.00 | | | |

Análise Pontual 8



| Element | Line Type | Apparent Concentration | k Ratio | Wt% | Wt% Sigma | Atomic % | Standard Label | Factory Standard | Standard Calibration Date |
|---------|-----------|------------------------|---------|--------|-----------|----------|----------------|------------------|---------------------------|
| C | K series | 2.77 | 0.02770 | 16.91 | 0.36 | 25.00 | C Vit | Yes | |
| O | K series | 19.34 | 0.06507 | 51.85 | 0.33 | 57.55 | SiO2 | Yes | |
| Mg | K series | 7.75 | 0.05142 | 12.58 | 0.12 | 9.19 | MgO | Yes | |
| Ca | K series | 16.80 | 0.15009 | 18.65 | 0.15 | 8.26 | Wollastonite | Yes | |
| Total: | | | | 100.00 | | 100.00 | | | |

Análise Pontual 9

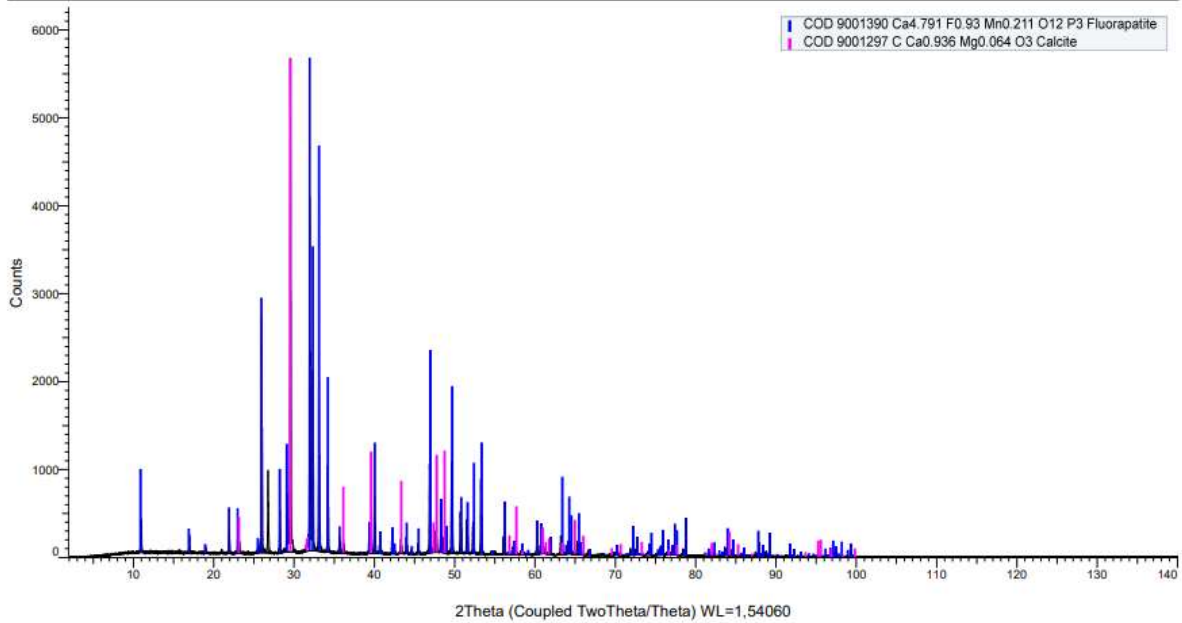


| Element | Line Type | Apparent Concentration | k Ratio | Wt% | Wt% Sigma | Atomic % | Standard Label | Factory Standard | Standard Calibration Date |
|---------|-----------|------------------------|---------|--------|-----------|----------|----------------|------------------|---------------------------|
| C | K series | 6.29 | 0.06289 | 32.71 | 0.38 | 44.79 | C Vit | Yes | |
| O | K series | 12.27 | 0.04131 | 40.41 | 0.36 | 41.54 | SiO2 | Yes | |
| Mg | K series | 6.38 | 0.04235 | 9.94 | 0.11 | 6.72 | MgO | Yes | |
| Ca | K series | 15.16 | 0.13547 | 16.94 | 0.15 | 6.95 | Wollastonite | Yes | |
| Total: | | | | 100.00 | | 100.00 | | | |

APÊNDICE C – DIFRATOMETRIA DE RAIOS-X

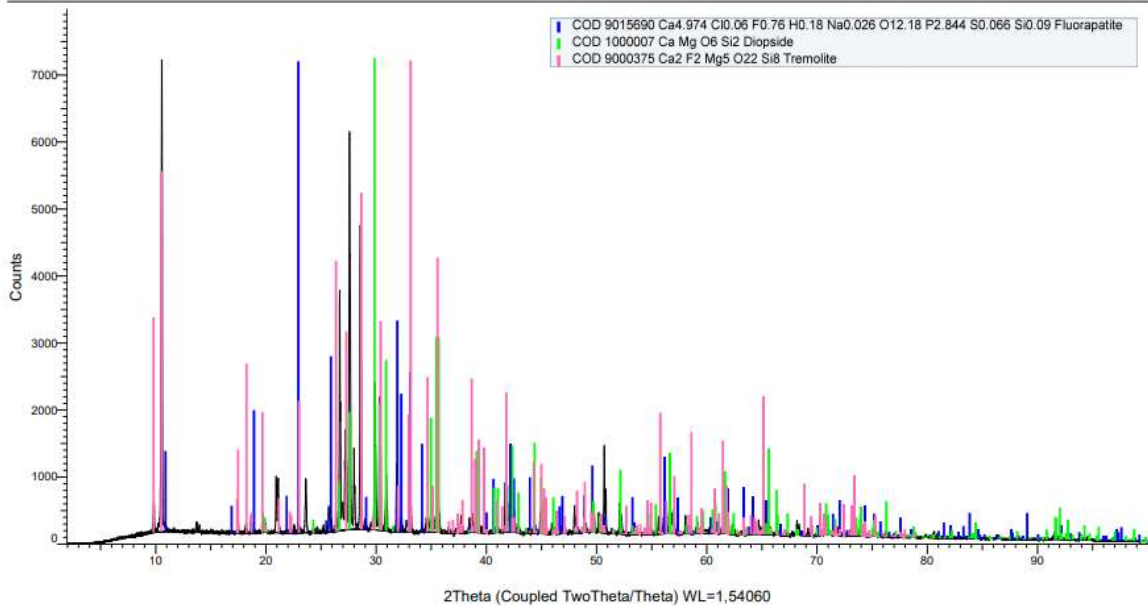
Amostra de mármore – TR-392 (Fluorapatita em azul e calcita em rosa)

(Coupled TwoTheta/Theta)



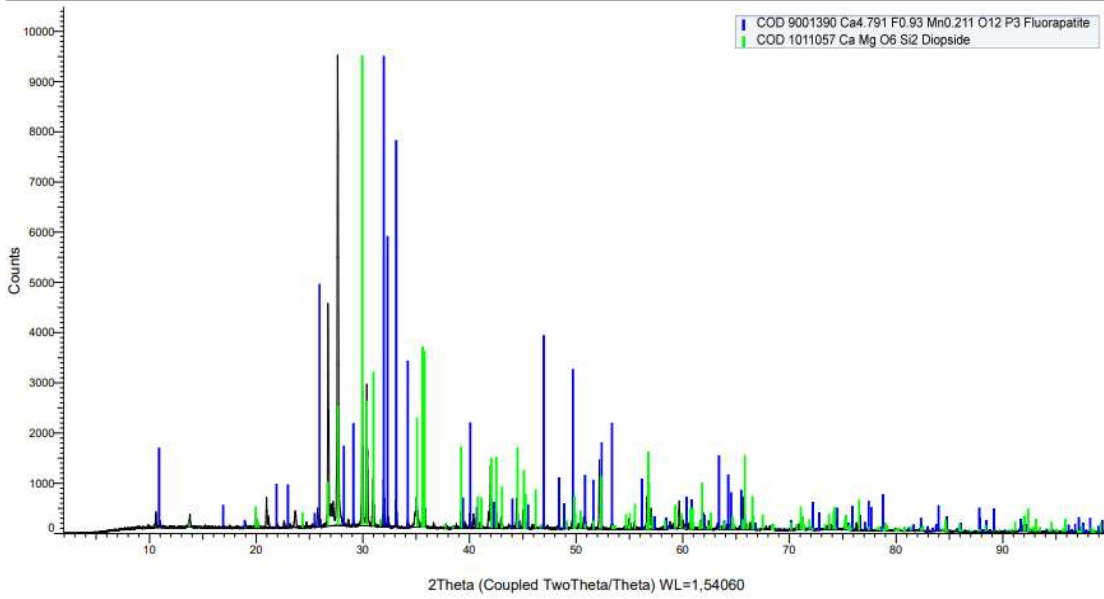
Amostra de rocha calcissilicática – TR389B (Fluorapatita em azul, diopsídio em verde e tremolita em rosa)

(Coupled TwoTheta/Theta)



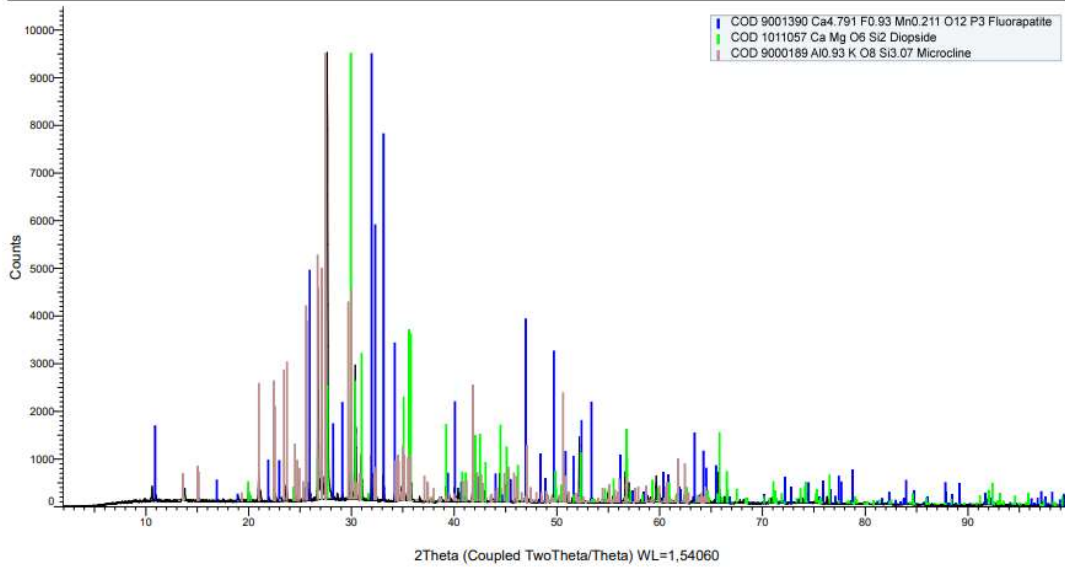
Amostra de rocha calcissilicática – TR-389A (Fluorapatita em azul e calcita em rosa)

(Coupled TwoTheta/Theta)

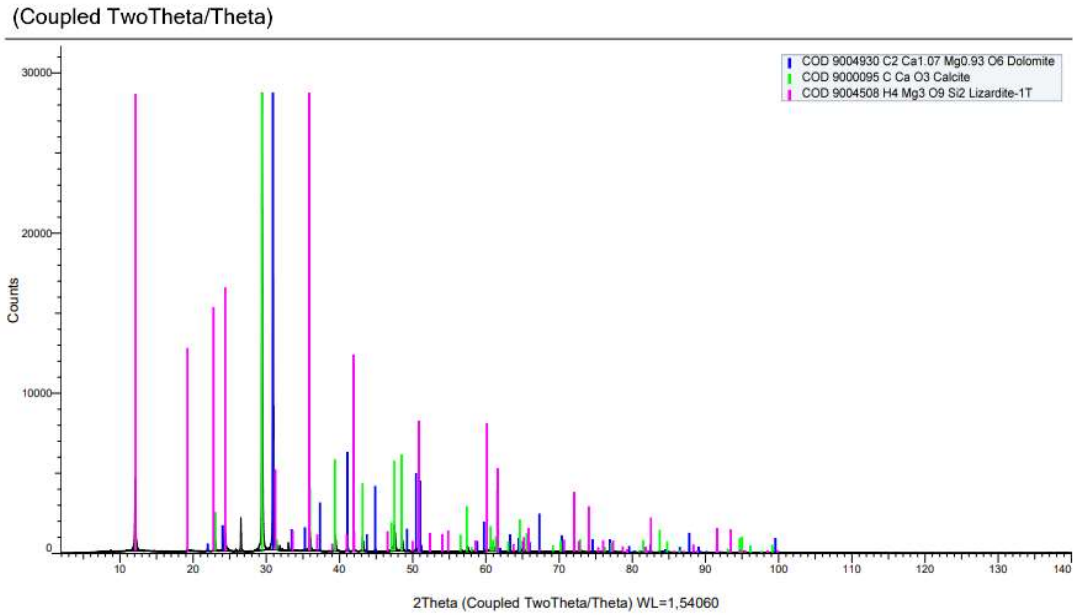


Amostra de rocha calcissilicática – TR-389A (Fluorapatita em azul , diopsídio em verde e microclima em rosa)

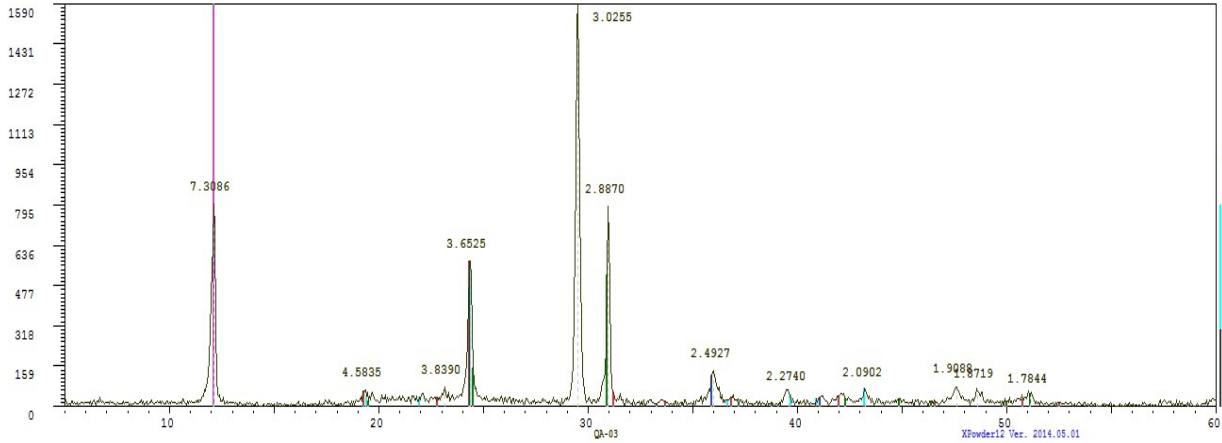
(Coupled TwoTheta/Theta)



Amostra de mármore – TR-302 (Dolomita em azul, calcita em verde e lizardita em rosa)



TR-302 – Identificação de minerais de serpentina em mármore

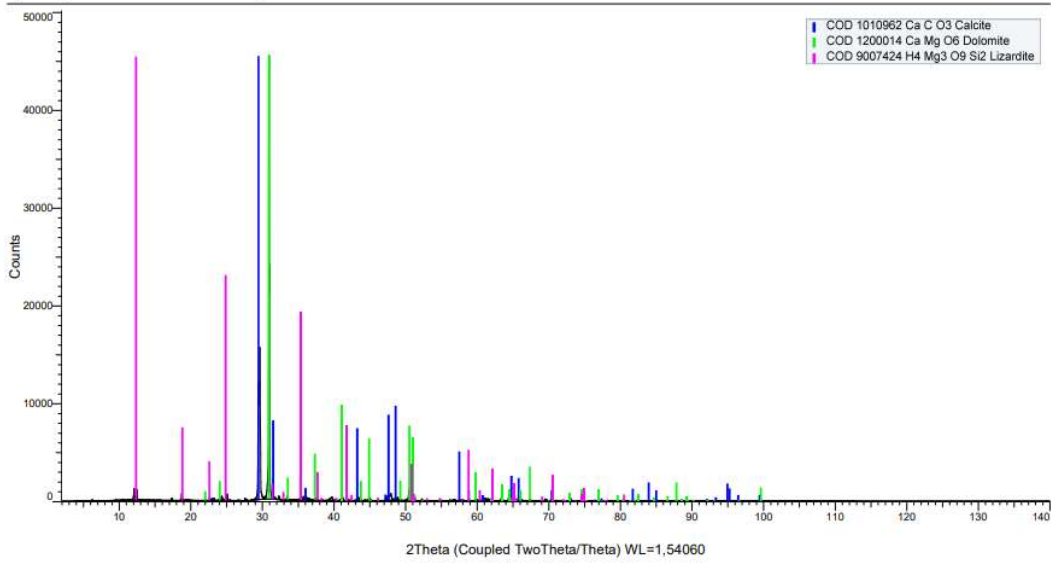


Fases Minerais: Nepouita (35%) $[(Ni, Mg)_3 Si_2 O_5 (OH)_4]$ [Serpentina] ; Crisotila 33%) $Mg_3 Si_2 O_5 (OH)_4$; Lizardita (26%) $Mg_3 Si_2 O_5 (OH)$.

- Amorfo (5,0%) Obs.: Três tipos de Serpentina - Obs.: O material efervesce moderadamente ao HCl frio.

Amostra de mármore – TR-69A (Calcita em azul, dolomita em verde e lizardita em rosa)

(Coupled TwoTheta/Theta)



ANEXO A – REGRAS DE FORMATAÇÃO DA BRAZILIAN JOURNAL OF GEOLOGY (ARTIGO 1)

BRAZILIAN JOURNAL OF GEOLOGY

Form and preparation of manuscripts

Initial Submissions

In order to simplify the submission process, authors may submit their manuscript (text, figures and tables) as a single file. This can be a Word or PDF file, in any format or layout, and figures and tables can be placed within the text. In this case, include the Cover Letter at the beginning of the PDF.

Article structure

There are no strict formatting requirements, but all manuscripts must contain the essential elements needed to convey your manuscript, for example, Abstract, Keywords, Introduction, Materials and Methods, Results, Conclusions, References, Data Availability, Artwork and Tables with Captions.

Electronic artwork

Figures can be placed within the text, but the authors must ensure the figures' quality is high enough for refereeing (all details must be clearly visible; a minimum resolution of 300 dpi is recommended).

Reference formatting

There are no strict requirements on reference formatting at submission. References can be in any style or format as long as the style is consistent. Where applicable, name(s) of author(s), journal title/book title, chapter title/article title, year of publication, volume number/book chapter and the pagination must be present. Use of DOI is highly encouraged. The reference style used by the journal will be applied to the accepted article at the proof stage. Note that missing data will be highlighted at proof stage for the author to correct.

Submission After Acceptance

Once your article has been accepted, editable files (e.g., Word) of the manuscript and tables, as well as high-resolution files of all electronic artwork (see below) are required to typeset your article for final publication. We cannot accept LaTeX source files; if you produce your article with LaTeX, after acceptance you must convert it to an editable format such as Word or RTF (we do not provide such service).

Use of word processing software

Regardless of the file format of the original submission, at revision you must provide us with an editable file of the entire article. Keep the layout of the text as simple as possible. Most formatting codes will be removed and replaced on processing the article. The electronic text should be prepared in a way very similar to that of conventional manuscripts.

To avoid errors, you are strongly advised to use the 'spell-check' and 'grammar-check' functions of your word processor.

Article structure

Divide the article into clearly defined and numbered sections. Subsections should be numbered 1.1 (then 1.1.1, 1.1.2, ...), 1.2, etc. (the abstract is not included in section numbering). Use this numbering also for internal cross-referencing: do not just refer to 'the text'. Any subsection may be given a brief heading. Each heading should appear on its own separate line.

Introduction

State the objectives of the work and provide an adequate background, avoiding a detailed literature survey or a summary of the results.

Material and methods

Provide sufficient detail to allow the work to be reproduced. Methods already published should be indicated by a reference. Only relevant modifications should be described.

Theory/calculation

A Theory section should extend, not repeat, the background to the article already dealt with in the Introduction and lay the foundation for further work. In contrast, a Calculation section represents a practical development from a theoretical basis.

Results

Results should be clear and concise.

Discussion

This should explore the significance of the results of the work, not repeat them. A combined Results and Discussion section is often appropriate. Avoid extensive citations and discussion of published literature.

Conclusions

The main conclusions of the study may be presented in a short Conclusions section, which may stand alone or form a subsection of the Discussion section.

Appendices

If there is more than one appendix, they should be identified as A, B, etc. Formulae and equations in appendices should be given separate numbering: Eq. (A.1), Eq. (A.2), etc.; in a subsequent appendix, Eq. (B.1) and so on. This also applies to tables and figures: Table A.1; Fig. A.1, etc.

Essential title page information

Title. Concise, informative, and interesting. Titles are often used in information-retrieval systems. Avoid abbreviations and formulae where possible.

Author names and affiliations. Please clearly indicate the given name(s) and family name(s) of each author and check that all names are accurately spelled. Present the authors' affiliation addresses (where the actual work was done) below the names. Indicate all affiliations with a lower-case superscript number immediately after the author's name and in front of the appropriate address. Provide the full postal address of each affiliation, including the country name and, if available, the e-mail address of each author.

Corresponding author. Clearly indicate who will handle correspondence at all stages of refereeing, publication, and post-publication. Ensure that the e-mail address is given and that contact details are kept up to date by the corresponding author.

Present/permanent address. If an author has moved since the work described in the article was done, or was visiting at the time, a 'Present address' (or 'Permanent address') may be indicated as a footnote to that author's name. The address at which the author actually did the work must be retained as the main affiliation address. Superscript Arabic numerals are used for such footnotes.

Abstract

A concise (maximum 400 words) and factual abstract is required. The abstract should state briefly the purpose of the research, the principal results and major conclusions. An abstract is often presented separately from the article, so it must be able to stand alone. For this reason, References should be avoided, but if essential, then cite the author(s) and year(s). Also, non-standard or uncommon abbreviations should be avoided, but if essential they must be defined at their first mention in the abstract itself.

Keywords

Immediately after the abstract, provide a maximum of 6 keywords, using American spelling and avoiding general and plural terms and multiple concepts (avoid, for example, 'and', 'of '). Be sparing with abbreviations: only abbreviations firmly established in the field may be eligible. These keywords will be used for indexing purposes.

Abbreviations

Define abbreviations that are not standard in this field in a footnote to be placed on the first page of the article. Such abbreviations that are unavoidable in the abstract must be defined at their first mention there, as well as in the footnote. Ensure consistency of abbreviations throughout the article.

Acknowledgements

Collate acknowledgements in a separate section at the end of the article before the references and do not, therefore, include them on the title page, as a footnote to the title or otherwise. List here those individuals who provided help during the research (e.g., providing language help, writing assistance or proofreading the article, etc.), as well as institutions and funding agencies.

Though it is not mandatory, it is always appreciated when authors thank the reviewers, Associate Editor and Editor-in-Chief in the Acknowledgments, by name if their identity has been revealed, or as "anonymous reviewers" if you do not know their names.

Units

Follow internationally accepted rules and conventions: use the international system of units (SI). If other units are mentioned, please give their equivalent in SI.

Math formulae

Please submit math equations as editable text and not as images. Present simple formulae in line with normal text where possible and use the solidus (/) instead of a horizontal line for small fractional terms, e.g., X/Y. In principle, variables are to be presented in italics. Powers of e are often more conveniently denoted by exp. Number consecutively any equations that have to be displayed separately from the text (if referred to explicitly in the text).

Electronic artwork

General points

- Make sure you use uniform lettering and sizing of your original artwork.
- Preferred fonts: use only sans-serif fonts such as Arial, Sans or Helvetica. For mathematical symbols and Greek letters, use Symbol.
- Number the illustrations according to their sequence in the text.
- Use a logical naming convention for your artwork files.
- For Word submissions only, you may provide figures, their captions, and tables within a single file at the revision stage.

Formats

Regardless of the application used, when your electronic artwork is finalized, please ‘save as’ or convert the images to one of the following formats (note the resolution requirements for line drawings, halftones, and line/halftone combinations given below):

- EPS (or PDF): Vector drawings. Embed the font or save the text as ‘graphics’.
- TIFF (or JPG): Color or grayscale photographs (half-tones): always use a minimum of 300 dpi.
- TIFF (or JPG): Bitmapped line drawings: use a minimum of 600 dpi.
- TIFF (or JPG): Combined bitmapped line/half-tone (color or grayscale) images: a minimum of 500 dpi is required.

Please do not:

- Supply files that are optimized for screen use (e.g., GIF, BMP, PICT, WPG); the resolution is too low.
- Supply files that are too low in resolution.
- Submit graphics that are disproportionately large for the content.

Color artwork

Please make sure that artwork files are in an acceptable format — TIFF (or JPEG), EPS (or PDF) — and with the correct resolution. If, together with your accepted article, you submit usable color figures, these will appear in color online.

Note: for maps of South America including political boundaries between Guyana and Suriname, consider using the limits provided in this file: http://sfbjg.siteoficial.ws/Sf/2023/borders_shp.zip

Figure captions

Ensure that each illustration has a caption. A caption should comprise a brief title (not on the figure itself) and a description of the illustration. Keep text in the illustrations to a minimum, but be sure to explain all symbols and abbreviations used.

Tables

Please submit tables as editable text and not as images. Tables can be placed either next to the relevant text in the article, or on separate page(s) at the end. Number tables consecutively in accordance with their appearance in the text and place any table notes below the table body. Be sparing in the use of tables and ensure that the data presented in them do not duplicate results described elsewhere in the article. Please avoid using vertical rules. Long tables should be published as Supplemental Material (i.e., deposited in a data repository), either by request of the authors or by suggestion of the editors.

Supplemental Material

Long tables, maps, analytic results or other material considered relevant to the article but not essential to the main text can be published in digital format as Supplemental Material. We request the authors to deposit all supplemental material for their articles in a data repository such as the BJGEO dataverse. Refer to these items in the manuscript as Supp.Tab.X, Supp.Fig.X.

Citation in text

Please ensure that every reference cited in the text is also present in the reference list (and vice versa). Any references cited in the abstract must be given in full. Unpublished results and personal communications are not recommended in the reference list, but may be mentioned in the text. If these references are included in the reference list, they should follow the standard reference style of the journal and should include a substitution of the publication date with either ‘Unpublished results’ or ‘Personal communication’. Citation of a reference as ‘in press’ implies that the item has been accepted for publication.

Web references

As a minimum, the full URL should be given and the date when the reference was last accessed. Any further information, if known (DOI, author names, dates, reference to a source publication, etc.), should also be given. Web references can be listed separately (e.g., after the reference list) under a different heading if desired, or can be included in the reference list.

Reference formatting

There are no strict requirements on reference formatting at submission. References can be in any style or format as long as the style is consistent. Where applicable, name(s) of author(s), journal title/book title, chapter title/article title, year of publication, volume number/book chapter and the pagination must be present. Use of DOI is highly encouraged. The reference style used by the journal will be applied to the accepted article by SCIELO at the proof stage. Note that missing data will be highlighted at proof stage for the author to correct.

Reference style

All publications cited in the text should be presented in a list of references following the text of the manuscript. In the text refer to the author's name (without initials) and year of publication (e.g. "Since Almeida (1986) has shown that..." or "This is in agreement with results obtained later (Trompette 1994; Heilbron and Machado 2003)").

For three or more authors use the first author followed by "et al.", in the text. The list of references should be arranged alphabetically by authors' names. The manuscript should be carefully checked to ensure that the spelling of authors' names and dates are exactly the same in the text as in the reference list.

References should be given in the following form:

Papers in scientific journals

Almeida F.F.M. 1986. Distribuição regional e relações tectônicas do magmatismo pós-paleozoico no Brasil. *Revista Brasileira de Geociências*, 16:325-349.

Costa I.P., Bueno G.V., Milhomem P.S., Silva H.S.R.L., Kosin M.D. 2007. Sub-bacia de Tucano Norte e Bacia de Jatobá. *Boletim de Geociências da Petrobras*, 15:445-453.

Escayola M.P., Pimentel M.M., Armstrong R. 2007. Neoproterozoic backarc basin: sensitive high-resolution ion microprobe U-Pb and Sm-Nd isotopic evidence from the eastern Pampean Ranges, Argentina. *Geology*, 35:495-498.

Heilbron, M. and Machado, N. 2003, Timing of terrane accretion in the Neoproterozoic-Eopaleozoic Ribeira orogen (SE Brazil). *Precambrian Research*, 125:87-112.

Books and book chapters

Bedell R., Crósta A.P., Grunsky E. (eds.). 2009. *Remote Sensing and Spectral Geology*. Littleton, Society of Economic Geologists, 270 p.

Kaufman A.J., Sial A.N., Frimmel H.E., Misi A. 2009. Neoproterozoic to Cambrian palaeoclimatic events in southwestern Gondwana. In: Gaucher C., Sial A.N., Frimmel H.E., Helverson G.P. (eds.). *Neoproterozoic- Cambrian tectonics, global change and evolution: a focus on southwestern Gondwana*. *Developments in Precambrian Geology*, 16, Amsterdam, Elsevier, p. 369-388.

Pankhurst R.J. & Rapela C.W. (eds.). 1998. *The Proto- Andean margin of Gondwana*. London, Geological Society of London Special Publication, 142, 382 p.

Trompette R. 1994. *Geology of western Gondwana (2000–500 Ma)*. Rotterdam, Balkema, 350 p.

Papers in scientific meetings

Astini R., Ramos V.A., Benedetto J.L., Vaccari N.E., Cañas F.L. 1996. La Precordillera: un terreno exótico a Gondwana. In: 13° Congreso Geológico Argentino y 3° Congreso Exploración de Hidrocarburos. Buenos Aires, Actas, v. 5, p. 293-324.

Leite-Junior W.B, Bettencourt J.S., Payolla B.L. 2003. Evidence for multiple sources inferred from Sr and Nd isotopic data from felsic rocks in the Santa Clara Intrusive Suite, Rondonia, Brazil. In: SSAGI, South American Symposium on Isotope Geology. Salvador, Short Papers, p. 583-585.

Milani E.J. & Thomaz-Filho A. 2000. Sedimentary basins of South America. In: Cordani U.G., Milani E.J., Thomaz-Filho A., Campos D.A. (eds.). Tectonic evolution of South America. 31st International Geological Congress. Rio de Janeiro, p. 389-452.

Thesis and dissertations

Paes V.J.C. 1999. Geologia da quadrícula Alvarenga, MG, e a geoquímica: implicações geotectônicas e metalogenéticas. MS Dissertation, Instituto de Geociências, Universidade Federal de Minas Gerais, Belo Horizonte, 144 p.

Ávila C.A. 2000. Geologia, petrografia e geocronologia de corpos plutônicos paleoproterozoicos da borda meridional do Cráton São Francisco, região de São João Del Rei, Minas Gerais. PhD Thesis, Universidade Federal do Rio de Janeiro, Rio de Janeiro, 401 p.

Printed maps

Inda H.A.V. & Barbosa J.F. 1978. Mapa geológico do Estado da Bahia, escala 1:1.000.000. Salvador, Secretaria das Minas e Energia, Coordenação da Produção Mineral.

Mascarenhas J.F. & Garcia T.M. 1989. Mapa geocronológico do Estado da Bahia, escala 1:1.000.000. Texto explicativo. Salvador, Secretaria das Minas e Energia, Coordenação da Produção Mineral, 186 p.

Schobbenhaus C. (coord.). 1975. Carta Geológica do Brasil ao Milionésimo – Folha Goiás (SD 22). Texto explicativo. Brasília, Departamento Nacional da Produção Mineral, 114 p.

Internal reports

Internal reports will not be accepted, unless of open access for the scientific community and authorized by ad hoc consultants.

Submission checklist

The following list will be useful during the final checking of an article prior to sending it to the journal for review. Please consult this Guide for Authors for further details of any item. Ensure that the following items are present:

One author has been designated as the corresponding author with contact details:

- E-mail address
- Full postal address

All necessary files have been uploaded, and contain:

- Keywords
- All figure captions
- All tables (including title, description, footnotes)

Further considerations:

- Manuscript has been ‘spell-checked’ and ‘grammar-checked’.
- All references mentioned in the Reference list are cited in the text, and vice versa.
- Permission has been obtained for use of copyrighted material from other sources (including the Internet).

Rapidcommunications

Rapid communications are limited to 2000 words, including references. Summary and abstract are limited to 100 words. At the discretion of the editors, these communications may be scheduled for the first available edition.

Articles with accelerated review process

An accelerated review process may be requested for complete original studies, for which urgency of publication is adequately justified. At the discretion of the editors, these can be programmed for the first available edition. They must follow the same format described for original articles.

Editorials

Editorials should cover some aspect of the broad spectrum of the Geological Sciences. They will be authored by the editors of BJT, by people linked to the Brazilian Geological Society or by industry personalities. These documents will not be submitted to peer review and will be published at the discretion of the editors.

Review

articles

Review articles should cover relevant topics of Geology. These articles may be requested by the editors, but recognized experts may spontaneously submit review articles in their field of expertise. In this case, potential authors should contact the editors to ascertain their interest prior to submitting the article

ANEXO B – REGRAS DE FORMATAÇÃO DA INTERNATIONAL GEOLOGY REVIEW (ARTIGO 2)

INTERNATIONAL GEOLOGY REVIEW

Article Types

Research Article

- Should be written with the following elements in the following order: title page; abstract; keywords; main text introduction, materials and methods, results, discussion; acknowledgments; declaration of interest statement; references; appendices (as appropriate); table(s) with caption(s) (on individual pages); figures; figure captions (as a list)
- Should contain an unstructured abstract of 200 words.
- At least 3 keywords.

Style Guidelines

Please use British (-ize) spelling style consistently throughout your manuscript.

Please use single quotation marks, except where ‘a quotation is “within” a quotation’.

Please note that long quotations should be indented without quotation marks.

Your paper should be compiled in the following order: title page; abstract; keywords; main text, introduction, materials and methods, results, discussion; acknowledgments; declaration of interest statement; references; appendices (as appropriate); table(s) with caption(s) (on individual pages); figures; figure captions (as a list).

Checklist: What to Include

1. **Author details.** All authors of a manuscript should include their full name and affiliation on the cover page of the manuscript. Where available, please also include ORCIDiDs and social media handles (Facebook, Twitter or LinkedIn). One author will need to be identified as the corresponding author, with their email address normally displayed in the article PDF (depending on the journal) and the online article. Authors’ affiliations are the affiliations where the research was conducted. If any of the named co-authors moves affiliation during the peer-review process, the new affiliation can be given as a footnote. Please note that no changes to affiliation can be made after your paper is accepted.
2. You can opt to include a **video abstract** with your article. Find out how these can help your work reach a wider audience, and what to think about when filming.
3. **Funding details.** Please supply all details required by your funding and grant-awarding bodies as follows:

| | | | |
|---|-----------------|---------------|---------------|
| <i>For</i> | <i>single</i> | <i>agency</i> | <i>grants</i> |
| This work was supported by the [Funding Agency] under Grant [number xxxx]. | | | |
| <i>For</i> | <i>multiple</i> | <i>agency</i> | <i>grants</i> |
| This work was supported by the [Funding Agency #1] under Grant [number xxxx]; [Funding Agency #2] under Grant [number xxxx]; and [Funding Agency #3] under Grant [number xxxx]. | | | |
4. **Disclosure statement.** This is to acknowledge any financial or non-financial interest that has arisen from the direct applications of your research. If there are no relevant competing interests to declare please state this within the article, for example: *The authors report there are no competing interests to declare.*
5. **Data availability statement.** If there is a data set associated with the paper, please provide information about where the data supporting the results or analyses presented in the paper can be found. Where applicable, this should include the hyperlink, DOI or other persistent identifier associated with the data set(s). Templates are also available to support authors.

6. **Data deposition.** If you choose to share or make the data underlying the study open, please deposit your data in a recognized data repository prior to or at the time of submission. You will be asked to provide the DOI, pre-reserved DOI, or other persistent identifier for the data set.
7. **Supplemental online material.** Supplemental material can be a video, dataset, fileset, sound file or anything which supports (and is pertinent to) your paper. We publish supplemental material online via Figshare. Find out more about supplemental material and how to submit it with your article.
8. **Figures.** Figures should be high quality (1200 dpi for line art, 600 dpi for grayscale and 300 dpi for colour, at the correct size). Figures should be supplied in one of our preferred file formats: EPS, PS, JPEG, TIFF, or Microsoft Word (DOC or DOCX) files are acceptable for figures that have been drawn in Word. For information relating to other file types, please consult our Submission of electronic artwork document.
9. **Tables.** Tables should present new information rather than duplicating what is in the text. Readers should be able to interpret the table without reference to the text. Please supply editable files.
10. **Equations.** If you are submitting your manuscript as a Word document, please ensure that equations are editable. More information about mathematical symbols and equations.
11. **Units.** Please use SI units (non-italicized).

ANEXO C – COMPROVANTE DE ACEITE DO ARTIGO 1**yahoo!mail**

Brazilian Journal of Geology - Decision on Manuscript ID BJGEO-2019-0137.R2 3

Yahoo/Entrada ☆

**Claudio Riccomini** <onbehalf@manuscriptcentral.com>
Para: tatiana_geologia@yahoo.com.br

qua., 31 de mar. de 2021 às 13:28 ☆

31-Mar-2021

Dear Mrs. Ribeiro:

It is a pleasure to accept your manuscript entitled "Evidence for paleoproterozoic phosphogenesis in the Salvador-Curaçá Orogen (Tanque Novo-Ipirá Complex), northeastern São Francisco Craton, Brazil" in its current form for publication in the Brazilian Journal of Geology. The comments of the reviewer(s) who reviewed your manuscript are included at the foot of this letter.

Thank you for your fine contribution. On behalf of the Editors of the Brazilian Journal of Geology, we look forward to your continued contributions to the Journal.

Sincerely,
Dr. Claudio Riccomini
Editor-in-Chief, Brazilian Journal of Geology
riccomin@usp.br

ANEXO D – COMPROVANTE DE PUBLICAÇÃO DO ARTIGO 1

DOI: <https://doi.org/10.1590/2317-4889202120190137>

The screenshot shows the article page for "Evidence of Paleoproterozoic phosphogenesis in the Salvador-Curaçá Orogen (Tanque Novo-Ipirá Complex), northeastern São Francisco Craton, Brazil". The page includes a navigation menu, a table of contents, an abstract, and the beginning of the introduction.

ARTICLE - Braz. J. Geol. 51 (03) - 2021 - <https://doi.org/10.1590/2317-4889202120190137> COPY

Evidence of Paleoproterozoic phosphogenesis in the Salvador-Curaçá Orogen (Tanque Novo-Ipirá Complex), northeastern São Francisco Craton, Brazil

AUTHORSHIP SCIMAGO INSTITUTIONS RANKINGS

- » Abstract
- » Text
 - INTRODUCTION
 - REGIONAL AND LOCAL ...
 - ANALYTICAL METHODS
 - FIELD ASPECTS AND FE...
 - RESULTS
 - DISCUSSION
 - CONCLUSIONS
 - » ACKNOWLEDGMENTS
 - » References
 - » ARTICLE INFORMATION
 - » Supplementary data
 - » Publication Dates
 - » History

Abstract

This paper analyzes mineralogical, geochemical, and geochronological aspects, along with the effect of hydrothermal/metamorphic overprints, to identify the presence of primary phosphate as well as depositional and paleoenvironmental conditions in marble and calcisilicate sequences recrystallized under transitional amphibolite-granulite metamorphic conditions in the Tanque Novo-Ipirá Complex within the Salvador-Curaçá Orogen, northeastern São Francisco Craton, state of Bahia, Brazil. Petrographic studies have identified up to 10 vol % disseminated apatite and whole-rock P_2O_5 contents up to 3.2 wt %. Post-depositional events affected the lithofacies to varying degrees. Late hydrothermalism did not modify the rare earth element and yttrium (REEY) patterns considerably. When normalized to Post-Archean Australian Shale (PAAS), these lithofacies are marked by flat pattern REEY, true negative Ce anomalies, and positive Y and Gd. The highly variable Eu anomalies were inherited from the source composition but may have been affected by interaction with fluids. U-Pb LA-ICP-MS (laser ablation multicollector inductively coupled plasma mass spectrometry) ages indicate a maximum depositional age of 2128 Ga, as well as Paleoproterozoic and Neoproterozoic sources. Samples with anomalous phosphorus show Y/Ho ratios >30 and Ce/Ce* anomalies between 0.53 and 1.0 with an average of 0.70, suggesting a sub-oxic environment for phosphate precipitation.

KEYWORDS:
phosphogenesis; Paleoproterozoic; Tanque Novo-Ipirá Complex; São Francisco Craton; paleobasin

INTRODUCTION

Calcisilicate rocks and marbles are common in metamorphic terrains associated with orogenic belts and are often intercalated with other

ANEXO E – COMPROVANTE DE SUBMISSÃO DO ARTIGO 2



Dear Tatiana Ribeiro,

Thank you for your submission.

| | |
|-------------------------|--|
| Submission ID | 244302730 |
| Manuscript Title | POSITIVE $\delta^{13}\text{C}_{\text{carb}}$ EXCURSIONS IN PALEOPROTEROZOIC MARBLES FROM THE NORTHEAST SÃO FRANCISCO CRATON, BRAZIL: A REVIEW, NEW DATA AND PHOSPHOGENETIC AND GEOTECTONIC IMPLICATIONS. |
| Journal | International Geology Review |

If you made the submission, you can check its progress and make any requested revisions on the [Author Portal](#)

Thank you for submitting your work to our journal.

If you have any queries, please get in touch with journalshelpdesk@taylorandfrancis.com.

Kind Regards,
International Geology Review Editorial Office